



**University of
Nottingham**
UK | CHINA | MALAYSIA

Core-level Spectroscopy of Photoactive Materials

Thesis submitted to the University of Nottingham for the degree of
Doctor of Philosophy, January 2023.

Jack R. Hart

14342025

Supervised by

**Dr. James O'Shea
Dr. Richard Campion**

Abstract

In order for next generation solar technologies to continue to improve, detailed chemical and electronic information is essential. Core-level spectroscopies, such as X-ray photoelectron spectroscopy, X-ray absorption spectroscopy, and resonant photoelectron and Auger spectroscopies are capable of providing this information. These techniques have been used for decades across many systems but are limited to ultra-high vacuum pressures, however more recently measurements at ambient pressures have become possible. The thesis presented herein applies core-level spectroscopies to two systems: dye sensitised solar cells and solar water splitting. In the former, ultra-high vacuum core-level spectroscopies are employed to probe the chemical and electronic coupling between the dye and substrate. For the latter, ambient-pressure X-ray photoelectron spectroscopy allows the oxidation of a potential solar water splitting catalyst to be monitored.

To begin, a relatively simple dye, C343, is investigated on different mesoporous substrates; TiO_2 and SrTiO_3 . These samples were prepared ex-situ and, in the case of TiO_2 , compared to samples prepared by thermally evaporating C343 in-situ. By also comparing to a multilayer of dye, a detailed description of how the dye is bonded to the substrates is presented and the density of states probed. To assist in the dye's analysis, a similar dye, C334, is also investigated.

Next, core-level spectroscopies are applied to a more complicated dye-TiO₂ system involving the well-known dye N3 as the sensitiser. Here, the bonding to the surface is confirmed by X-ray photoelectron spectroscopy. In addition, resonant Auger electron spectroscopy is used to quantify both charge delocalisation within the molecule as well as injection into the substrate conduction band. Hard X-rays are used to study excitations from both the S 1*s* and Ru 2*p*_{3/2} core levels. The effect of the substrate is seen on the calculated charge transfer dynamics, and a picture of charge transfer from the thiocyanate ligand discussed.

Two further dye-TiO₂ systems are investigated using core-level spectroscopies; RuP and RuC. These dyes are qualitatively very similar, differing only in their anchoring group. Resonant Auger electron spectroscopy is again employed, alongside resonant photoelectron spectroscopy, to quantify the charge injection and delocalisation times of both dyes. In this context, the measurements are a probe of how the anchoring group influences the injection dynamics of dye-sensitised solar cells. It is found that both dyes are capable of sub-femtosecond charge injection in the Ru 2*p*_{3/2} excited regime, however that RuP is favoured for its slower relaxation.

Finally, ambient pressure X-ray photoelectron spectroscopy is used to study the oxidation chemistry of a prospective solar water splitting catalyst: TiSi₂. Both powder and thin-film samples are investigated, where the latter were employed in order to remove the natural oxidation caused by air. To do so, different passivation layers were investigated to preserve the TiSi₂ layer. From the measurements, it is suggested that the reported catalytic activity of TiSi₂ is related to the growth of a sub-stoichiometric silicon oxide, and the minimisation of SiO₂ at the TiSi₂ surface.

List of Publications

R. Temperton, J. Hart, N. Verykokkos, E. Gibson, and J. N. O’Shea, “A soft x-ray probe of a titania photoelectrodesensitized with a triphenylamine dye,” *J. Chem. Phys.*, vol. 154, no. 23, pp. 234707, 2021.

J. Castillo-Rodriguez, P. Ortiz, M. Isaacs, N. P. Martinez, J. N. O’Shea, J. Hart, R. Temperton, X. Zarate, D. Contreras, and E. Schott, “Highly efficient hydrogen evolution reaction, plasmon-enhanced by AuNP-L-TiO₂NP photocatalysts”, *New J. Chem.*, vol. 44, pp. 16491-16500, 2020.

S. Doherty, J. G. Knight, T. Backhouse, T. S. T. Tran, R. Paterson, F. Stahl, H. Y. Alharbi, T. W. Chamberlain, R. A. Bourne, R. Stones, A. Griffiths, J. P. White, Z. Aslam, C. Hardare, H. Daly, J. Hart, R. H. Temperton, J. N. O’Shea, and N. H. Rees, “Highly efficient and selective aqueous phase hydrogenation of aryl ketones, aldehydes, furfural and levulinic acid and its ethyl ester catalyzed by phosphine oxide-decorated polymer immobilized ionic liquid-stabilized ruthenium nanoparticles,” *Catal. Sci. Technol.*, vol. 12, no. 11, pp. 3549-3567, 2022.

H. Gotfredsen, J-R. Deng, J. M. Van Raden, M. Righetto, J. Hergenahn, M. Clarke, A. Bellamy-Carter, J. Hart, J. O’Shea, T. D. W. Claridge, F. Duarte, A. Saywell, L. M. Herz, and H. L. Anderson, “Bending a photonic wire into a ring,” *Nat. Chem.*, vol. 14, no. 12, pp. 1436-1442, 2022.

Acknowledgements

Sat here at the end of four (and a bit) years, hovering over the ‘submit’ button, it is easy to forget one of the defining things about a PhD; they are hard. As such, this thesis would not be what it is without the vast support of those around me, professionally and personally.

First and foremost, I would like to thank my supervisor James O’Shea, for his support, patience, and guidance. I also would like to thank Rob Temperton for taking the brunt of what can only be described as a barrage of questions when on beamtime or in A15. Both have gone above and beyond and I am incredibly grateful. I also thank Richard Campion with whom it has been an absolute pleasure to demonstrate for. I thank Andrew Rushforth, whose heroic effort in fabricating the thin film TiSi_2 samples is greatly appreciated. I also thank the staff at FlexPES, I09, and GALAXIES for their support on beamtime, without which this thesis would not have been possible.

I thank my friends: Ben, Josh, Magdi, James W., James F., Marcus, the entire D-floor office, and all those in computational chemistry. They have made this time amazing, particularly for someone who was terrified that their PhD would be lonely. I thank my family: Mum, Dad, Meg, Hayley, and Zak, who may not know what it is I do exactly, only that I love it, which has always been enough for them. Particular thanks goes to my partner Gabbie, whose support during my PhD, if listed, would add another chapter to this thesis.

Contents

| | |
|--|------------|
| Abstract | i |
| List of Publications | iii |
| Acknowledgements | iv |
| Abbreviations | 1 |
| Chapter 1 Photovoltaics for Energy Production | 1 |
| 1.1 Solar Energy Conversion | 1 |
| 1.2 Dye-sensitised Solar Cells | 2 |
| 1.3 Solar Water Splitting | 8 |
| 1.4 Suitability of Core-level Spectroscopies | 14 |
| 1.5 Aims & Structure of the Thesis | 16 |
| Chapter 2 Methods | 17 |
| 2.1 X-ray Photoelectron Spectroscopy | 19 |
| 2.2 X-ray Absorption Spectroscopy | 31 |
| 2.3 Resonant Photoelectron Spectroscopies | 35 |
| 2.4 X-ray Sources | 44 |
| 2.5 Sample Preparation Techniques | 47 |
| 2.6 Adjacent Techniques | 49 |
| Chapter 3 Synchrotron-based Electron Spectroscopy of Coumarin-Sensitised Photoanodes Supported by Laboratory XPS | 51 |
| 3.1 Introduction | 53 |
| 3.2 Methods | 54 |
| 3.3 Results & Discussion | 60 |

| | | |
|------------------|--|------------|
| 3.4 | Conclusions | 82 |
| Chapter 4 | Competition between sub-femtosecond charge injection and relaxation in a Ru complex at the S 1s and Ru 2p_{3/2} edges | 84 |
| 4.1 | Introduction | 86 |
| 4.2 | Methods | 87 |
| 4.3 | Results & Discussion | 90 |
| 4.4 | Conclusion | 111 |
| Chapter 5 | Influence of the anchoring group on the charge transfer dynamics in Ru-based Dye-sensitised Solar Cells | 113 |
| 5.1 | Introduction | 115 |
| 5.2 | Methods | 117 |
| 5.3 | Results & Discussion | 120 |
| 5.4 | Conclusion | 138 |
| Chapter 6 | Oxidative behaviour of TiSi₂ at ambient pressures for solar water splitting | 140 |
| 6.1 | Introduction | 142 |
| 6.2 | Methods | 143 |
| 6.3 | Results & Discussion | 145 |
| 6.4 | Conclusion | 172 |
| Chapter 7 | Conclusions | 174 |
| | Bibliography | 177 |
| | Appendices | 206 |

Chapter 1

Photovoltaics for Energy

Production

1.1 Solar Energy Conversion

Solar technology is widely expected to feature prominently in any future energy mix that shuns carbon-rich fuels. In 2021, solar photovoltaics (PV) accounted for 60% of the global increase of renewables and remains the cheapest way to expand electricity capacity [1]. It is largely for this reason that direct conversion of solar energy into usable power continues to attract significant research activity. Despite this, at present, the capacity of solar photovoltaics (PV) lags behind that required to achieve net zero [2]. As such, further cost reductions in solar PV could make integration with more costly energy storage technologies more economical, and thus increase market penetration [3]. This is essential to continue fostering widespread adoption of solar PV and, as a result, third generation solar cells continue to attract significant attention.

As alluded to above, one of the biggest factors holding back solar PV (and indeed most renewable technologies) is the lack of a suitable energy storage solution. One solution could be to integrate battery storage into PV infrastructure [4]. Alternatively, the energy could be converted to a fuel instead; the simplest of which is hydrogen. Termed photoelectrochemical (herein referred to as solar) water splitting, the solar energy absorbed would be used to drive electrolysis of water molecules at a photoactive material's surface. Related to this process is direct photocatalysis, which shares much of the underlying physics of solar water splitting. The hydrogen produced would then be collected and stored for future use. This has one clear advantage over fossil fuels; hydrogen burns clean. Furthermore, hydrogen is a crucial feedstock for a number of industries; for example as a reducing agent in steel manufacturing or for ammonia production. At present, hydrogen is produced overwhelmingly from steam methane reforming, emitting CO₂ [5].

1.2 Dye-sensitised Solar Cells

Over the decades, dye sensitised solar cells (DSSCs) have been extensively researched as a low-cost alternative to traditional silicon photovoltaics, with the potential to reduce the impact of energy generation on the climate [6, 7, 8]. Unlike more traditional solar cell technologies, DSSCs are highly versatile. They have shown high power conversion efficiencies under both AM 1.5G (a standard solar spectrum) and ambient light conditions [9], show promise for large scale manufacturing [10], can be made flexible [11], and come in a range of colours [12]. Despite practical efficiencies approaching their theoretical maximum [13, 14, 15], they are lower compared to both existing solar cells and those offered by their third generation

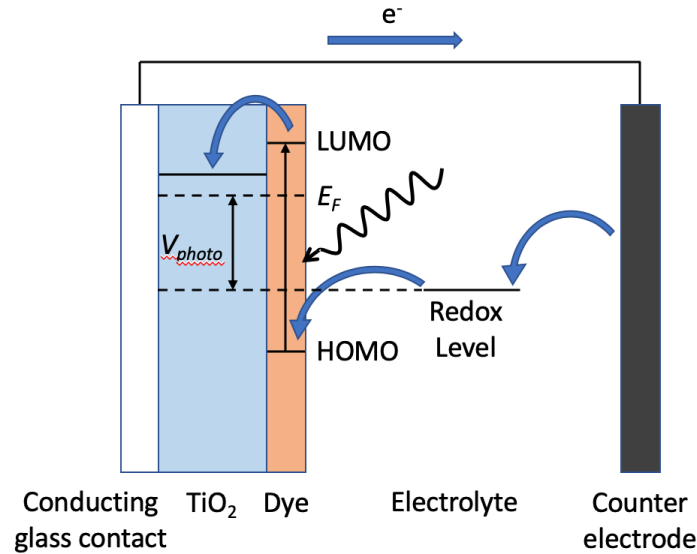


Figure 1.1: Operating principal of a DSSC. Light is absorbed by the dye, exciting an electron from the highest occupied molecular orbital to the lowest unoccupied molecular orbital. From there, it transfers to the conduction band of the semiconducting substrate, and conducts through a glass back contact to the counter electrode. The circuit is completed by a redox couple, which regenerates the dye (fills the valence hole) and is itself regenerated by the counter electrode.

counterparts [16]. Aside from low efficiencies, many dyes rely on expensive noble metals [17] or suffer from stability issues [18, 19]. Critically, however, the energy payback time for DSSC devices is approximately 1 year, much shorter than the 3 years for silicon solar cells [20]. Therefore, despite their drawbacks, DSSCs continue to represent an attractive candidate for niche solar applications.

1.2.1 Mechanism

DSSCs operate by decoupling charge carrier generation and transportation, wherein the former is facilitated by a photoactive dye and the latter through a semiconductor substrate [21, 22]. This sidesteps the trade off between these properties often found in solar cell materials. A simplified operating scheme is shown in figure 1.1. Here, light is absorbed by a dye chemisorbed

to a mesoporous TiO_2 layer, generating electron-hole pairs. The frequency of light absorbed is governed by the energy separation between the dye's occupied and unoccupied levels, the smallest of which is the gap between the highest occupied (HOMO) and lowest unoccupied (LUMO) molecular orbitals. With the dye in an excited state, the electron tunnels from the dye into the TiO_2 layer, passes to the conducting glass back contact, through an external load, before finishing at the counter electrode. In the meantime, the oxidised dye is regenerated by electron transfer from the electrolyte redox couple. Finally, the original photo-excited electron at the counter electrode reduces the redox couple, completing the circuit. The extractable photovoltage provided by the cell is then given by the difference between the Fermi level of TiO_2 and the redox potential of the couple used. The photovoltage is sometimes described by referencing the conduction band minimum (CBM) instead [23]. While this is where the electron is passed, there is an inherent loss of energy as it makes its way around the circuit equal to the difference between the conduction band edge and Fermi level. As such, this means that the extractable photovoltage is always less than the dye's 'bandgap', no matter how well matched the LUMO, CBM, HOMO, and redox potential are. Energy can also be lost via other mechanisms on top of this [13]. Typically, the back contact onto which TiO_2 is printed is conducting glass (e.g. fluorine-doped tin oxide, FTO) and the electrolyte used the iodide/triiodide redox couple [24].

The picture presented in figure 1.1 has changed little since the first demonstration of viable power generation from a DSSC [21]. As such, research has largely focused on addressing the issues around DSSC efficiency and stability. The first of these areas is linked to the suppression of several loss mechanisms within the cell. For example, back-transfer of the excited electron from the TiO_2 conduction band to the oxidised dye or oxidised redox

couple may occur if regeneration (i.e. filling the electron holes) is slow. The iodide/triiodide redox couple excels at regenerating the oxidised dye, however its energetics relative to the TiO_2 conduction band lead to a diminished photovoltage [23, 25]. The example of the iodide/triiodide redox couple illustrates well the difficulty in optimising DSSC energetics. Often, the photovoltage and photocurrent cannot be altered in isolation, which can be visualised using figure 1.1. If the redox level were brought closer in energy to the HOMO, the photovoltage is increased. However, simultaneously the impetus for an electron from the redox couple to regenerate the dye is reduced. Similar considerations apply to the LUMO and CBM. It has been shown that an accumulation of charge in the TiO_2 layer increases the occupation of its trap states, increasing the rate of recombination with the oxidised dye in turn [26]. As such, increasing the energy separation between the CBM and LUMO may yield increasingly rapid injection, but often comes at the cost of increased recombination [27]. Considerations on what constitutes ‘fast enough’ for electron injection are discussed further in chapter 5. The difficulties in maximising both photovoltage and photocurrent are in addition to other losses familiar to other solar technologies, such as a sufficiently long excited state.

The aforementioned issues surrounding DSSC efficiency are important; however, the most prominent limitation on their practical application is their stability. Firstly, they are prone to the electrolyte leaking, prompting research into quasi-solid, gel, electrolytes [28, 29]. Secondly, the dyes themselves can degrade, usually via photodegradation by UV or by desorbing from the TiO_2 [30]. Combined with issues relating to the price of conducting glass [20], it is for these reasons that the roll-out of DSSCs is limited to niche applications, at present.

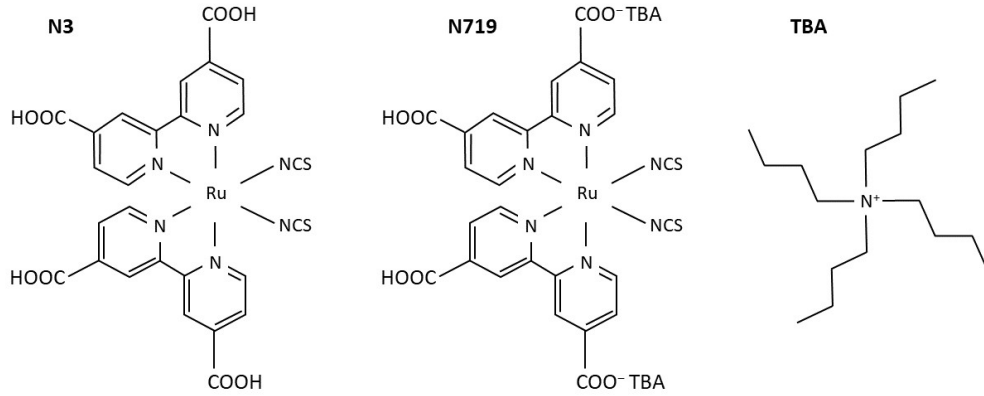


Figure 1.2: Schematic of both N3 and N719 dyes, including the tributylammonium (TBA) counter ion present in N719. Both dyes are similar in structure, save where TBA deprotonates two of N719's carboxylic acid groups.

1.2.2 Noble-metal DSSCs

Historically, DSSCs employing ruthenium dyes have been the go-to choice for fabricating cells with good performance. The first DSSC used one such dye; a trimer formed through the CN ligands of three ruthenium complexes [21, 31]. The efficiency of this type of cell was found to be around 7% under simulated sunlight, rising to 12% under diffuse daylight [21]. At the time, this represented a significant improvement in the field, but still far from the efficiencies on offer from conventional PV technologies. Following on from this work, the same group presented a dye similar in structure to the central unit of the trimer system as a sensitiser in its own right, *cis*-bis(isothiocyanato)bis(2,2-bipyridyl-4,4-dicarboxylato)-ruthenium(II), which has become commonly known as 'N3' [32]. Here, the two CN ligands were substituted for thiocyanate, resulting in a new efficiency benchmark at 10%, whilst taking advantage of the stability, efficient injection, and light absorption characteristics of this class of dyes [32]. Further work into ruthenium DSSCs eventually led to N3 being supplanted by its derivative, N719. This dye is essentially N3, but deprotonated by tetrabutylammonium, where it was found that the triple

deprotonated form of the dye gave the highest efficiency (11.2 %) [33]. This improvement in efficiency was attributed to an increase in the photovoltage caused by the Fermi level shifting more negatively compared to more protonated forms of N719 [33].

While the above describes the main step-changes in improving the efficiency of ruthenium DSSCs, considerable research has focussed on addressing their other issues. One example is replacing the thiocyanate ligands present in N3 and N719 that, while stable relative to the first dyes tested for DSSC applications, can bind to the central Ru ion through either the nitrogen or sulphur atoms and are easily substituted by undesirable species [34]. To combat this, new dyes have been synthesised without thiocyanate ligands, which have greater molar extinction coefficients compared to N719 [35]. Another example is seen in the addition of highly conjugated groups to ruthenium dye complexes, which have also been reported to increase the molar extinction coefficient and efficiency relative to N719 [36].

1.2.3 Organic DSSCs

Although they have traditionally held the highest efficiencies, there is an inherent issue with DSSCs based on ruthenium dyes; ruthenium is an expensive, noble, metal. As such, much research has been devoted to development metal-free, purely organic, dyes. In general, efficiencies have been lower compared to their ruthenium counterparts, but they are cheaper and have high extinction coefficients [37]. However, in recent years organic dyes have surpassed the efficiency records set by ruthenium dyes under laboratory conditions. One example of this is seen from the dye known as R6, which reached an efficiency of 12.6 % [12]. This dye possess a relatively long excited state lifetime relative to injection and good photostability, whilst

also expanding the range of DSSC colours to include blue hues [12].

The current record holder of DSSC efficiency is held by the organic dye LEG4, co-sensitised with an alkoxysilyl-anchor dye named ADEKA-1 [15], yielding an efficiency of 14.3 %. The success of this work is attributed to two factors: the use of a cobalt-based electrolyte and cosensitising the TiO_2 . The former improved the photovoltage of the cell, caused by the redox level of the cobalt electrolyte being lower relative to the traditional iodide/triiodide couple, however the decrease in photocurrent had to be compensated for elsewhere in the cell [15, 38]. This again illustrates the difficulty in optimising parameters separately, discussed above. Co-sensitisation of the TiO_2 with two dyes resulted in an improvement in the absorption of the solar spectrum, in addition to taking advantage of a synergistic charge transfer mechanism; where ADEKA-1 passed its excited electron to LEG4, which in turn passes it more efficiently to the TiO_2 [15]. The above work is a good example of how co-sensitisation can improve the efficiency of DSSCs, and has been employed more recently to combine ruthenium and organic dyes, enhancing the efficiency of the subsequent cell above that achievable using either one individually [39]. Despite holding the record for efficiency, organic dyes have their drawbacks. These include issues around aggregation of the dyes, a narrower spectral absorption, and shorter excited state lifetimes [40].

1.3 Solar Water Splitting

While DSSCs offer a route towards decarbonising electrical power generation in niche applications, solar water splitting has the potential to decarbonise broad sections of the global economy. However, efficiencies are

generally low, especially compared to running an electrolyser using solar PV, which has been shown to deliver a solar-to-hydrogen (STH) efficiency of 30 % [41]. This being said, there are advantages from solar water splitting compared to direct coupling of an electrolyser to PV. Most importantly, hydrogen from solar water splitting has the potential to be cheaper than from solar powered electrolysis [42]. If possible, this will largely be due to the fact that solar water splitting requires no components to integrate light absorption and hydrogen generation, as they occur at the same place (depending on the strategy used). Common to all designs, however, is the expectation that fewer packaging or interconnections will be needed [43].

At present, solar water splitting is much less technologically mature compared to DSSCs; despite being researched for a comparable amount of time [44], there remains no universally agreed upon strategy. In addition, DSSCs have more or less met the efficiency threshold for practical applications; as discussed above it is other factors that limit their adoption. This is not the case for solar water splitting cells, which have not reached an efficiency high enough to be considered economically feasible; 10 % is the threshold broadly recognised [45]. As such, much work remains to boost the efficiency of the process before it can be considered viable.

1.3.1 Mechanism

The chemistry involved in both DSSC and solar water splitting technologies is similar (see section 1.2.1), save that hydrogen is produced in the latter rather than electricity. This occurs through the following half reactions:



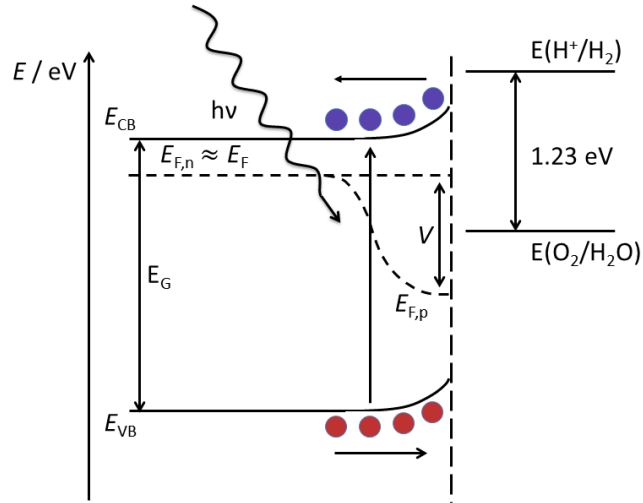


Figure 1.3: Illustrative example of solar water splitting using a semiconducting photoanode. An electron-hole pair is generated by the light, and the electron and hole driven in different directions by band bending at the surface. In this example, holes oxidise water molecules into oxygen and an external potential is needed to evolve hydrogen. The change in population of the electrons and holes from equilibrium gives the photovoltage, V . Adapted from reference [46].



where 1.23 eV of energy is required at minimum to split water by equation 1.1c. These half reactions are termed the oxygen (1.1a) and hydrogen (1.1b) evolution reactions respectively. The energy associated with the overall reaction corresponds to a wavelength of about 1000 nm, meaning visible light carries more than enough energy for the reaction. However, as with traditional electrolysis, there are energy losses and kinetics to consider. For example, energy is inherently lost moving the electron from the photoanode to the counterelectrode, from the holes moving to the water molecules, and ohmic losses are present. Kinetically, extra energy is needed to provide the impetus for charge transfer. Usually, a band gap around 2

eV is often regarded as the compromise between a high enough photovoltage and sufficient photocurrent in the absence of an external bias [47]. This latter point is important; clearly if the band gap is greater, more energetic light is absorbed, and the matching to the solar spectrum poor.

There are several strategies worth mentioning that photoelectrochemically evolve hydrogen from water. Firstly, illustrated in figure 1.3, the semiconductor catalyst can be connected to a metal counter electrode. Here, a photon is absorbed by the semiconductor creating an electron-hole pair, which gets separated by band bending induced by contact with the electrolyte. The holes migrate to the semiconductor-electrolyte interface and oxidise water molecules, whereas the electrons move to a counter electrode. What happens next depends on the alignment between the bands of the semiconductor and both redox potentials of OER and HER. If both potentials fall within the band gap, the electrons and holes have sufficient energy for HER and OER respectively. As a result, both gases are evolved. As mentioned above, this would require a wide gap semiconductor, leading to poor solar-to-hydrogen (STH) efficiencies. Conversely, only one redox potential may fall within the band gap, in which case only that gas is evolved; typically oxygen from n-type and hydrogen from p-type photoanodes. In this case, a bias is required to evolve the companion gas and complete the circuit.

Unlike DSSCs, the photovoltage for solar water splitting from semiconducting photoanodes is given by the difference between the quasi-Fermi levels for electrons and holes respectively. These describe the Fermi level under non-equilibrium conditions, such as under illumination, and are worth explaining. Consider an n-type semiconductor, which by definition has far more conducting electrons than holes. Under illumination, the percentage increase of holes is far greater than that of the electrons, and the semi-

conductor is no longer in equilibrium. As a result, the Fermi level is no longer well defined, and the Fermi-Dirac distribution no longer applies in its traditional form. To understand how the charge carriers are distributed, the concept of ‘quasi’ thermal equilibrium is introduced. This states that, provided the perturbation is not too strong or fast and that the carriers relax within their respective bands faster than they recombine, the carriers will distribute themselves as though at equilibrium in their band. As a result, individual Fermi-levels and effective temperatures can be defined. To see how the splitting between the quasi-Fermi levels is equivalent to the photovoltage, how energy is extracted from a solar cell needs to be considered. To measure the photovoltage, an electrical connection to the semiconductor must be made. This aligns the Fermi-level of the metal and semiconductor and the charge carriers lose some energy by migrating from their band to the metal Fermi level. This was briefly mentioned above and explains why the photovoltage is inherently less than the band gap energy.

Figure 1.3 describes only the simplest water splitting architecture and is similar to the first practical setup, which used a TiO_2 photoanode and platinum counter electrode without an external bias [44]. This showed that TiO_2 was able to split water from the energy of its bandgap alone, however, like most metal oxides its band gap is too wide to absorb much below UV light. This is in addition to problems common to most solar water splitting cell designs, such as poor charge transport and the prevalence of recombination centres [48, 49].

1.3.2 Strategies to Improve Efficiency

There are several strategies that have been employed to improve upon the limitations mentioned above. Much research has been conducted on het-

erojunction photoanodes. These use p-n junction photoanodes to separate the charge carriers, thereby reducing recombination, however can lead to a lesser oxidative or reductive power overall due to energy losses as the carriers move through the junction [50]. Similarly, examples exist of heterojunction photoanodes internally biased by a photovoltaic material, which are capable of unassisted water splitting [51, 52]. Finally, semiconducting photocathodes have been used for HER in conjunction with photoanodes that deal with OER [53]. Detailed diagrams of these three approaches to solar water splitting can be found in reference [46], and while each represents a significant improvement over the original design discussed above [44], efficiencies remain far below that needed for their adoption.

One of the most appealing qualities of using TiO_2 (and other metal oxides) is that it exhibits exceptional stability under solar water splitting conditions. It is often for this reason TiO_2 is used to passivate less stable electrodes, where it doesn't play a leading role in the evolution of either gas [53, 54, 55]. As discussed above, it is let down by its wide band gap, and thus research has worked to address this. One strategy to reduce the band gap has been to dope the TiO_2 with non-noble metals. This has been shown experimentally to reduce the band gap for iron doped TiO_2 [56]. Theoretically, it has been suggested that iron and nickel doping improves light absorption, reduces recombination, and increases the reductive power of the electrons generated [57]. This was attributed to the introduction of states within the TiO_2 band gap and changes in electronegativity [57]. It is also worth noting a strategy somewhat similar to doping, where a metal oxide is decorated with noble-metal nanoparticles. Here, the performance of the photoanode is enhanced by surface-plasmon resonance of the nanoparticles, with gold typically used [58].

Finally, nanostructuring has been a common method of enhancing the per-

formance of photoanodes. Doing so offers benefits such as reducing the distance the carriers have to diffuse, enhancing surface area, and scattering light to increase absorption in the horizontal plane [59]. Nanostructuring can also reveal new information about materials themselves. An interesting example of this relates to TiO_2 , where a surface was found that showed a band gap of ~ 2 eV [60]. It was suggested this is caused by surface states within the band gap that arise from the largely Ti terminated surface [60]. In addition, a particularly reactive step-edge, which introduces a similar mid-gap state, was identified [60]. Both discoveries allow TiO_2 , one of the most intensively researched catalysts, to be viewed in new light.

1.4 Suitability of Core-level Spectroscopies

Common to both DSSCs and solar water splitting catalysts is the importance of charge transfer dynamics and knowledge of the chemical state of the systems. For DSSCs, how fast the excited electron is passed to the TiO_2 support has a large effect on the efficiency of the overall system, and knowing how a dye will bond to the surface is key. For solar water splitting catalysts, chemical information is arguably more important, particularly how the surface reacts with water. Core-level spectroscopies have been applied to both areas previously.

For solar water splitting, X-ray photoelectron spectroscopy (XPS) has been used to great effect. In its simplest application, XPS has been used to study catalysts at ultra-high vacuum (UHV), either post mortem or before they are used. This can confirm the makeup of the catalyst or gain electronic information, for example [53, 61]. More recently, ambient pressure XPS (AP-XPS) has provided the ability to characterise the sample *operando*

conditions; where the catalyst can be measured as it reacts. AP-XPS has been used to study photoanode/electrolyte interfaces under illumination [62] and the nature of the sites that water absorbs to on photoanodes [63, 64, 65]. None of the photoanodes investigated in the references highlighted in the previous line are particularly complex (e.g. BiVO_4 , TiO_2), which demonstrates how AP-XPS can provide information previously inaccessible at UHV pressures, even in the case of well known catalysts.

For DSSCs, aside from the utility of chemical information they provide, core-level spectroscopies are able to quantify charge transfer times. Within the DSSC field, this is most commonly investigated by transient absorption spectroscopy (TAS). In TAS, molecules are promoted to an excited state through a ‘pump’ laser pulse and measured by a ‘probe’ laser pulse after some time; the difference between the excited and ground state absorption spectra is then taken [66]. TAS has been used to provide information on the recombination and regeneration times, in addition to charge injection times [67, 68, 69]. However, while powerful, the time resolution of transient resolution measurements is ultimately limited by the frequency of the lasers used. Alternatively, core-level spectroscopies (specifically X-ray absorption and X-ray resonant spectroscopies) are capable of quantifying the charge transfer dynamics of a system with femtosecond precision via the ‘core-hole clock’ method. In some cases, sub-femtosecond precision can be achieved depending on the core-level under investigation [70]. Multiple examples exist of core-level spectroscopies quantifying the charge transfer time for dye molecules in this way, with femtosecond, or below, precision [71, 72, 73, 74]. Aside from the increased precision, these spectroscopies allow dye molecules to be probed with elemental specificity by virtue of the localised nature of the core energy levels. As such, charge transfer can be probed from different parts of the dye, which is not available using TAS.

1.5 Aims & Structure of the Thesis

This work aims to apply core-level spectroscopies to deepen understanding of charge transfer in DSSC systems and the chemical changes that occur at the surface of a relatively unexplored solar water splitting catalyst. For the former, the techniques that facilitate this understanding are demonstrated in chapter 3 on a simple organic dye, which are then used to quantify the charge injection and delocalisation times in chapter 4 for a more complicated ruthenium complex. The work on DSSC molecules culminates in chapter 5, where the core-hole clock method is used to access how the anchoring moieties of dyes can influence injection into TiO_2 . The final results chapter of the thesis, chapter 6, aims to demonstrate the ability of ambient pressure X-ray spectroscopy to characterise the processes that occur during heterogeneous catalysis. The material studied, TiSi_2 , is a highly reactive surface that exhibits unusual oxidation chemistry and is thus a prime candidate for this kind of study. Lastly, the conclusions of the thesis are summed up overall in chapter 7. What follows summarises the background physics of the techniques utilised and relevant processes conducted to meet these aims.

Chapter 2

Methods

Contents

| | | |
|-------|--|-----------|
| 2.1 | X-ray Photoelectron Spectroscopy | 19 |
| 2.1.1 | Technique | 19 |
| 2.1.2 | Processing | 23 |
| 2.1.3 | Interpretation | 26 |
| 2.1.4 | Ambient Pressure X-ray Photoelectron Spec- troscopy | 29 |
| 2.2 | X-ray Absorption Spectroscopy | 31 |
| 2.2.1 | Technique | 31 |
| 2.2.2 | Processing & Interpretation | 33 |
| 2.2.3 | Density of States Plots | 34 |
| 2.3 | Resonant Photoelectron Spectroscopies | 35 |
| 2.3.1 | Resonant Processes | 35 |
| 2.3.2 | Resonant Auger Electron Spectroscopy | 36 |
| 2.3.3 | Resonant Photoelectron Spectroscopy | 42 |
| 2.3.4 | Core-hole Clock Spectroscopy | 43 |
| 2.4 | X-ray Sources | 44 |
| 2.5 | Sample Preparation Techniques | 47 |
| 2.5.1 | Thermal Deposition | 47 |
| 2.5.2 | Electrospray Deposition | 48 |
| 2.6 | Adjacent Techniques | 49 |
| 2.6.1 | Scanning Electron Microscopy | 49 |
| 2.6.2 | Density Functional Theory | 49 |

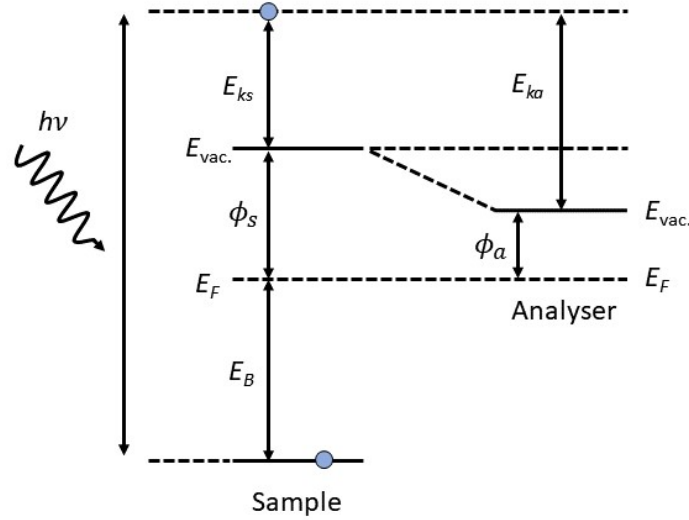


Figure 2.1: Sketch of the working principle of XPS. The energy given to the electron from the photon is split into three parts: bringing the electron to the Fermi level, E_F , overcoming the work function of the sample, with the rest going into the kinetic energy of the electron. Also shown is how the photoelectron is measured by the analyser. Here, subscript ‘s’ denotes the sample and ‘a’ the analyser.

2.1 X-ray Photoelectron Spectroscopy

2.1.1 Technique

X-ray photoelectron spectroscopy (XPS) is a technique that enables the chemical environment of a sample to be investigated in great detail. It relies on the photoelectric effect, where an incoming photon has sufficient energy to ionise the material under investigation. By measuring the kinetic energy, the binding energy of the photoelectron before ionisation can be determined by energy conservation

$$h\nu = E_B + E_{ks} + \phi_s \quad (2.1a)$$

$$E_B = h\nu - E_{ks} - \phi_s \quad (2.1b)$$

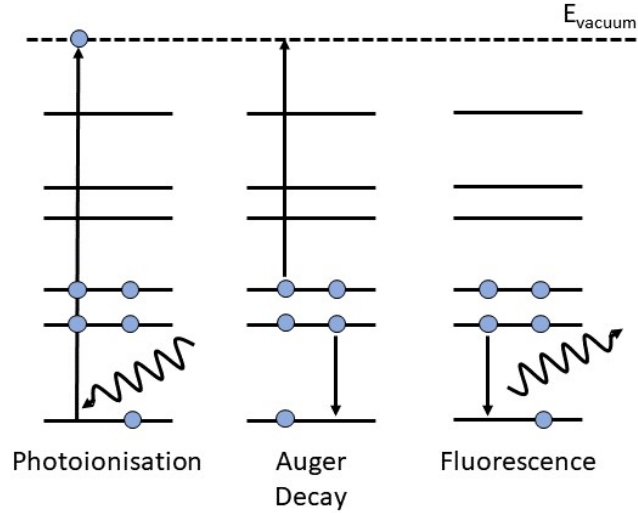


Figure 2.2: Energy level diagrams of XPS and the relaxation processes that occur post ionisation: Auger decay (non-radiative) and fluorescence (radiative).

where $h\nu$ is the photon energy, E_B the binding energy, E_{ks} the kinetic energy, and ϕ_s the work function of the sample. This is illustrated in figure 2.1. However, the photoelectron's kinetic energy must be measured somehow, and the analyser will have its own work function, ϕ_a , which is also shown in figure 2.1. Depending on the relative magnitude of ϕ_s to ϕ_a , the electrons either speed up or slow down as they are detected by the analyser (the former is shown in figure 2.1). Thus, upon measurement, equation 2.1 becomes

$$E_B = h\nu - E_{ka} - \phi_s + (\phi_s - \phi_a) \quad (2.2a)$$

$$E_B = h\nu - E_{ka} - \phi_a \quad (2.2b)$$

From the diagram, equation 2.2 makes sense, as its terms equal the photon energy arrow on the left of figure 2.1. Importantly, the sample work function is not required to measure the photoelectrons' kinetic energy; only the analyser's. As such, ϕ_a can be considered as a correction and is a known

quantity, allowing the calculation of E_B . As binding energy is sensitive to the chemical environment of the electron in the initial state, XPS is a direct probe of chemical information as well as electronic information.

Once the sample has been photoionised, it is left in an excited state. This is unstable and after some time will decay. For the core-excited state, this can proceed in one of two ways, which are shown in figure 2.2. Both Auger decay and fluorescence begin the same way: the core-hole is filled by an electron relaxing from a higher energy level. However, for Auger decay, this is accompanied by the autoionisation of another electron, whereas in fluorescence a photon is emitted. As XPS is a photon-in, electron-out spectroscopy, it is not sensitive to fluorescence. However, Auger electrons can be detected and often appear in spectra. The key difference between Auger and photoelectron peaks in the recorded spectrum is in how they respond to increasing the photon energy. As the photon energy increases, the kinetic energy of the photoelectron increases in kind, and E_B remains constant by equation 2.2. However, the converse is true for Auger electrons, where an increase in photon energy does not increase its kinetic energy. This is because the kinetic energy of the Auger is determined from energy difference between the core-excited and ground states, not the photon, and as a result, Auger peaks shift on the binding energy scale.

Typically, XPS employs hemispherical analysers to measure the kinetic energy of the photoelectrons. The working principal of this type of electron analyser is shown in figure 2.3. The sample is irradiated, producing photoelectrons from various energy levels, with their kinetic energy governed by equation 2.2. These then pass into the hemispherical analyser, having been focused and slowed by two electrostatic lens systems. The former lens is important as it allows electrons that enter the analyser to reach the entrance slit of the hemisphere, and the latter because often the kinetic

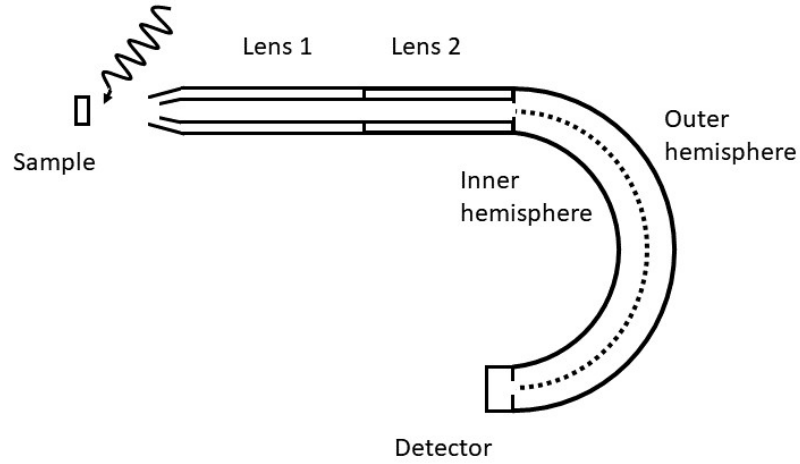


Figure 2.3: Sketch of a hemispherical analyser used to determine the kinetic energy of the photoelectrons. The photoelectrons are focused and slowed by an electrostatic lens system before entering the hemisphere. Adapted from [75].

energy of the photoelectrons is much too high for sufficient resolution [75]. Upon entering the hemisphere, the electrons only reach the detector if they follow the path defined by

$$E = ke\Delta V \quad (2.3)$$

where E is the energy corresponding to the dashed path shown in figure 2.3, e the elementary charge, ΔV the potential difference between the hemispheres, and k the spectrometer constant defined by the inner and outer radius of the hemisphere [75]. Electrons that enter the analyser with too much, or too little, energy will thus not be measured.

There are different modes that hemispherical analysers can be used to record a spectrum, however the only one pertinent to this thesis is constant analyser energy (CAE). This operates by selecting a ‘pass energy’ that defines the path the photoelectrons must follow to reach the detector. The electrons are accelerated or decelerated to this energy by the lens system, the voltage of which varies to select which kinetic energies are being measured, allowing

the hemispherical analyser to measure the intensity of the photoelectrons as a function of kinetic energy. The choice of pass energy largely depends on the situation, as there exists a trade-off between intensity and resolution. High pass energies give higher intensities compared to lower values, but worse resolution, and vice-versa. This is caused by the energy dispersion of the photoelectrons as they travel around the hemisphere; at high pass energies, small differences in kinetic energy are bent to similar regions on the detector, reducing the resolution but increasing the intensity.

Other than the pass energy, the entrance slit of the analyser also plays a role in setting the resolution. The larger this is, the more electrons enter the hemisphere and can reach the detector, however again resolution is lost. The overall energy resolution of XPS is governed by

$$\Delta E = E_P \left(\frac{W}{2R} + \frac{\alpha^2}{2} \right) \quad (2.4)$$

where ΔE is the resolution, E_P the pass energy, W the entrance slit width, R the radius of the path defined by E_P , and α the angle at which the photoelectrons enter the hemisphere [75].

2.1.2 Processing

Like many spectroscopies, XPS spectra can not be taken straight at face value, to do so leads to misinterpretation of the data. As such, there are several considerations to make before conclusions can be drawn. Firstly, as the sample is losing electrons constantly while irradiated, it can develop a net positive charge. As a result, the outgoing photoelectrons lose kinetic energy as they are attracted to the sample, shifting their binding energy

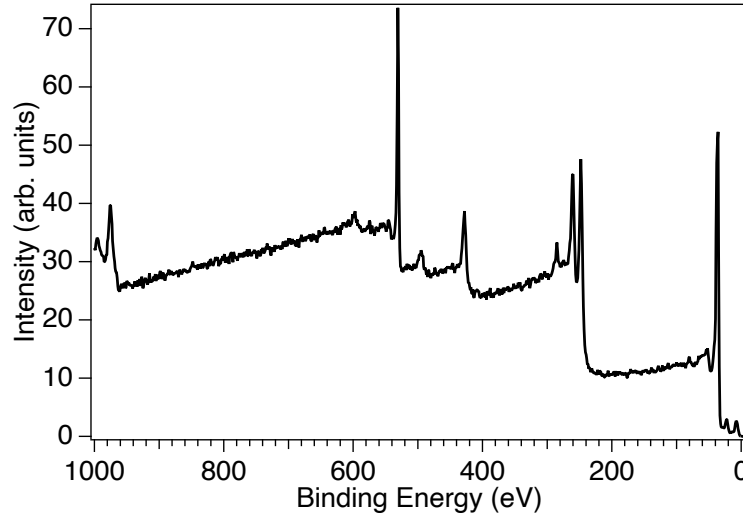


Figure 2.4: Wide scan of WO_3 , illustrating how the background of a spectrum changes with kinetic energy. The background decreases in a step-like fashion after each peak as more photoelectrons are excluded.

higher. Clearly, the magnitude of the shift depends on how conductive the sample is and how effectively it is grounded. Consequently, the spectra need to be calibrated to allow comparison between experiments. This can be achieved by shifting a specific core-level environment to a known binding energy value, then applying the shift to the rest of the data. Often, the C-C environment is chosen and aligned to 284.8 eV, however the work presented herein uses the O 1s of TiO_2 . Alternatively, for metallic samples the Fermi edge can be measured, which should appear at 0 eV binding energy.

Once suitably calibrated spectra are obtained, the background of the spectra needs to be dealt with to allow fitting. The background of XPS spectra is caused by inelastically scattered electrons and decreases as the analyser detects higher kinetic energies. As the voltage of the lens system approaches the value necessary to detect a particular peak, it is also detecting the electrons from this peak that have lost energy. Once the voltages are such that the photoelectrons of this peak no longer have sufficient energy to make it around the hemisphere, the background decreases accordingly. This can be seen by how the background changes during a wide, survey, scan (figure

2.4).

Several background removal procedures are used in this thesis: linear, Shirley, and Tougaard. The first of these is the simplest, as it only draws a straight line between two points. Shirley and Tougaard backgrounds are more complex, however. The former assumes that intensity of the scattered electrons that form the background is proportional to the area of the peak at higher kinetic energy [76], and the latter describes the spectrum in terms of the measured electron flux, inelastic mean free path of the electrons, and scattering cross-section [77, 78]. Generally, Shirley and linear backgrounds are used for XPS, and a combination of linear, Shirley, and ‘psuedo-Tougaard’ backgrounds for RAES. RAES (discussed below) is broadly measured in the same way as XPS and as such the processing described here applies to it also. The mixing of different backgrounds is described elsewhere [79], however it is worth briefly mentioning the rationale for doing so here. A psuedo-Tougaard component was incorporated into the background as it appeared to give the best fit for the RAES of one the dyes studied, which is likely due to the width of the kinetic energy window and the recorded Auger lying on the background of another feature.

With the background dealt with, the next step is to begin fitting peaks to the spectra. For XPS, there are several lineshapes that can be employed that adequately describe the spectral profile of the photoelectrons. Most relevant to these thesis is the Voigt function; specifically pseudo-Voigts. A Voigt function represents a convolution of a Gaussian with Lorentzian, where the former represents processes that broaden linewidth via random processes (e.g. by the spectrometer, slightly different sample environments, temperature), and the latter due to the Heisenberg’s uncertainty principle. As Voigts can be computationally expensive to incorporate, often they are approximated as ‘psuedo-Voigts.’ Instead of a full convolution, pseudo-

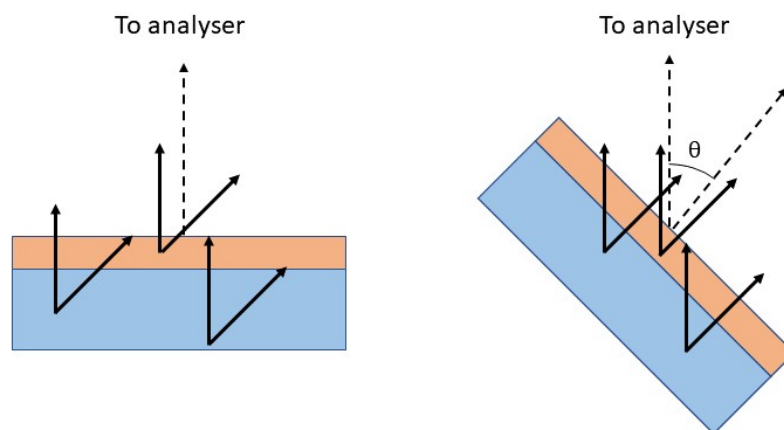


Figure 2.5: Sketches of XPS measurements taken at normal (left) and grazing (right) emission. In the former, electrons are measured from deeper within the sample compared to the latter.

Voigts are instead constructed by a weighted, linear, combination of Gaussian and Lorentzian peaks. As such, a parameter is defined that governs the Gaussian to Lorentzian contribution to the lineshape, referred to herein as the Gaussian-to-Lorentzian (GL) ratio. In general, metals have higher GL ratios (i.e. more Lorentzian lineshape) than molecules or compounds [80], thus the exact value is usually determined during the fitting procedure. An important point to note is that, as in the case of this data, the ratio should not change within the same core-level spectrum without justification.

2.1.3 Interpretation

Depth-Profiling

Part of the appeal of XPS is that small extensions to the technique or analysis itself can yield additional information about a sample. One example of this is to increase the surface sensitivity of the spectra by increasing the angle between the analyser and surface normal of the sample (figure 2.5). When these are not parallel (so-called normal emission), the surface sensitivity of the measurement is increased because the photoelectrons that are

detected have travelled through more of the material. As the inelastic mean free path (IMFP) is the same whatever the angle, this must mean that the signal measured has to have originated from nearer the surface. In short, the photoelectrons that have been ionised from deeper within the sample are rotated to lie outside the acceptance angle of the analyser. For samples that consist of layers (e.g. oxidised material), the ratio of surface to bulk signal changes with angle, and thus can be used to non-destructively depth profile.

In a similar vein, XPS can be used to calculate the thickness of the layers that make up a sample. As long as the layer is thin such that the buried layer is visible through the top layer, as is the case in figure 2.5, then this can be done by virtue of the photoelectron's IMFP and the Beer-Lambert law. This is given by

$$\frac{I}{I_0} = \exp\left(-\frac{d}{\lambda}\right) \quad (2.5)$$

where I is the intensity of the core-level under investigation through the layer, I_0 the intensity without the top layer, d the thickness of the top layer, and λ the IMFP. Thus, by measuring a signal originating from the buried layer, then measuring again once that layer is exposed (e.g. by sputtering), can yield the thickness of the top layer provided that the IMFP is known.

Features of XPS

There are a number of features that are routinely encountered during XPS. Most obviously is that for some core-levels, multiple peaks can appear to represent the same chemical environment. This arises as a result of spin-orbit coupling. This happens to all core-levels where the orbital angular

momentum quantum number is not equal to one and is caused by an interaction between the electron's spin and orbital motion. There are two cases: where the spin and angular momentum align, and when they do not. This is represented by the total angular momentum quantum number, j ,

$$j = l + s \quad (2.6)$$

where s is the spin quantum number and l is the orbital angular momentum quantum number. As the electron can either be spin-up or spin-down, j can take two values; one representing the aligned case and the other the anti-aligned. As there is an energy associated with both cases, the energy level splits, and the photoelectrons produce two peaks of different energy. The ratio and splitting of these levels are well defined; with the former being determined by the electron degeneracy ($g = 2j + 1$) and the latter from Hund's third rule.

Spin-orbit coupling, where relevant, is expected to appear in most XPS spectra. However, other features are rarer, many of which fall under the umbrella term of 'satellites.' Shake-up satellites are one type that appear in the spectra shown in later chapters. In this case, as the photoelectrons leave the sample, they excite higher energy electrons to unoccupied states. As examples, this could be electrons in the valence band being excited to the conduction band, or electrons in the highest occupied molecular orbitals being excited to the lowest unoccupied molecular orbitals. As a result, anomalous peaks that do not correspond to any chemical environment can arise at lower kinetic energy than the main structure. Plasmon excitations are another type of satellite that commonly occur in the spectra of metals. In this case, energy is lost in a similar manner as during shake-up excitations, however instead plasmons in the conducting electron

distribution are excited. The end result is also similar; new peaks appear at lower kinetic energy. Sometimes these features can be ignored during fitting, particularly if they lie outside the region of interest, but can be important when subtracting an appropriate background. Further, for some transition metals peak fitting is generally ill advised due to the complexity of the spectra, and the satellite structure is instead used to differentiate between chemical environments.

2.1.4 Ambient Pressure X-ray Photoelectron Spectroscopy

Since its inception, XPS has been a vacuum technique; the inelastic mean free path of the electrons is far too short to make it to the detector if ultra high vacuum conditions are not met. Despite this, the utility of XPS is such that it has become a staple technique in the physical sciences, particularly in heterogeneous catalysis. This being said, the strict pressure requirement means that only post mortem studies of catalysts are possible, if information on how the surface changes under reaction is sought. As a consequence, XPS has broadly not been the go-to technique for determining the mechanisms that occur during catalysis. This was disappointing, as clearly XPS would be powerful in this regard due to its surface sensitivity and chemical specificity.

Largely due to this potential, there has been a push to enable the use of XPS at pressures relevant to catalysis in recent years. This has become known as ‘bridging the pressure gap’ within the surface science community, and has been done for several analytical techniques. For XPS, the result is ambient pressure X-ray photoelectron spectroscopy, AP-XPS. There are other names in circulation, but all represent the same thing; for example,

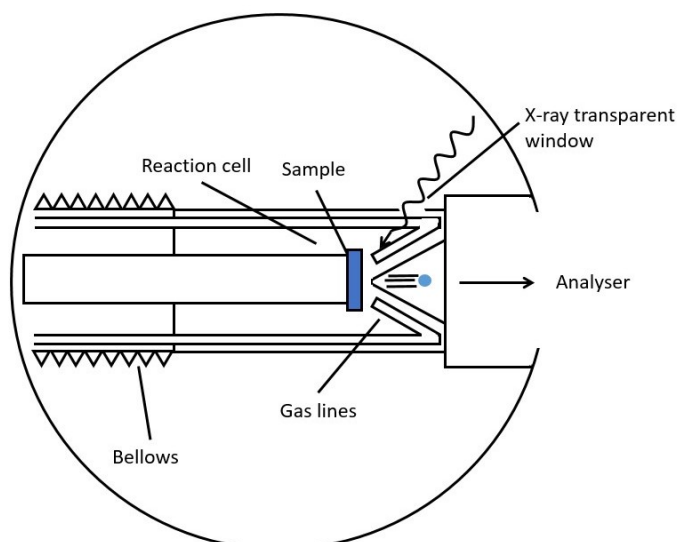


Figure 2.6: Schematic of the Lund cell approach to facilitating AP-XPS. The sample is exposed to far greater pressures compared to traditional XPS by housing it in a reaction cell, within the vacuum chamber. The X-rays pass into the cell through an X-ray transparent window and ionise the sample. The photoelectrons then are collected by a cone positioned close to the sample surface, pass through several differential pumping stages, until measured by the analyser.

near ambient pressure XPS (NAP-XPS) or high pressure XPS (HP-XPS). One AP-XPS design, known as the Lund cell, is shown in figure 2.6. Here the sample is loaded from the main vacuum chamber into a reaction cell, which is mounted onto the front end of the analyser. The cell is isolated from the main chamber and only has an opening to the analyser, through a cone with an opening in place of the tip. The sample is then driven close to this opening, within one IMFP of the photoelectrons. Typically, the cone is positioned about two aperture diameters away to preserve the pressure at the surface [81]. It is then irradiated by the X-rays, which have passed through an X-ray transparent window. Thus, a sample can be exposed to reacting pressures of various gases and vapours and the photoelectrons can still be collected before the signal is attenuated beyond recognition. The photoelectrons then pass through differential pumping stages until they reach the analyser at, or near to, UHV conditions. The first of these stages is created by the aperture of the cone near the sample, where the pressure

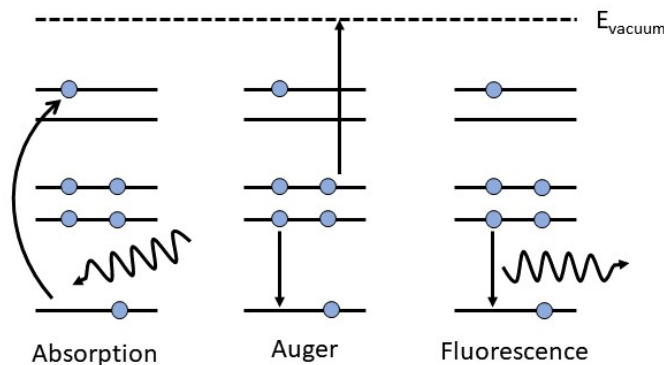


Figure 2.7: Schematic of the processes that occur during XAS. A photon is absorbed, and the relaxation products, either Auger electron or photon emission, measured.

can be in the mbar range sample side, but around 10^{-3} mbar on the other side. It is this setup that was utilised in chapter 6.

The reaction cells can be designed with specific environments in mind and are thus made interchangeable. For example, a Peltier device can be used to heat or cool with precision in the -10 °C to 100 °C range, however an electron beam can be used to reach up to 1000 °C. Examples also exist of cells that specialise in electrochemistry [82]. As a result, *operando* studies can be designed that take full advantage of the versatility on offer from AP-XPS setups using reaction cells.

2.2 X-ray Absorption Spectroscopy

2.2.1 Technique

X-ray absorption spectroscopy (XAS) is another core-level spectroscopy that can be operated as either photon-in, photon-out, or photon-in, electron-out. It can be known by other names, such as near-edge absorption fine structure (NEXAFS), however the underlying physics is identical and is

outlined in figure 2.7. A photon is absorbed by the sample if its energy matches the separation between the ground and an unoccupied state (referred to as a resonance). This event is correlated to the various decay channels by detecting their associated products, giving the absorption at a particular photon energy. As the energy of the photon is known, XAS provides a route to mapping the unoccupied states of the sample in the energy domain.

There are a number of ways to measure absorption during XAS. First and simplest is to measure the current of the sample as it is irradiated. This works on the principal that as the X-ray is absorbed, a core-hole of some description is created, thus a current induced. Called ‘total’ electron yield, absorption events are correlated to an increase in current through the sample (and ultimately the UHV manipulator), however as the magnitude of the current is usually small, noise and artifacts can cause issues. Another possibility is to measure the Auger electrons that are emitted using the hemispherical analyser in so-called ‘Auger-yield.’ Here, the analyser naturally excludes the contributions from other processes (such as further decay if the core-hole is deep). Thus, by recording the Auger as the photon energy changes and integrating the subsequent data, an absorption spectrum is obtained. Unfortunately, this is quite slow, as the spectra must be measured for long enough to reduce noise, in addition to any dead-time of the analyser and beamline optics.

Finally, and usually most preferred, is to make use of a microchannel plate (MCP) detector. Here, the incoming electron enters the MCP through one of the channels and collides with the internal wall, producing secondary electrons. These then produce more electrons themselves as they collide with the walls of the channel, amplifying the signal far above that expected for the original electron. It is possible to exclude undesired electrons from

the spectrum by applying an opposing voltage that must be passed through before entering the MCP. For example, the N 1s edge is at roughly 400 eV, meaning photons of this energy will create N 1s Auger electrons whilst photoionising any core-levels below 400 eV binding energy. Thus, applying a voltage of 300 V can exclude a large portion of the photoelectrons. The Augers, however, still have enough energy to pass into the MCP for detection and the resulting spectrum is said to be recorded in ‘partial’ electron yield. In addition, the surface sensitivity is increased as only electrons that have undergone elastic scattering have high enough kinetic energy to reach the detector. Of less relevance to this thesis is that absorption can be correlated to the emission of a photon via fluorescence, as shown in figure 2.7, which can be more sensitive to the bulk.

2.2.2 Processing & Interpretation

Generally, it is difficult to assign exact chemical or electronic information to an XAS spectrum without the assistance of computational calculations. However, it does give an idea of the location of the unoccupied states in the energy domain, and thus some light processing is required. Firstly, where possible, the absorption can be normalised to the flux of the incoming radiation. As the photon energy must incrementally change, XAS is a synchrotron technique, and the flux of the X-ray beam decreases with time. Clearly this means the measured absorption similarly decreases, and can be accounted for by normalising to the X-ray flux. Often, the flux of the beam is measured well before the sample stage on a gold mesh. Secondly, as there is an error in the photon energy each time the monochromator moves, the photon energy may require calibration. To do so, the second order reflections of the incoming X-rays can be used, where the difference

in energy between features excited by first order and second order light gives the exact photon energy.

2.2.3 Density of States Plots

As XPS probes the occupied states of a sample, and XAS the unoccupied, it would be convenient to combine the two to form a density of states (DOS) plot of a particular sample. This has been described previously in reference [83]. Essentially, the unoccupied and occupied halves of the DOS are put onto the same binding energy axis by subtracting the binding energy of the appropriate core-level from the photon energy scale of the XAS. Initially the XAS spectrum is essentially referenced to the ground state energy of the sample, with the energy difference given by the photon energy. This can instead be written in terms of the Fermi energy via

$$h\nu = E_{XAS} - E_i \quad (2.7a)$$

$$h\nu = E_{XAS} - (E_F - E_B) \quad (2.7b)$$

$$E_{XAS} - E_F = h\nu - E_B \quad (2.7c)$$

where E_{XAS} is an energy in the XAS spectrum, E_i the ground state energy, E_F the Fermi energy, and E_B the binding energy of the core-level that is excited from. It is important to note that the above equations describe the sample in a particular core-excited state, and as such should not be taken to represent the DOS for all excitations.

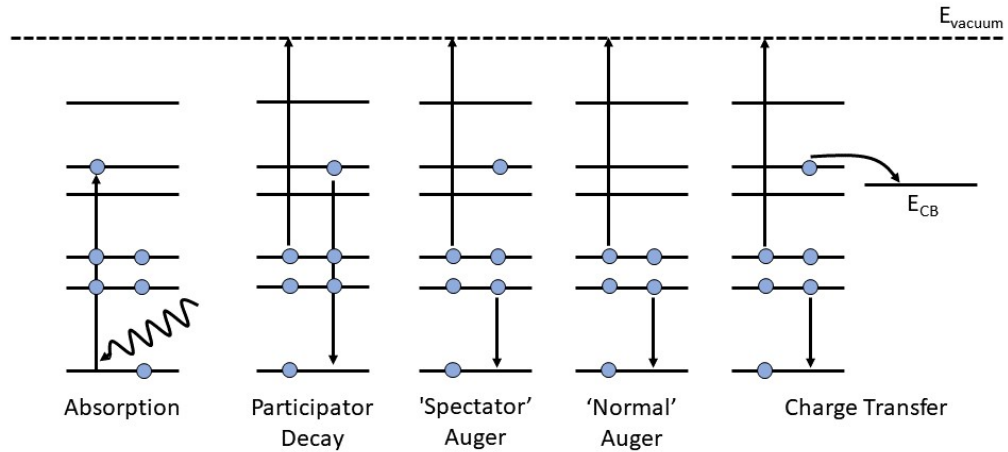


Figure 2.8: Adsorption, participator, and spectator transitions enabling the implementation of the core-hole clock method in RAES. How the transitions are changed by charge transfer to the substrate is also indicated.

2.3 Resonant Photoelectron Spectroscopies

2.3.1 Resonant Processes

Until now, when discussing XPS and XAS, the state of the sample after an X-ray is absorbed has not been critical to understanding either technique; the former mostly concerns itself with the initial state and the latter with correlating relaxation products to absorption events. However, both act as precursor events to processes where the state of the sample post ionisation is important. These are demonstrated in figure 2.8 and rely on the core-hole generated after an electron is either promoted to a higher energy orbital or photoionised. With the system in a high energy state (herein referred to as ‘on-resonance’), there are several possible pathways for relaxation, depending on whether the electron is still present. If it is, it could itself recombine with the core-hole, ejecting a different electron via Auger emission. This special case is called ‘participator decay’ and leaves the sample in the same final state as if direct photoemission of the ejected electron had occurred. This decay underpins resonant photoelectron spectroscopy

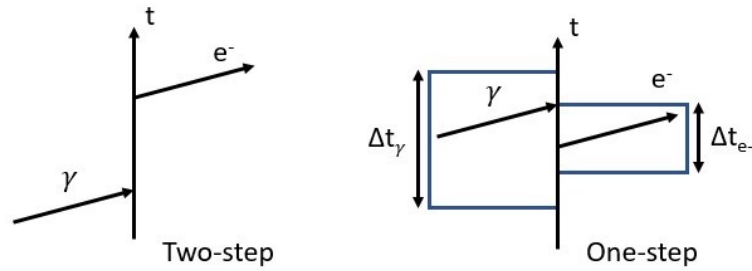


Figure 2.9: Qualitative description of the difference between one and two step scattering process from resonant X-ray Raman scattering theory. In the left diagram, the photon, γ , is absorbed at the time axis, t , and an electron, e^- , subsequently emitted. As such, absorption and emission occur at two, separate, well-defined times. This is not true for the right diagram, where the bandwidth of the photon is small, thus the absorption time, Δt_γ , more ambiguous than the emission time, Δt_{e^-} , hence absorption and emission cannot be decoupled from each other.

(RPES), described below.

It is also possible, however, that another electron will instead fill the core-hole instead of the excited electron. In this case, Auger decay again occurs, with the excited electron spectating the process; leading to this transition being termed ‘spectator Auger decay.’ As illustrated in figure 2.8, this is similar to normal Auger decay, just with the spectating electron present. An important result of this is that the Auger electron ejected during the process has a higher kinetic energy relative to the normal Auger decay channel, as it is shielded by the spectator electron. This means that spectator decay is resolvable from normal Auger decay and is the foundation of resonant Auger electron spectroscopy (RAES), again discussed below.

2.3.2 Resonant Auger Electron Spectroscopy

As stated in the previous section, RAES involves pathways where the excited electron ‘spectates’ the rearrangement of the bound charge density

via Auger emission. The challenge when handling RAES data, particularly for complex molecules, then becomes the accurate assignment of spectator and normal Auger peaks within the same spectrum. Fortunately, some behaviour can be used to fingerprint spectator Auger peaks from normal Augers. Most commonly seen is that spectators follow a linear dispersion in kinetic energy around the resonance and are narrower than their normal counterparts, potentially below that expected from lifetime broadening [84]. Both arise from the inclusion of the excited state's broadening into the convolution of the photon bandwidth with the lifetime broadening of the core-excited and final states, which governs the overall probably distribution of a spectator peak [85].

The origins of these identifying phenomena are described by resonant X-ray Raman scattering (RXRS), a full description of which is presented elsewhere [86]. Key to this framework is that absorption of the photon and emission of the Auger electron can not be described as a two step process. To see this, consider figure 2.9. Here, whether or not the process is regarded as one- or two-step depends on the photon energy bandwidth. If the bandwidth is broader than the lifetime of the excited state, the time of absorption is well defined according to Heisenberg's uncertainty principle, and absorption and Auger emission can be separated into individual steps. Otherwise, if the bandwidth is narrower than the excited state lifetime, then the absorption time is poorly defined and lasts longer than Auger decay. Absorption and Auger emission are not independent of each other in this case, as illustrated by figure 2.9. Given the resolution possible at modern beamlines, resonant Raman conditions are often met, causing the features in RAES to exhibit behaviour atypical of other spectroscopies.

One consequence of RXRS is that the peaks from the spectator decay channel (herein referred to as spectators) shift in kinetic energy around a

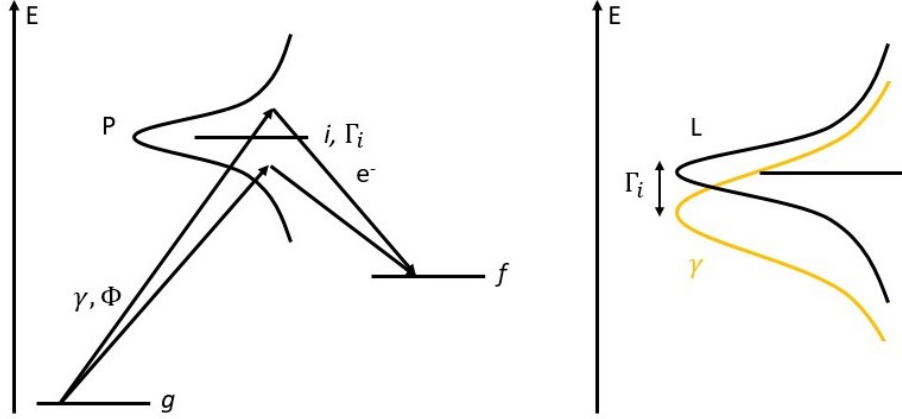


Figure 2.10: Illustration of the detuning (left) and asymmetry (right) in RAES spectra. Φ represents the bandwidth of the photon source γ , and Γ_i the broadening of the intermediate state. L and P represent the Lorentzian and overall probability function of the intermediate state respectively. As the detuning increases, the arrows shown grow together, representing how the energy of the photon influences the observed energy of the Auger electron. Diagram adapted from [85].

resonance. This is different to the normal Auger decay channel, where peaks keep their kinetic energy constant regardless of the photon energy. This behaviour is built in to the cross-section, σ , for non-radiative RXRS into a solid angle, do , given by Fermi's golden rule

$$\frac{d^2\sigma}{d\varepsilon do} = 4\pi^2\alpha\omega \sum_f |D_{fE}|^2 \Delta(\varepsilon + \xi_f - \xi_i - \omega, \Gamma_f) \quad (2.8)$$

where ε is the energy of the electron, α is the fine structure constant, ω is the frequency of the incoming radiation, D_{fE} the dipole matrix element, and $\Delta(\varepsilon + \xi_f - \xi_i - \omega, \Gamma_f)$ a Lorentzian function depending on the ground and final states, ξ_i and ξ_f , and the lifetime broadening of the final state, Γ_f [86]. It can be seen that the argument of the Lorentzian function depends on the difference between the energy of the incoming radiation and energy of the excited state relative to the ground, with the maximum of the function when $\varepsilon = \omega - \omega_{fi}$, where ω_{fi} is the energy difference between the ground

and excited state (in atomic units). This is referred to as the detuning of the X-ray source from resonance and is equal to zero on resonance; schematically illustrated in figure 2.10. However, what is measured by the analyser does not depend solely on equation 2.8. As the photon energy, intermediate state, and final state all have an associated broadening and thus distribution function, the observed distribution of electron energies is represented by a convolution of these three functions. Therefore, as the detuning changes, the overall distribution shifts accordingly; the maximum of the measured distribution increases in kinetic energy with photon energy. In figure 2.10, this is named P, and the arrows representing γ and the Auger electron indicate the relationship is, at essence, a consequence of energy conservation. For simplicity, the broadening of the final state is ignored in the remainder of the RXRS description given here; this is generally the case in other descriptions, but is unlikely to apply physically for the HAXPES energies used in chapters 4 and 5 [85].

Figure 2.10 also shows how the interplay of the photon energy bandwidth and lifetime broadening can lead to asymmetric lineshapes. As the photon energy approaches the resonance (i.e. when the detuning is small), one side of the Lorentzian distribution of the intermediate state is preferentially excited over the other. Clearly, the convolution of these functions then becomes asymmetric to lower kinetic energy when the detuning is negative, and asymmetric to higher kinetic energy when positive.

For both phenomena described above, the interplay between the intermediate state and photon energy bandwidth is important. First, consider the case where the photon energy bandwidth is much larger than the lifetime broadening of the intermediate state. In this situation, the convolution is effectively between a Lorentzian and a constant, yielding a Lorentzian. Thus, no dispersion or asymmetry occurs; the system is either excited to

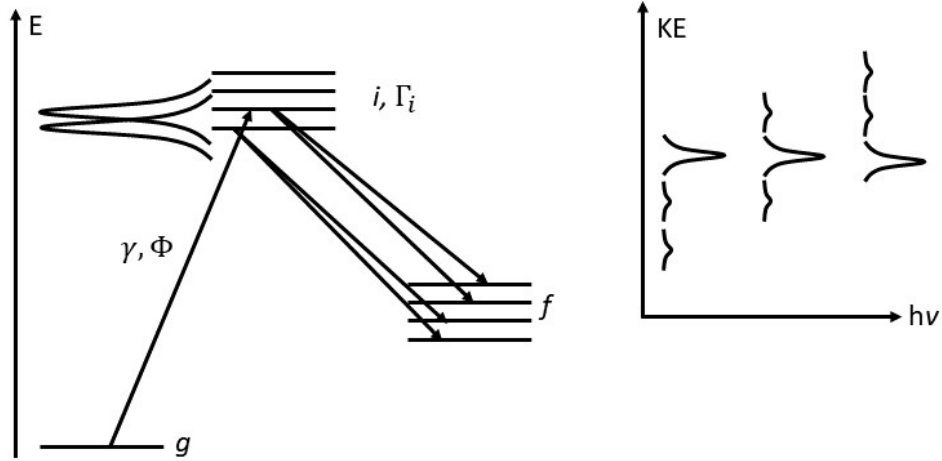


Figure 2.11: RXRS of a molecule with a monochromatic X-ray source, where the vibrational energy levels and lifetime broadening are on the same order. The energy level diagram shows how interference effects can arise, and the inset graph how dispersion can be affected. Adapted from [87].

the intermediate state or it is not. If the converse is true, then dispersion and asymmetry are present by the mechanisms described above. However, the latter of these will be subtle. To see this, it is helpful to picture the convolution of a Lorentzian with a Dirac delta function. Doing so yields the Lorentzian, unchanged, but at the position of the Dirac delta. The measured distribution function follows the form of the exciting photon band, and is usually considered to be Gaussian [85]. A consequence of the distribution being determined by the photon bandwidth is that the observed distribution function can narrow significantly, potentially below that imposed by Heisenberg [84, 87]. With both examples above in mind, there remains one case to be considered: when the photon energy bandwidth and lifetime broadening are similar. The situation here is not simple as the measured distribution of electron energies can not be reduced to either contribution. Looking at figure 2.10, however, it is clear that dispersion and asymmetry of the spectator peaks will occur as described above.

Until now, the discussion of RXRS has been from the point of view of a singular atom. The situation for molecules, however, can differ. Under the

correct conditions, coherent excitation of individual vibrational states is possible, which can lead to non-linear dispersive behaviour [86, 87]. If the photon bandwidth is small, it becomes possible to coherently excite individual vibrational excited states of the molecule. As a result, interference can be observed if the lifetime broadening is of the same order as the separation between the vibrational states. The intermediate state then becomes a superposition of vibrational states and the measured electron distribution changes with photon energy. This is demonstrated in figure 2.11, which shows decay from the superimposed, vibrational, state populating different final states of the molecule. Also shown is an example of how this can lead to non-linear dispersive behaviour: as the photon energy increase, the measured distribution disperses as expected, but the population changes, offsetting the change. Clearly if the photon bandwidth is too large or the resolution of the spectrometer poor, this phenomena can be ignored. For the data presented in chapters 4 and 5, the dispersion is seen to be linear, thus it is assumed vibrational effects are minimal.

Given the content of this section, it is clear that there are certain processes that dramatically affect the measured spectra, over and above those encountered when analysing XPS; all of which should be considered. As a result, care has to be taken when fitting RAES data, as the lineshape can be complicated. This is especially true for quantifying the charge transfer times, which feature heavily in the later chapters of this thesis. In that work, psuedo-Voigt functions have been used to fit the RAES data due to their versatility, however often there are many ways of fitting the spectra. As such, much attention was paid to isolate the fit parameters for spectator and normal peaks respectively. In addition, the photon bandwidth used, and lifetime broadening of the states studied, are taken to be different enough that complicated convolutions for the lineshape are avoided.

2.3.3 Resonant Photoelectron Spectroscopy

RPES is qualitatively similar to RAES; an electron is promoted to some unoccupied orbital and eventually relaxes. The key difference is that the excited electron participates in the Auger process, leaving the system in a final state with one hole and no excited electron, rather than two holes with one excited electron (figure 2.8). Like RAES, RPES is an example of non-radiative RXRS, and parts of the above discussion remain applicable. However, importantly, because the excited electron is involved in the relaxation, whichever electron that ultimately ends up autoionising is not shielded by it. Hence, there is no kinetic energy difference between the resonant decay channel and non-resonant photoionisation of that electron, thus the former adds to the intensity of the latter. Both participator and spectator peaks disperse in kinetic energy, but this behaviour is not as unexpected in RPES. Here it is more intuitive that more energy given to the participator results in the more energy being lost to the autoionised electron as the system relaxes into the final state of RPES.

Fortunately, the analysis of RPES avoids much of the considerations applied to RAES because it does not require the data to be fit. Typically, the autoionised electron comes from the valence orbitals, and thus this region is measured exactly as it would be for XPS. However, for RPES, this region is measured repeatedly as the photon energy is scanned over a resonance (usually identified using XAS). Lining up these spectra to form a map then shows which orbitals have been enhanced by RPES. Integrating over the photon energies of this map yields a spectrum that is qualitatively similar to an XAS spectrum and it used in quantifying charge transfer time. This is discussed further below. Unfortunately, compared to RAES, the resonant enhancements in RPES tend to be more subtle and as such

balancing measuring time with beam damage becomes crucial.

2.3.4 Core-hole Clock Spectroscopy

Both RAES and RPES are able to reveal the charge transfer dynamics of dye-semiconductor systems with remarkable precision using the core-hole clock method. This is possible by virtue of the core-holes generated upon excitation to an unoccupied state of the molecule. As discussed above, new features appear in the spectrum as the photon energy approaches that associated with an electronic transition of the dye. In the case of RAES, this manifests as the appearance of ‘spectator’ Auger structure at higher kinetic energy compared to normal Auger decay and for RPES enhancements in features already present.

Clearly, resonant processes only happen if the excited electron remains localised to the dye. If it does not, then the core-hole is filled by traditional means; e.g. normal Auger decay or fluorescence, as appropriate. Therefore, in the context of DSSCs, if charge injection into TiO_2 is fast relative to the core-hole lifetime, few resonant features are observed. Formalising this, charge transfer times are linked to intensity through

$$\tau_{\text{CT}} = \tau_{\text{CH}} \frac{[I_{\text{RPES}}/I_{\text{XAS}}]_{\text{mono}}}{[I_{\text{RPES}}/I_{\text{XAS}}]_{\text{multi}} - [I_{\text{RPES}}/I_{\text{XAS}}]_{\text{mono}}} \quad (2.9)$$

for RPES and

$$\tau_{\text{CT}} = \tau_{\text{CH}} \frac{I_{\text{Res}}}{I_{\text{Aug}}} \quad (2.10)$$

for RAES [88]. Here, τ_{CT} is the charge transfer time, τ_{CH} the core-hole

lifetime, I_{RPES} and I_{XAS} the intensity of the unoccupied state in question measured during RPES and XAS respectively, and I_{Res} and I_{Aug} the intensity of the spectator and normal Auger signals in RAES respectively. Common to both equations is the core-hole lifetime, τ_{CH} , which sets the precision of the transfer times calculated. Typically this is on order of femtoseconds (some are faster and feature in later chapters) and the techniques themselves rely on how accurately the intensities can be determined. As a result, it has been estimated that this can be done such that charge transfer time can be quantified an order of magnitude above and below τ_{CH} .

At this point, it is worth making explicit how, practically, the charge transfer time is calculated from a RAES or RPES spectrum. For the former, an on-resonant spectrum is fit in order to identify resonant and non-resonant features. The intensities of the respective features are summed together, and the ratio related to the charge transfer time via equation 2.10. For RPES, a map of valence spectra recorded at varying photon energy is constructed. The resonant energies are identified and the relevant region integrated to give an absorption spectrum similar to XAS. From here, the intensity of the participator is determined and compared to a corresponding XAS spectrum, which determines the state's sensitivity to RPES compared to XAS. These ratios are fed into equation 2.9 to calculate charge transfer times.

2.4 X-ray Sources

Within this work, two sources of X-rays have been used; those generated using a lab-source and those available at synchrotron facilities. The former generates X-rays by accelerating electrons from a hot filament towards

a metal target. At impact, the electrons lose kinetic energy, which is given off as X-rays. There are two types generated: characteristic and Bremsstrahlung radiation. The latter occurs as the electron is decelerated by the metal atoms, losing the energy by emitting a smear of X-ray energies. Characteristic X-rays are caused by the electrons from the filament transferring energy to bound electrons in the metal upon impact, promoting them to a higher state or removing them from the metal, as appropriate. The core-hole is then filled by a more energetic electron after some time, releasing an X-ray in a process recognised as fluorescence (figures 2.2 and 2.7). As the energy of the X-rays emitted depends on the separation between the initial and final states, the energy of the X-rays emitted is determined by the material of the anode. Examples include aluminium, silver, tungsten, and copper.

A further feature of characteristic X-rays is that multiple, discrete, photon energies are generated. This is caused by different electrons filling the core-hole and the energies seen is governed by the selection rules for electronic transitions. These are summarised as

$$\Delta S = 0 \tag{2.11a}$$

$$\Delta L = 0, \pm 1 \tag{2.11b}$$

$$\Delta J = 0, \pm 1 \tag{2.11c}$$

where ΔS , ΔL , and ΔJ are the total change of spin, angular momentum, and total angular momentum respectively. As a result, only certain transitions are possible, which are denoted using the Siegbahn notation. As an example, in this work Al $K\alpha$ is used for the lab-source experiments,

which corresponds to the aluminium $1s$ core-hole being filled by an electron from the $2p$ orbital (specifically, $1s_{1/2}^{-1} \rightarrow 2p_{3/2}^{-1}$). As a result of the discrete nature of the X-rays emitted in this way, the photon energy can not be changed incrementally during an experiment, ruling out XAS and resonant spectroscopies.

Synchrotrons generate X-rays in a fundamentally different manner. Here, electrons are accelerated by a linear accelerator and enter a storage ring, where the path of the electrons is controlled by bending magnets. As the electrons change direction around the ring, they lose energy, and X-rays are emitted. By precise control of the path of the beam, low pressures that minimise scattering, and periodic small accelerations to replace the energy lost, the lifetime of the electrons in the ring is long, and the term ‘storage ring’ becomes appropriate. To utilise the radiation generated as the electrons travel around the ring, beamlines are positioned at regular points around the ring to receive the radiation. These are linear assemblies consisting of several stages of optics to focus and select the desired energy of the X-rays. At the end of the beamline lies the experimental endstation, at which spectra are recorded.

As mentioned above, the X-rays are emitted when the electron changes direction at the bending magnet. However, it was soon realised that this radiation was not the ideal solution because the radiation is emitted spread in the horizontal direction and thus not all of the radiation could be used by the endstation [89]. As a result, in modern synchrotrons, insertion devices are common. These provide very intense X-rays there are two well known, qualitatively similar, types; wigglers and undulators. Only, undulators are used in this work, however both are constructed from a series of magnetic poles and perturb the beam as it travels along its path, oscillating it. The result is a coherent X-ray beam with a continuous energy

distribution, where the brilliance of the source is proportional to the number of oscillations squared, N^2 [89].

For synchrotron radiation, a continuous spectrum of X-rays is present. Conversely, the spectrum from a lab-source is discrete. In both cases, monochromators are used in order to filter out unwanted radiation. For hard X-rays, the separation between the planes of atoms in crystals is of the correct order to cause diffraction, and is governed by Bragg's law ($n\lambda = 2d\sin\theta$). As a result, the wavelengths are diffracted differently, allowing the energy to be selected by rotating the crystal. This latter point is of particular use at synchrotrons as it allows the photon energy to be selected as required. For soft X-rays this is more challenging, as the appropriate crystals can struggle with the thermal load or damage [90], thus plane gratings are often employed instead.

2.5 Sample Preparation Techniques

2.5.1 Thermal Deposition

As much of the work herein relates to how molecules are bound to the surface of a material, a description of the vacuum techniques used to achieve this is warranted. A simple way to achieve this at UHV is to use a Knudsen cell (K-cell). This was used in chapter 3 and involves heating a crucible of powdered molecule, under vacuum, to the point that it begins to evaporate. As this begins to happen, a valve to the main UHV chamber is opened, depositing the molecule onto the substrate. The time the valve is open and temperature can be varied to control the thickness of the film deposited, and resulting sample is relatively free of contamination.

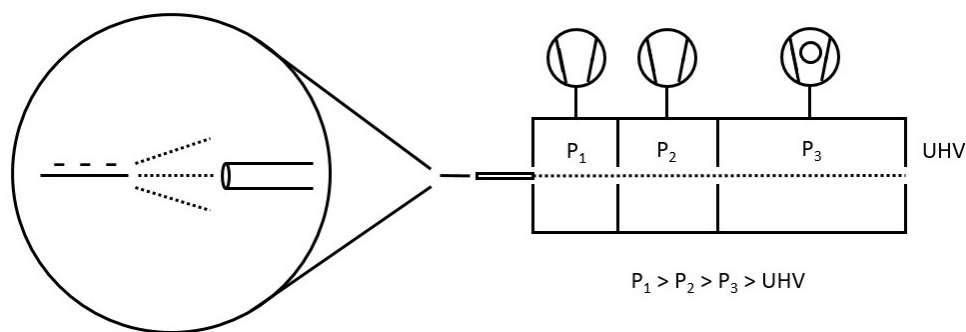


Figure 2.12: Diagram of the working principle of electrospray deposition. A jet of molecule solution is ionised and forced into a series of differentially pumped chambers, where the pressure eventually reaches UHV.

2.5.2 Electrospray Deposition

Some molecules are too fragile to deposit thermally, thus an alternative method is required. Electrospray deposition is one technique that allows the deposition of large molecules (such as N3 in chapter 4) without degradation. The setup for electrospray deposition is shown in figure 2.12. The molecule is dissolved in solution and pumped at a steady rate through an emitter; functionally, a tube with a narrow inner radius. By applying a voltage between the emitter and inlet to the system, the molecule solution is ionised and emerges from the emitter as a fine spray. This then enters a series of differentially pumped chambers where the solvent molecules evaporate, leaving increasingly small droplets molecule to enter the UHV system and deposit onto a sample. As for thermal deposition, the thickness of the deposited film can be controlled by the deposition time, however the overall process is much gentler on the molecules involved as high temperatures are not involved.

2.6 Adjacent Techniques

2.6.1 Scanning Electron Microscopy

Aside from photoelectron spectroscopies, some other techniques have briefly been used to gain further insight into the samples used, one of which is scanning electron microscopy (SEM). In this technique, a conductive sample is placed in the path of a beam of electrons, which is scanned across the surface. As a result of the beam's collision with a sample, secondary electrons and X-rays are produced, which are collected to form an image of the surface of the sample. As electrons are used instead of light, the ability to resolve structure is greatly increased.

2.6.2 Density Functional Theory

Density functional theory (DFT) is a powerful computational technique that can be used to predict a host of chemical and electronic properties of a system. A full theoretical description of DFT is far beyond the scope of this thesis; but at essence, in lieu of an exact, analytical, solution to the many-body wavefunction itself, DFT solves the Schrödinger equation numerically by considering the electron density. By then representing the electron density as a non-interacting cloud of electrons, which satisfy a non-interacting Schrödinger equation, the ground state and its energy can be found [91]. In this picture, 'exchange-correlation' energy terms are included to account for the interactions present in the real system. When running calculations, this is approximated by an exchange-correlation functional, which is chosen carefully by the user. Practically, solving this Schrödinger equation is done iteratively starting from some initial guess until the calculated values

no longer meaningfully change with each iteration. This threshold is set by the user and called a self-consistent field calculation, and once satisfied, the solution is said to have converged. At this point, an approximation for the ground state electron density has been found. In addition, basis sets are chosen to represent the orbitals of the non-interacting electron density. However, DFT only describes the ground state of a system; to calculate excited states, time-dependent DFT (TD-DFT) is required.

Chapter 3

Synchrotron-based Electron Spectroscopy of Coumarin-Sensitised Photoanodes Supported by Laboratory XPS

Contents

| | | |
|-------|--|-----------|
| 3.1 | Introduction | 53 |
| 3.2 | Methods | 54 |
| 3.2.1 | Synchrotron Measurements of Mesoporous Photoanodes | 54 |
| 3.2.2 | Laboratory XPS of Single Crystal Photoanodes | 57 |
| 3.2.3 | Computational Details | 58 |
| 3.3 | Results & Discussion | 60 |
| 3.3.1 | XPS | 60 |
| 3.3.2 | Occupied States | 71 |
| 3.3.3 | Unoccupied States | 74 |
| 3.3.4 | Density of States | 78 |
| 3.4 | Conclusions | 82 |

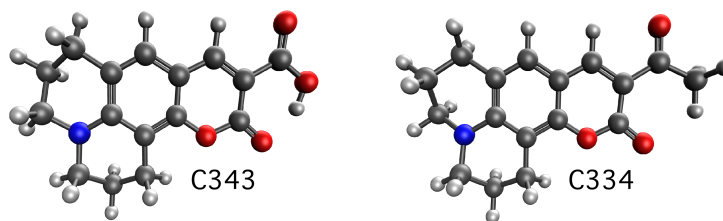


Figure 3.1: Coumarin 343 and 334. In both, the ring system containing nitrogen (blue) is linked to the carboxylic acid moiety by a coumarin skeleton, however the hydroxyl group in C343 is replaced by a methyl group in C334.

3.1 Introduction

Coumarin 343 (C343), Figure 3.1, is a pale yellow organic dye that has undergone development to extend its absorption into the visible range [92]. As a result, its derivatives have reached power conversion efficiencies of up to 5.6% and 8.2% [93, 94]. While these values are only just comparable to the first practical DSSC [21], the dyes contain no noble metals, reducing their cost. Despite its poor efficiency, C343 has been reported to present ultrafast charge carrier injection into the conduction band of TiO_2 substrates, occurring on a timescale between 100-200 fs [95, 96]. Rapid charge transfer is vital to the efficient function of a DSSC, as the excited electron must pass to the substrate before recombination can occur. We note that while 100-200 fs is considered ultra-fast for some spectroscopies, often this label is used to also describe the low-femtosecond (1-10 fs) regime that has been reported for other dye molecules [71, 97, 98, 99, 100, 101]. In such studies, resonant photoelectron spectroscopy (RPES), X-ray photoelectron spectroscopy (XPS) and near edge X-ray absorption fine structure (NEXAFS) are used to determine the charge transfer dynamics of the systems studied. These techniques act synergistically to provide detailed information on both the electronic and chemical structure of a system, and have been applied to dyes on more realistic mesoporous substrates [74, 102, 103, 104].

Due to their propensity for rapid charge transfer and relatively simple structure, we investigated C343-sensitised photoanodes prepared ex-situ on mesoporous TiO_2 and SrTiO_3 substrates. For the case of TiO_2 , we compare these samples to C343, and a similar dye C334 (Figure 3.1), deposited in-situ onto $\text{TiO}_2(110)$ substrates. C334 is identical to C343 save that it possesses a methyl group in place of the hydroxyl found in C343. Additionally, multilayers of both molecules are also studied, allowing comparison between the chemisorbed and physisorbed forms of the dyes. Using both synchrotron-based spectroscopy and laboratory-based XPS, this chapter presents a thorough analysis of the chemical and electronic structure of C343 photoanodes.

3.2 Methods

3.2.1 Synchrotron Measurements of Mesoporous Photoanodes

Sample preparation

To prepare a monolayer, mesoporous TiO_2 on FTO glass (Solaronix) was sensitised by immersing the electrode in a solution of C343 dissolved in acetonitrile for 12 hours. The electrode was then washed and soaked further in fresh acetonitrile repeatedly until the solvent was no longer discoloured by the dye. To create a multilayer, the dissolved solution was drop deposited onto the mesoporous TiO_2 and allowed to dry with no subsequent washing stages. This process was conducted in a glove box under a nitrogen atmosphere, and the samples stored in nitrogen during transportation to the beamline. Once opened, the samples were exposed to air for under 1

hour before measurements were taken. SrTiO₃ substrates were made using a screen printing technique; SrTiO₃ paste was spread onto FTO glass and heated in excess of 450 °C in air for approximately 10 minutes until the cellulose binder had burned away. Doing so left behind mesoporous SrTiO₃, which was then sensitised using the same procedure as above to give another monolayer of C343.

Beamline details

The experiment was performed at the Surface & Material Science endstation of the FlexPES beamline at the MAX-IV synchrotron, Sweden. The beamline is equipped with a planar undulator and collimated plane-grating monochromator, providing photons at energies between 40-1500 eV. The beam was defocussed to 1×0.4 mm (up from 65×10 μ m) in order to reduce beam damage to the molecules and to average out local variations in the mesoporous oxide supports. For photoelectron spectroscopy, the analysis chamber is equipped with a Scienta SES-2002 hemispherical analyser, orientated 40° from the beam. For X-ray absorption measurements, both total (TEY) and partial electron yields (PEY) could be measured using the sample drain current or an in-house built microchannel plate (MCP) detector respectively. All measurements were recorded with the electron analyser normal to the sample surface. The accuracy of the photon energy scales and reproducibility of the beamline energy was verified to be within 50 meV by measuring the difference in kinetic energy between photoemission features produced by first and second order light.

Core-level electron spectroscopy

At the synchrotron, XPS measurements were recorded using a photon energy of 600 eV in swept mode and, unless otherwise stated, valence spectra were recorded at 220 eV, giving theoretical resolutions of 0.21 and 0.19 eV respectively. Pseudo-Voigt functions were used to fit the XPS, where the Lorentzian widths were fixed across each core spectra and based on those reported in reference [105]. For each spectrum, the Gaussian widths of the substrate contributions to the fit were allowed to differ from those of the molecule. In addition, the Gaussian widths of the molecule features were allowed to vary from each other within realistic constraints. Each spectrum has had either a linear or Shirley background subtracted.

The spectra were calibrated to the Ti $2p_{3/2}$ at 458.8 eV for TiO₂, which was determined from the XPS of a non-sensitised electrode where the O $1s$ was set to 530.05 eV [106]. The same calibration method was applied to the SrTiO₃ sample, placing the O $1s$ at 529.9 eV, similar to previous reports [107]. This procedure ensures the binding energy scale is consistent with our previous studies on energy materials [65, 71, 99, 103, 108, 109, 110, 111]. In contrast, when there is no strong substrate signal, the ex-situ prepared multilayer XPS is instead calibrated to the C $1s$ of the calibrated ex-situ TiO₂ monolayer. In addition, the multilayer spectra were recorded slightly off of the TiO₂ onto the FTO portion of the substrate, where the molecule lay thickest. XPS of the bare mesoporous electrodes is shown in figure A1. RPES measurements were recorded using photon energies corresponding to specific features observed in the N and C K-edge NEXAFS spectra, with a theoretical resolution of 0.38 eV. To highlight the resonances, difference spectra were generated using an off-resonant spectrum.

NEXAFS spectroscopy was measured over both the N and C K-edges. The

presented spectra are PEY, where the background intensity from low energy electrons was reduced by applying a 300 V or 200 V retardation potential during the N and C K-edge measurements respectively. The XAS was normalised to the incident flux, which was measured using a gold mesh in the path of the beam. Beam damage was easiest to identify in the N K-edge NEXAFS, and was thus used to indicate such. With this information, beam damage was regularly checked for and avoided by moving the sample in the beam. To create density of states plots, the photon energy scale of the NEXAFS was shifted by the relevant core-level binding energy to place the data on a common binding energy scale with the calibrated valence spectra. This procedure has been described previously elsewhere [83].

3.2.2 Laboratory XPS of Single Crystal Photoanodes

To support measurements taken at the beamline, C343 and C334 were sublimated onto TiO₂(110) under UHV conditions. To do so, TiO₂(110) was sputter cleaned at 1 keV for \sim 10 minutes and annealed until only the Ti⁴⁺ remained (see appendices, figure A2). Once clean, a crucible containing either C334 or C343 was heated to 97 °C or 136 °C respectively to sublime the molecules. This procedure was carried out in the analysis chamber of a SPECS DeviSim NAP-XPS system fitted with a Phoibos 150-NAP hemispherical analyser equipped with a monochromatic Al K- α X-ray source (1486.6 eV). Measurements were taken at both normal and grazing emission. Calibration and curve fitting of the data was done with the same procedures described in section 2.1.3. Details of the bare TiO₂(110) electrode can be found in figure A2.

3.2.3 Computational Details

Density functional theory (DFT) calculations were performed using the Q-Chem 5.3.1 computational chemistry software [112]. Geometry optimisation of an isolated C343 molecule was carried out using the B3LYP exchange correlation functional [113] with the 6-311G** basis set [114, 115], where the self-consistent field calculation was set to converge at 10^{-8} eV. The calculated orbitals were then visualised using IQmol 2.14.1 [116] with an isovalue of 0.04 \AA^{-3} . Time-dependent DFT (TD-DFT) was used to simulate K-edge XAS using the first form of the short-range corrected functional (SRC1-R1) [117] and 6-311G** basis set. These TD-DFT calculations used a restricted excitation space to allow only singlet excitations from the $1s$ orbitals of interest to any virtual orbital. The first 100 roots (excited states) were calculated and aligned to the experiment by applying shifts of -0.68 and 0.49 eV to the N and C simulated spectra respectively.

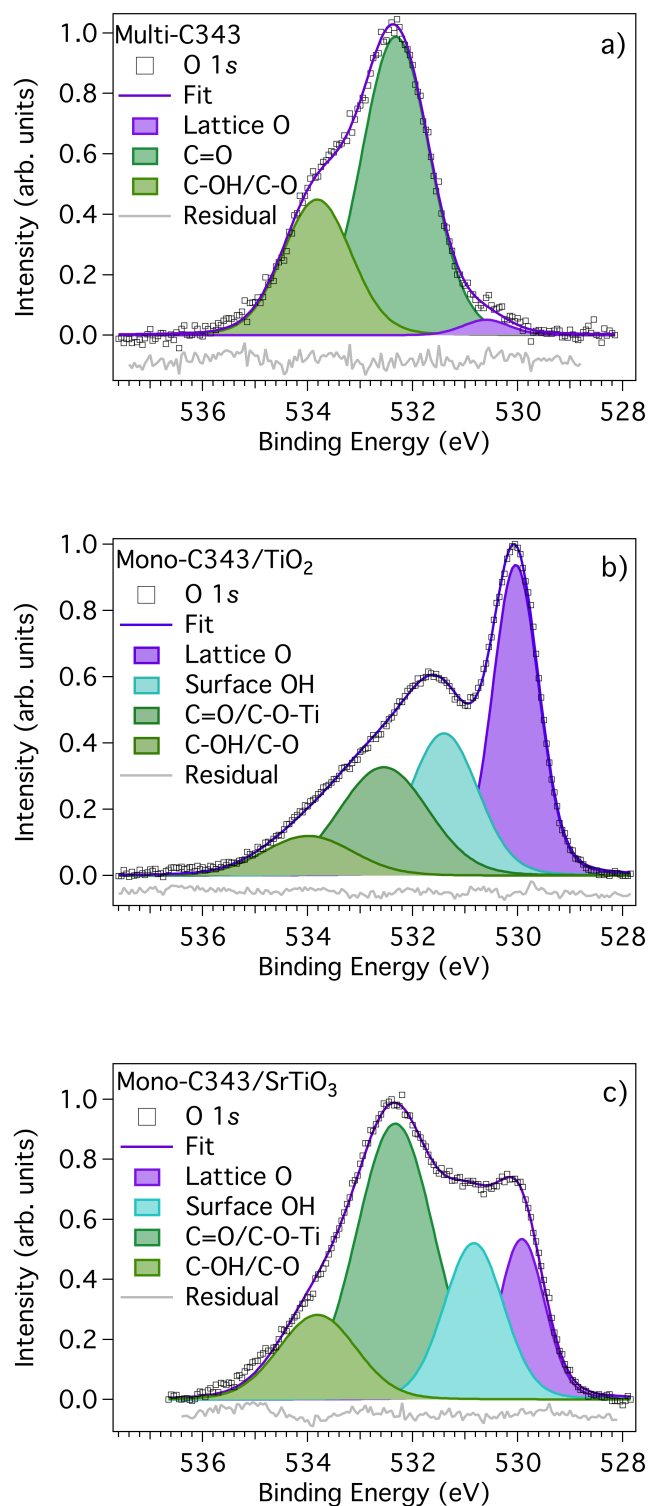


Figure 3.2: O 1s XPS of the ex-situ, C343-sensitised, mesoporous samples: multilayer on FTO (a), monolayer on TiO₂ (b), and monolayer on SrTiO₃ (c). The spectra were recorded at 600 eV photon energy and have had linear backgrounds subtracted. Each peak has a fixed Lorentzian contribution of 0.17 eV [105].

3.3 Results & Discussion

3.3.1 XPS

Figure 3.2 shows the O 1s XPS for the ex-situ prepared monolayers and multilayer on mesoporous TiO₂, SrTiO₃, and FTO respectively. For the multilayer (Figure 3.2a) three peaks are seen at 530.6, 532.3, and 533.8 eV. The smallest peak at the lowest binding energy is assigned to FTO (see methods). The two dominant peaks are then assigned to the carbonyl (C=O), ester-linking oxygen (C-O), and hydroxyl (C-OH) groups of the dye, where the hydroxyl and ester-link components are taken to overlap. The assignment of the carbonyl and hydroxyl oxygens is broadly similar to reports on both organic [103] and Ru [118] dyes, where the hydroxyl component is found at higher binding energy than the carbonyl. Additionally, the ester-linking oxygen has previously been found to occur at similar binding energy to the hydroxyl group in fluorescein [108]. As shown in Figure 3.1, C334 is identical to C343 in all aspects save that the hydroxyl in the carboxylic acid is replaced by a methyl group. Therefore, to confirm that the hydroxyl and ester oxygens overlap in the XPS of C343, the O 1s of C343 and C334 deposited in-situ on TiO₂(110) are compared in Figure 3.3, and the molecular features' binding energies summarised in Table 3.1. In Figure 3.3a, the ester-linking oxygen of monolayer C334 is seen to overlap strongly with its analogous peak for monolayer C343. There is also overlap in Figure 3.3b for the in-situ prepared multilayers, where some differential charging appears to occur in the thicker C343 layer, shifting its molecule peaks to higher binding energy. Altogether, the XPS of the in-situ samples supports the assignment of the hydroxyl and ester-linking oxygens to the highest energy peak in each ex-situ spectrum in Figure 3.2, regardless of the thickness of the dye layer.

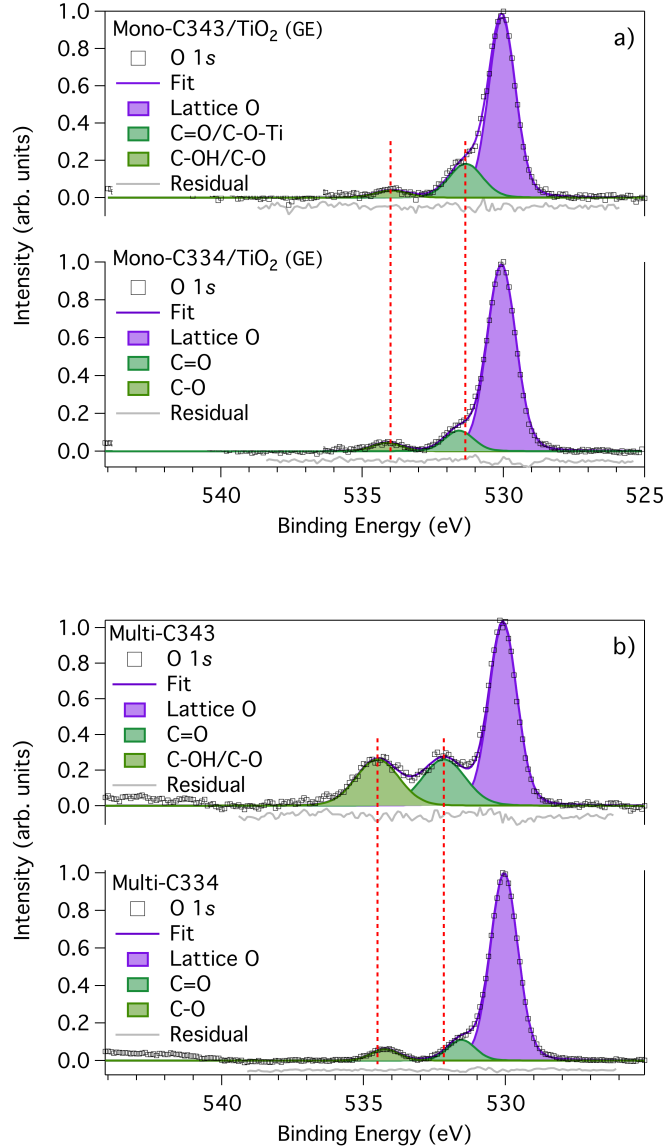


Figure 3.3: O $1s$ XPS of the in-situ depositions of C343 and C334 on $\text{TiO}_2(110)$: comparison between monolayers (a) and multilayers (b). The vertical dashed lines indicate the binding energy of the C343 molecular features. Both samples were measured using 1486.6 eV photons and have had Shirley backgrounds removed, where the monolayer and multilayer spectra were recorded at grazing and normal emission respectively. All components have a fixed Lorentzian contribution of 0.17 eV [105].

For monolayer C343 on mesoporous TiO_2 , four peaks are observed in Figure 3.2b, appearing at 530.0, 531.4, 532.6, and 534.0 eV. Four peaks are also found in Figure 3.2c for the dye on mesoporous SrTiO_3 . In both cases, the first two peaks are attributed to lattice oxygen in TiO_2 and SrTiO_3

Table 3.1: O 1s binding energies for ex-situ C343-sensitised samples, for C343 and C334 samples deposited in-situ, and the ratio of the area of the carbonyl and carboxylate peak to the area of the hydroxyl and ester-linking oxygen peak.

| | | C=O (eV) | C-OH/C-O (eV) | $A_{C=O/C-O-Ti} : A_{C-OH/C-O}$ |
|-------------------------|--------------------|----------|---------------|---------------------------------|
| C343 _{ex-situ} | SrTiO ₃ | 532.33 | 533.81 | 3.3:1 |
| | TiO ₂ | 532.55 | 533.99 | 2.7:1 |
| | Multi | 532.32 | 533.82 | 2.2:1 |
| C343 _{in-situ} | Mono | 531.35 | 533.99 | 4.7:1 |
| | Multi | 532.17 | 534.51 | 1:1 |
| C334 _{in-situ} | Mono | 531.57 | 534.13 | - |
| | Multi | 531.55 | 534.25 | - |

and surface hydroxyls, where the binding energies are similar to previously reported values [65, 107]. The hydroxyl peak on SrTiO₃ is quite large, which could be caused by overlap with a defect peak. Given the position of the lattice O signal (529.9 eV), a defect peak could appear around the hydroxyl peak [119], however its presence is not obvious. These peaks are then followed by the molecule features, with the surface bound carboxylate form of C343 indicated (C-O-Ti).

The positions of C343's C=O and C-OH/C-O peaks (table 3.1) are consistent across the ex-situ, mesoporous, samples, however there are discrepancies when comparing to those prepared in-situ on TiO₂(110). The in-situ depositions provide clean, contaminant-free, samples for comparison to the ex-situ prepared samples and although the latter are realistic, contamination is inevitable and unavoidable. Clearly, hydroxyl groups on the substrate make up a large component of the ex-situ monolayer spectra TiO₂ in Figure 3.2, and are likely present at the multilayer dye-semiconductor interface also. Conversely, no major hydroxyl contributions are observed in the in-situ spectra in Figure 3.3. It is noted that Figure 3.3 was recorded at a much higher photon energy and is thus less sensitive to surface species. However, no obvious contamination is seen in figure A2 for clean TiO₂(110),

nor is it expected from the sublimation procedure. It is possible that the hydroxyls' presence alters the electronic structure of the surface enough to cause an observable shift in the binding energy of the ex-situ mesoporous samples, but it is unlikely that the dye binds to them explicitly. While hydroxylation has been reported to improve the adsorption of some dyes [120, 121, 122], this appears to rely on the influence of positively charged groups, which C343 lacks. However, it is clear based on the ratio of molecule peaks in Figures 3.2b and 3.2c (discussed below) that the dye is largely deprotonated by the surface, and thus the hydroxyls do not appear to block chemisorption.

From Figure 3.1, the ratio between the C=O and C-OH/C-O groups of the dye is expected to be 1:1. However, the ex-situ mesoporous spectra in Figure 3.2 do not match this ratio, instead exhibiting ratios of 2.2:1 (3.2a), 2.7:1 (3.2b), and 3.3:1 (3.2c). In addition, the ratios calculated from Figure 3.3 for the in-situ C343 monolayer and multilayer on TiO₂(110) are 4.7:1 and 1:1 respectively. In the case of the monolayers, these deviations are attributed to deprotonation of the carboxylic acid moiety, which is most likely to occur through a bidentate chelating structure [123] and derivatives of C343 have been observed to adopt this arrangement [124]. Previously, carboxylate oxygens have been found to appear at a similar binding energy to carbonyl groups in a Ru complex dye bound to TiO₂(110) in a bidentate bridging geometry [71], and it is expected that the same occurs here in the the bidentate chelating case. As a result, if deprotonation is complete, a ratio of 3:1 is expected. The ratios in the ex-situ monolayer spectra match this well, showing that the molecule is likely deprotonated and thus bonded to the mesoporous surface through its carboxylic acid group. However, we note that the in-situ deposited monolayer exceeds this ratio, which is attributed to the poor signal-to-noise ratio of the C-OH/C-O peak when

measured using 1486.6 eV photons. This is less important for the in-situ multilayer, where the correct value is found, because much more dye is present and thus the signal greater.

Contrary to expectations, the ex-situ prepared multilayer ratio is roughly double its theoretical value, although this is unlikely caused by deprotonation of the dye on the FTO portion of the substrate. It has been reported that the dye N719 can bind to FTO substrates [125]. However, this could result from N719's COO^- groups rather than deprotonation of its carboxylic acid moieties. As such, contamination of the multilayer is perhaps a better explanation for the ratio calculated. Both ex-situ monolayer samples show significant hydroxyl contamination in Figure 3.2, which is very likely present in the ex-situ multilayer also. As the surface is just visible through the dye in Figure 3.2a, it stands to reason that the C=O peak will also contain a significant surface hydroxyl component, increasing its intensity and altering the ratio of the molecule peaks. For this reason, it is assumed that the ex-situ multilayer spectra largely represent protonated C343.

Figure 3.4 shows the C 1s XPS for each ex-situ sample, where the C-C bond components of the fits are found at 285.1 eV (3.4a, 3.4b) and 285.3 eV (3.4c). Across the three samples, the C-N, C-O, and COOH carbons are determined to be +1.2 eV, +1.7 eV, and +3.48 eV above the main C-C peak. These assignments bear similarities to those reported for fluorescein, i.e., the separation between the C-C and C-O peaks and absolute positions of the carboxylic acid features [108]. While the above fits work well for both ex-situ sensitised monolayers on mesoporous SrTiO_3 and TiO_2 , the difficulty of assigning features to the C 1s spectra with complete confidence should be acknowledged. By sensitising the samples ex-situ they are subject to contamination from both the atmosphere and solvent. However, despite this, the C 1s spectra of in-situ sensitised C343 on $\text{TiO}_2(110)$ shown in

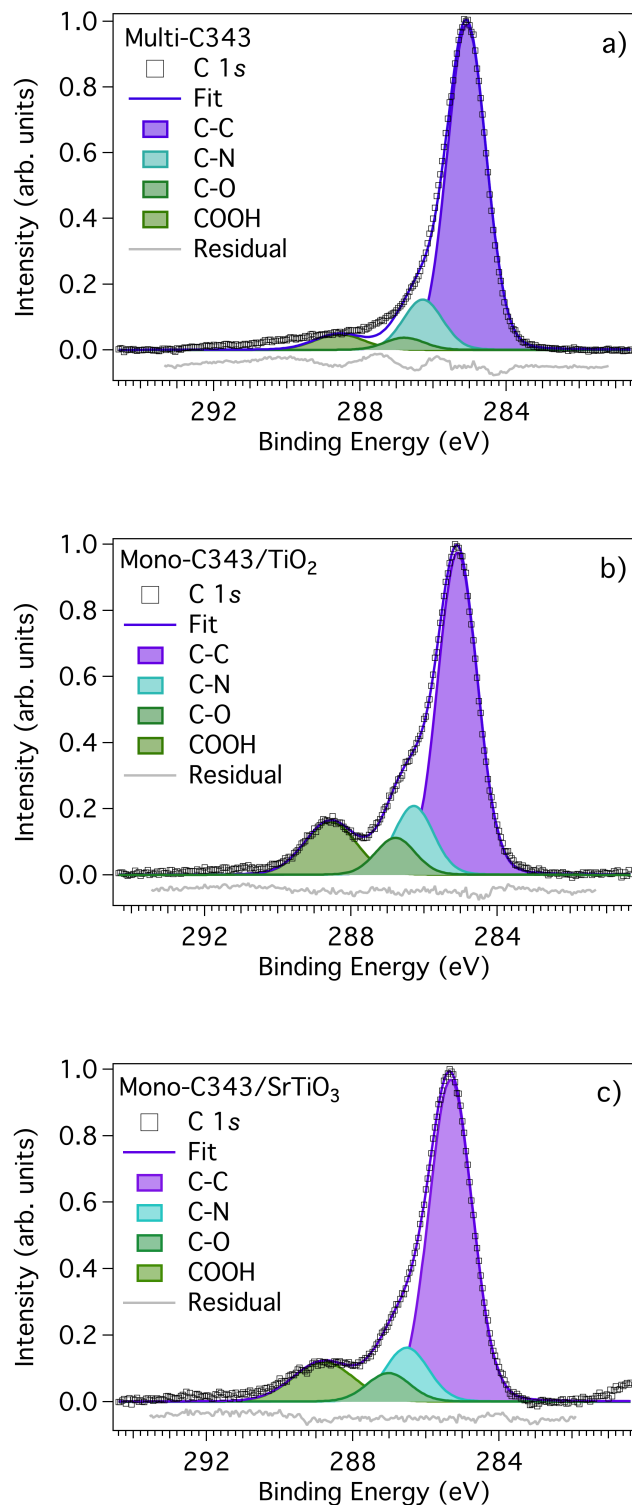


Figure 3.4: C 1s of the ex-situ C343-sensitised electrodes: multilayer on FTO (a), monolayer on TiO₂ (b), and monolayer on SrTiO₃ (c). The spectra were recorded at 600 eV and Shirley backgrounds have been subtracted. Note, the uptick in intensity at low binding energy in (c) is due to the Sr 3p_{1/2} spin couplet that lies close by. All components have a fixed Lorentzian contribution of 0.1 eV [105].

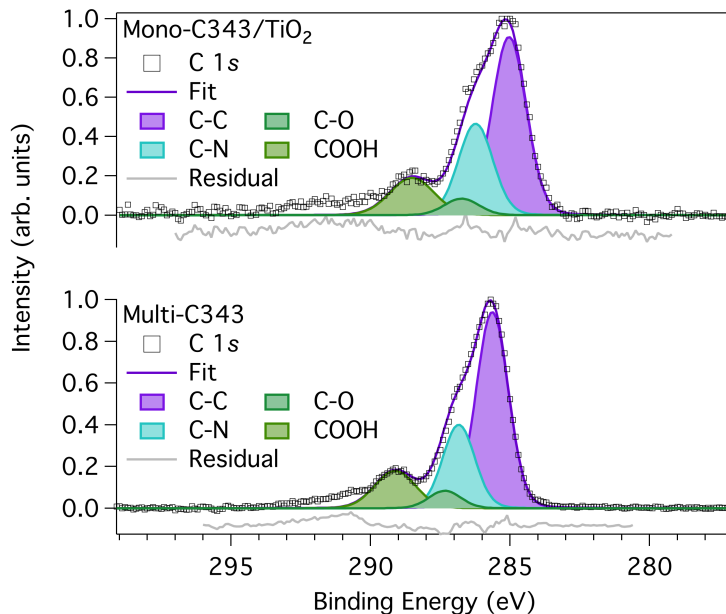


Figure 3.5: C $1s$ of the in-situ prepared C343 monolayer (top) and multilayer (bottom). The spectra were recorded at 1486.6 eV and have had Shirley backgrounds removed. All components have a fixed Lorentzian contribution of 0.1 eV [105].

figure 3.5 are very similar to those in Figure 3.4; where four main components are again identified at similar positions. Negligible contamination is expected during sublimation, thus we can be reasonably confident in our fitting of the ex-situ samples. That being said, the ex-situ multilayer C $1s$ does not match the shape of its in-situ counterpart, which shows distinct peaks. This suggests that the ex-situ prepared multilayer in particular is susceptible to contamination.

In addition to contamination, there are ambiguities introduced from the dye itself, particularly with regards to the carboxylic acid peak. Across the samples, there will inevitably be both deprotonated and protonated dye, in addition to the ester-link. Resolving each of these features from each other is difficult, and complicates analysis of the peak intensities. Consequently, the carboxylic acid features are found to be consistently broader compared to other peaks. Taking the ex-situ prepared multilayer in Figure 3.4a as an example, only the C-C component is obvious, before smoothly decreasing

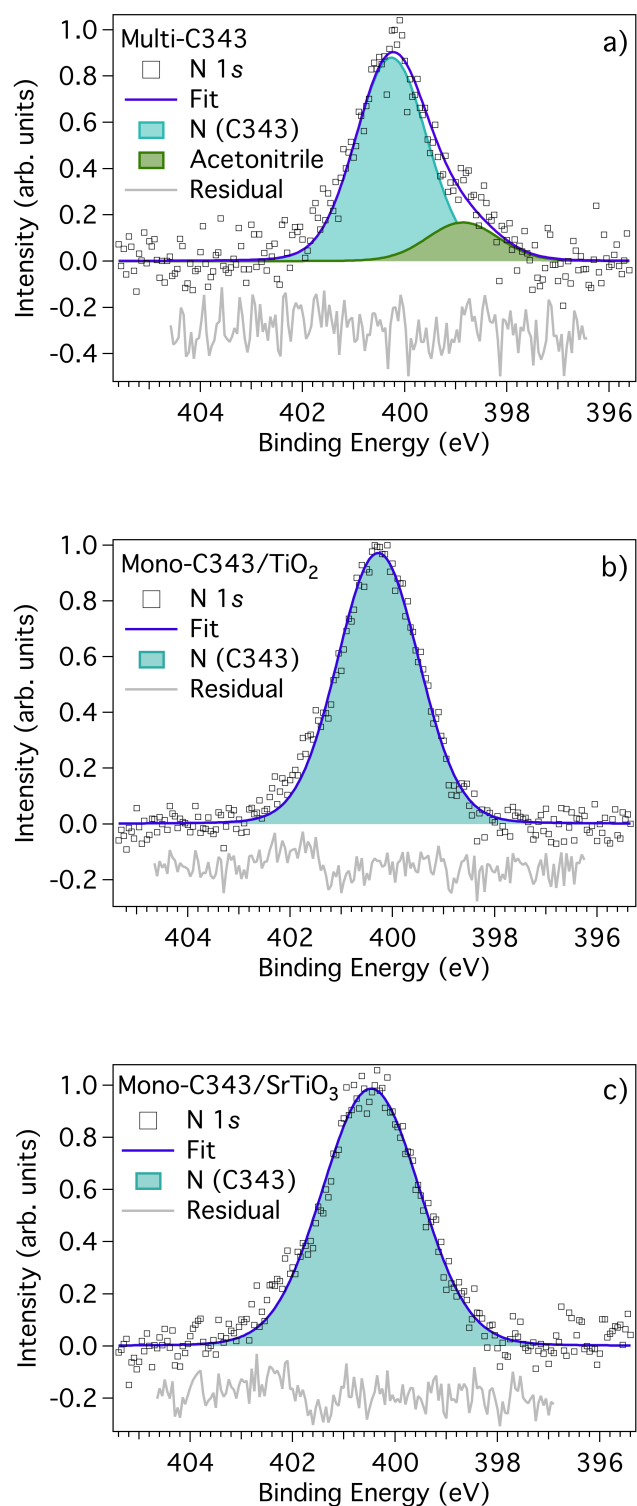


Figure 3.6: N 1s of the ex-situ C343-sensitized electrodes: multilayer (a), monolayer on TiO₂ (b), monolayer on SrTiO₂ (c). As before, the spectra were recorded at 600 eV and linear backgrounds have been subtracted. All components have a fixed Lorentzian contribution of 0.13 eV [105].

with increasing binding energy. As a result, applying the monolayer parameters leaves gaps in the fit, which are highlighted in the residual. Unassigned and contaminating species may help explain these deviations, however the existence of shake up satellites should also be considered. These are common in aromatic molecules [126] and it is expected that they will appear in the C 1s of C343 also. The absorption spectrum of C343 peaks around 440 nm (2.8 eV) [127], thus any satellite structure is likely to manifest around the carboxylic acid peak, which appears to be the case in Figures 3.4a and 3.5. The exact number of peaks needed to fit this region is not clear from the spectra, but up to four could be expected (one for each feature), thus it is left to the residual to highlight the areas where satellite structure may be present.

Figure 3.1 predicts that only one peak should be present in the N 1s XPS of C343, which is observed to be the case for both ex-situ prepared monolayers in Figure 3.6. This, however, is not the case for the ex-situ multilayer, where two peaks are detected. The minor peak in Figure 3.6a is interpreted as contamination from the acetonitrile solvent used to dissolve the dye during preparation. This is supported by our in-situ C343 spectra, in which only one molecule N 1s peak is observed no matter the thickness of the deposited layer (figure A3). The contaminating peak aside, the main component assigned to C343 is found at approximately the same binding energy in each ex-situ spectrum; 400.5 eV on SrTiO₃ and 400.3 eV for TiO₂ and the multilayer. However, despite this consistency, it is obvious that the peak observed for the molecule on SrTiO₃ is much broader than that on TiO₂. While contamination from acetonitrile cannot be ruled out entirely for the monolayers, the greater width in Figure 3.6c is likely caused by the mesoporous substrate itself. SrTiO₃ has a perovskite structure in which the Sr atoms are surrounded by TiO₆ octahedra [128], and it has been

suggested that a mix of both Sr- and Ti-containing surfaces are exposed in its mesoporous form [129]. As such, the availability of multiple facets for C343 to bind to could cause subtle shifts in binding energy, resulting in multiple, unresolvable, peaks. Broader peaks are seen in the C 1s XPS of C343 on SrTiO₃ also, but not the O 1s. Why the trend is not observed in the O 1s is likely related to the overall complexity of the region; the broadening from multiple facets is assumed to be insignificant compared to that of having many similar oxygen environments present.

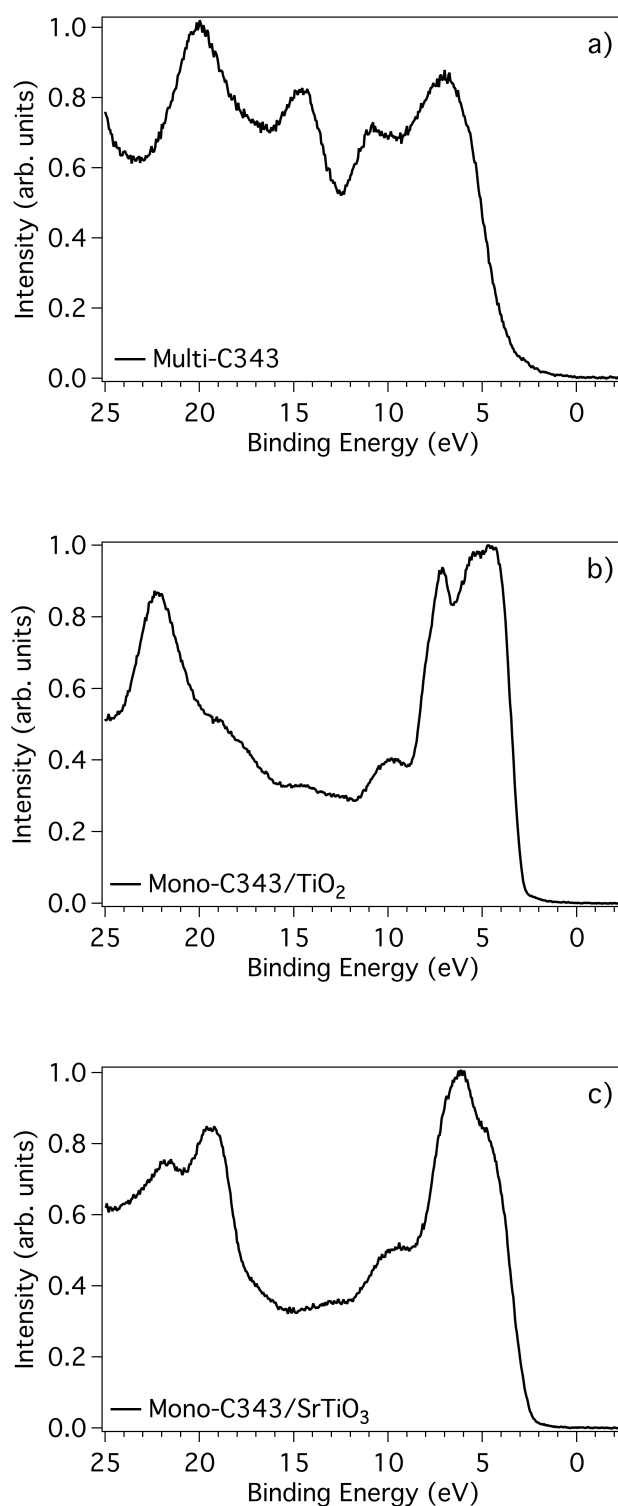


Figure 3.7: Valence spectra of the ex-situ C343-sensitised electrodes: multilayer (a), on TiO₂ (b), and monolayer on SrTiO₃ (c). Each spectrum was recorded at 220 eV.

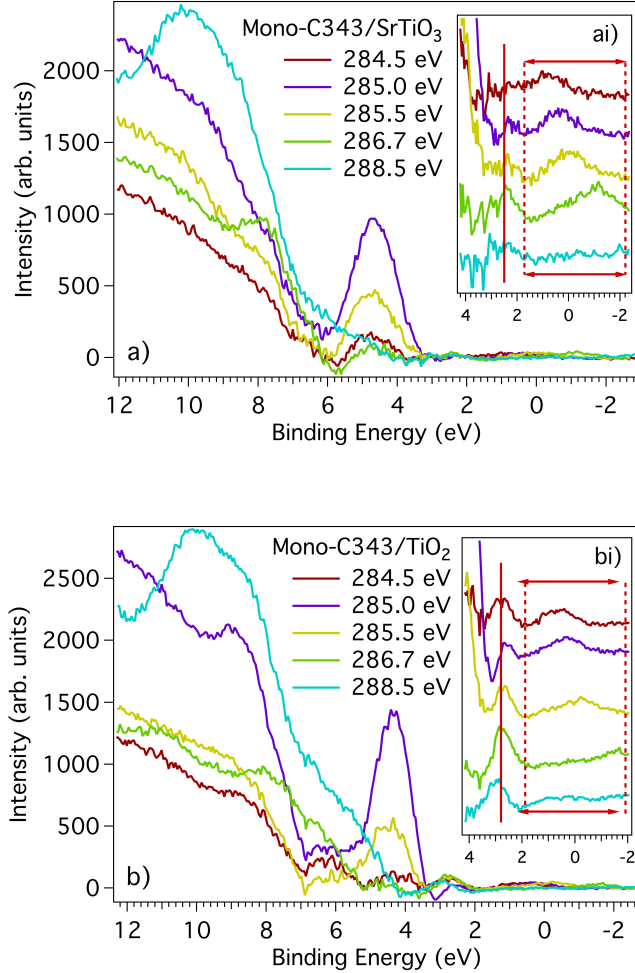


Figure 3.8: Difference spectra of the RPES of C343 on SrTiO₃ (a, ai) and TiO₂ (b, bi) measured over the carbon edge. The regions of interest are magnified with the average position of the HOMO marked by a vertical line. The regions in which 2nd order excitations appear are marked with dashed lines. An off resonant scan has been subtracted from both plots.

3.3.2 Occupied States

Figure 3.7 shows the valence spectra for each ex-situ, C343-sensitised, sample. At first glance it is clear that the monolayer spectra differ significantly to the multilayer, sharing few common features. This suggests that the monolayer valence bands are dominated by signals from their respective substrates and the multilayer by the molecule, as expected. We note how-

ever that the multilayer is not thick enough to eliminate the signal from the substrate, as surface contributions are seen in the core-level spectra above, where the kinetic energy of the photoelectrons is much less. Unfortunately it is not possible to see the highest occupied molecular orbitals (HOMOs) in any of the spectra in Figure 3.7, only to estimate their presence by the tail of the valence bands around 2-3 eV. In order to resolve the HOMOs from the monolayer valence bands, resonant photoelectron spectroscopy was used. By matching the photon energy to that between the relevant core and unoccupied levels, as determined by NEXAFS (Figure 3.10), it is possible for participant decay of the excited electron to enhance the HOMO signal [97].

Figure 3.8a and 3.8b are examples of RPES measurements conducted over the C K-edge for both samples. Here, an off-resonant scan recorded at a photon energy of 283 eV was subtracted from all spectra to establish a baseline for determining any resonant enhancement of the valence band. Strong enhancements for both samples are observed between 4-6 eV, particularly for scans recorded at 285.0 and 285.5 eV. Less obvious however are the enhancements between 2-3 eV. For the TiO₂ substrate, Figure 3.8b shows peaks at 2.8 eV on average across the photon energies. Similarly, there are peaks at approximately 2.5 eV on average in Figure 3.8a, however the signal is very weak. These peaks are assigned to the HOMO of C343 on both substrates. As the resonances are weak, it is important to consider the spectral contribution of C 1s photoemission from second order light. These features are seen between ± 2 eV and drift to more negative values with increasing photon energy. As a result, they do not appear to interfere with the HOMOs in Figure 3.8, however the same cannot be said for the off-resonant scan used as a baseline (figure A4). This overlap will alter the intensity of the HOMO enhancements in Figure 3.8 and appears to have

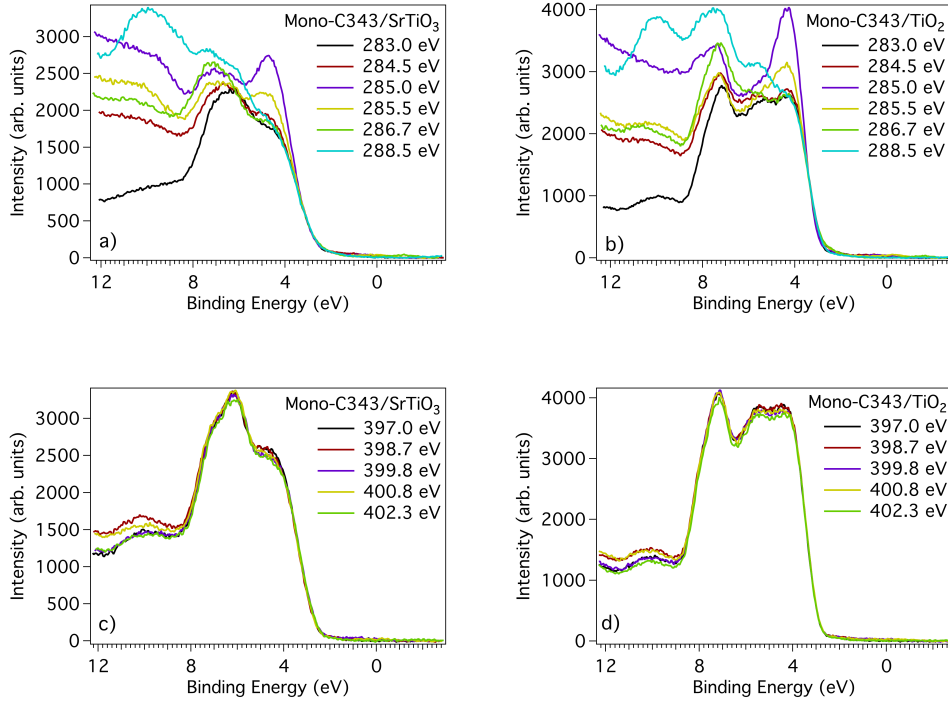


Figure 3.9: RPES of monolayer C343 on both SrTiO_3 (a, c) and TiO_2 (b, d). The top two graphs were recorded over the C K-edge, and the bottom two over the N K-edge. Each scan is aligned to a valence band recorded at a photon energy of 220 eV and has had a constant background subtracted. Little resonant enhancement is seen in (c) and (d).

a greater influence on the SrTiO_3 spectra than the TiO_2 , where the shape of the first three traces (284.5, 285.0, 285.5 eV) is particularly affected. With this in mind, enhancement of the HOMO appears less in Figure 3.8a than Figure 3.8b, which could incorrectly be interpreted qualitatively as increased competition between resonant transitions and charge transfer to the SrTiO_3 substrate. However, this is not supported by the DOS maps discussed below (Figure 3.13) and is instead most probably caused by a combination of the second order excitation in the off-resonant spectrum and the lack of proper normalisation between scans.

RPES measurements were also carried out over the N K-edge for both samples, however no significant enhancements were observed (figure 3.9). This is emphasised by difference spectra shown in the appendices (figure

A5). This could imply that the HOMO lies mostly on the carbon atoms in C343, rather than localised to the nitrogen atom. However, calculations shown in Figure 3.11 predict that there is some probability density from the HOMO around the nitrogen atom. Why the resonances are absent is then a question of the intensity of the N 1s signal. There are far fewer nitrogen atoms than carbon in the molecule, thus fewer N 1s photoelectrons are produced, which is apparent from wide scans taken of each sample (figure A6). As a result, direct photoemission of the valence band (containing contributions from all atoms in the sample) dominates over any possible resonant enhancement caused by core-excited N 1s electrons.

3.3.3 Unoccupied States

Figure 3.10 shows the NEXAFS for the ex-situ sensitised samples over both the N and C K-edges, including the excited states of C343 that make up the spectra as calculated by TD-DFT, which have been aligned to the first peak of the multilayer spectrum (see methods). Overall, the simulated and experimental spectra are in reasonable agreement. In Figure 3.10a, the TD-DFT calculated transitions show that the excited state appearing at 400.8 (monolayers) and 401.0 eV (multilayer) is dominated by the transition from the N 1s core level to the LUMO of the molecule. Unsurprisingly, subsequent excitations are then found to represent transitions to increasingly energetic unoccupied orbitals. The only substantive difference between the monolayer and multilayer spectra is the presence of the peak at 398.7 eV, which is discussed below.

Unlike Figure 3.10a however, the shape of the C K-edge spectra in Figure 3.10b is complex. The first six excited states predicted by TD-DFT result from transitions between various ring carbons in the molecule's coumarin

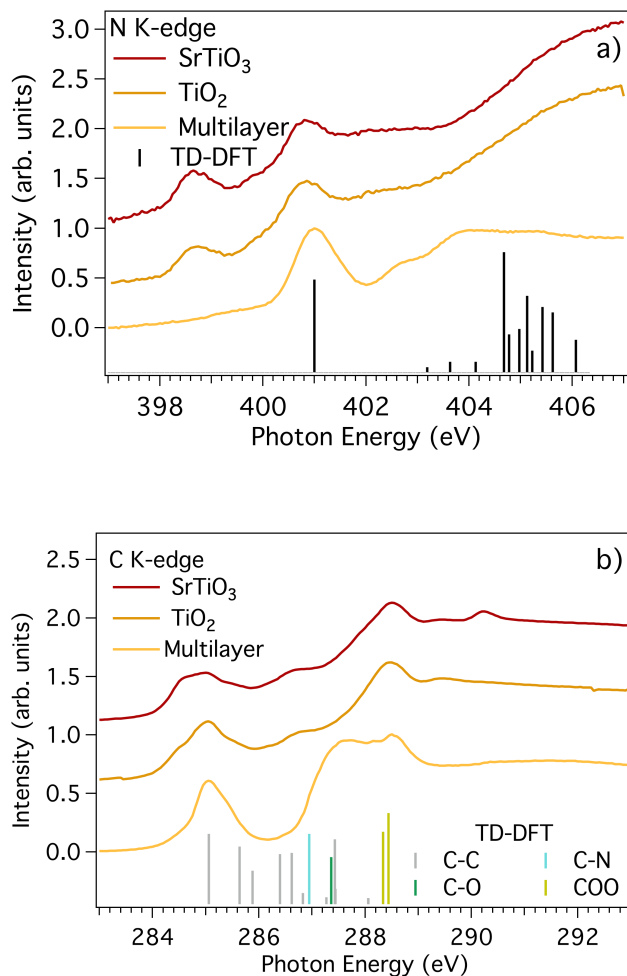


Figure 3.10: XAS recorded over the N (a) and C K-edges (b) for both monolayers and the multilayer in partial electron yield. Also included are the transitions as predicted by TD-DFT, which in the case of carbon are labelled by the environment the electron is excited from.

backbone and the first three unoccupied levels of the molecule. It is probable that the first peak in each spectrum results from a combination of these carbon environments. It is worth noting, however, that transitions involving the ring carbons are found throughout the spectra, and thus will likely overlap with peaks from other groups. At higher energies, the monolayer spectra begin to differ from the multilayer. The peak at 286.7 eV in both monolayer spectra is not immediately seen in the multilayer. Based on the TD-DFT, this excited state is taken to contain contributions from transitions from the C-N and C-O carbons of the dye. It is very likely that this

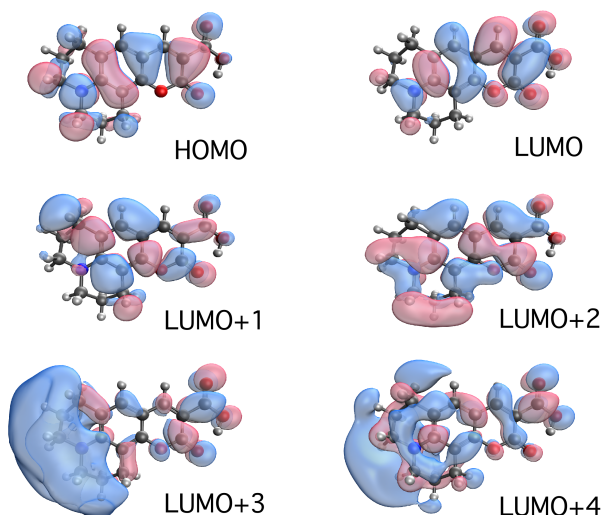


Figure 3.11: Visualisation of the HOMO and first five LUMOs of C343 calculated by DFT.

peak is overshadowed by the large peak at 287.5 eV in the multilayer scan, which itself is unassigned and appears to be the source of the differences between the monolayer and multilayer spectra. It could be argued that there is good alignment between the peak at 287.5 eV and the calculated transition from the C-O carbons of the dye, however, if caused by this group, it should also dominate the monolayer spectra. Hence, the contribution from C-O is instead assigned to the peak at 286.7 eV as stated previously. There are two potential differences between the monolayers and multilayer: protonation and contamination. As discussed in the context of the O 1s XPS, the carboxylic acid is largely deprotonated for the monolayers and likely protonated for the multilayer. Comparison to the TD-DFT, which represents the protonated molecule, implies that protonation is not the origin of the additional feature at 287.5 eV in the multilayer scan. It is instead attributed to a contaminant, which is likely present in the multilayer as evidenced in the C and N 1s XPS (Figure 3.6a).

As mentioned above, both monolayer N K-edges in Figure 3.10a show a pre-edge feature at 398.7 eV. It would seem obvious that the lowest excited

state of C343 is represented by this peak. However, this contradicts the TD-DFT results and no similar feature is detected in the multilayer scan. Furthermore, DFT predicts that the unoccupied orbitals are delocalised (Figure 3.11); thus, the peaks should also appear in the C K-edge spectra if they represent a low-energy excited state of C343. This is not the case and, as a result, it is not immediately obvious what the peaks at 398.7 eV in Figure 3.10a are. We can infer from their absence from the multilayer and C K-edge NEXAFS that the peak arises from near the substrate surface and likely involves a nitrogen atom. A potential explanation could be acetonitrile contamination from the sensitising process. However, subsequent NEXAFS measurements of non-sensitised, mesoporous, TiO_2 that had been immersed ex-situ in acetonitrile for 30 minutes showed little sign of contamination (figure A7). In addition, only the multilayer showed acetonitrile contamination in the N 1s XPS, not the monolayers. Thus solvent contamination is unlikely to be the source of the unknown features. With this in mind, it is worth considering if some unexpected bonding geometry of C343 on TiO_2 is responsible for the unidentified peaks. Given the above discussion, such a bonding arrangement must involve the lone pair on the nitrogen atom contained within the julolidyl group of the dye. Several small amine molecules have been shown to bind to $\text{TiO}_2(110)$ via donation of their nitrogen lone pair electrons to Ti^{4+} cations (or oxygen vacancies if present) in a Lewis acid-base reaction [130]. However, triphenylamine (a moiety often found in organic dyes) exhibits little basicity due to the nitrogen lone pair's ability to delocalise across its phenyl groups [131], hence is unlikely to bind to TiO_2 in this way. Therefore, whether C343 can bind to TiO_2 through its nitrogen atom depends on how localised its lone pair is compared to these molecules. If the dye were able to do so, it is reasonable to expect this to cause a shift in the NEXAFS. By donating its lone pair, the nitrogen atom is left net positive, meaning that electrons excited from

the N 1s core level will feel increased electrostatic attraction towards it. This would reduce the energy of the N 1s to LUMO transition relative that seen for deprotonated C343.

Finally, in addition to the calculated transitions, several orbitals are visualised in Figure 3.11. Both the HOMO and LUMO shown qualitatively agree with previous calculations of C343 [123]. Our calculations show that both the HOMO and the lowest energy unoccupied orbitals are delocalised across the molecule. However, only the LUMO tends to the anchoring side of C343, with the rest lying towards the nitrogen atom. This may reduce the degree of coupling between the substrate conduction band and unoccupied states, potentially reducing the charge injection efficiency.

3.3.4 Density of States

The electronic structure of the dye-semiconductor interface is intrinsically linked to the function of a DSSC, governing its absorption characteristics and charge transfer dynamics. By combining the occupied and unoccupied states of the ex-situ samples via the method described in reference [83], DOS maps can be formed. These plots reflect the electronic structure of the samples under X-ray irradiation, and thus the unoccupied spectra are shifted to higher binding energy by the presence of the core-valence exciton. Therefore, it should be noted that these maps do not reflect the situation under normal DSSC operation. The plots are shown in Figure 3.13 for both monolayer samples, where the valence band maximum (VBM) and conduction band minimum (CBM) are marked. The VBM were determined by finding the intersection between a fit of the linear region of the VBM and background at low binding energy in the XPS of non-sensitised electrodes (figure 3.12). This method has been shown to approximate well values ob-

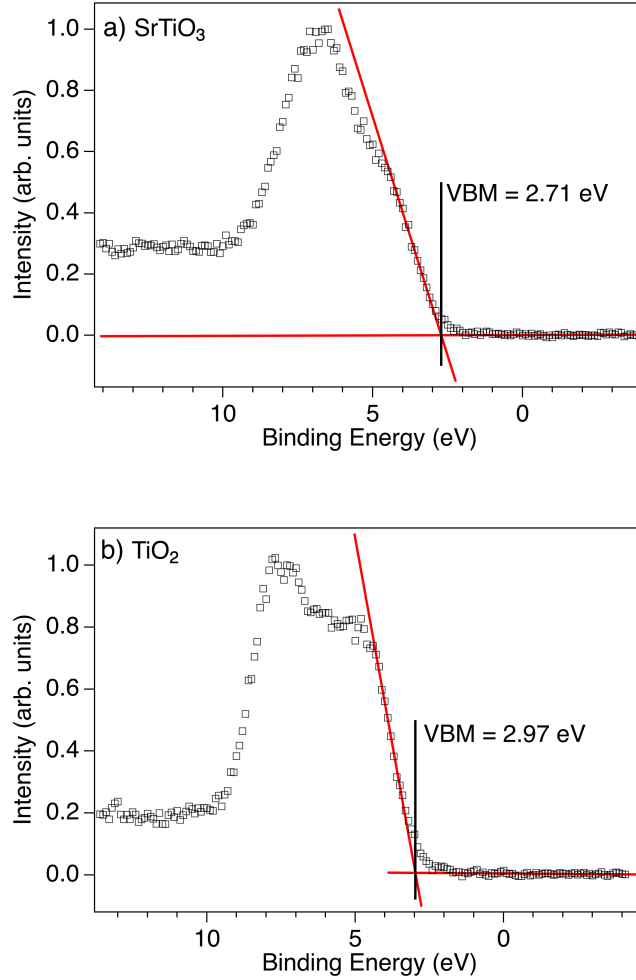


Figure 3.12: valence XPS of bare mesoporous SrTiO₃ (a) and TiO₂ (b). The valence band maxima (VBM) were determined utilising the method described in reference [132] and recorded using 1486.6 eV photons on a lab-based Al source.

tained from mixed experimental/theoretical methods for SrTiO₃ and other materials [132]. The CBM values were then found simply by adding the band gap of each material to its respective VBM (3.25 eV SrTiO₃ [133], 3.0-3.2 eV TiO₂ [60, 134]). Thus, the binding energy positions of the bands are approximated as 2.71 eV and -0.54 eV on SrTiO₃, and 2.97 eV and -0.23 eV on TiO₂, for the VBM and CBM respectively. Altogether we see that the first peaks in both K-edge spectra appear below the CBM for SrTiO₃ (Figure 3.13a). This, however, is not the case for TiO₂ (Figure 3.13b); the first peak of the N K-edge spectrum lies above the CBM. This difference

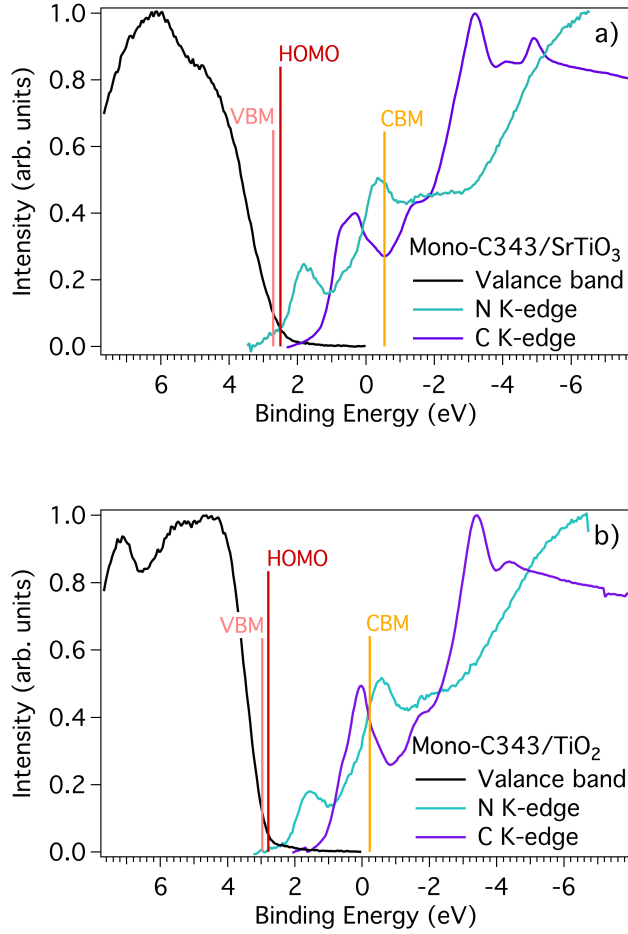


Figure 3.13: DOS plots for monolayer C343 on SrTiO₃ (a) and TiO₂ (b), where the HOMO, VBM and CBM positions have been marked. These plots are formed by aligning the valence XPS and XAS data.

is caused by the interplay between the the VBM position, band gap, and binding energies of the core-levels used to set the valence XPS and NEX-AFS on the same energy scale. It should also be noted that the CBM in Figure 3.13b corresponds to the anatase band gap and thus represents the most negative energy that this band can appear.

Previously, insufficient dye coverage has been suggested as the reason for lower photocurrent values on DSSCs utilising SrTiO₃ substrates [129]. However, in light of figure 3.13, we predict that the photocurrent of C343 sensitised SrTiO₃ may also be intrinsically reduced compared to TiO₂, where

the energetics for charge transfer are more favourable. While the NEXAFS in Figure 3.13 is influenced by the X-ray induced core-valence exciton, both samples should be affected similarly. Therefore, the dye's favourable energetics on TiO_2 should be preserved under visible light. The core-hole clock implementation of RPES could help clarify to what extent a greater separation between the unoccupied dye and substrate states affects the charge transfer time, and thus the efficiency, of C343 photoanodes. Such an experiment would likely find a faster charge transfer time on TiO_2 than SrTiO_3 and be independent of monolayer coverage.

Figure 3.13 can also provide context to the RPES in Figure 3.8, where the weaker enhancement of the HOMO on SrTiO_3 could incorrectly be interpreted as increased charge transfer from the dye to the substrate. As the unoccupied states measured over the C K-edge largely lie below the SrTiO_3 CBM, only electrons promoted to the higher unoccupied states of C343 are permitted to tunnel into the conduction band. As a result, for the least energetic excited states, there is no competition from charge transfer and participant decay of the excited electron can proceed unhindered. In addition, the excited states whose energetics are favourable for tunneling lie closer to SrTiO_3 's CBM than those on TiO_2 , reducing the impetus for charge transfer. Taken together, both factors point to greater competition between resonant processes and charge transfer on TiO_2 , which would be expected to reduce the RPES signal compared to SrTiO_3 . However, the opposite is found in Figure 3.8; C343 on SrTiO_3 shows lesser resonant enhancement compared to TiO_2 . This supports the interpretation in the previous section that C 1s photoemission from second order light in the off-resonant scan causes muted enhancement of the HOMO on SrTiO_3 to be seen in the difference spectrum.

3.4 Conclusions

Through a combination of synchrotron core-electron spectroscopy, DFT, and laboratory XPS, photoanodes based on the organic dye C343 have been analysed in depth. Using XPS, it was found that monolayer C343 prepared ex-situ was deprotonated by both TiO_2 and SrTiO_3 substrates, and protonation of the ex-situ prepared multilayer was assumed. Similarly, the in-situ C343 monolayer and multilayer are found to be deprotonated and protonated respectively. Further, hydroxyl contamination was identified in all ex-situ samples and it is expected that this caused the binding energy differences between the O 1s of the in-situ and ex-situ samples. Although XPS was unable to determine the position of the HOMO, its binding energy was identified for both ex-situ prepared monolayers using RPES. NEXAFS of C343 on both substrates was analysed using TD-DFT and the likelihood that the dye can bond through its nitrogen atom discussed. For this work, contamination was a recurring theme for the ex-situ prepared samples, and highlights the difficulty it can cause for this kind of experiment. To minimise this, in-situ deposition and air-free transport to the beamline should be considered.

The XPS, NEXAFS, and RPES were then combined to form the density of states for C343 on both TiO_2 and SrTiO_3 , where TD-DFT was used to elucidate the transitions involved. As a result, it was seen that the lowest energy excited states for C343 on SrTiO_3 lay below the CBM, forbidding them from charge transfer in the core-excited regime. This was not true for TiO_2 , where only the lowest energy C 1s excitations appear below the CBM. In addition, those states where charge transfer could occur were found to lie closer to the SrTiO_3 's CBM than on the TiO_2 substrate. From this, it was suggested that the energetics for C343 on SrTiO_3 are less favourable for

charge transfer, which could contribute to an inherently worse photocurrent compared to TiO_2 , under visible light. Further experiments into C343 photoanodes may validate the previous statement; particularly the core-hole clock implementation of RPES, which could quantify how the choice of substrate influences the charge transfer time of a particular dye. The results presented herein will be valuable for such a study, and will also assist future core-level electron spectroscopy of organic dyes, particularly those based on coumarin.

Chapter 4

Competition between
sub-femtosecond charge
injection and relaxation in a
Ru complex at the S 1s and
Ru $2p_{3/2}$ edges

Contents

| | | |
|-------|--|------------|
| 4.1 | Introduction | 86 |
| 4.2 | Methods | 87 |
| 4.2.1 | Sample Preparation | 87 |
| 4.2.2 | Beamline | 88 |
| 4.2.3 | Spectroscopy | 89 |
| 4.3 | Results & Discussion | 90 |
| 4.3.1 | Hard X-ray Photoelectron Spectroscopy | 90 |
| 4.3.2 | Sulphur KLL & Ruthenium LMM Augers | 97 |
| 4.3.3 | Partial Density of States (pDOS) | 100 |
| 4.3.4 | Charge Relaxation at the First Resonance | 101 |
| 4.3.5 | Charge Injection at the Second Resonance | 108 |
| 4.4 | Conclusion | 111 |

4.1 Introduction

To facilitate high efficiencies, the time taken for the excited electron to transfer away from the dye must be fast, outpacing recombination. Typically, this is achieved by ensuring good spatial overlap and favourable energetic alignment between the unoccupied states of the molecule and conduction states of the semiconductor respectively [135]. The dye *cis-bis(isothiocyanato)-bis(2,2-bipyridyl-4,4-dicarboxylato)-ruthenium(II)*, commonly referred to as ‘N3’, is one such sensitiser that shows good coupling between its excited state and the conduction band of TiO_2 [32]. In this context, N3 exhibits ultra-fast charge injection, reportedly occurring within 16 fs [71]. It is expected that N3 bonds to TiO_2 through deprotonation of its carboxylic acid groups located on the bipyridine ligands, however it has been observed that alternative bonding modes involving the thiocyanate ligands are also possible [118]. The former of these ligands has been investigated using photoelectron spectroscopy previously, finding an injection time of <3 fs on bi-isonicotonic acid after excitation from the N $1s$ [97], but little is known of charge injection involving excitations from the S $1s$ core levels.

Resonant Auger electron spectroscopy (RAES) is among the core-level X-ray spectroscopies capable of accurately quantifying charge transfer processes with sub-femtosecond precision via ‘core-hole’ clock analysis [136, 137]. Like other core spectroscopies, RAES offers chemical specificity, enabling selective excitation from individual atoms within a molecule. However, unlike other photoelectron spectroscopies, RAES must be regarded as a one-step scattering process, complicating its analysis. A full theoretical description of RAES, sometimes referred to as non-radiative resonant X-ray Raman scattering (RXS), can be found elsewhere [85, 86, 87]. However, a

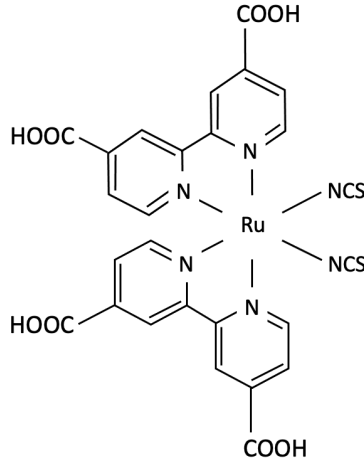


Figure 4.1: Schematic of N3 dye. The molecule is a ruthenium complex with two bipyridine ligands, which have two COOH anchoring groups each, and two thiocyanate ligands.

brief explanation is presented in chapter 2.

In this chapter, RAES is used to quantify the charge transfer dynamics of model N3 photoanodes at the S $1s$ and Ru $2p_{3/2}$ absorption edges, focussing on the sulphur KLL and ruthenium LMM Augers. Monolayer and multilayer samples are studied to probe both charge injection from, and relaxation within, the molecule. As a result, charge injection times for N3 are obtained with greater precision than previously, due to the shorter core-hole lifetimes of the regions studied, and a picture of injection involving the thiocyanate ligand presented.

4.2 Methods

4.2.1 Sample Preparation

Monolayer samples were prepared by soaking mesoporous TiO_2 on FTO glass (Solaronix) in a solution of N3 dissolved in ethanol for 12 hours, un-

der a nitrogen atmosphere. The soaked electrodes were then washed and soaked further in ethanol to desorb physisorbed dye. Multilayers of N3 were deposited via in-situ UHV electrospray deposition onto Si/SiO₂ substrates, which were heated previously to $\sim 200^\circ\text{C}$. This was conducted in a SPECS DeviSim NAP-XPS system fitted with a Phoibos 150 hemispherical analyser, equipped with an Al K α X-ray source (1486.6 eV). A concentrated solution of N3 was pumped through a stainless steel emitter (internal diameter 100 μm , New Objective, USA) at a rate of 0.3 mlhr⁻¹. The emitter was held at a voltage of 2.3 kV relative to the ground, ionising the solvent, and ejecting a jet of dye solution. The electrospray plume is drawn into an entrance aperture (internal diameter 0.5 mm), passing through a series of differentially pumped stages with increasingly wider entrance apertures where the solvent evaporates. The base pressure of the UHV chamber sits at 1×10^{-9} mbar normally, which increased to 10^{-8} mbar with the gate valve to the electrospray opened and voltage off. With the valve open and voltage on, the pressure varied between low to mid 10^{-7} mbar, showing that the majority of the spray consisted of N3. As a result, it is largely only the dye deposited, with thickness and purity monitored by XPS.

4.2.2 Beamline

The experiment was performed at the I09 beamline at Diamond Light Source, U.K. The beamline offers both soft and hard X-ray beams, where the former was used for X-ray absorption spectroscopy (XAS) at the nitrogen edge and the latter for photoelectron spectroscopy (PES) and RAES measurements. To minimise beam damage and average variations due to the mesoporous substrate, the beam was defocussed to $400 \times 400 \mu\text{m}^2$. Further, the undulators were detuned and defocussed by a factor of $\times 20$ for

the soft beam and $\times 40$ for the hard beam, again to reduce beam damage. The beamline has a resolving power of $\times 10,000$, giving resolutions of ~ 0.25 and ~ 0.28 eV at the S $1s$ and Ru $2p_{3/2}$ edges respectively. The beamline is equipped with a VG Scienta EW4000 analyser with an angular acceptance of 56° , and measurements were taken at 10° from normal emission (80° from the axis of the beam).

4.2.3 Spectroscopy

XPS was measured using a photon energy of 2.7 keV and a pass energy of 100 eV in swept mode. All Ru RAES was conducted using a pass energy of 200 eV in swept mode, whereas the S RAES maps were taken using a pass energy of 500 eV in fixed mode and supplemented with high-resolution swept mode scans recorded at 200 eV pass energy for the monolayer. To fit S KLL spectra of the multilayer, slices were taken from the map and the shape of the detector corrected for before fitting. Due to long measurement times, these parameters were chosen to avoid artefacts in the data resulting from top-up injections of the ring. For this reason, only the first resonance of the Ru RAES was measured. Beam damage was monitored using the N $1s$ XAS signal in total electron yield (TEY), measured using the sample drain current, where no major differences are observed when comparing before and after RAES data was taken (figure A8).

All kinetic energy scales were calibrated to the Ti $2p_{3/2}$ peak at 458.8 eV, which was determined from the O $1s$ of a non-sensitised electrode being set to 530.05 eV [106]. For the multilayer, this was achieved by lining up features with those in the calibrated monolayer spectra. Peak fitting was carried out using a pseudo-Voigt function that has been modified to include asymmetry as required [138]. For the PES, the Gaussian-Lorentzian

ratio was kept constant for features arising from the same core-level, with the widths allowed to vary within realistic constraints. The same rule was applied for analysing the RAES data, however it should be noted that parameters such as the Gaussian and Lorentzian widths lose some of their physical meaning. The probability distribution is governed by a convolution of the lifetime broadening, photon energy bandwidth, and spectrometer function, with the narrowest width determining the overall peak shape [85]. For the data presented in this report, the lifetime broadening of the S $1s$ is comparable to the photon bandwidth, whereas the Ru $2p_{3/2}$ broadening is much greater; 0.52 eV (1.27 fs) vs. 1.87 eV (0.35 fs) respectively [139]. As a result, for the Ru RAES, it is expected that the Ru resonant Auger peaks (‘spectators’) will be largely Gaussian in character, however no such approximation can be made confidently in the case of S. Shirley backgrounds were employed for both the PES and the S RAES, where linear slopes were incorporated if required. This was found to be inadequate to fit the background in the Ru RAES, thus a combination of linear slope and Tougaard-type backgrounds were employed instead [79].

4.3 Results & Discussion

4.3.1 Hard X-ray Photoelectron Spectroscopy

Figure 4.2 shows the O $1s$ of both samples. The multilayer (figure 4.2b) shows peaks at 531.8 and 533.1 eV, which are attributed to the oxygen species within the molecule’s carboxylic acid moieties [71]. These same species are identified in the monolayer (figure 4.2a) at 531.9 and 533 eV, with a further peak at 531 eV attributed to hydroxyl groups from water contamination. These were most likely adsorbed from the atmosphere onto

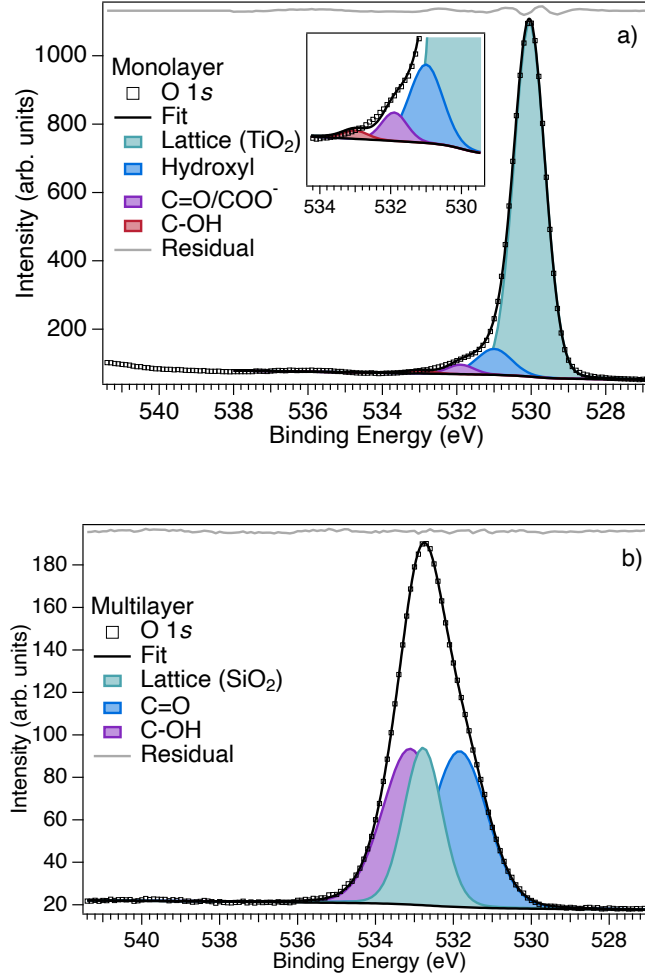


Figure 4.2: O 1s XPS of monolayer (a) and multilayer (b) N3. The ratio of molecular features in the O 1s is 3.4:1 on the monolayer and 1:1 on the multilayer. Measured using a photon energy of 2700 eV at a pass energy of 100 eV in swept mode. Fit using a combination of linear and Shirley backgrounds.

the electrode pre-sensitisation; hydroxyl groups have previously been found to appear around 531.2 eV on TiO₂ [65]. Lastly, the peaks at 530.05 and 532.8 eV are attributed to the TiO₂ and SiO₂ substrates for the monolayer and multilayer respectively [106, 140]. The inset of figure 4.2a shows that the fit is not perfect, which is attributed to the background rising over the data at higher binding energies. This spectrum in particular is difficult to fit at this photon energy, as the substrate dominates.

From the stoichiometry of the molecule, it is expected that the ratio of

C-OH to C=O peaks is 1:1. Applying this to the multilayer works well, indicating that the signal represents molecules that are protonated and physisorbed to the substrate. However, the monolayer instead exhibits a ratio of 3.4:1. The deviation between samples is caused by deprotonation of one of the bi-isonictonic acid ligands utilised for bonding. Here, the hydrogen atoms in the carboxyl moieties are lost and the now chemically equivalent oxygen atoms form a bond with the surface [141]. The subsequent carboxylate species shows a bidentate bridging bonding geometry and manifests at a similar binding energy to the C=O on the unaffected ligand, leading to an expected ratio of 3:1 [71]. The value calculated from figure 4.2a thus indicates that the majority of the molecule is deprotonated and it is inferred that contaminating hydroxyl groups do not interfere with adsorption.

Figure 4.3 shows the S 1s for both samples. Three components are identified, appearing at 2469.8, 2471.8, 2477.8 eV on the monolayer in figure 4.3a. The first of these peaks appears at the same binding energy in the multilayer and is thus attributed to non-bonded thiocyanate ligands. The remaining peaks in figure 4.3b appear at lower binding energy compared to the monolayer: 2471.5 and 2477.2 eV. The highest energy peak in both figures 4.3a and 4.3b is attributed to oxidised sulphur [142], likely as a result of beam damage. However, in both spectra this component makes up a small fraction of the overall intensity ($\sim 5\%$) and thus is not anticipated to meaningfully affect the charge transfer times calculated later in this work. It is not clear what is responsible for the high binding energy shoulders on the main peaks in both figure 4.3a and 4.3b, however it is likely that they indicate a bonding interaction involving the thiocyanate and surface. This has previously been reported to cause a 0.7 eV shift to higher binding energy in the S 2p region compared to non-bonded thiocyanate [71, 118]. Instead, for the S 1s in figure 4.3, shifts of ~ 2 eV are found. This difference

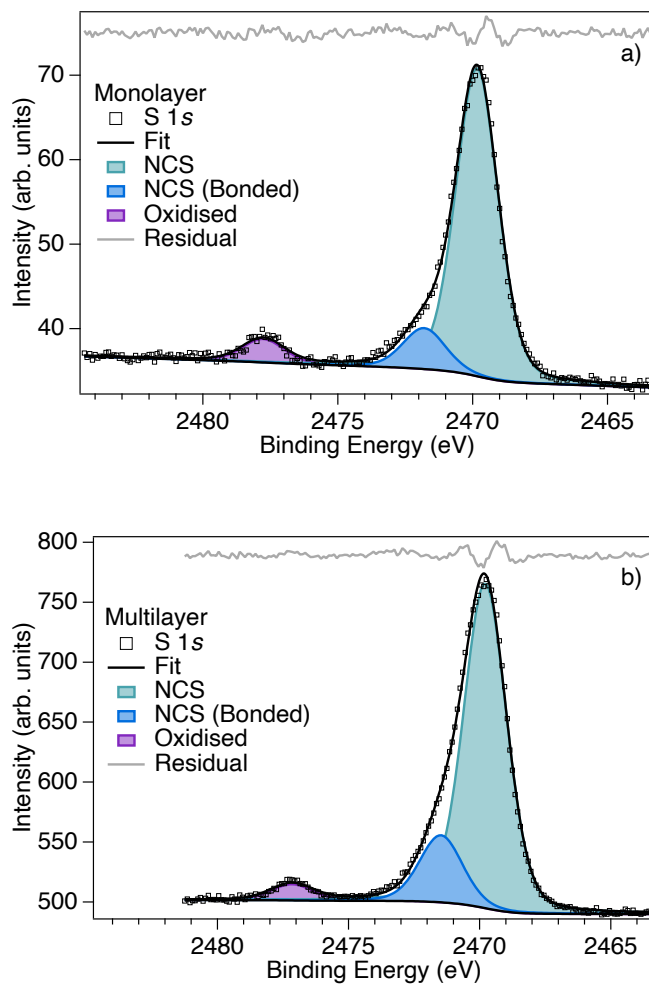


Figure 4.3: S 1s XPS of monolayer (a) and multilayer (b) N3. Measured using a photon energy of 2700 eV at a pass energy of 100 eV in swept mode. The multilayer was fit with a Shirley background, and the monolayer using a combination of Shirley and linear backgrounds.

is attributed to differences in shielding caused by the removal of an S $1s$, compared to an S $2p$, electron.

In principle, it is possible that some thiocyanate-surface interaction could be detected in the multilayer, due to the kinetic energy of the recorded photoelectrons (~ 200 eV). However, the proportion of bonded thiocyanate in the multilayer is comparable to the monolayer, which is unexpected for a species buried under a thick dye layer. Therefore, in the case of the multilayer, this peak may also represent donor interactions between the thiocyanate and neighbouring dye molecules. If this were the case, the electropositive hydrogen atom in the COOH anchor group is the likeliest target. No deprotonation is observed in figure 4.2b, which suggests that N3 is largely physisorbed on SiO_2 in the multilayer, lending credence to intermolecular bonding as the origin of greater than expected intensity of the ‘bonded’ thiocyanate peak. Here, it is noted that the kinetic energy of the O $1s$ photoelectrons is on order of 2.2 keV, meaning any deprotonated dye contribution would be detected, if significant. Thus, the coupling between the unoccupied states and Si conduction band is taken to be minimal and charge injection is not expected to influence RAES of the multilayer.

The C $1s$ and Ru $3d$ spectra for the monolayer and multilayer are shown in figure 4.4a and 4.4b respectively. Peaks are located at 280.9, 285.1, 285.05, 286.2, and 288.6 eV on the monolayer. These match the multilayer, with the exception of the highest binding energy peak, which appears at 288.8 eV. The first two features of this list are assigned to the central Ru^{2+} ion of the molecule [143]. The remaining peaks are assigned to bonds with C-C/C-S character, C-N environments, and COOH respectively, in-line with previous reports of similar dye molecules [71, 108, 144]. Contamination is not expected to be a problem for the in-situ prepared multilayer; thus it is taken that the signal in figure 4.4b is mostly from N3 molecule. With

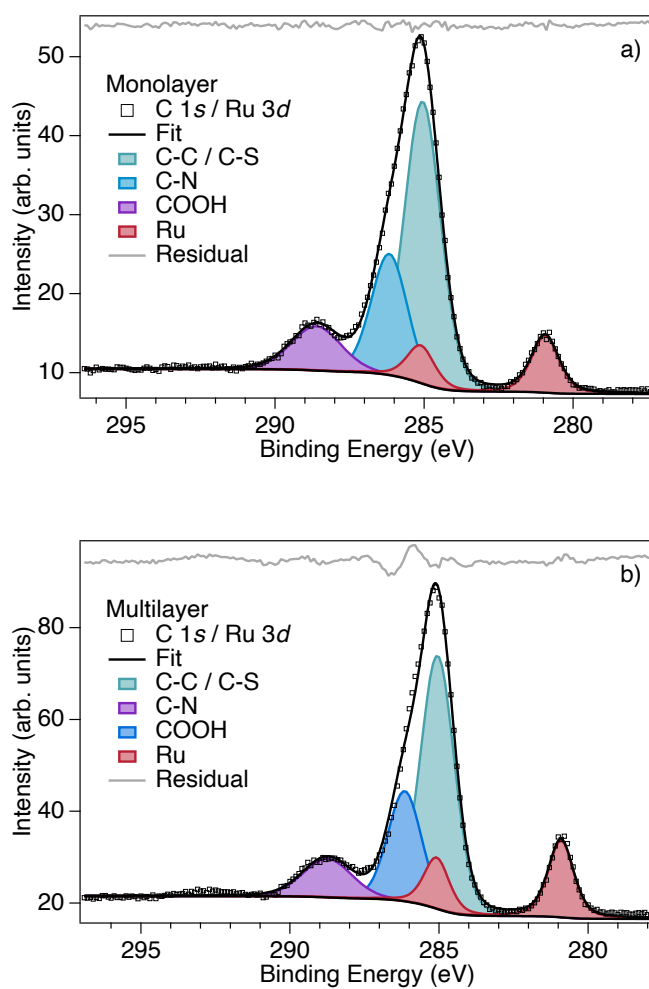


Figure 4.4: C 1s XPS of monolayer (a) and multilayer (b) N3. Measured using a photon energy of 2700 eV at a pass energy of 100 eV in swept mode, and fit using Shirley backgrounds.

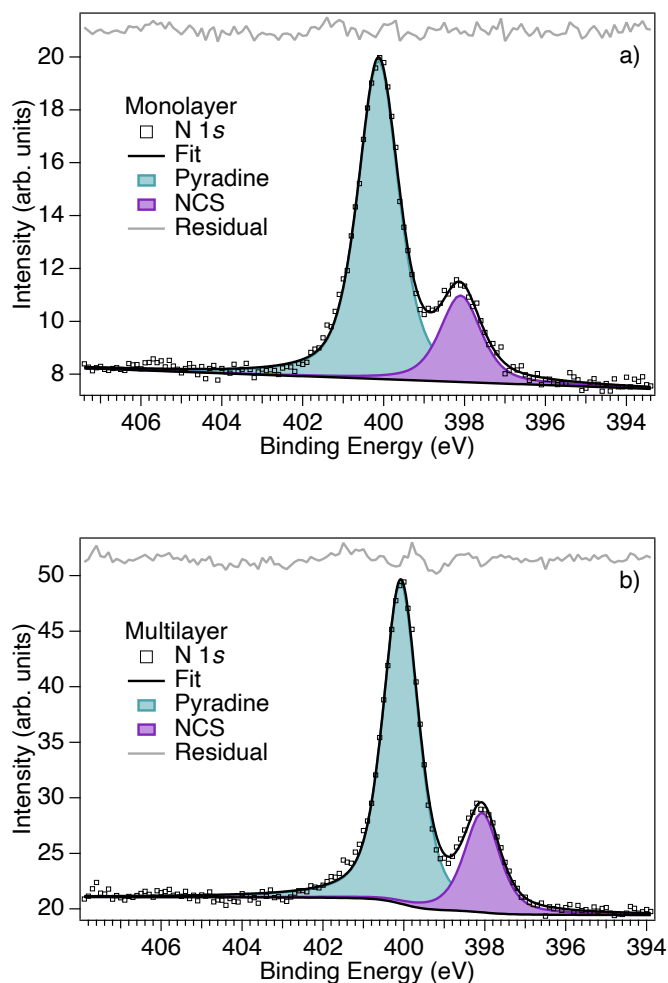


Figure 4.5: N 1s XPS of monolayer (a) and multilayer (b) N3. Measured using a photon energy of 2700 eV at a pass energy of 100 eV in swept mode. The monolayer spectrum was fit using a linear background and the multilayer using a Shirley background.

this in mind, it is reassuring that the ex-situ prepared monolayer C 1s matches the multilayer well, also suggesting minimal contamination of this sample. Both samples were transferred into I09 from atmosphere, thus some contamination may be present, however the photon energies used in this work are unlikely to detect it.

From the molecule's structure, it is expected that the ratio of pyridine to thiocyanate signals in the N 1s should be approximately 2:1, but this does not appear to be the case in either figure 4.5a or 4.5b. Instead, the ratios

are 3.7 and 3.2 for the monolayer and multilayer respectively. One possible explanation is that beam damage of the thiocyanate ligands (as seen in figure 4.3) results in the removal of nitrogen, giving a lesser intensity in the N 1s from that ligand. However, this is too small a fraction of the total intensity to account for the difference alone, based on the S 1s. A further possibility is that bonding with thiocyanate positions its nitrogen close to the substrate surface, leading to the rest of the molecule shadowing its signal. This has previously been reported for organic dye molecules on TiO₂ [145]. However, the kinetic energy is large here. As such, it would be expected that this effect is small, if it is present at all. With the above phenomena determined to be unlikely, the deviation from the expected ratio of pyridine to thiocyanate signals is taken to be caused by shake up structure overlapping with the pyridine peak.

4.3.2 Sulphur KLL & Ruthenium LMM Augers

Figure 4.6 shows how the S KLL Auger varies with the photon energy. Two resonances are seen, one at 2467 eV common to both maps, and another at 2476 and 2477 eV on the multilayer and monolayer respectively. In the maps, both spectator and normal Augers overlap significantly, thus, it is essential to separate them. The S KLL Auger recorded off-resonance on the monolayer (figure 4.6c) corresponds to the minimum resonant case, i.e. maximum charge transfer. As a result, little-to-no spectator peaks are expected, highlighting the normal Auger contribution to the region. The peaks at 2095.3 and 2103.5 eV in this spectrum are assigned to the ¹S and ¹D transitions of the $2p^{-2}$ final state [146]. The opposing case is shown in figure 4.6d, which is recorded just below the S 1s ionisation threshold on the multilayer, representing the maximum spectator case. Six peaks

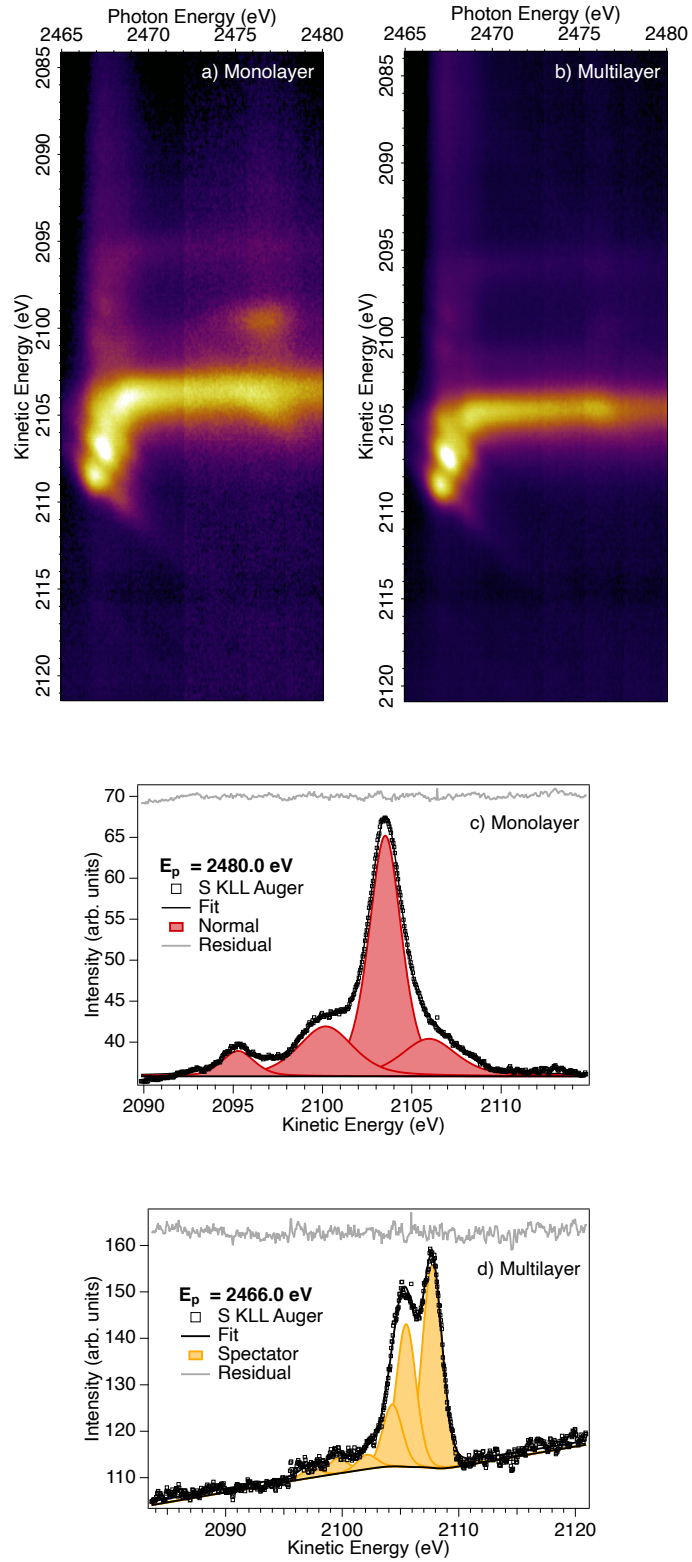


Figure 4.6: S KLL Auger measured whilst varying the photon energy over the first two resonances on monolayer (a) and multilayer (b) N3. Also shown is the Auger recorded off-resonance on the monolayer (c) and below the ionisation threshold on the multilayer (d). These indicate the minimum and maximum resonant cases. Recorded using a pass energy of 500 eV in fixed mode.

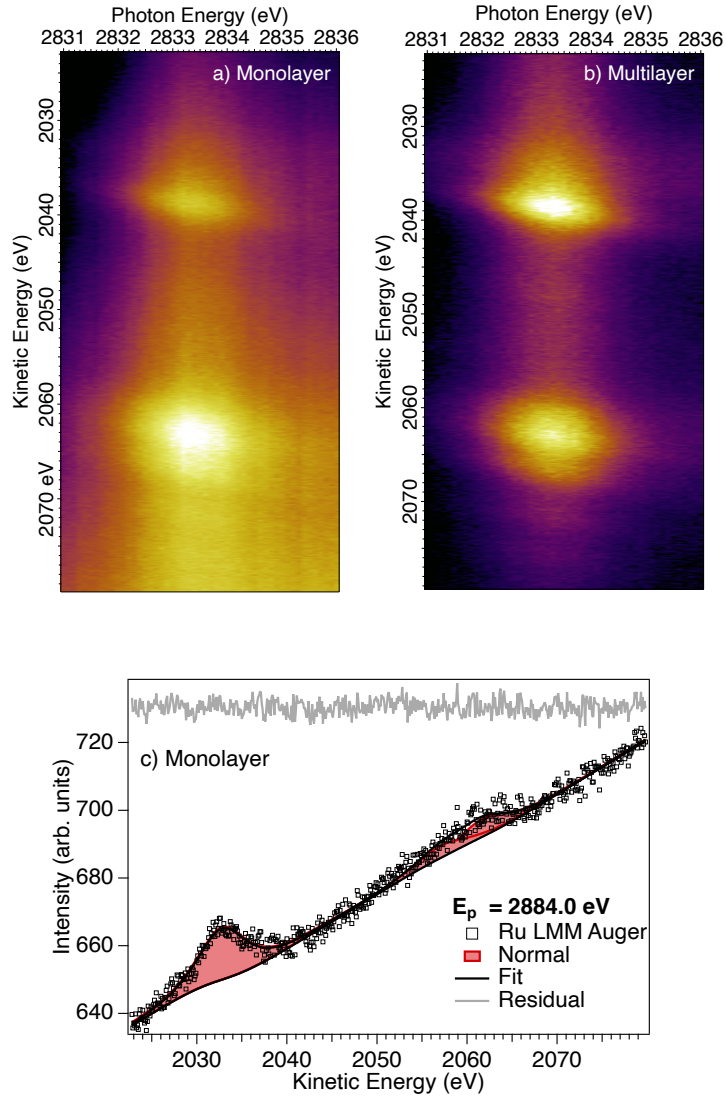


Figure 4.7: Ru LMM Auger measured while varying the photon energy over the first resonance, on the monolayer (a) and multilayer (b). The Auger recorded on the monolayer at 2884 eV, ~ 50 eV above resonance, shows the minimum resonant case (c). All spectra here were recorded at 200 eV in swept mode.

are identified that disperse in kinetic energy; however, further peaks may appear as the resonance is approached. With the different Auger contributions identified, the complication of the post collision interaction (PCI) between the outgoing photoelectron and normal Auger electron must be considered. This occurs close to the S $1s$ ionisation threshold and shifts the normal Auger's kinetic energy higher, distorts its lineshape, and introduces asymmetry [147]. As a result, the PCI-affected Auger will overlap strongly with the dispersing spectators, particularly the peak appearing at 2104.3 eV in figure 4.6d, and must be considered when fitting.

The Ru LMM Auger is shown in figure 4.7 at the first resonance. As before, dispersing spectators overlap strongly with the normal Auger; however, no PCI is observed (figure A9). Like above, it is difficult to see the position of each spectator, but several dispersive trails can be identified around the resonance in figure 4.7b. Highlighting the minimum resonant case by recording at an off-resonant photon energy on the monolayer (figure 4.7c), three normal Auger peaks are identified. These are very broad, largely due to the short lifetime of the Ru $2p_{3/2}$ core hole.

4.3.3 Partial Density of States (pDOS)

Key to facilitating charge transfer is the appropriate alignment of the molecule's unoccupied states with the conduction band of the semiconductor support. Integrating the RAES maps presented in figures 4.6 and 4.7 gives an Auger yield X-ray absorption spectrum, which can be aligned with the system's valence band [83]. Superimposing the band positions of TiO_2 as was done in chapter 3, determined from XPS of an unsensitised electrode (figure 3.12) [132], shows from which states charge transfer is possible in the core-excited regime. By doing so, figure 4.8 is constructed,

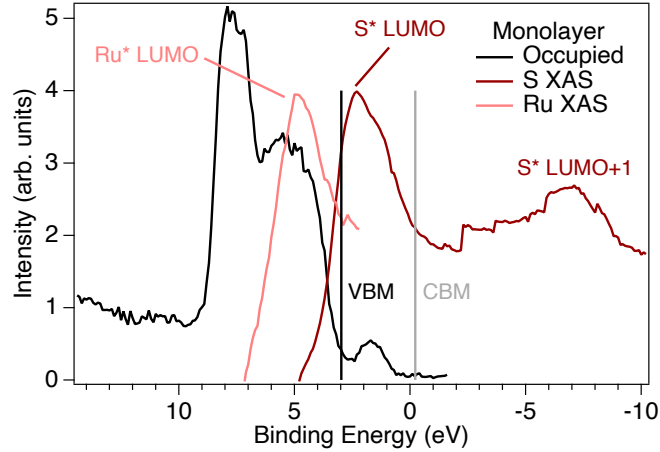


Figure 4.8: S and Ru partial density of states formed by aligning the valence XPS with the auger-yield XAS, showing that charge injection is only possible from the second S resonance.

showing that both the first S and Ru resonances fall comfortably below the TiO_2 conduction band minimum (CBM), forbidding any charge injection to the surface. In contrast, the second S resonance lies far above the CBM and thus can act as a probe for charge injection to TiO_2 . This alignment between the occupied states and TiO_2 CBM is similar to previous experiments on N3 excited at the N 1s edge, with energy of the HOMO appearing at a similar binding energy [71]. However, the excitonic shift of the Ru^* excited states is quite extreme. This may reflect the situation at the sample, however while charge injection is still taken to not occur from the first resonance, there will also be an error associated with the photon energy. This is discussed further in chapter 5.

4.3.4 Charge Relaxation at the First Resonance

The S KLL Auger changes dramatically at 2467 eV, shown in the figure 4.9, indicating excitation to the first accessible unoccupied states of the molecule. The maps in figure 4.6 show significant enhancement in intensity at this photon energy, which is reflected by the identification of several spec-

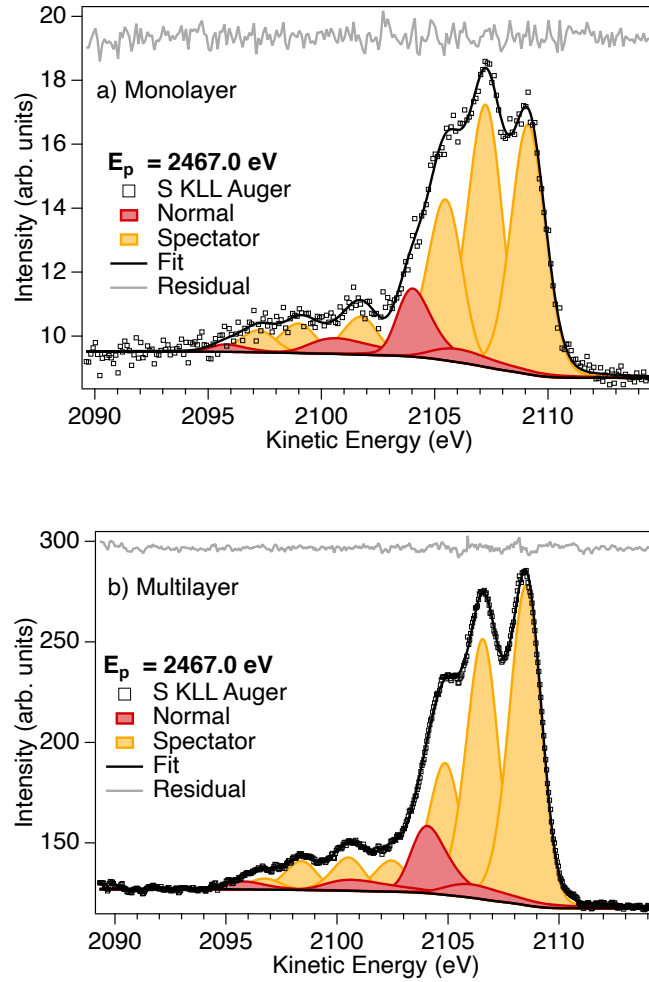


Figure 4.9: S KLL Augers recorded on resonance at 2467 eV on monolayer (a) and multilayer (b) N3. Both spectra were fit using Shirley backgrounds alone. The monolayer spectrum was recorded at 200 eV pass energy in swept mode. The multilayer was recorded at 500 eV pass energy in fixed mode, where the shape of the detector was accounted for by comparing fixed and swept scans of the same region.

tators in figure 4.9. The kinetic energies of the spectator peaks identified at 2467 eV are summarised in table 4.1, with the dominant 1D transition of the normal Auger appearing at 2104 eV for both samples. The spectators are grouped together in table 4.1 by the likelihood that each peak corresponds to the same transition. Some variation in kinetic energy between the peaks is expected; at 2467 eV photon energy, not all spectators are recorded exactly on resonance as shown in figure 4.6 thus dispersion becomes relevant. It should be noted that there are more peaks detected in the multilayer than the monolayer, where it is unclear if the monolayer peak at 2097.2 eV corresponds to either of the peaks at 2096.7 or 2098.4 eV in the multilayer. The addition of an extra peak in the multilayer is unlikely caused by overfitting, but if it were, removing the weaker peak at 2096.7 eV would be the obvious solution. However, this would mean the 1S component of the normal Auger must become more intense, wider, and shift to higher kinetic energy. While the absolute position of all normal Auger components changes with photon energy around the ionisation threshold (as the result of PCI with the outgoing S $1s$ photoelectron) the width and intensity are tied to the main 1D transition itself. This has been determined by fitting the Auger off-resonance and is functionally independent of photon energy over the range studied in figure 4.6. Thus, to keep the normal Auger contributions consistent, an additional peak in the multilayer scan is required. With it established that two peaks give the best fit to the multilayer data, the fact that the monolayer peak in question does not match the kinetic energy of either suggests that it is an analogue of neither. It is unlikely that charge injection into TiO_2 has resulted in a monolayer peak vanishing; from figure 4.8 this is energetically forbidden at the first resonance. As a result, it is concluded that the monolayer peak at 2097.2 eV indicates a transition unique to the bound dye.

Table 4.1: Kinetic energies of the spectator features seen in figure 4.9.

| | $h\nu$ / eV | $E_k^{spect.}$ / eV | | | | | | |
|--------------|-------------|---------------------|--------|--------|--------|--------|--------|--------|
| Mono | 2467 | 2097.2 | 2098.9 | 2101.7 | 2105.4 | 2107.2 | 2109.1 | |
| Multi | 2467 | 2096.7 | 2098.4 | 2100.5 | 2102.4 | 2104.9 | 2106.5 | 2108.5 |

Complicating the analysis of figure 4.6 is the strong overlap between the 1D transition and the spectators at 2105.4 and 2104.9 eV on the monolayer and multilayer respectively. As a result, several equally valid fits could be applied to the spectra, each of varying normal Auger contribution. However, it is expected that the normal Auger is relatively weak given that the photon energy of these spectra is below the S 1s threshold (consider their positions in figure 4.6). In addition, the position of the 1S normal Auger component at the lowest kinetic energy would have to shift higher in order to be stronger, worsening the fit in this portion of both spectra. This overlap between normal and spectator peaks is further compounded by asymmetry, which in the case of the normal Auger is caused by the PCI with the S 1s photoelectron. Spectator peaks in RAES can also exhibit asymmetry due to the photon energy being slightly off-resonance, which is strongest at photon energy detunings equal to the lifetime broadening, if the latter is of comparable width to the photon bandwidth (see section 2.3.2) [85]. This can be visualised as the photons preferentially exciting one side of the excited state distribution as the resonance is approached. In figure 4.6, all save the highest kinetic energy spectator are slightly below their maximum intensity when recorded at 2467 eV and thus asymmetry to lower kinetic energy is anticipated. The detuning of the spectator at 2107.2 (monolayer) and 2106.5 eV (multilayer) is closest to the value of the lifetime broadening of the S 1s core-hole, and thus should exhibit the most asymmetry, however this was found to be minor. Consequently, slight asymmetries to lower kinetic energy on each detuned spectator were found to give the best fit. At this point, it is noted that the dispersion of each

spectator is linear and thus vibrational effects are taken to be absent, which would instead cause non-linear dispersion [86, 87].

At this point, it is worth considering if Stokes doubling is present within the spectra recorded at the S 1s edge. This is the appearance of peaks that do not correspond to RAES, but rather to stray light in the optics of the beamline causing excitations also [87]. This cannot immediately be disregarded because the photon energy resolution is not especially small relative to the S 1s core-hole lifetime broadening (0.25 eV vs. 0.52 eV). However, despite this, some facts suggest that the spectator peaks are real and not artifacts of the beamline. Firstly, whilst the photon energy resolution is of similar order to the lifetime broadening, the latter is still twice its value. Thus, if a Gaussian profile of the photon energy distribution is assumed, the overlap between the two is likely limited, meaning any doubling must occur over a small energy range [148]. Secondly, the undulator was detuned by a factor of 40 to reduce beam damage during these measurements. This has the additional benefit of reducing the scattered contribution to the light emerging from the monochromator, which reduces the strength of Stokes doubles and leaves the resonant peaks largely unaffected [149]. Taken together, these points support the conclusion that Stokes doubling is either not present, or minimal, in the RAES data here.

Calculating the ratio of spectator to normal contributions in figure 4.9 gives charge relaxation times of 6.8 fs on the monolayer and 6.9 fs on the multilayer. The marked similarity between both samples indicates that no charge injection is possible at 2467 eV on the monolayer, as expected from the excited state lying within the TiO₂ bandgap. There are some conclusions that are worth discussion from this analysis. Firstly, given that the S 1s core-level is highly localised to the wing of the thiocyanate ligand, there must still be an appreciable level of coupling with the unoccupied states

of the molecule for spectator peaks to occur at all. Previous computational work on fully deprotonated N3 has found that the highest occupied molecular orbital (HOMO) is largely Ru in character, but with notable density on the thiocyanate ligands, and that the first eight unoccupied levels are bipyridine in nature [150]. Therefore, if the S 1s can couple to these bipyridine LUMOs, it follows that some HOMO density spreading across the thiocyanate ligand is not necessarily disadvantageous. Secondly, charge relaxation of the core-excited state of the molecule is ultra-fast even in the absence of the influence of TiO₂, implying significant intra-ligand coupling. Intramolecular relaxation has previously been reported to proceed via inter-system crossing for N3 [69], thus it is likely that the values calculated above reflect this process in the S 1s core-excited regime. Intersystem crossing can be described thus: upon excitation, the total spin of the system does not change as described by the selection rules (equations 2.11), making the excited state a singlet state (no unpaired spins). However, the electron can relax by moving down through vibrational levels into a triplet state (total spin equal to one).

In the context of charge relaxation, it is helpful to also consider the Ru LMM Auger, shown in figure 4.10. Here, four spectators are identified on the monolayer (2038.6, 2062.2, 2066.1, 2071.5 eV), and five on the multilayer (2038.6, 2048.9, 2061.8, 2065.7, 2071.2 eV). Compared to the S 1s RAES, the normal Auger contributes more to the overall intensity. This is reflected in the calculated charge relaxation times, giving 1 fs on the monolayer and 0.9 fs on the multilayer, again suggesting no charge injection into TiO₂ from the monolayer. The core-hole lifetime at the Ru 2p_{3/2} edge is much less compared to at the S 1s (0.35 fs vs. 1.27 fs), however, this should not be interpreted as the cause of the difference between the calculated relaxation times. The difference in core-hole lifetimes controls the precision

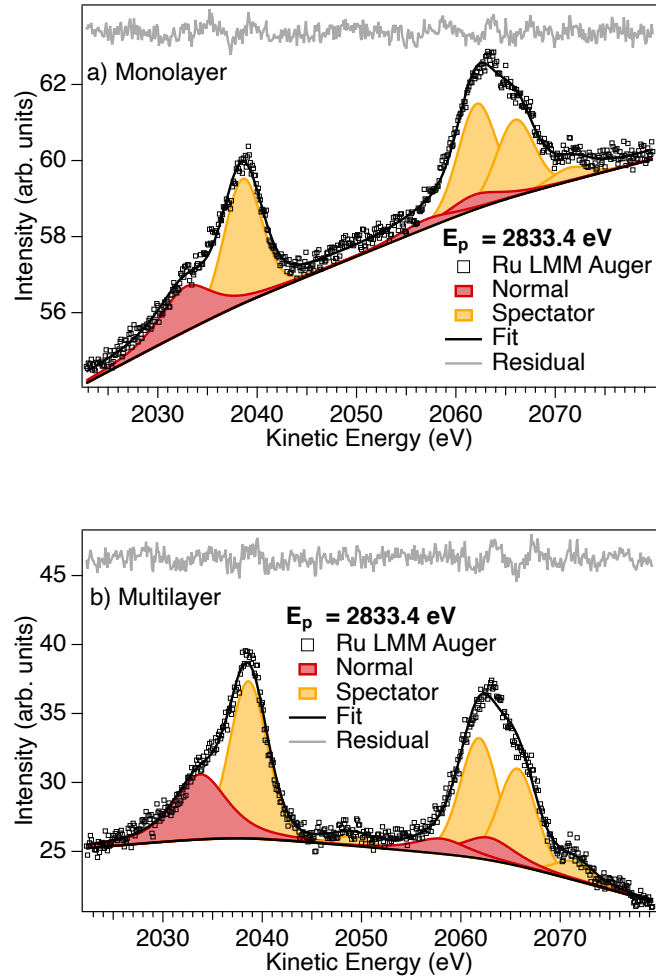


Figure 4.10: Ru LMM Augers measured at 2833.4 eV on the monolayer (a) and multilayer (b). Here, the pass energy was 200 eV in swept mode. A combination of a linear slope and Tougaard-type backgrounds has been employed in both cases.

at which charge transfer processes can be measured, rather than influencing the values themselves. As such, the much faster relaxation at the central Ru atom indicates that the excited Ru $2p_{3/2}$ electron can delocalise easier compared to the excited S $1s$ electron. In terms of intersystem crossing, this suggests that the triplet state is easier to establish from the Ru $2p_{3/2}$ excited state compared to the S $1s$ excited state.

4.3.5 Charge Injection at the Second Resonance

Unlike the first resonance, charge transfer from the second is possible. This causes a much greater normal Auger contribution in both spectra of figure 4.11, where only three spectators are observed for the monolayer (2099.6, 2101.9, 2104.8 eV) and five for the multilayer (2096.2, 2098.8, 2101.5, 2104.4, 2106.2 eV). The fitting here has been conducted in the same manner as at the first resonance, where the fit parameters have been informed by figure 4.6. Two peaks have disappeared from the monolayer spectrum, the analogues of which appear at 2096.2 and 2106.2 eV in the multilayer; showing the influence of TiO_2 . The remaining multilayer spectators are identified in the monolayer spectrum, albeit with slightly different energies. This is likely caused by slightly different detuning values in each spectrum, leading to different degrees of dispersion. Differences in charging are ruled out because the ^1D transition occurs at the same kinetic energy in both cases (2103.6 eV). Asymmetry on the spectator peaks is neglected at this resonance, as the spectators are all largely centred on 2477 and 2476 eV in figure 4.6, and attempts to incorporate asymmetry had little effect on the calculated charge injection time. The most obvious difference between the two spectra is the strong (relative to the normal Auger) spectator at 2099.5 eV in figure 4.11a. Looking further into the changes in intensity between

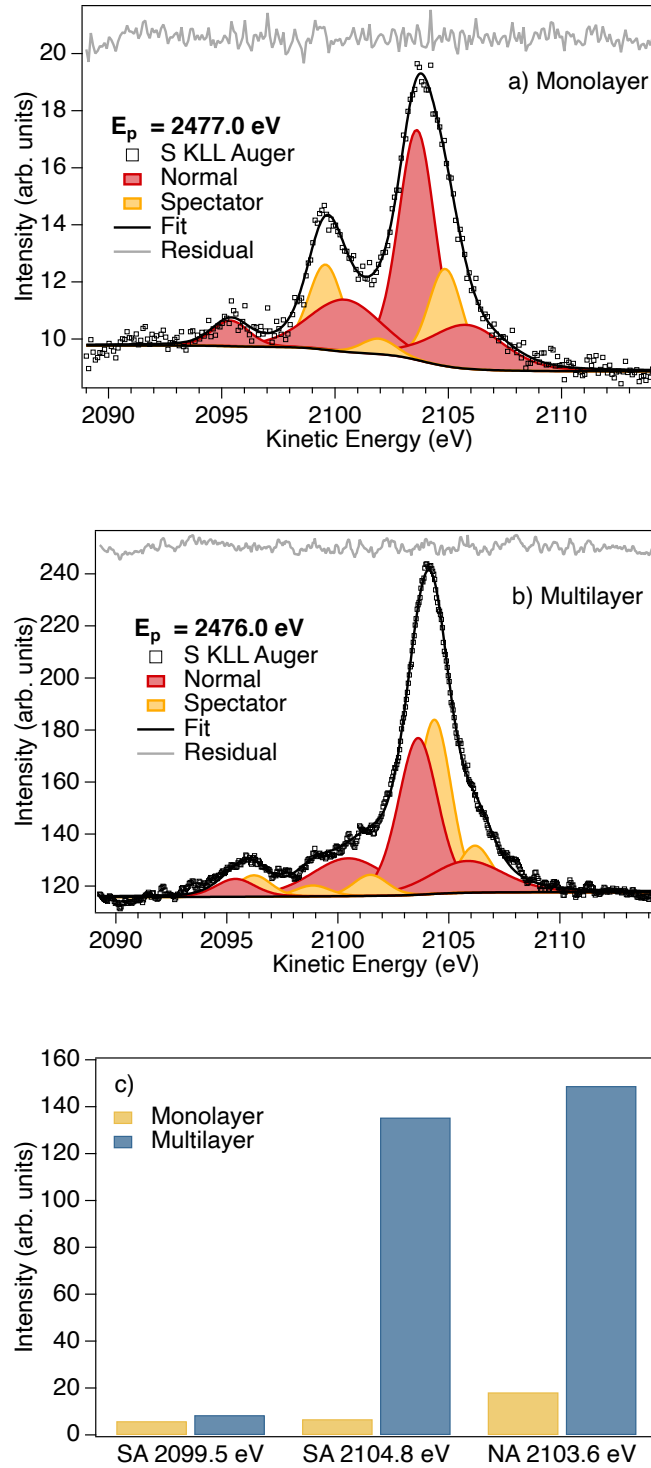


Figure 4.11: S KLL Augers recorded at 2477 eV on the monolayer (a) and 2476 eV on the multilayer (b). The spectra were recorded using a pass energy of 200 eV in swept mode. Also included is the change in intensity between monolayer and multilayer peaks, with SA = ‘Spectator Auger’ and NA = ‘Normal Auger’ (c).

samples in figure 4.11c, the 1D transition of the normal Auger decreases by 88% and the strongest spectator (at 2104.8 eV) by 95%. For the former, the combination of fewer molecules and differences in X-ray flux accounts for the overall decrease in intensity and the decrease beyond this for the latter is attributed to charge injection. In contrast, the spectator at 2099.5 eV is only 30% weaker compared to its multilayer analogue. Counterintuitively, this means that it is actually stronger on the monolayer, offsetting some of the reduction expected from the normal Auger. From this, it is inferred that on TiO_2 this Auger transition occurs faster than its counterparts; making a greater contribution to the total spectator intensity than in the multilayer.

From figure 4.11, the charge transfer times are found to be 0.5 and 1 fs for the monolayer and multilayer respectively. The difference in these values indicates charge injection into TiO_2 from the monolayer, which occurs twice as fast compared to relaxation within the molecule at this photon energy. While injection in 100s of attoseconds is rapid, its similarity to the time calculated on the multilayer means that it is unlikely to eliminate relaxation completely, even at this relatively energetic state. It has been estimated that around 60% of the excited electrons in N3 are injected into TiO_2 from the singlet state, with the remaining injecting via the triplet state after intersystem crossing occurs [69]. From the multilayer, the excited S $1s$ electron has been shown to take 1 fs to delocalise from the S atom, meaning that the only way that the excited electron can delocalise faster is to inject directly into TiO_2 . This would have to be mediated through the bonding interaction that is seen in figure 4.3a, which has been reported previously in the S $2p$ spectrum of N3 monolayers [118]. Otherwise, if injection from the S atom were not feasible, it would be expected that the charge injection time would be longer than the charge relaxation time.

This can be envisioned as the excited electron needing to inject via two steps: delocalisation from the S atom, followed by injection mediated by the anchoring bipyridine ligand. As the injection time is faster than the relaxation time, injection into TiO₂ in one step is more likely.

4.4 Conclusion

In this work, core-level spectroscopies using hard X-rays have been used to investigate the charge transfer dynamics of monolayer and multilayer N3 on TiO₂. XPS was used to confirm bonding to the substrate in the monolayer sample, and the lack of it for the multilayer. Further, a suspected bonding interaction is seen in the S 1s, indicating that bonding involving the thiocyanate ligand is present. It was unexpected that a similar peak was seen in the multilayer, which was rationalised as an interaction between neighbouring molecules.

With the bonding of the samples confirmed, the charge transfer dynamics were probed using resonant Auger electron spectroscopy, and a density of states plot constructed. Due to the crowded nature of the spectra, great care was taken to identify the normal and resonant decay channels by selecting photon energies that promote one over the other. In doing so at both absorption edges, charge relaxation and injection was quantified. At the first S 1s resonance, relaxation occurred in 6.8 and 6.9 fs on the monolayer and multilayer respectively. This result supported the interpretation of the density of states that charge injection is not possible from the first excited state of N3 in the S 1s excited regime. A similar result was found at the first Ru 2p_{3/2}, where relaxation occurred in 0.9 and 1 fs on the monolayer and multilayer respectively. Both results were taken to reflect

intersystem crossing from the excited singlet state into a triplet state of N3.

From the density of states, charge injection from the second resonance of the S 1s excited regime is possible and was able to be quantified; giving 0.5 and 1 fs on the monolayer and multilayer respectively. This shows the influence of the substrate on the charge transfer dynamics of the system, however it is suggested the similarity of the values implies that intersystem crossing likely still occurs. In addition, as the time calculated on the monolayer is faster than on the multilayer, it is interpreted that injection from the singlet state can proceed from the thiocyanate ligand to the substrate. This final result in particular demonstrates the utility of core-level spectroscopies to dye-semiconductor systems.

Chapter 5

Influence of the anchoring group on the charge transfer dynamics in Ru-based Dye-sensitised Solar Cells

Contents

| | | |
|-------|--|------------|
| 5.1 | Introduction | 115 |
| 5.2 | Methods | 117 |
| 5.2.1 | Sample Preparation | 117 |
| 5.2.2 | Spectroscopy | 117 |
| 5.3 | Results & Discussion | 120 |
| 5.3.1 | Hard X-ray Photoelectron Spectroscopy | 120 |
| 5.3.2 | Relaxation within the Molecule | 128 |
| 5.3.3 | Charge Injection into TiO ₂ | 132 |
| 5.3.4 | Charge Relaxation vs. Injection | 136 |
| 5.4 | Conclusion | 138 |

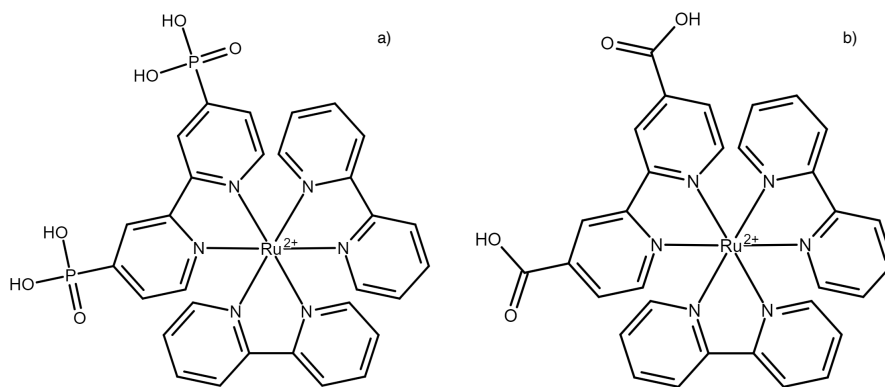


Figure 5.1: RuP (a) and RuC (b) dyes. Both are almost identical, with only the anchoring group differing between the complexes; PO(OH)₂ for RuP and COOH for RuC

5.1 Introduction

During the operation of a DSSC, the time taken for the excited electron to transfer from the dye to the support must be quick, occurring before recombination takes place. This process is heavily dependent on the energetic alignment and electronic coupling between the unoccupied states of the dye and surface. For example, organic ‘donor- π -acceptor’ (D- π -A) dyes are designed to have their virtual, electron deficient, states near the anchoring end of the dye [12, 151], ensuring maximum spatial overlap with the semiconductor’s conduction states. Likewise, DFT calculations on N3 (the prototypical, Ru-based, sensitiser) show that its lowest unoccupied states are bipyridine in character, close to its anchoring ligands [150]. As a result, it is clear that the choice of anchoring group holds sway over the charge transfer dynamics between the dye and semiconductor.

Phosphonic and carboxylic acid groups are widely used as anchoring moieties in DSSCs. The former is known to bind much stronger to TiO₂ [152], however the picture of electron injection is nuanced. Theoretical

studies on charge injection from phosphonate indicate that injection is faster compared to carboxylate anchors for bidentate bonding modes, and slower from monodentate; with experimental values likely representing an average [153, 154]. However, examples exist of slower injection times from phosphonate groups, which can be rationalised by lesser projection of the unoccupied state onto phosphonate compared to carboxylate [155]. Similarly, different anchoring groups on Zn-porphyrins have been evaluated in terms of their molecular conductivity and injection efficiency using time-resolved spectroscopy, with phosphonate again ranking below carboxylate in both respects [156]. This disparity highlights the importance of the availability of complementary experimental studies, and with this in mind the following chapter presents the charge injection times of the dyes RuP (ruthenium(II)bis(2,2'-bipyridine)([2,2'-bipyridine]-4,4'-diylbis(phosphonic acid) dibromide) and Ru455 (cis-bis(2,2-bipyridyl)-(2,2-bipyridyl-4,4-dicarboxylic acid)-ruthenium(II), herein referred to as RuC) Both dyes are shown in figure 5.1.

RuP and RuC have been compared previously [157], but not in terms of quantifiable charge injection times. However, individual attempts have been made to determine the injection timescale; resonant photoelectron spectroscopy (RPES) puts injection from the LUMO+2 of RuC as occurring in under 18 fs [99] and transient absorption experiments suggest that some injection from RuP may occur within 200 fs [158]. The former example illustrates the ability of resonant core-level spectroscopies to probe element-specific transitions within a molecule and quantify charge injection times precisely (usually an order of magnitude above/below the lifetime of the core-hole generated). Here, RPES is utilised to quantify the charge injection times between TiO₂ and the Ru complexes, RuP and RuC, upon excitation from the Ru 2*p*_{3/2} core-level. In doing so, the precision of our re-

sults is enhanced compared to previous RPES studies on similar molecules that used soft X-rays to excite from the N 1s (by virtue of the much shorter lifetime of the Ru $2p_{3/2}$ core-hole) [71, 97, 99]. In addition, resonant Auger electron spectroscopy (RAES) is used to probe relaxation of the excited state where charge injection is absent; revealing the extent of its competition with direct injection.

5.2 Methods

5.2.1 Sample Preparation

Monolayer samples were prepared by soaking mesoporous TiO_2 on FTO glass (Solaronix) in a solution of either RuP or RuC dissolved in ethanol for 12 hours, under a nitrogen atmosphere. The soaked electrodes were then washed and soaked further in ethanol to desorb any physisorbed dye. To form multilayers, dye/ethanol solutions were spin coated onto Si/ SiO_2 substrates at 3000 rpm, leaving the Si substrates visibly stained. The thickness of the multilayers was confirmed by XPS using a lab-based SPECS DeviSim NAP-XPS system, fitted with a Phoibos 150 hemispherical analyser, utilising an Al $K\alpha$ X-ray source (1486.6 eV). All samples were transported to the beamline under nitrogen until transferred into vacuum.

5.2.2 Spectroscopy

The experiment was carried out at the GALAXIES beamline at SOLEIL, Paris, France [159]. The X-ray spot was approximately $80 \times 30 \mu\text{m}^2$ in area, thus to minimise beam damage the sample position was varied often, with the state of the sample monitored using the C 1s XPS (figure A10).

X-ray photoelectron spectroscopy (XPS) was carried out in swept mode, at a photon energy of 3200 eV, using a pass energy of 200 eV or 100 eV. The latter energy was employed to avoid saturation of the detector for some spectra of RuP. For RuC, the pass energy used for the RAES and RPES was 500 and 200 eV respectively. However, 200 eV was used in both spectroscopies for RuP to again avoid saturation. All kinetic energy scales featured herein have been calibrated to the Ti $2p_{3/2}$ (458.8 eV), determined from the O $1s$ of a non-sensitised electrode at 530.05 eV [106]. To calibrate the multilayer XPS, either the N $1s$ (RuC) or Ru $2p$ (RuP) XPS were aligned to their monolayer counterparts. Similarly, the resonant data was aligned to analogous regions recorded in the XPS at 3200 eV.

Peak fitting was conducted using pseudo-Voigt functions that have been modified to incorporate asymmetry as required [138]. When fitting the XPS, the Gaussian-Lorentzian (GL) ratio was kept constant across each feature in a spectrum, but the widths allowed to vary if physically realistic. Conversely, the GL ratio and widths were allowed to vary between the two different types of peak in the RAES. Here it should be noted that the GL ratio loses some of its traditional meaning because the photon energy bandwidth becomes involved in determining the peak shape under resonant conditions, and as a result the resolution of the beamline influences resonant behaviour [85]. On GALAXIES, at the Ru $2p_{3/2}$ edge this is on the order of 0.5 eV using its double-crystal Si(111) monochromator, much less than the lifetime broadening of the Ru $2p_{3/2}$ core hole at 1.87 eV (0.35 fs) [139]. It is thus expected that the resonant Auger peaks will have more Gaussian character compared to the normal Auger peaks, exhibit little-to-no asymmetry, and disperse linearly with photon energy [85, 86, 87].

Shirley backgrounds were employed when fitting the XPS, occasionally combined with a linear slope as required. However, the RAES required

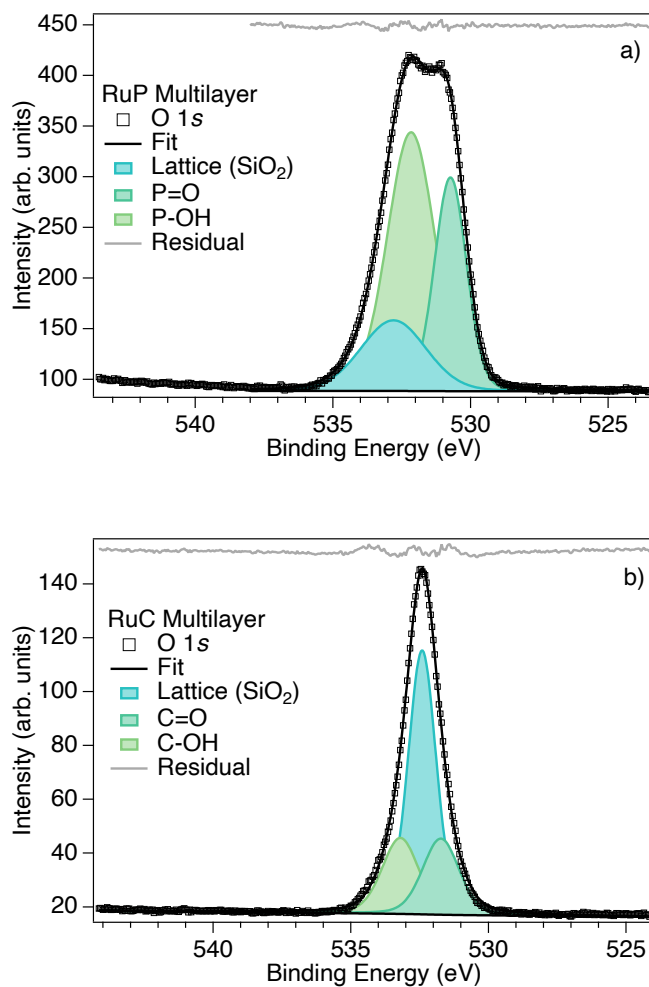


Figure 5.2: O 1s XPS of RuP (a) and RuC (b) multilayers. In both cases the substrate peak remains visible due to the high photon energy (3200 eV). The pass energy is 200 eV for the RuC spectrum and 100 eV for RuP.

a combination of Shirley, Tougaard-type, and linear backgrounds to fit the data adequately [79]. To facilitate core-hole clock calculations using RPES, step backgrounds were subtracted from the integrated spectra. This was applied to the Auger-yield XAS measurements also and for both datasets linear slope backgrounds were incorporated if required.

5.3 Results & Discussion

5.3.1 Hard X-ray Photoelectron Spectroscopy

To confirm bonding between the dyes and surfaces, the O 1s of each sample was recorded. For RuP, peaks are identified at 530.7, 532.2, 532.8 eV on the multilayer (figure 5.2a). The highest binding energy peak is consistent with the native oxide of the Si substrate [140], with the phosphonic acid groups appearing at lower binding energy. The phosphonic features appear at similar binding energy in the monolayer spectrum (figure 5.3a), however the substrate peak is instead at 530 eV, in keeping with lattice oxygen from TiO₂ [106]. The ratio of P=O to P-OH peaks differs between the spectra; 1:1.8 in the multilayer compared to 5.2:1 in the monolayer. The former ratio is close to what is expected from an isolated molecule, which has two P-OH groups for every P=O. There are two good reasons to conclude that any surface-bound dye signal is suppressed in the multilayer. Firstly, Si-O-P bonds are susceptible to nucleophilic attack from water molecules [160], which are almost certainly present, making bonding to SiO₂ difficult. Secondly, the thickness of the dye layer buries the surface-bound molecules' signal under physisorbed dye. However, clearly the situation is not the same for the monolayer. The deviation from the isolated molecule ratio is attributed to deprotonation of the P-OH groups as the dye binds to the surface, similar to XPS studies of dyes containing carboxylic anchor groups [141]. Dyes that bind using phosphonic acid can exhibit several bonding modes simultaneously, not all of which lead to complete deprotonation of the moiety [161]. As such, it is not expected that the P-OH feature disappears completely. Regardless, the size of the skew towards P=O suggests that a sizeable portion of the dye is fully deprotonated.

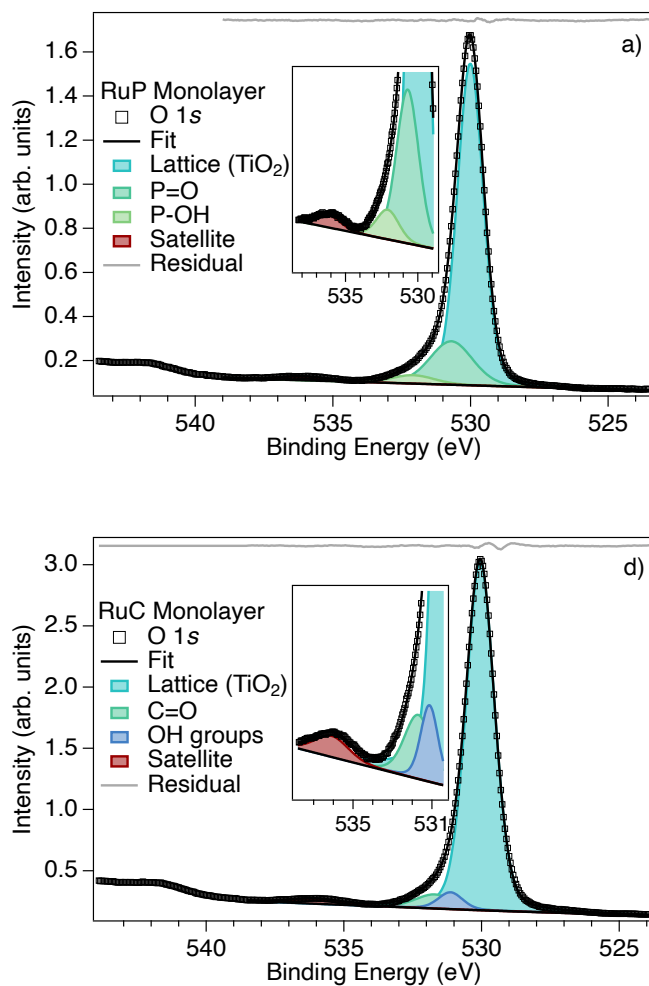


Figure 5.3: O 1s of RuP (a) and RuC (b) monolayers. As the spectra are recorded at 3200 eV photon energy, the high binding energy sides of the spectra are enhanced to emphasise the molecule features (inset). Here, the pass energy is 200 eV for the RuC spectrum and 100 eV for RuP.

The O 1s of both multilayer and monolayer RuC are shown in figures 5.2b and 5.3b. For the multilayer, peaks are found at 531.7, 532.4, and 533.2 eV, which are taken to correspond to C=O, lattice oxygen from SiO₂ [140], and C-OH respectively. The COOH assignment is similar to other dyes with this moiety [71, 103, 108]. Only C=O is observed in the monolayer spectrum from the molecule (again at 531.7 eV), with the additional feature at 531.1 eV attributed to surface adsorbed hydroxyls [65]. As above, the peak at 530 eV is assigned to lattice oxygen from TiO₂ [106]. These spectra were measured using a photon energy of 3200 eV and as a result both monolayers are dominated by lattice oxygen, with satellite structure comparable to the molecule features. This is not a particular problem for RuP in figure 5.3a, as the more electropositive P atom leads to more electron density lying on the oxygen, shifting its features to lower binding energy. However, in this case this leads to stronger overlap between the P=O feature and any potential hydroxyl peak, thus the presence of surface hydroxyls in the RuP monolayer cannot be ruled out. Conversely, the overlap with the satellites is stronger for RuC, which obscures any potential C-OH peak. However, in this case the absence of an obvious peak suggests that the molecule is largely deprotonated. Comparison to figure 5.2a suggests that the RuC multilayer is thinner than the RuP but, given the photon energy, is still thick enough to approximate isolated molecules. This is confirmed by the ratio of C=O to C-OH features for the multilayer, which is found to be 1:1, as expected from the structure of the molecule.

Figures 5.4 and 5.5 show the C 1s and Ru 3d of the dyes. For multilayer RuC (figure 5.4b), C 1s features are seen at 285.1, 286.3, and 289.1 eV, with the monolayer (figure 5.5b) only differing significantly in the highest binding energy peak, which is found at 288.8 eV. These features are assigned to C-C/C=C, C-N, and COOH respectively. The width of the

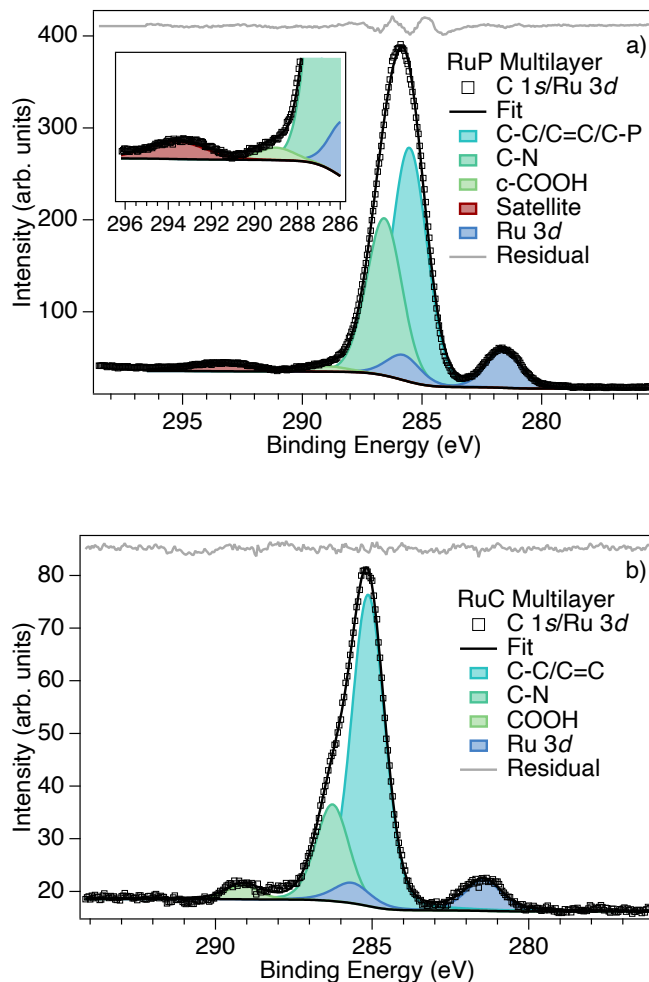


Figure 5.4: C 1s XPS of RuP (a) and RuC (b) multilayers. The RuP samples have some minor contamination (labelled c-COOH), as highlighted by the inset plot. Measured using a photon energy of 3200 eV, however the RuP spectrum is recorded at 100 eV pass energy, and the RuC at 200 eV.

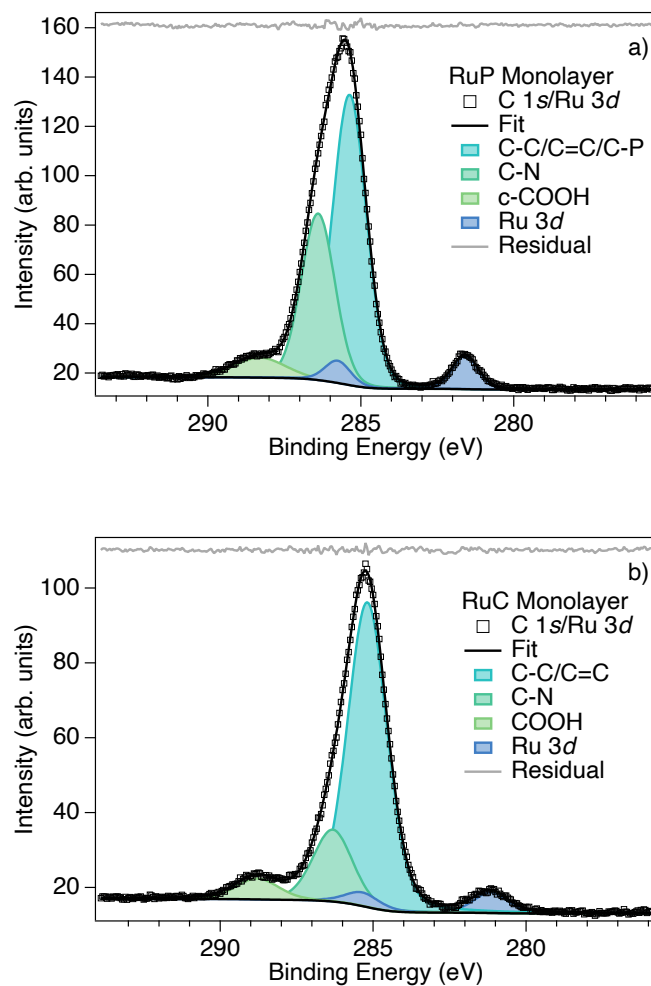


Figure 5.5: C 1s XPS of RuP (a) and RuC (b) monolayers. The RuP samples have some minor contamination (labelled c-COOH). Both spectra are measured using a photon energy of 3200 eV, however the RuP spectrum is recorded at 100 eV pass energy, and the RuC at 200 eV.

latter is greater compared to its counterpart in the monolayer, which is likely caused by a small amount of protonated molecule being measured in the multilayer. The Ru $3d$ also manifests in these region, with the Ru $3d_{5/2}$ appearing at 281.5 for the multilayer and 281.2 eV for the monolayer. The RuP C $1s$ /Ru $3d$ is similar to RuC; multilayer peaks are found at 281.6, 285.5, 286.6, and 289 eV. These do not change significantly for the monolayer, save that the highest binding energy peak is more prominent and is found at 288.3 eV. Given that RuP lacks a COOH group, the detection of a peak around this energy means the surface of the TiO_2 must be slightly contaminated. This is not especially surprising given the soaking method used and that its transfer into GALAXIES was not air-free, and likely reflects the situation of commercially manufactured cells.

Figures 5.6 and 5.7 show the N $1s$ of each sample. The major components are found at 399.9 eV (figure 5.6a) and 400.4 eV (figures 5.6b, 5.7a, 5.7b) and are attributed to the pyridine nitrogen from the molecule [99]. The peaks at 398.9, and 398.7 eV in figures 5.7a, and 5.7b for the monolayers are assigned to beam damage. In both cases, the damage is minor, reaching its greatest extent for the RuC monolayer, where it accounts for $\sim 15\%$ of the total spectral intensity. An extra peak is also seen in the RuP multilayer (5.6a) at 401.1 eV, on the other side of the main peak. This attributed to some monolayer intensity being visible through the thicker layer, and given that it is weak, is not expected to influence the results in this chapter.

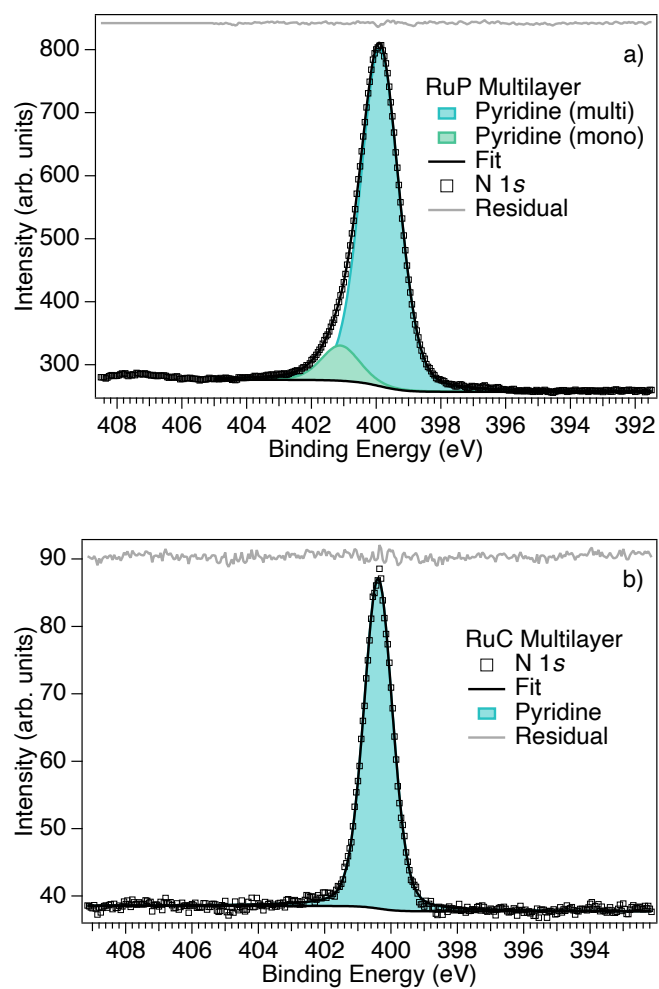


Figure 5.6: N 1s XPS of RuP (a) and RuC (b) multilayers. The RuP multilayer shows a minor monolayer component. Recorded using a photon energy of 3200 eV and a pass energy of 200 eV.

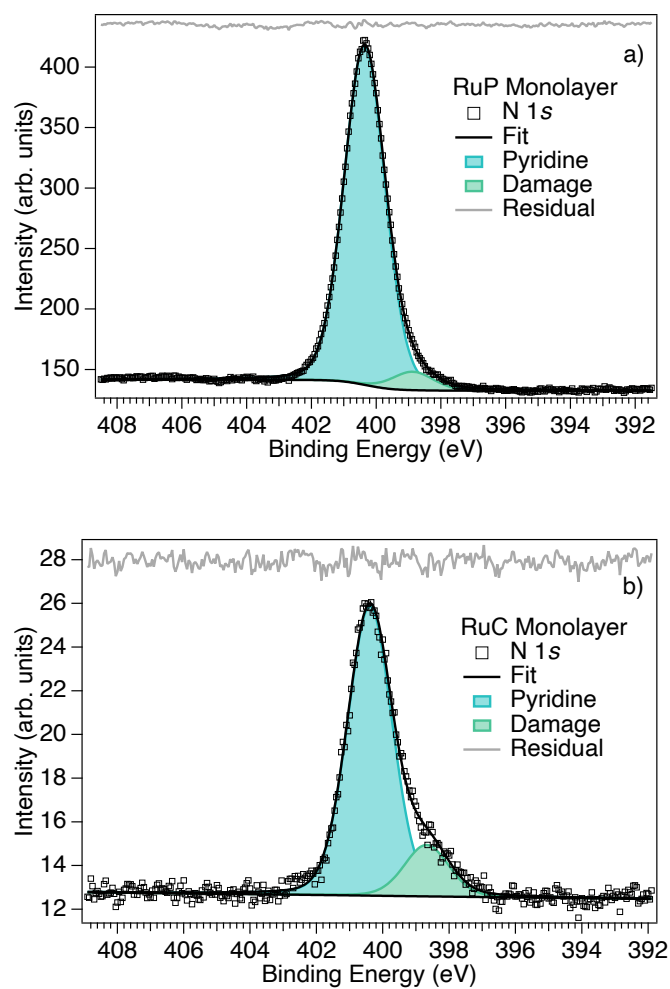


Figure 5.7: N 1s XPS of RuP (a) and RuC (b) monolayers. Both spectra show minor beam damaged components. Recorded using a photon energy of 3200 eV and a pass energy of 200 eV.

Table 5.1: Kinetic energies of the spectator ($E_k^{spec.}$) and normal ($E_k^{norm.}$) Auger features seen in the RAES of both RuP and RuC at different photon energies ($h\nu$).

| | $h\nu$ / eV | | $E_k^{spec.}$ / eV | | | | $E_k^{norm.}$ / eV | |
|------------|-------------|--------|--------------------|--------|--------|--------|--------------------|--------|
| RuP | 2841.8 | 2081 | 2075 | 2071.2 | 2057.3 | 2047.3 | 2069.5 | 2044.6 |
| | 2851.7 | 2080.8 | - | - | 2058 | - | 2069.5 | 2044.6 |
| RuC | 2841.8 | 2082.3 | 2076.1 | 2072 | 2057.7 | 2048.4 | 2070.8 | 2043.4 |
| | 2852.5 | - | - | 2072.4 | - | 2048.2 | 2070.8 | 2043.4 |

5.3.2 Relaxation within the Molecule

It has been established by XPS that the multilayers of both dyes are protonated; with physisorbed molecules approximating dye isolated from the substrate, where the likelihood of charge transfer vanishingly is small. The validity of this assumption has been demonstrated previously [162]. As a result, it is tempting to say that no normal Auger contributions should appear, only the narrower resonant peaks characteristic of RAES. This, however, is not the case; both figures 5.8 and 5.9 still show normal Auger structure.

The kinetic energies of each peak are summarised in table 5.1. For both dyes, the Auger is found at the same kinetic energy regardless of photon energy, which taken with the maps in figures 5.8 and 5.9 rules out any post collision interactions [147]. The positions, widths, and GL ratios of the normal Augers were informed by figures 5.8d and 5.9d of the Auger recorded far from resonance. The overall form of the Auger structure for both dyes is similar between spectra, particularly at 2841.8 eV (figures 5.8b, 5.9b); however, the kinetic energies of the spectators from RuC are greater overall. Charging alone cannot account for these differences, given that the O 1s of RuC shows that lattice oxygen from SiO₂ is only 0.4 eV lower in binding energy than that for RuP. Instead, the differences likely reflect

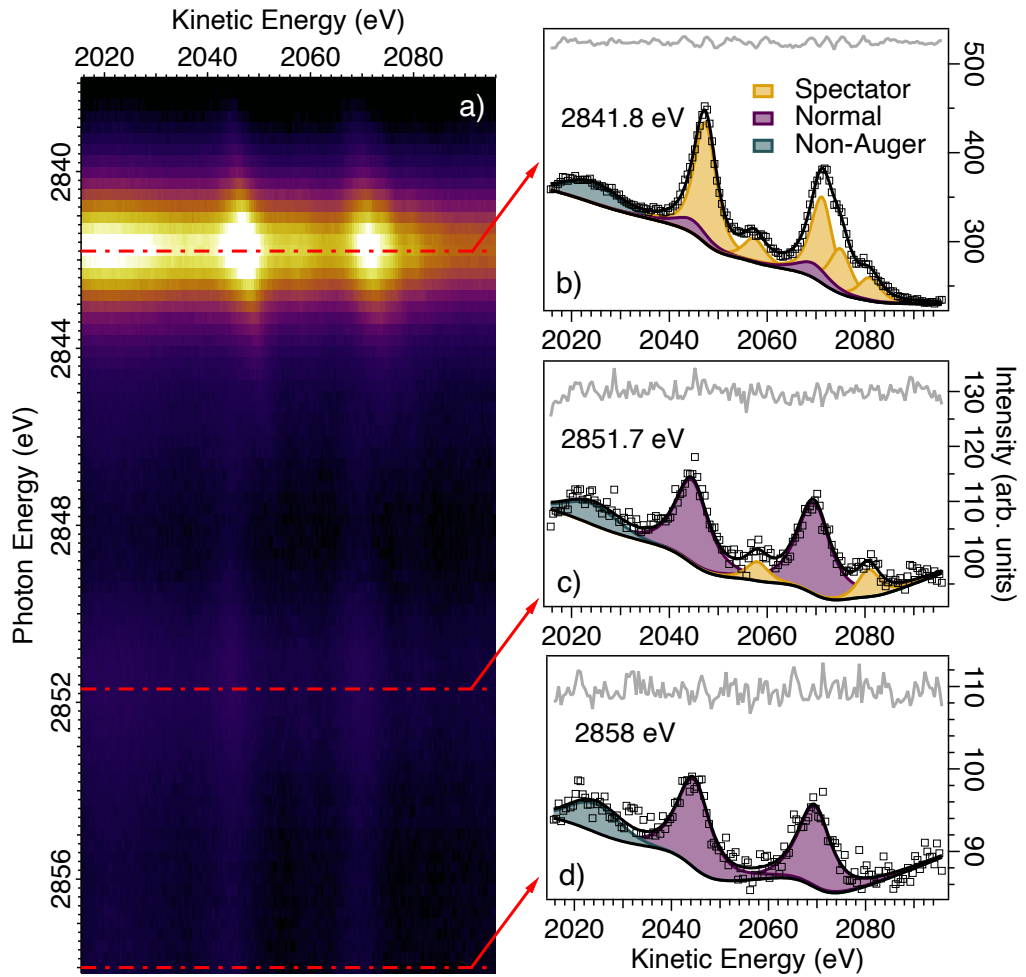


Figure 5.8: RAES of multilayer RuP at the Ru $2p_{3/2}$ edge (a), with spectra at key energies shown: at the first resonance (b), second resonance (c), and far from resonance (d). A low kinetic energy feature is found throughout the map that is not assigned to the Auger structure. The background in each case is complex, and a combination of Shirley, linear, and pseudo-Tougaard was required to generate a meaningful fit. Recorded at 200 eV to avoid saturating the detector.

the ability of the excited electron to shield the outgoing Auger electron. However, it is possible that dispersion of the peaks around the resonances contributes to the shifts. This arises due to the interplay between the broadening of the excited state with the photon bandwidth and lifetime broadening of the core-excited and final states [85]. As such, if the spectra are not recorded exactly on resonance, some variation in the spectators' kinetic energy is expected. Variations in where the spectra are recorded relative to the resonances are likely present, but not significant enough to account for the kinetic energy differences alone. With the above in mind, Table 1 groups the spectators into categories based on the likelihood that the peaks represent the same resonant Auger transition, rather than absolute assignment. It is entirely possible that the peaks found at 2081 eV (RuP) and 2082.3 eV (RuP) arise from different transitions, for example. The above discussion is applicable to the second resonances also, which are less distinct.

The presence of any normal Auger component in the multilayer RAES suggests that the excited state can relax via some route. As discussed for the O 1s, the dye molecules are effectively isolated, meaning the relaxation occurs in the absence of any substrate effects. Through the core-hole clock implementation of RAES, it is possible to calculate how long this relaxation takes upon excitation to the first and second unoccupied states of both dyes. Doing so, relaxation of the first excited state is calculated to take 2.7 fs on RuP (figure 5.8b) and 0.8 fs on RuC (figure 5.9b). At the second resonance, this becomes 1.2 fs for RuP (figure 5.8c) and 0.1 fs for RuC (figure 5.9c). Immediately the times calculated for RuC stand out as much faster than RuP, which arises from the much stronger normal Auger contribution relative to the spectators. This is particularly apparent when comparing the first resonances in figures 5.8b and 5.9b. It should be noted

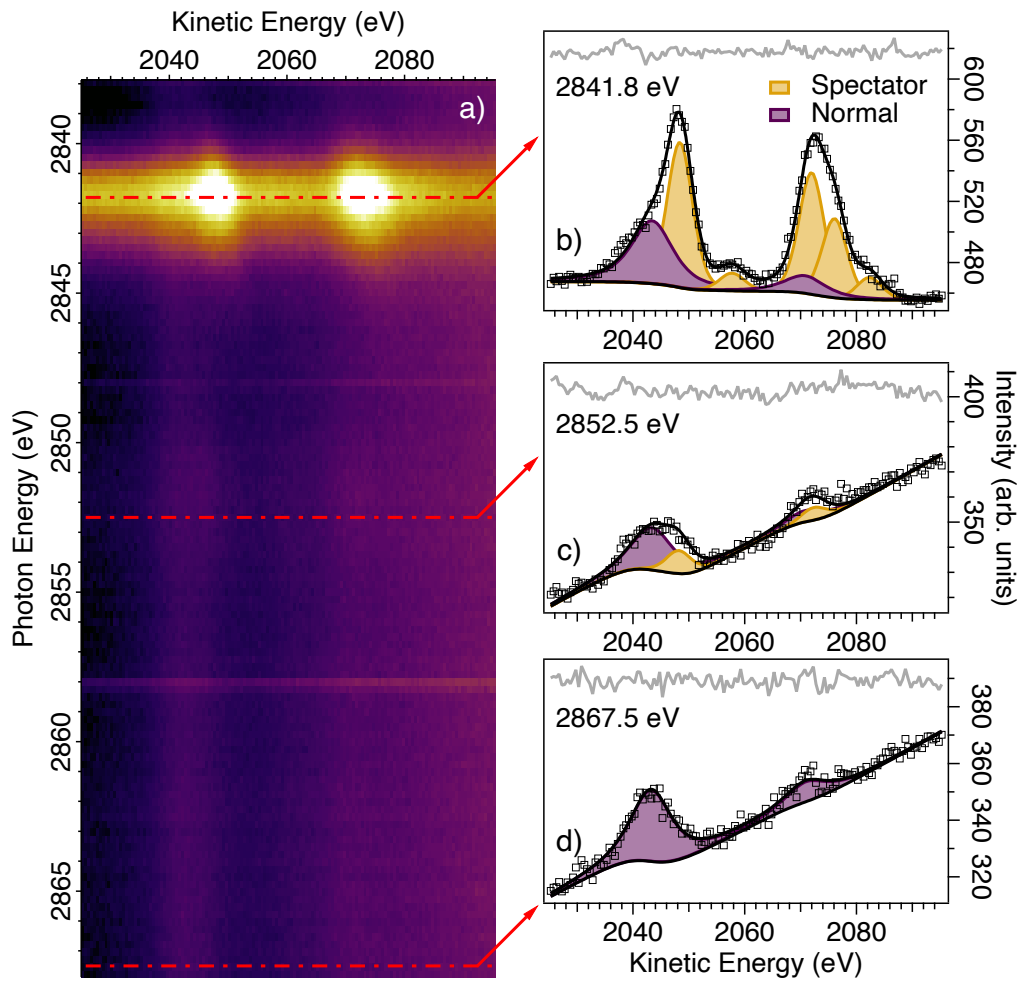


Figure 5.9: RAES of multilayer RuC at the Ru $2p_{3/2}$ edge (a), with important photon energies highlighted as above: first resonance (b), second resonance (c), and far from resonance (d). Recorded at 500 eV pass energy and fit using a combination of a linear slope and Shirley background.

that a feature appears in the RuP RAES (figure 5.8), which is far below the Auger structure. It is not clear what this is, and while it could be related to the normal Auger structure given it is present at high photon energies, it does not follow the associated fit parameters. To fully determine the nature of this peak, the kinetic energy window should be widened and the noise reduced. For purposes of the times calculated herein, it is taken to not be part of the Auger structure given that it does not meaningfully change with either the normal Auger or the spectators.

DFT calculations have shown that the LUMO lies largely on the anchoring ligand of RuC with some density around the Ru atom [99, 163]. These calculations do not fully represent the conditions of this experiment however, due to the presence of the Ru core-hole. With this being said, it is not expected that the situation changes so dramatically to alter this picture in our analysis; the unoccupied states must have some overlap with the Ru $2p_{3/2}$ for enhancements to appear in figures 5.8 and 5.9, and the RPES presented below shows that these states are coupled to the substrate. This latter point suggests that the core-excited states lie (at least in part) on the anchoring ligand. This informs us that, in order to be consistent with figures 5.8 and 5.9, the orbital that the excited electron relaxes into must have no appreciable Ru character.

5.3.3 Charge Injection into TiO₂

Figures 5.10 and 5.11 show the RPES measurements of multilayer RuP and RuC respectively. Enhancements due to participator decay are present in both (figures 5.10a and 5.11a), but more obvious on RuP, where they are seen beyond the highest occupied molecular orbital (HOMO). RPES maps of the monolayers are shown in the appendices, but the signal is

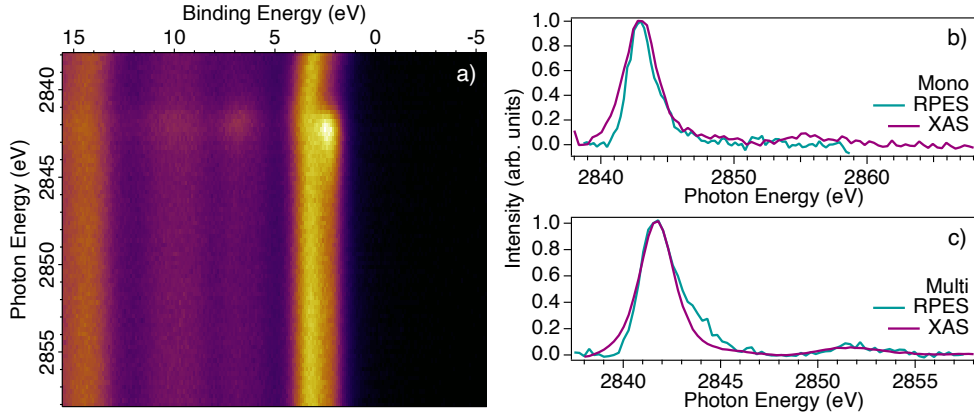


Figure 5.10: RPES of multilayer RuP at the Ru $2p_{3/2}$ edge. Participant decay is seen clearest in the map (a). Integrated RPES and RAES from the monolayer (b) and multilayer (c) give the XAS spectra used for core-hole clock analysis. Recorded at 200 eV pass energy in swept mode.

much weaker (figure A11). Figures 5.10b and 5.11b show the integrated RPES and RAES spectra for both monolayers. The latter is labelled ‘XAS’ in these plots as the integrated RAES is at essence an absorption spectrum measured with Auger electrons (maps shown in figure A12); so-called ‘Auger yield.’ In addition, the RPES has been aligned to the XAS to adjust for inconsistencies in the photon energy scale. Two resonances are present for both dye multilayers, one at 2841.8 eV and one much weaker around 2852 eV. This, however, is not exactly the same for the monolayer spectra. Instead, in both cases the RPES shows only the strongest peak. This discrepancy is attributed to charge injection into the conduction band of TiO₂.

To quantify charge injection from the excited state seen at approximately 2852 eV in figures 5.10 and 5.11, the core-hole clock implementation of RPES is used. Comparing the intensity of the state between monolayer and multilayer, RPES and XAS, and using equation 2.9 gives the charge injection time on RuP to be less than 0.07 fs. By the same method, the charge injection time from RuC is less than 0.35 fs. Both values are interpreted as upper bounds because no peaks are detected in the monolayer

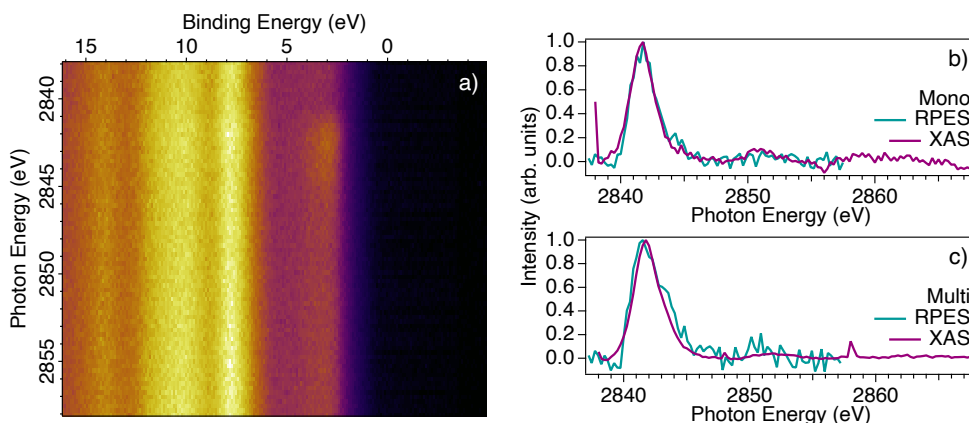


Figure 5.11: RPES of multilayer RuC at the Ru $2p_{3/2}$ edge. Participant decay is again shown by the map (a), alongside XAS plots from the monolayer (b) and multilayer (c) used for core-hole clock analysis. Enhancement is less clear overall compared to figure 5.10, where a faint mark is just visible around 2842 eV. Recorded at 200 eV pass energy in swept mode.

RPES spectra of either dye, meaning that any resonant intensity is below the level of noise. Consequently, charge injection from RuP only appears faster because the magnitude of the noise is greater in the RuC RPES.

Clearly, the ability of a dye to pass electrons to the mesoporous support quickly is vital for the efficient function of a DSSC. However, it is important to clarify what quantifying the charge injection time does, and does not, say about a dye. Both charge injection values could feasibly be even faster if the noise were reduced, however from the point of view of cell design, this means little. The injection times found above are ultra-fast compared to other mechanisms in a cell [164] and thus the marginal difference between them is unlikely to lead to vastly different cell efficiencies. Therefore, because RuP and RuC both exhibit ultra-fast charge injection, it should not be the determining factor in deciding whether $\text{PO}(\text{OH})_2$ anchoring groups are used over COOH . What quantifiable charge injection times instead offer is a check on whether the coupling between the dye and substrate is sufficient for ultra-fast charge injection. In this regard, both dyes pass this test comfortably. The concept of injection being ‘fast enough’ has been termed

kinetic redundancy and has discussed for N719 previously [165, 166].

In each case, the RPES and XAS spectra have been normalised to the lowest unoccupied molecular orbital (LUMO). This is valid if the LUMO lies within the TiO_2 bandgap, which forbids charge transfer and thus its effect on intensity [167]. The unoccupied halves of both dyes' density of states (DOS) are presented in figure 5.12, which shows that both LUMOs lie above the conduction band minimum (CBM). This presents a problem when applying the core-hole clock method, as the LUMO is potentially affected by charge injection and thus an inappropriate choice for normalisation. However, to rule out the LUMO as a normalisation aid fully, figure 5.12 should be scrutinised. Firstly, in DOS plots constructed in a similar fashion for other Ru dyes, the LUMO tends to lie below the CBM upon core-excitation [71, 99, 168]. Of particular relevance is that a DOS has been constructed for RuC previously using XAS at the N $1s$ edge, placing the LUMO approximately 1 eV below the CBM [99]. In principal, the binding energy of the core exciton formed between the Ru $2p_{3/2}$ core-hole and LUMO could be less than that formed with an N $1s$ core-hole. This is because the Ru $2p_{3/2}$ has a far greater binding energy than the N $1s$, thus more bound electron density is available to shield the excited electron. Practically, this would cause the Ru-excited LUMO to appear at more negative binding energy in the DOS. However, there are few bound states between Ru $2p_{3/2}$ and N $1s$ for these samples, hence the magnitude of the shielding is likely not sufficient to push the LUMOs above the CBM.

It is most likely that the photon energy scale itself leads to misinterpretation of figure 5.12. Consider studies conducted at the N $1s$ and Ru $2p_{3/2}$ edges using photons at 400 eV and 2840 eV respectively. To have confidence of ± 1 eV in the peaks of the DOS formed using an XAS spectrum at the N $1s$ edge, the relative error in photon energy would need to be around

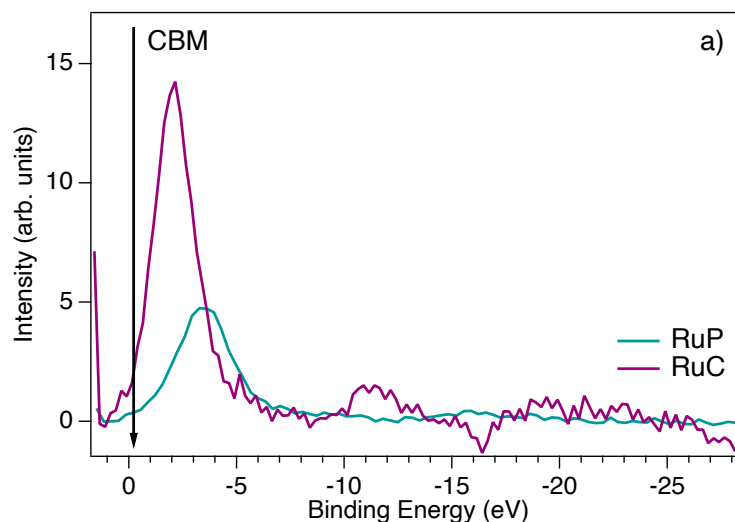


Figure 5.12: Unoccupied portion of the density of states of both RuP and RuC dyes, where the conduction band maximum (CBM) is marked by an arrow. In both cases, the LUMO lies above the CBM of TiO_2 .

0.25%. To achieve the same confidence when using the Ru $2p_{3/2}$ edge, this becomes 0.03%. Any error is more pronounced during HAXPES due to the level of precision required to construct DOS plots in this way. Thus, the binding energy scale above likely has a significant error. Fortunately, this has no bearing on the RAES data, only the RPES. As a result, it is assumed that the LUMOs lie below the conduction band, in-line with the literature referred to above and the DOS in chapter 4.8.

5.3.4 Charge Relaxation vs. Injection

As discussed in the previous section, the charge injection time alone is not a suitable parameter to judge whether RuP or RuC is the superior dye; functionally they are as good as each other in this regard. However, some conclusions can be drawn by comparing to the relaxation times determined by RAES. As calculated above, at the second resonance, relaxation occurs in 1.2 fs for RuP and 0.1 fs for RuC. The upper bound of the injection time for RuC (<0.35 fs) is inflated by the level of noise, causing it to encompass

the relaxation time. Thus, it should not necessarily be interpreted that relaxation outpaces injection; the latter is still most likely faster. Regardless, it is clear that relaxation is able to compete far more effectively compared to RuP (injection in <0.07 fs).

As mentioned in chapter 4, intramolecular relaxation has been described previously for the similar dye, N3 [69]. In this work, it was determined that roughly 60% of electrons injected into TiO_2 came straight from a metal-to-ligand charge transfer (MLCT) singlet state, with the remaining undergoing intersystem crossing [69]. These electrons instead inject from a MLCT triplet state after relaxing, slower than from the singlet state. The authors concluded that the appeal of N3 as a sensitiser is, at least in part, because the majority of the excited electrons undergo direct transfer to TiO_2 . For the qualitatively similar dye N719 (see figure 1.2), injection has been determined to progress via intersystem crossing instead, which despite being slow has a high quantum efficiency due to the long lifetime of the triplet state formed [166]. In this latter example, the authors suggest that to promote faster injection from the singlet state would likely harm the overall efficiency. Based on these studies and chapter 4.8, the relaxation of both RuP and RuC is taken to proceed via intersystem crossing. This is consistent with the requirement from RAES that the state into which each system relaxes has minimal Ru character, as it has been reported that the excited electron in Ru polypyridyl dyes is randomly localised between the ligands as the triplet MLCT state thermalises [169].

For the dyes studied herein, the competition between the injection and relaxation times implies different injection pathways. For RuP, relaxation is far slower than injection; hence, injection is taken to proceed through direct charge transfer from the singlet state formed upon excitation. However, this is not the case for RuC. Instead, relaxation can compete with injection, and

thus more electrons undergo intersystem crossing to a triplet state and then inject. Moreover, this means that the injection time found from RPES likely contains contributions from intersystem crossing as well from the singlet state. These results suggest that for Ru polypyridyl dyes, the anchoring group $\text{PO}(\text{OH})_2$ facilitates direct injection into the TiO_2 conduction band, whereas COOH does not. As a result, from the perspective of electron injection, $\text{PO}(\text{OH})_2$ is preferred.

5.4 Conclusion

By utilising resonant Auger and resonant photoelectron spectroscopies, a detailed description of the charge transfer dynamics has been presented. To do so, as in the previous chapter, XPS was used to confirm the nature of the bonding of each dye to the surface. With this established, the same process as before was undertaken, where the Auger spectrum was recorded at different photon energies to accentuate either the normal or resonant features. Overall, this was easier at the Ru $2p_{3/2}$ edge than at the S $1s$ as there are less features in total, which are spread out further. As a result, the charge relaxation times for each dye, both monolayer and multilayer, were calculated at the first and second resonance. These were 2.7 and 0.8 fs for RuP and RuC respectively, at the first resonance, and 1.2 and 0.1 fs at the second. For injection, this was less than 0.07 fs for RuP and less than 0.35 fs for RuC. The unexpected alignment shown in the density of states plot was discussed in terms the precision required to construct it and what is expected from similar measurements of other ruthenium complexes.

Comparison between the injection and relaxation times was discussed, and thus by proxy the efficacy of the different anchoring groups. As in the

previous chapter, intersystem crossing (see section 4.3.4) was proposed as the origin of relaxation. Injection from both dyes is ultra-fast, hence the efficiency of RuP and RuC based DSSCs is dominated by other processes. However, it was decided that RuP, and by extension the PO(OH)₂ anchoring group, facilitates superior charge injection. This work demonstrates that charge injection times themselves are not the best metric for the determining whether one dye is superior over another.

Chapter 6

Oxidative behaviour of TiSi_2 at ambient pressures for solar water splitting

Contents

| | | |
|-------|--|------------|
| 6.1 | Introduction | 142 |
| 6.2 | Methods | 143 |
| 6.2.1 | Sample Preparation | 143 |
| 6.2.2 | AP-XPS | 144 |
| 6.2.3 | Data Processing | 144 |
| 6.3 | Results & Discussion | 145 |
| 6.3.1 | Powdered TiSi ₂ XPS | 145 |
| 6.3.2 | Powdered TiSi ₂ APXPS | 147 |
| 6.3.3 | Thin Film TiSi ₂ XPS | 155 |
| 6.3.4 | Thin Film TiSi ₂ APXPS | 159 |
| 6.3.5 | Strategies to Prevent Oxidation | 163 |
| 6.3.6 | Solar Water Splitting with TiSi ₂ | 171 |
| 6.4 | Conclusion | 172 |

6.1 Introduction

While DSSCs offer a route towards decarbonising electrical power generation in niche applications, photoelectrochemical (solar) water splitting has the potential to decarbonise broad sections of the global economy. The chemistry involved in both technologies is similar (chapter 1), save that hydrogen is produced in the latter rather than electricity. Unfortunately, solar water splitting devices are less mature than DSSCs, with efficiencies generally low. Many strategies have been employed to overcome this barrier [52, 60, 170], however it is not straightforward to solve, as the overall efficiency depends on the semiconductor band gap, charge transfer ability, prevalence of recombination centres, and surface morphology [48, 49]. As with DSSCs, these factors are rarely able to be improved in isolation.

TiSi₂ is a proposed catalyst that exhibits behaviour atypical of more established materials that are able to facilitate solar water splitting. Firstly, it itself is not a semiconductor; historically, it has been utilised as an interconnect or contact in circuitry [171, 172]. Clearly, for a process that fundamentally relies on the absorption of incident sunlight, this is an issue. Despite this, TiSi₂ has been shown to split water under the correct conditions [173]. In this work, TiSi₂ was able to split water provided that it was exposed to both light and water simultaneously, in the presence of a small amount of residual oxygen. The authors concluded that TiSi₂ evolves hydrogen via sacrificial oxide formation (during which unspecified catalytic centres for water splitting are formed) and water splitting [173]. At present, this is the only example of TiSi₂ being utilised directly as a water splitting catalyst; otherwise it has been used as a conducting support or interlayer [174, 175, 176]

Solar water splitting with TiSi₂ is complex and, as such, in-situ measure-

ments are well placed to elucidate the reaction between its surface and water. Information such as this is important for the future design of water splitting catalysts, particularly for improving the efficiency of those based on TiSi_2 . In this regard, ambient pressure XPS (AP-XPS) is in a unique position to provide detailed information at the vapour-solid interface in a realistic reaction environment. As such, this chapter aims to determine the nature of the catalytic sites that enable TiSi_2 to split water under solar illumination. As a result, the conditions that lead to the formation of these sites will be highlighted.

6.2 Methods

6.2.1 Sample Preparation

Commercial TiSi_2 powder (Alfa Aesar, 99.5%, 74 μm particle size) was mounted to a sample plate using a carbon sticky pad and transferred to vacuum directly from atmosphere. Due to its exposure to air, all powder is oxidised initially, but unoxidised TiSi_2 remained visible. However, when repeating experiments, it was seen that samples left at atmosphere for longer had different peak shapes compared to younger samples. No further processing of the powder was conducted before XPS.

TiSi_2 thin films were deposited onto $\text{MgO}(001)$ crystals using magnetron sputtering to a thickness of ~ 100 nm. The samples were then transferred into vacuum for XPS from atmosphere. As was the case for the powder samples, oxidation of the TiSi_2 occurred before the samples were taken into vacuum. To attempt to combat this, further samples were passivated with thin Ti or Au over-layers (~ 5 nm). Depth profiling of the thin film samples

was carried out by Ar ion sputtering at various energies (typically between 0.5 - 2 keV, at approximately 9×10^{-6} mbar).

6.2.2 AP-XPS

AP-XPS was carried out in a SPECS DeviSim AP-XPS system featuring a Phoibos 150-NAP hemispherical analyser and Al K α X-ray source (1486.6 eV). Oxygen or water were dosed at 2 mbar and the sample illuminated using a Sciencetech Lightline A1 solar simulator. The solar simulator is equipped with an AM1.5G filter to produce light with the global standard spectrum. The simulator is aligned to a window on the reaction cell and positioned approximately 30 cm away from the sample. This is shorter than the one-sun distance of the simulator, however the light passes through two windows before hitting the sample, thus it is not expected that the intensity is especially high. This is reflected by the temperature of the sample, which only increased slightly above room temperature when irradiated (~ 30 °C).

6.2.3 Data Processing

To calibrate the spectra, the TiSi₂ component of the Ti 2*p* spectrum was set to 453.2 eV [177]. For UHV XPS, spectra were recorded using a pass energy of 20 eV, however this was increased to 40 eV at ambient pressures. Wide spectra were recorded at 100 eV pass energy. To fit the spectra, a pseudo-Voigt function was employed [138]. Of each region, only the TiSi₂ component of the Ti 2*p* required an asymmetric lineshape. As for the previous chapters, the GL ratio was held constant within a spectrum, with the widths varying as appropriate. For each fit, a Shirley background was applied, with a linear background incorporated if required.

6.3 Results & Discussion

6.3.1 Powdered TiSi₂ XPS

Figure 6.1 shows the XPS of TiSi₂ powder that has been exposed to air. The TiSi₂ components appear at 453.2 eV and 98.5 eV, in the Ti 2*p* and Si 2*p* respectively. This is in agreement with previous XPS studies of TiSi₂ [177]. It is clear that the majority of the signal comes from an oxidised outer layer, where a higher oxidation state for Ti appears at 459 eV. This is assigned to the Ti⁴⁺ of TiO₂. In the work describing TiS₂'s ability to split water [173], it is suggested that its catalytic activity does not arise from TiO₂, as the amount of hydrogen produced is more than expected. Figure 6.1a does not identify any Ti environments other than TiO₂, thus whatever the catalytic centres are, they do not appear to feature metallic Ti. It could be said that these centres include Ti⁴⁺, the signal of which would overlap with TiO₂. However, if this were the case, it would have to form some kind of compound containing silicon as well as oxygen, which is unlikely to not be resolved at this pass energy.

There is a different story told by the Si 2*p*, however. Here, peaks are seen at 99.3 eV and 103.7 eV, which are assigned to elemental Si and SiO₂ respectively [140]. The origin of the elemental Si likely reflects the Si-Si bonds that form part of the C54, face-centred orthombric, crystal structure of TiSi₂ [178]. Some SiO₂ is not surprising, due to the length of time the powder has seen air, and the presence of elemental Si should be taken to indicate TiSi₂ in the same way as the peak at 98.5 eV does. At this point, the final peak at 102.5 eV in figure 6.1b should be discussed. It is not immediately clear what causes this peak, however the fact it dominates the spectrum implies that it is caused by the reaction of the surface

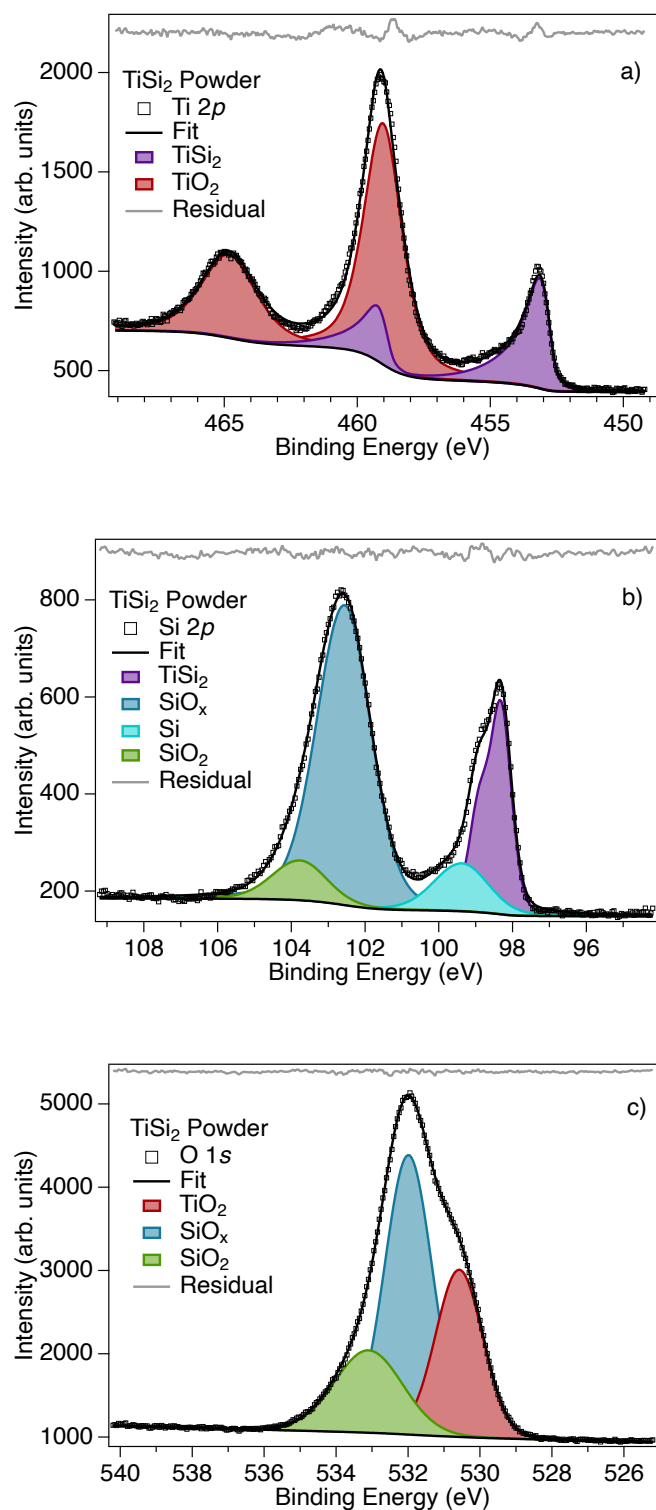


Figure 6.1: Ti 2p (a), Si 2p (b), O 1s (c) XPS of commercial TiSi_2 powder, previously exposed to atmosphere. The powder is heavily oxidised, however the silicide core remains visible. Recorded at 20 eV pass energy.

with air. This is perhaps evidence of the unidentified catalytic centres described in reference [173] and, taken in conjunction with the lack of any unexpected features in the Ti 2*p*, would imply that they consist of some sub-stoichiometric combination of Si and O. This is not certain, however, and further work would be needed to correlate this phase with any solar water splitting ability. A less exciting possibility to consider is that this peak is simply SiO₂, where differential charging in the powder causes two peaks to appear. TiSi₂ is reportedly conductive [172], but is encapsulated by oxide here, thus a lack of a sufficient ground is not hard to imagine. The fact that the sample is powdered also does not help in this regard. These arguments can be similarly applied to the O 1*s* spectrum, figure 6.1c. Three peaks are found at 530.5, 531.9, and 533 eV, the former and latter of which are assigned to TiO₂ and SiO₂. The binding energies of these peaks are in broad agreement with expectations [106, 140]; both sit slightly higher compared to literature, which is caused by the sample being powdered, not single crystal. The unknown peak is again present, making its absence in the Ti 2*p* conspicuous.

6.3.2 Powdered TiSi₂ APXPS

AP-XPS of the TiSi₂ powder is presented in figure 6.2, where the sample was exposed to approximately 2 mbar of oxygen followed by 2 mbar of water. Before fitting, some qualitative changes can be observed in the spectra between the water and oxygen scans, but these are subtle and the noise makes a more definitive comparison difficult. Firstly, the changes in the O 1*s* are dominated by features that appear to high binding energy, which correspond to gas-phase oxygen and water vapour. Secondly, it appears as though the main peak in the water scan is slightly narrower compared to

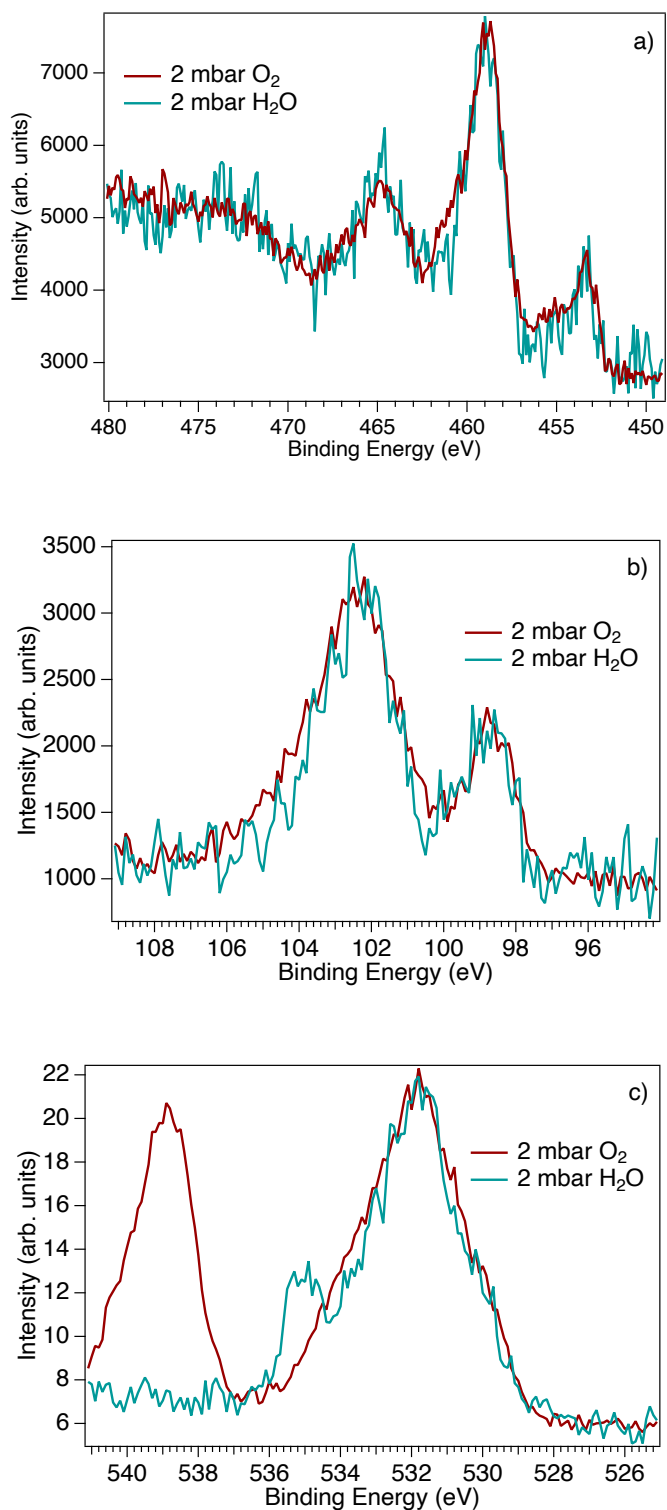


Figure 6.2: Comparison Ti 2*p* (a), Si 2*p* (b), and O 1*s* (c) of TiSi₂ APXPS under H₂O and O₂ environments. The spectra have had their backgrounds aligned and were normalised to each other to allow the overall shape to be compared. Recorded at 40 eV pass energy.

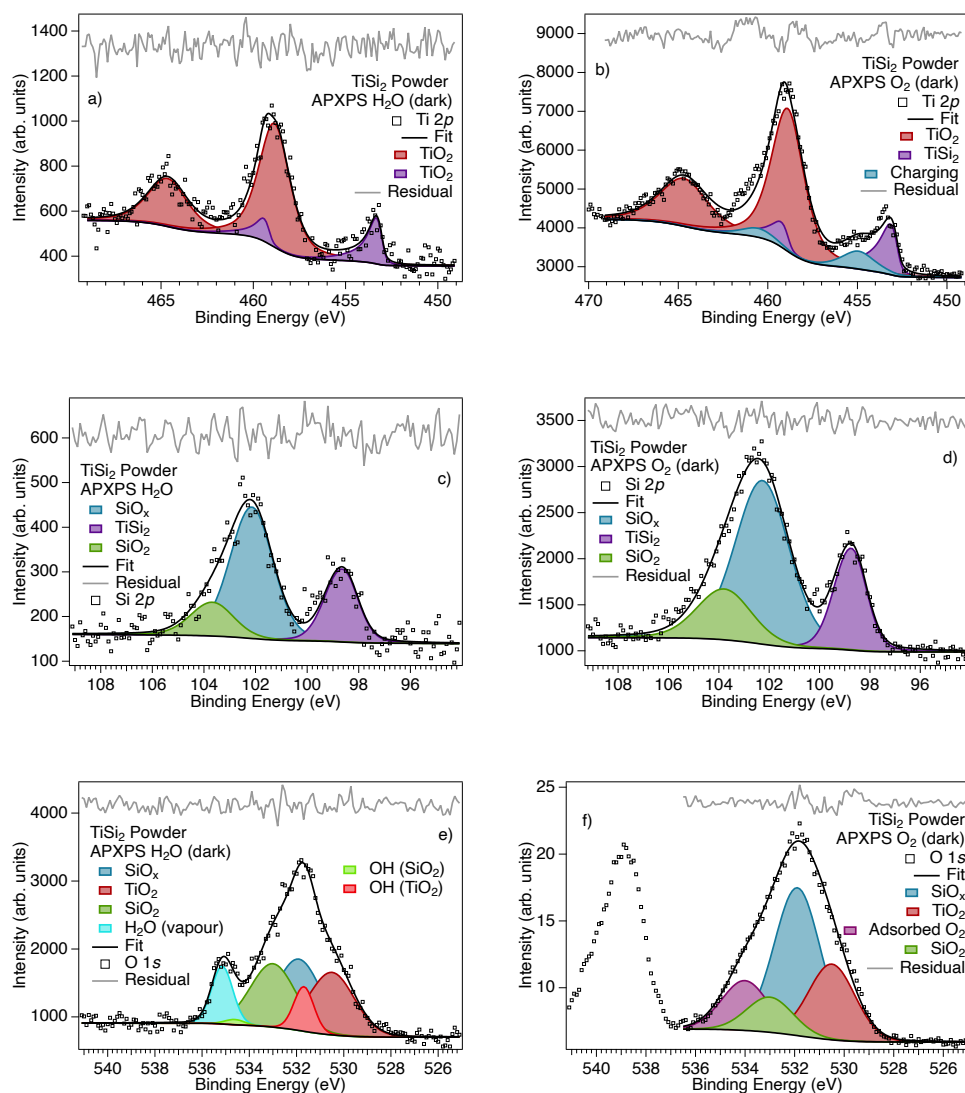


Figure 6.3: AP-XPS fits of TiSi_2 under water (a, c, e) and oxygen (b, d, f). All were recorded at 40 eV pass energy at approximately 2 mbar.

the oxygen. This also appears to be so for the water-exposed Ti $2p$ and Si $2p$, which in places are narrower compared to the oxygen. In all cases, the overall form of the spectra remains more or less constant despite the change in environment, which in itself is not surprising. 2 mbar is far below the partial pressure the powder would have experienced at atmosphere for both oxygen and water. As a result, no further oxidation would be expected to occur in the reaction cell, and most changes are likely caused by the adsorption of either oxygen or water.

Despite the noise, some information can still be extracted by fitting the AP-XPS. Beginning with the Ti $2p$ (figures 6.3a and 6.3b), the TiO_2 and TiSi_2 components are seen at similar binding energy as at UHV. The spectrum recorded under water is similar to that in figure 6.1, however the spectrum recorded under oxygen is noticeably different. Here, an unknown peak appears around 455 eV. Even with the presence of this peak and its spin couplet, the high binding energy sides of the TiO_2 and TiSi_2 peaks are still poorly fit. Ti does not have any oxidation states above Ti^{4+} , thus is unlikely that there is another chemical environment to the left of the TiO_2 . Ti^{3+} and Ti^{2+} do appear to higher binding energy compared to the silicide, however the binding energy of the peak in figure 6.3 does not match [64, 65]. Consequently it is not clear what this peak could be, as further oxidation of the TiSi_2 is unlikely. The spin-orbit splitting has been chosen to correspond to Ti^{3+} because this pushes the couplet further into the region where the fit requires more intensity. In addition, as these spectra were recorded in the same experimental session with the sample being exposed to oxygen first, it could be inferred that the water removes this peak or that it is unique to high oxygen partial pressures. This being said, as this broadening appears to the right hand side of both the main features in the spectrum, differential charging is the most probable explanation. Why this broadening appears to vanish in the water spectrum could be either that water is better at compensating the charge at the surface, or that the noise is too high to resolve the charging sufficiently.

Figure 6.3 also shows the Si $2p$ and O $1s$, where the situation is clearer. The Si $2p$ is essentially the same as figure 6.1b, but with the elemental Si component missing. This should not be interpreted as the Si oxidising into SiO_2 or the sub-stoichiometric feature, because it is seen below in figure 6.4 recorded in the absence of either reactant. Thus, the silicon is most likely

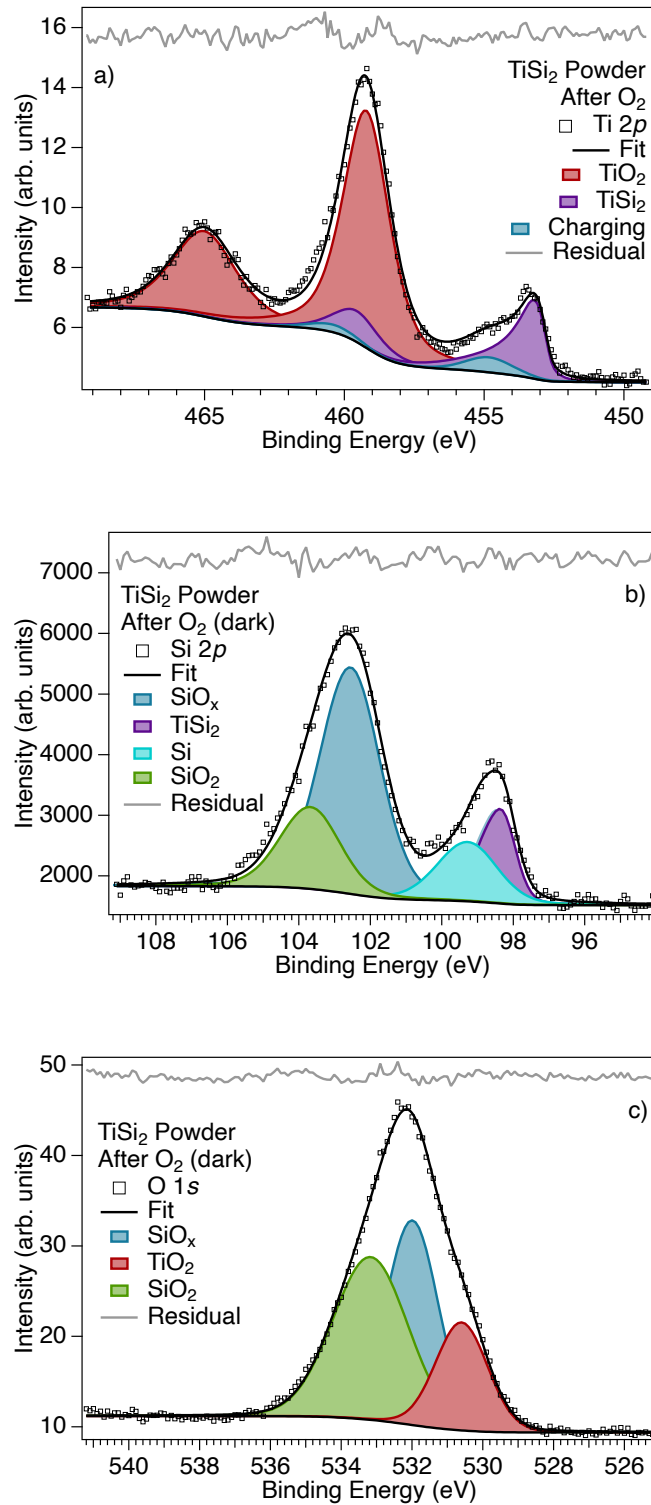


Figure 6.4: Ti 2*p*, Si 2*p*, and O 1*s* recorded in the reaction cell, but with the oxygen and water evacuated. Recorded at 40 eV pass energy.

unresolved at this pass energy. For the O 1s, the spectra are broadly the same as at UHV, with two exceptions. Firstly, new peaks have appeared due to the adsorption of water and oxygen at the surface, most obviously hydroxyls on TiO₂ and surface absorbed oxygen. For the water spectrum, if these peaks are omitted, the sub-stoichiometric peak dominates the spectrum beyond what is expected and tends to have an unrealistically large width. Including surface hydroxyls brings this back into line with expectations, but reduces the overall intensity of the sub-stoichiometric peak. This can be interpreted as the feature lying deeper into the bulk than the oxides and thus being attenuated more by the layer of surface absorbed hydroxyls. For the oxygen spectrum, if the surface absorbed oxygen peak is removed, the SiO₂ must move to higher binding energy to compensate and get wider, both of which are inconsistent with previous spectra. Secondly, the ratio of SiO₂ to TiO₂ appears to have changed in the water AP-XPS spectrum. This could be caused by underestimating the intensity of hydroxyls adsorbed onto SiO₂ sites or if a peak is needed to represent hydroxyls on the sub-stoichiometric oxide. The O 1s recorded after AP-XPS in figure 6.4 also shows that the intensity ratio of the oxides is changed at UHV, which would suggest that further oxidation has occurred. However, the spectra changes above what can reasonably be expected given the level of oxidation prior to the AP-XPS. It is more probable that hydroxyls are still present on the sample at UHV, making the SiO₂ peak broader and more intense than expected.

Clearly the situation at the surface is complicated, and as the powder is already oxidised by air and potentially charging, it is difficult to assign any feature to TiSi₂'s water splitting ability with confidence. One fact that can be discerned, however, is that illuminating the sample with a solar spectrum changes little, shown in figure 6.5. In this plot, light does not

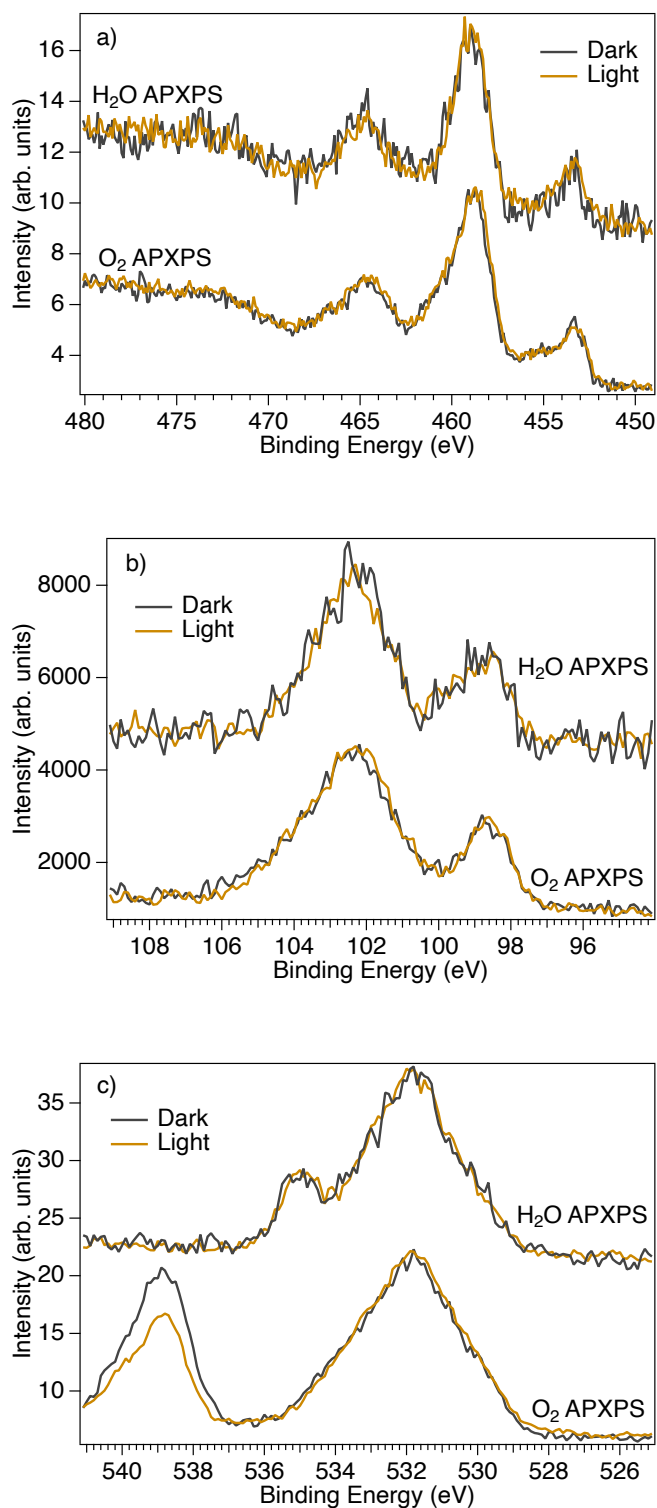


Figure 6.5: Comparison of the Ti $2p$, Si $2p$ of powder TiSi_2 , and O $1s$ under ambient pressure light and dark reaction conditions. Recorded at 40 eV pass energy.

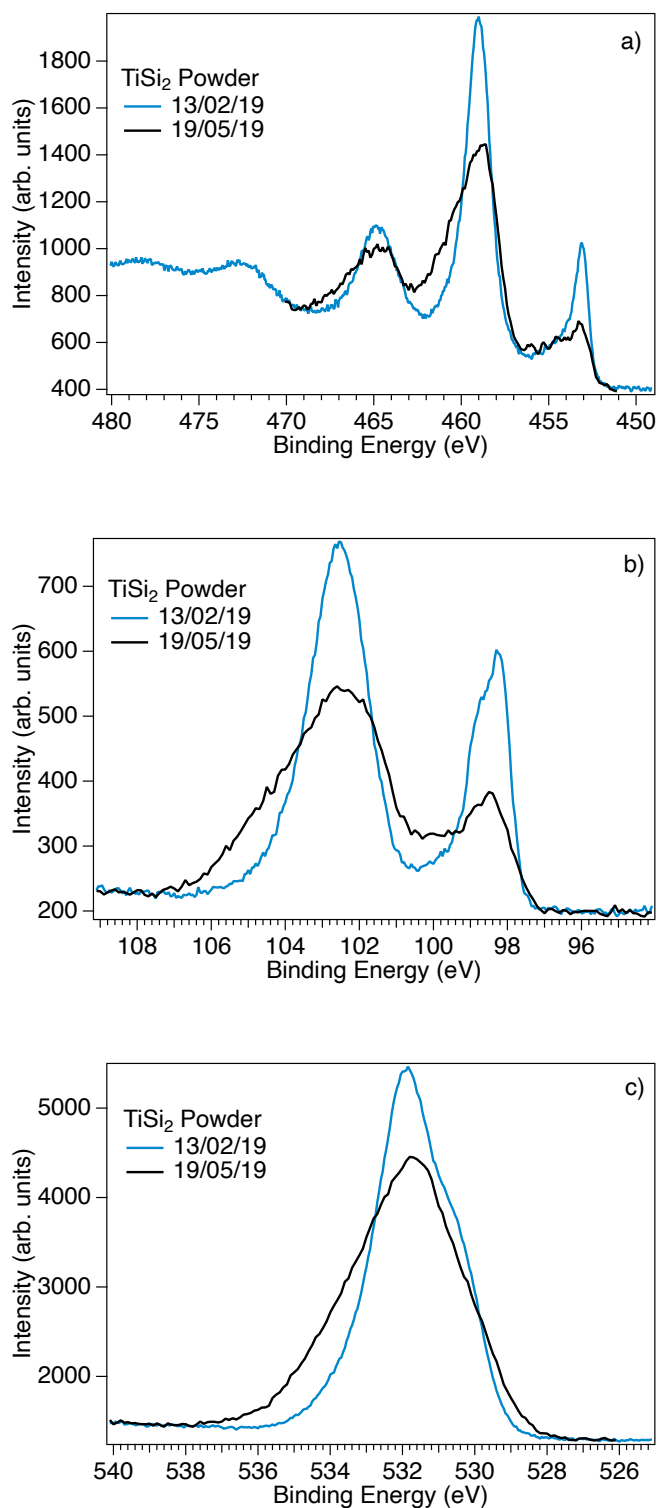


Figure 6.6: UHV XPS of Ti 2*p*, Si 2*p*, and O 1*s* of two different TiSi_2 powder samples, recorded three months apart. Each region was recorded at 20 eV pass energy and were scaled such that their backgrounds aligned.

effect either spectrum under their respective reaction environments. The work describing TiSi_2 for solar water splitting states that light is key when the powder is initially reacted to get any catalytic activity later on [173]. No evidence of any change at the surface is observed under light, again likely because the powder has already reacted with oxygen and water from the atmosphere. However, commercial powder is also used in reference [173], which presumably saw air as same as the sample investigated here. Thus, the effect of light on the already oxidised powder may instead become prominent for TiSi_2 immersed in water, rather than when exposed to its vapour.

While some information has been obtained from the AP-XPS of powdered TiSi_2 , as discussed above, there are caveats. Most important of these is that charging effects can not be ruled out. This is demonstrated in figure 6.6, which compares two samples from the same source, where one has sat at atmosphere longer. The peaks are broader across all the regions, which is indicative of differential charging. As a result, two requirements are imposed on future samples of TiSi_2 . Firstly, the sample must be conductive enough to eliminate charging effects, or at least minimise them. Secondly, as most of the chemistry pertinent to solar water splitting appears to happen during the initial oxidation, the surface must be well defined so that any oxide layers can be removed.

6.3.3 Thin Film TiSi_2 XPS

In order to address some of the aforementioned problems, a thin-film of TiSi_2 was deposited onto MgO by magnetron sputtering. The UHV XPS of the first sample grown is shown in figure 6.7, recorded at normal (NE) and grazing emission (GE). The Ti $2p$ and Si $2p$ show that the oxide lies

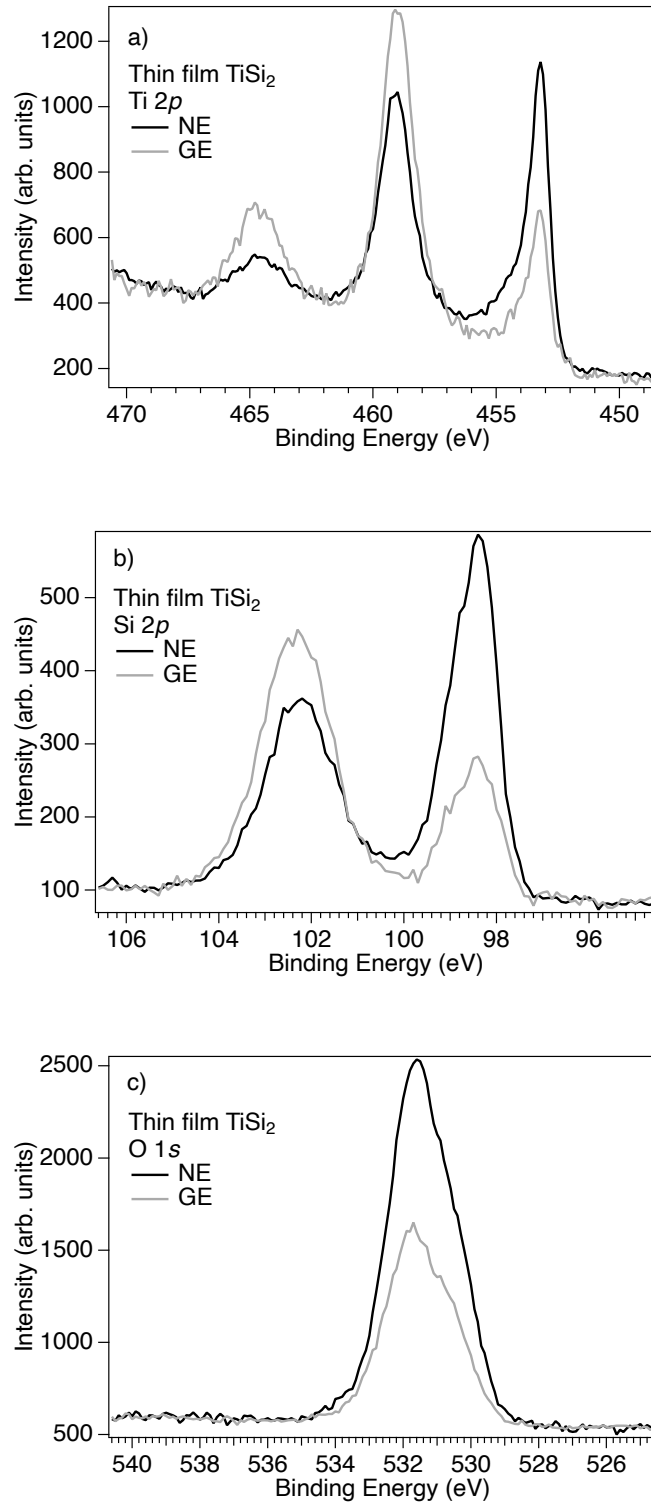


Figure 6.7: Comparison of Ti 2p (a), Si 2p (b), O 1s (c) record at normal (NE) and grazing (GE). The spectra have been scaled to match backgrounds and were recorded at 20 eV pass energy.

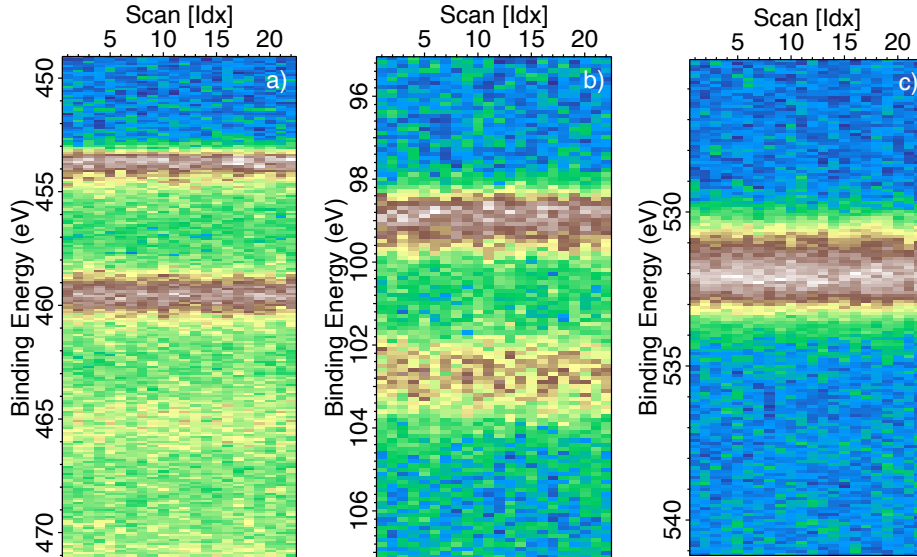


Figure 6.8: Maps of Ti $2p$ (a), Si $2p$ (b), O $1s$ (c) XPS under solar illumination. The spectra do not shift, implying no significant photovoltage is generated. Recorded at 20 eV pass energy.

at the surface, as expected, however the reduction of intensity of the O $1s$ implies that the oxidation is deeper than the information depth at GE. The spectra of figure 6.7 again highlight TiSi_2 's instability in air.

Given that the sample sees significantly more oxygen and water at atmosphere than under AP-XPS conditions, it is worth checking if any photovoltage is generated by light when it is oxidised. Any semiconducting behaviour caused by the oxide layer could shift the spectra as the sample becomes reverse biased by the charge carriers. This applies to the powder sample also, however as the electrical contact between grains is poor compared to a single crystal, the lack of any significant shift is not surprising. Shifts caused by optical illumination been shown to occur in the XPS of Si previously [179]. The spectra of the illuminated sample is shown in figure 6.8. As no shifts are observed, no significant photovoltage is generated, and thus it is unlikely that air-oxidised TiSi_2 is semiconducting in the way described in reference [173].

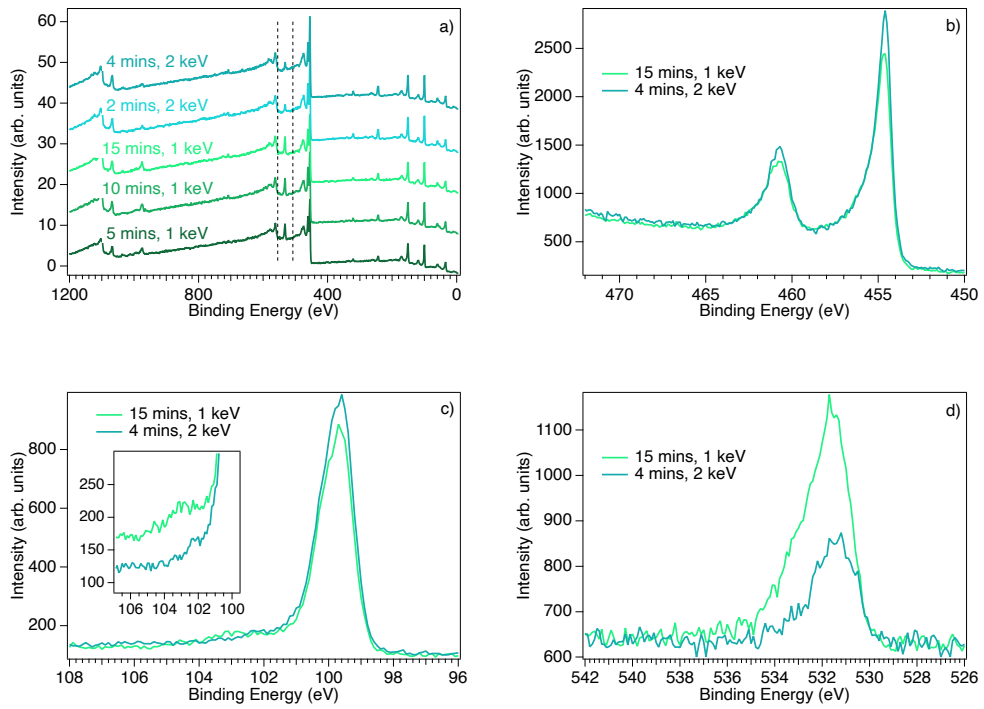


Figure 6.9: Wide (a), Ti $2p$ (b), Si $2p$ (c), and O $1s$ (d) depth profiles of thin film TiSi_2 . The high resolution regions show the result of moderate and heavy sputtering. The spectra are presented as they were recorded, with the exception of the O $1s$, which has the backgrounds aligned. The O $1s$ is highlighted by dashed lines in the wide scans. Survey spectra and high resolution regions were recorded at 100 eV and 20 eV pass energy, respectively.

The biggest appeal of thin film TiSi_2 is that it can be sputtered effectively, the results of which are shown in figure 6.9. Looking at the wide and O 1s spectra, it appears that oxygen is present throughout the TiSi_2 layer, suggesting that the sample is not completely passivated upon exposure to air. Thus, AP-XPS was unable to be conducted on this sample for two reasons. Namely, the failure to remove all the oxygen, and the subsequent destruction of the TiSi_2 layer in pursuit of this goal. This fits with the ageing behaviour of the powder samples in the previous section, the conductivity of which seemed decrease with longer exposure to air. The prevalence of the oxide to a depth of 100 nm (the thickness of the TiSi_2 layer here) may run counter to the assertion that TiSi_2 can be used as a solar water splitting catalyst because of its ability to passivate under reaction conditions [173]. However, this assumes that the mechanism is the same in aqueous environments as in air. Sufficient passivation may occur by the reaction with water in the presence of a small amount of oxygen (as the authors suggest [173]), rather than with oxygen in the presence of a small amount of water.

6.3.4 Thin Film TiSi_2 APXPS

With the oxide found to penetrate through the TiSi_2 layer, it is useful to confirm that no further changes occur due to exposure to water and oxygen. This allows any changes in the AP-XPS of minimally oxidised TiSi_2 to attributed to oxidation, presented further in this section. To achieve this, another thin film sample was required, the UHV XPS of which is shown in figure 6.10. Beginning with the Ti $2p$, the TiSi_2 and TiO_2 components are found at 453.2 and 458.6 eV. For the Si $2p$, the TiS_2 , elemental Si, and sub-stoichiometric oxide are found at 98.3, 99.6, and 102.2 eV. These all

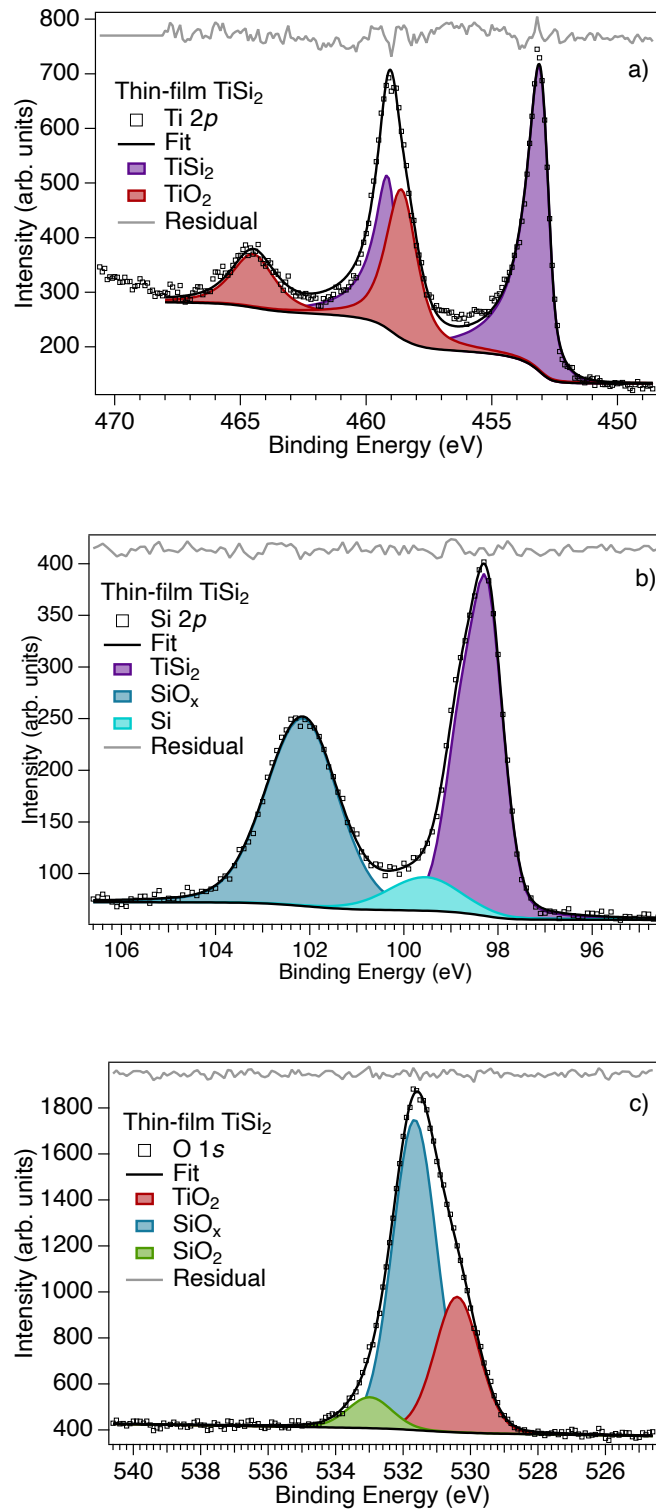


Figure 6.10: UHV Ti 2*p* (a), Si 2*p* (b), and O 1*s* (c) XPS of thin film TiSi_2 . The sample is very similar to the powder XPS in figure 6.1, but with less SiO_2 . Recorded at 20 eV pass energy.

bear similarity to the powdered TiSi_2 XPS in figure 6.1. In general, the exact binding energy values are slightly less compared to the powder XPS, however this can be attributed to the increased conductivity of the film. This holds for the O $1s$ also, which are also similar to the powder XPS; here the TiO_2 appears at 530.4 eV, SiO_2 at 533 eV, and the sub-stoichiometric oxide at 531.7 eV. Most notably in figure 6.10 is that there is no obvious SiO_2 component to the Si $2p$, with only a small fraction appearing in the O $1s$. This is most probably due to the much reduced surface area of the film versus the powder and, as a result, potentially a reduction in the sites appropriate for Si oxidation. As such, it could be that any signal in the Si $2p$ XPS from SiO_2 is obscured on account of its proximity to the sub-stoichiometric oxide and that the cross-section for Si $2p$ photoelectrons is much lower than that for the O $1s$.

The AP-XPS of the air-oxidised sample is presented in figure 6.11, alongside comparisons of the spectra before and after AP-XPS. As is shown, no significant changes have occurred under reaction conditions, nor do any become apparent when the sample is taken back to UHV conditions where the counts are higher. Like the powder, this again confirms that TiSi_2 is highly susceptible to oxidation by air and thus the chemistry relating to solar water splitting is obscured. Notably absent are any peaks corresponding to absorbed hydroxyls, the addition of which would not improve the fit meaningfully. This should not be interpreted as water not binding to the surface, however, only that the peaks are not resolved in this case.

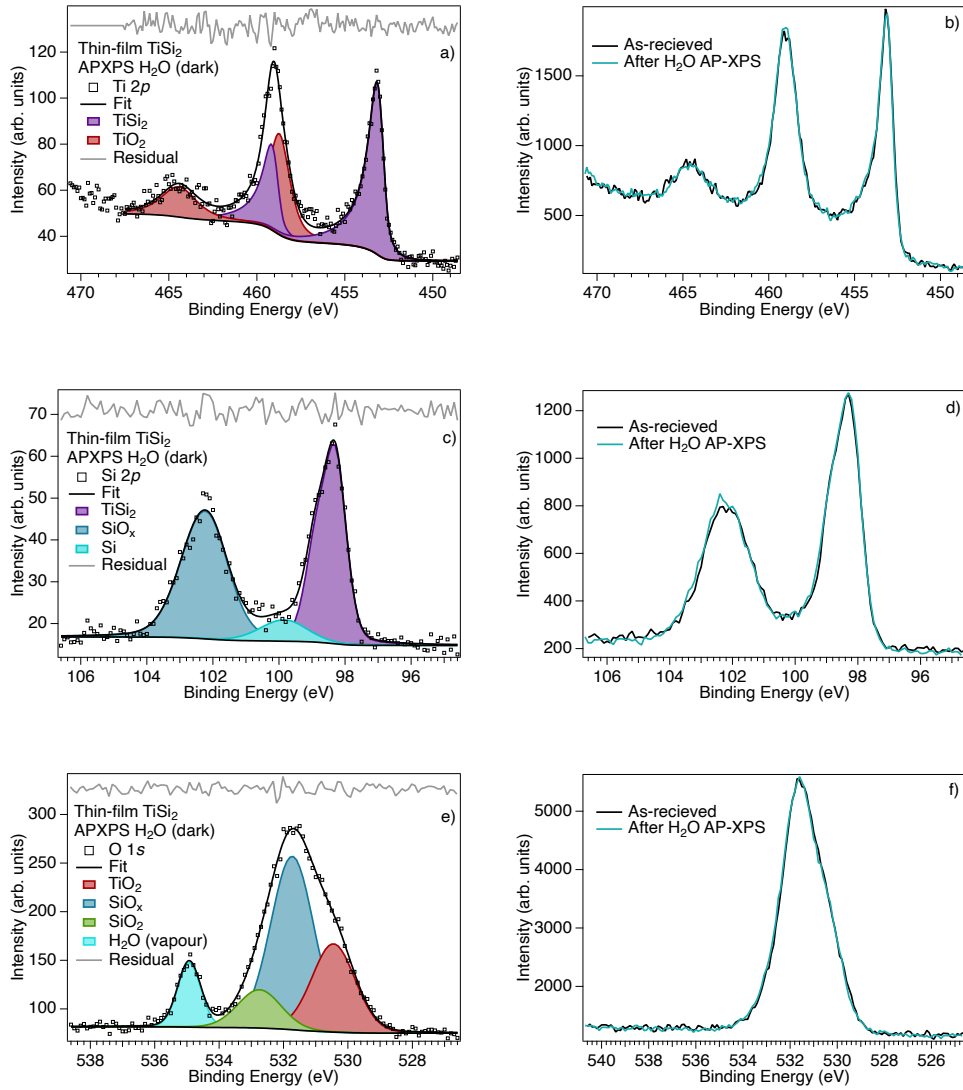


Figure 6.11: Ti 2*p*, Si 2*p*, and O 1*s* spectra taken at (a, c, e), and after (b, d, f), H₂O AP-XPS of thin film TiSi₂, oxidised by air. No significant change has occurred during, or after, being introduced to the reaction environment. Here, the pass energy is 20 eV for each spectra.

6.3.5 Strategies to Prevent Oxidation

The previous sections have firmly established the importance of removing the oxide from TiSi_2 in order to study its oxidation chemistry, before any comment can be made on its water splitting ability. To achieve this aim, two different materials were tested as overlayers to passivate the TiSi_2 thin films; Ti and Au metal. Figure 6.12 shows the UHV XPS of TiSi_2 capped with metallic Ti. Initially, the result is promising; the structure of the Si $2p$ resembles that of TiSi_2 with no oxidation. This being said, the opposite is true for the Ti $2p$, where only a small amount of TiSi_2 is seen through the overlayer, which is highly oxidised to TiO_2 . This is also reflected in the O $1s$, where a peak that appears in the expected position of TiO_2 dominates the spectrum.

Figure 6.13 shows how the Ti $2p$ and O $1s$ change as the sample is sputtered. The Ti $2p$ eventually resembles TiSi_2 , with little obvious oxide component visible, however the O $1s$ remains prominent even after heavy sputtering has occurred. After the last round of sputtering, there was a visible shadow on the sample, indicating that the TiSi_2 layer had become optically thin. As a result, it is concluded that passivating the TiSi_2 layer with metallic Ti is only partially effective. Potentially, this could be related to the fact that the overlayer itself oxidises, which may allow oxygen to reach the TiSi_2 . Alternatively, the presence of oxygen in the overlayer may introduce oxygen to the TiSi_2 during the sputtering process.

5 nm of gold was also used in an attempt to passivate the TiSi_2 layer, and as shown in figure 6.14, the initial results were not promising. Here, the sample appeared oxidised through the gold overlayer in both the wide and the Ti $2p$, where a large O $1s$ and TiO_2 contributions are seen. However, both were easily removed by lightly sputtering the sample; implying that

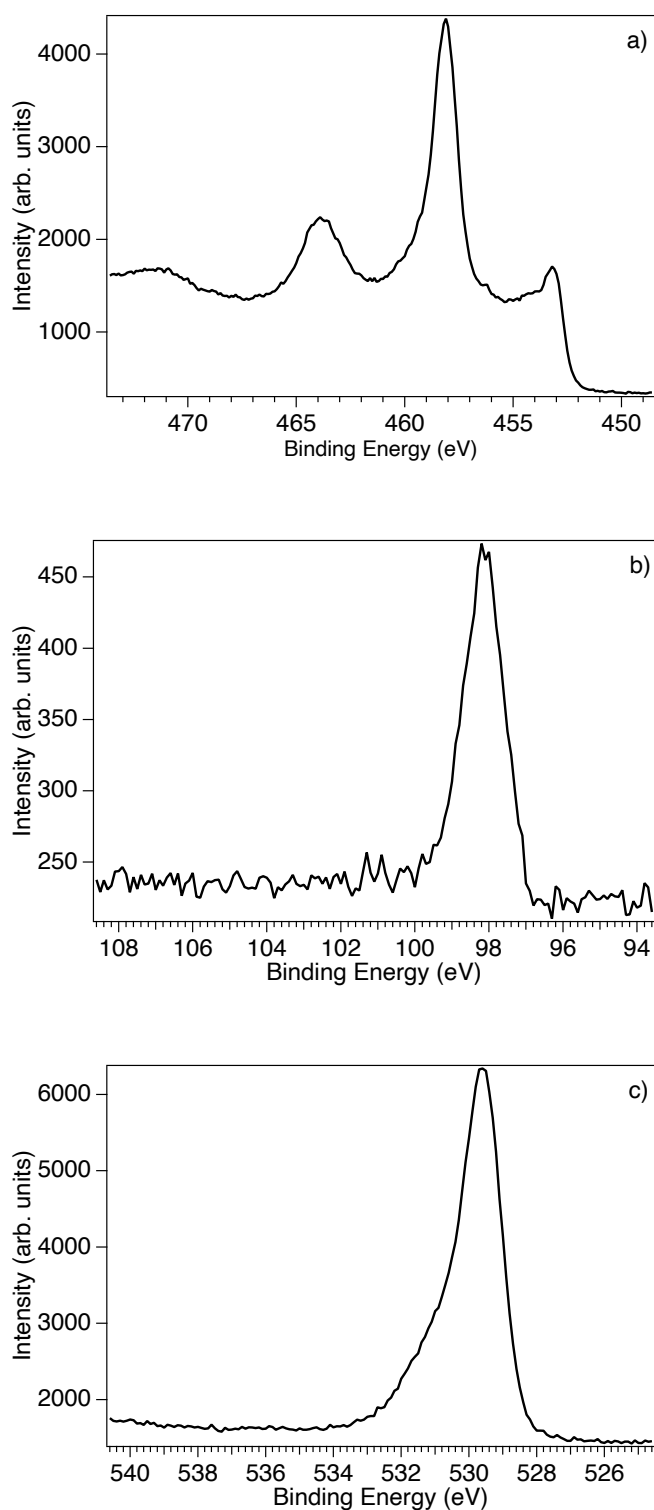


Figure 6.12: Ti 2*p* (a), Si 2*p* (b), and O 1*s* (c) UHV XPS of TiSi₂ passivated by a 5 nm thick Ti overlayer. The spectra are dominated by the oxidised Ti overlayer. All UHV spectra were recorded at 20 eV pass energy.

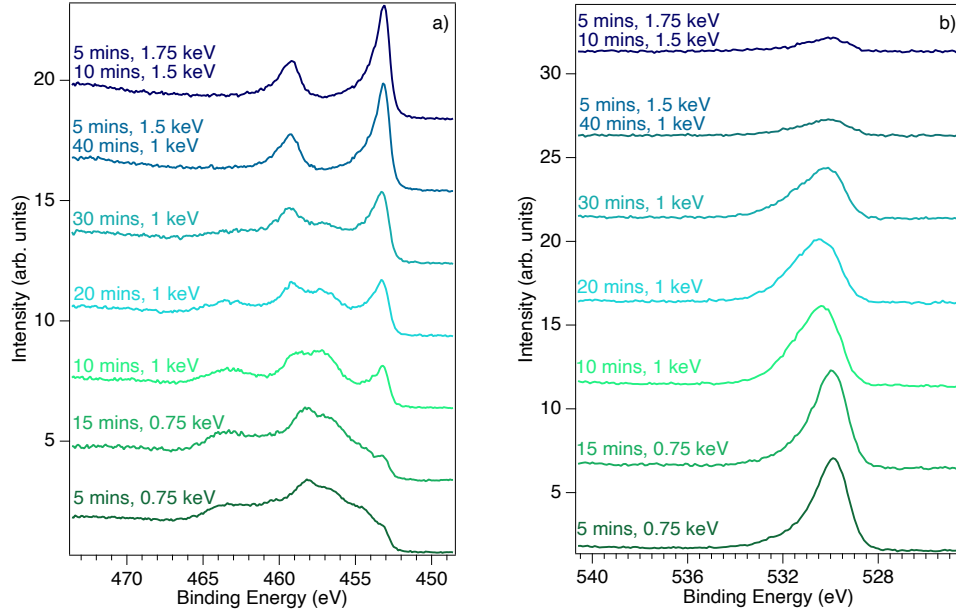


Figure 6.13: Ti $2p$ (a) and O $1s$ (b) UHV XPS of Ti-capped TiSi_2 as it is sputtered for increasingly longer durations, using increasingly energetic ions. The oxygen is never fully removed, despite removing a substantial portion of the layer. Here, the pass energy is 20 eV.

the excess oxygen and oxidised Ti lay on top of the gold layer. The origin of these contaminating features is not obvious and may not be related to the TiSi_2 . With the contamination removed, the TiSi_2 can be viewed through the intact gold overlayer, where only a small O $1s$ contribution to the wide scan is observed. Combined with no obvious oxidised component in the Ti $2p$, gold appears to be effective at passivating TiSi_2 .

While the above is encouraging, the Ti overlayer also appeared promising until sputtering was attempted. Thus, the ability of overlayers to prevent oxidation of TiSi_2 should be judged by both how well it protects against oxidation and how easily it is removed. Fortunately, the gold was able to be completely removed, as indicated by the wide scans in figure 6.15a. Unexpectedly, during sputtering, peaks corresponding to Fe $2p$ appear. The only possible source of iron, which is not present in the sample or its substrate, is the sample mounting assembly itself. When sputtered, the

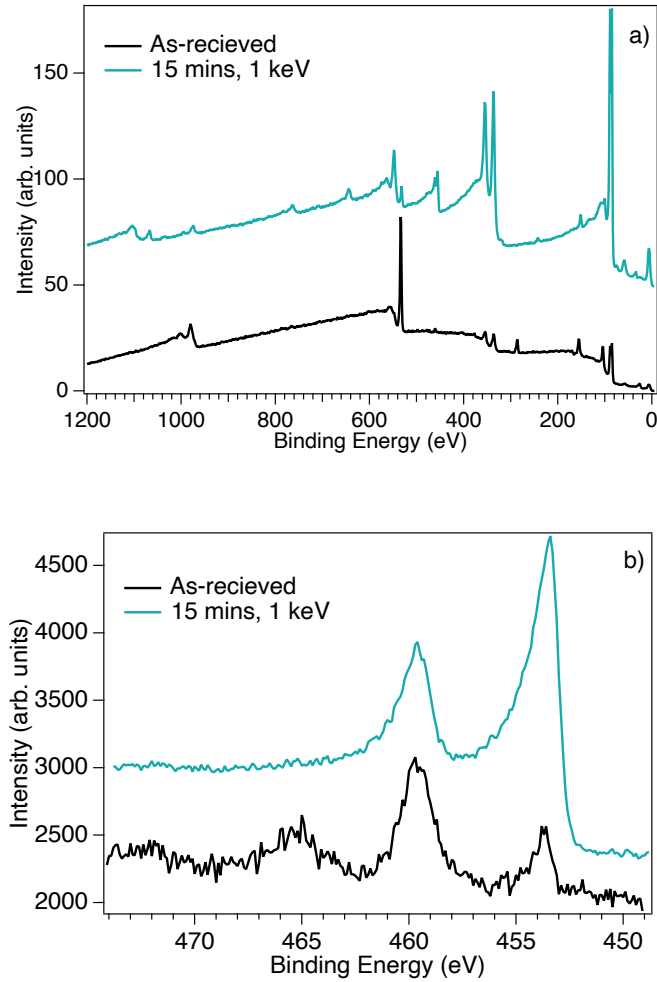


Figure 6.14: Initial wide (a) and Ti 2p (b) UHV XPS of Au-capped TiSi_2 , before and after sputtering. The backgrounds are offset, and the as-received Ti 2p enhanced to highlight the oxide. The pass energy is 100 eV and 20 eV for the survey and high resolution scans, respectively.

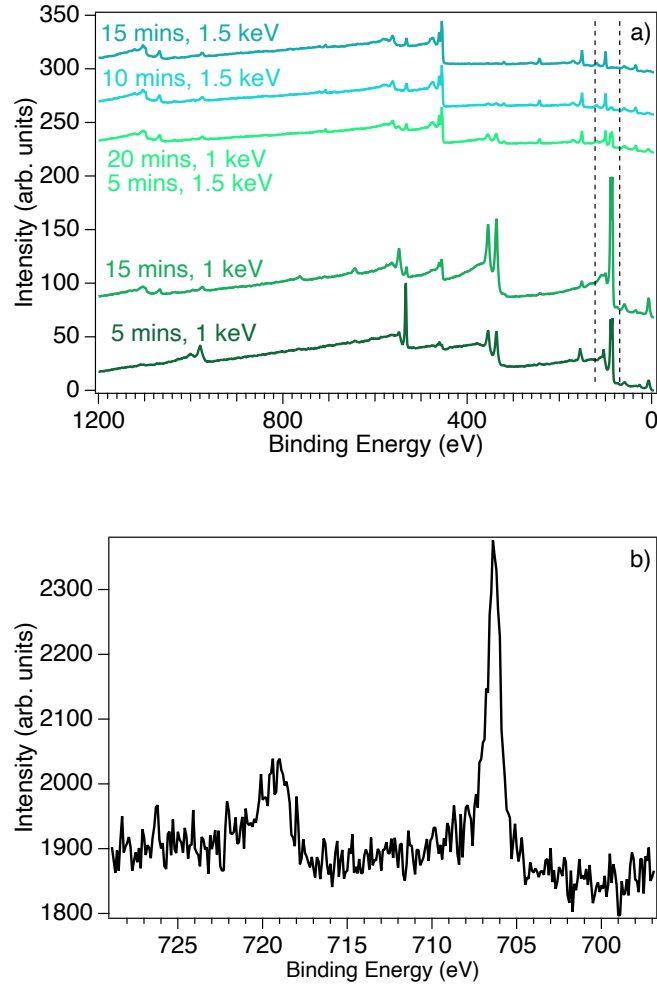


Figure 6.15: Wide (a) and Fe $2p$ (b) XPS of Au-capped TiSi_2 as the overlayer is sputtered through. The Au $4f$ is indicated by vertical dashed lines and is completely removed by sputtering. Note, the Si $2p$ region also lies within these lines. The survey and Fe $2p$ scans were recorded at 100 eV and 20 eV pass energies respectively.

area covered by the ions is large, and it is possible that the clip mounting the TiSi_2 to the sample plate is also hit. This could deposit a small amount of iron onto the TiSi_2 surface.

With the gold removed, only TiSi_2 remains; the fitted spectra both before, and after, AP-XPS are presented in figure 6.16. For the UHV spectra (figures 6.16a, 6.16c, and 6.16e), the Ti $2p$ and Si $2p$ spectra are dominated by TiSi_2 , with only small indications of oxidation. For the former, small TiO_2 and Ti^{3+} peaks are required to fit the area between the TiSi_2 spin

couplets. The Ti^{3+} likely is caused by the sputtering, rather than being related to the TiSi_2 itself. For the Si $2p$, only a small sub-stoichiometric peak is seen, which given its presence in the other spectra in this chapter can be attributed to slight oxidation of the silicide. There are still oxide peaks present, however to remove this would risk the integrity of the sample, thus the goal of the sputtering became to minimise the oxide component, rather than completely remove it. This may have been beneficial for a different reason, however. Considering that iron appeared in the spectrum likely as a result of sputtering, it is not impossible that oxygen is deposited in a similar manner, rather than originating from the sample.

The effect of water exposure to the sample is readily apparent in figure 6.16; in all cases the oxidised component of each spectrum is increased. In the Ti $2p$, this manifests as an increase in the TiO_2 component of the spectrum. In the Si $2p$, the sub-stoichiometric peak increases significantly, and the elemental silicon peak is again not resolved at this pass energy (see figure 6.17). It is interesting that no feature corresponding to SiO_2 appears in the Si $2p$ despite the sample unequivocally oxidising. As a result, the interpretation of the O $1s$ needs to be carefully considered.

Figure 6.16f shows that a peak appears in the region where SiO_2 is expected at ambient pressures of water, similar to previous figures of both the powder and oxidised thin-film samples. For figures 6.3 and 6.4, which show the spectra during and after AP-XPS of powdered TiSi_2 , it was suggested that the reason for the different intensity ratios compared to the spectrum before APXPS could have been caused by some hydroxyls still being present on the sample. This is likely the case here as well, and the O $1s$ and Si $2p$ recorded at UHV after APXPS support this (figure 6.17). The first thing to note here is that the elemental Si has not disappeared, again confirming that it is not resolved at higher pass energies. Secondly, the highest binding

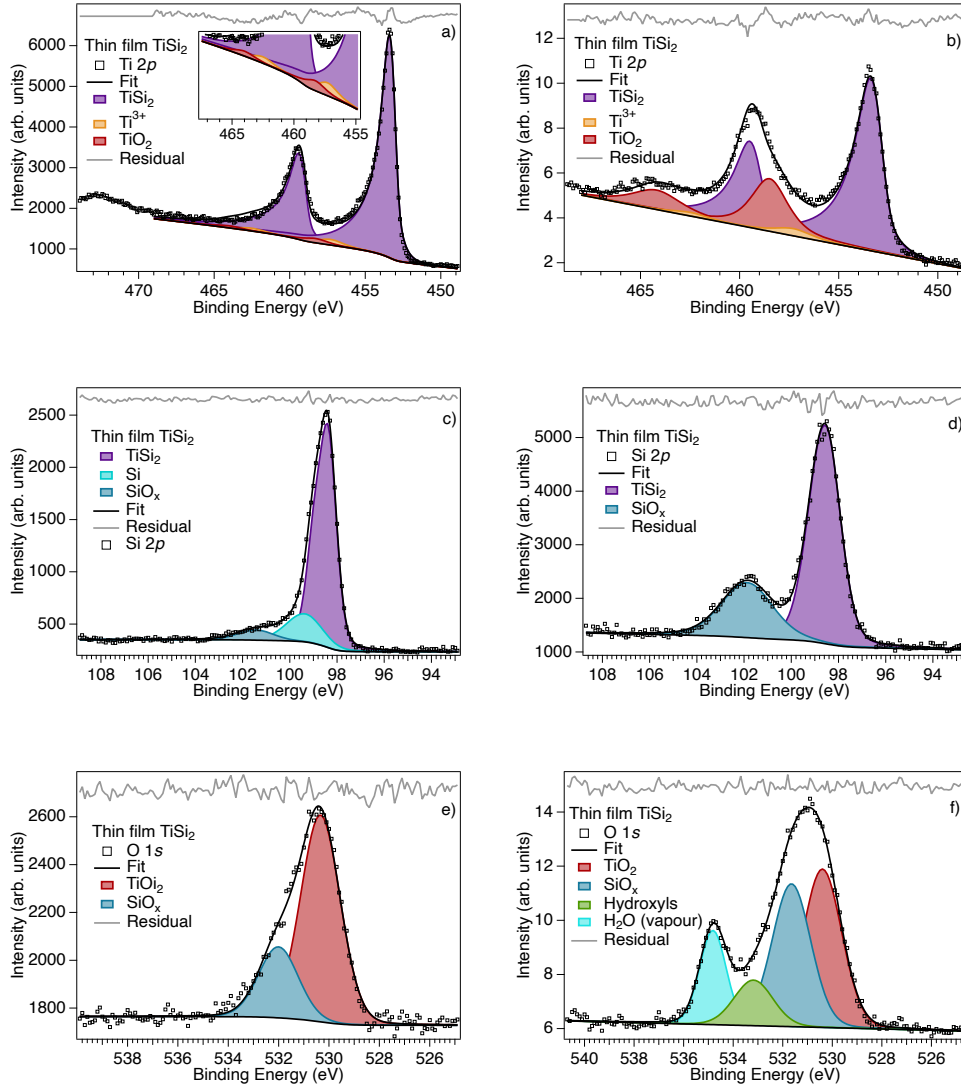


Figure 6.16: UHV (a, c, e) and H₂O APXPS (b, d, f) fits of TiSi₂ after the Au-overlayer has been removed. The sample becomes significantly oxidised by water in the absence of light. Here, pass energy was set to 50 eV for the AP-XPS measurements.

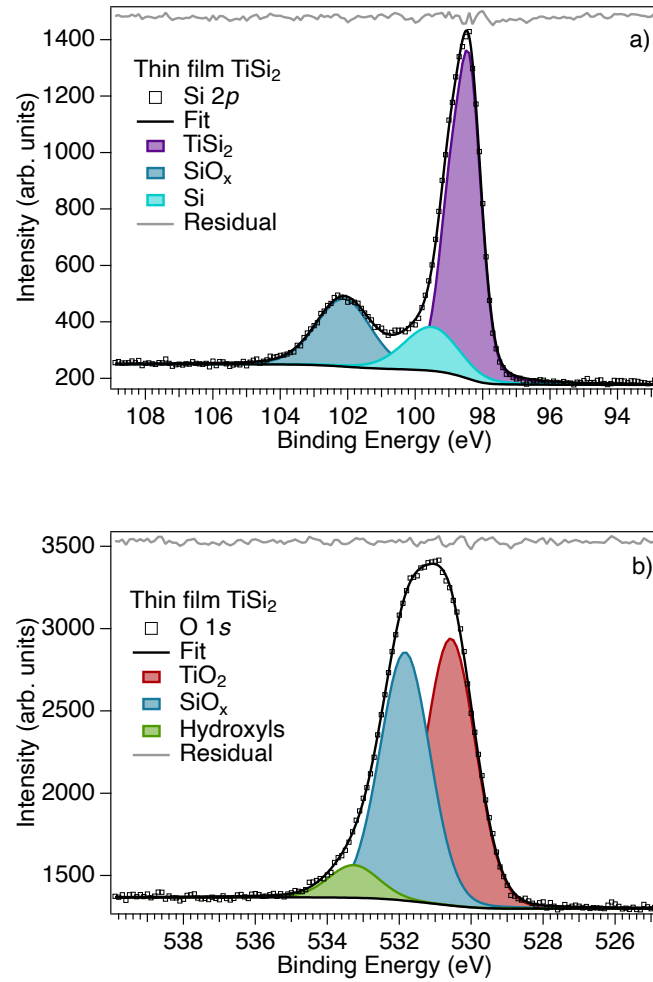


Figure 6.17: UHV $\text{Si } 2p$ (a) and $\text{O } 1s$ (b) XPS of thin film TiSi_2 , recorded after AP-XPS in a water environment was conducted. Both hydroxyls and the sub-stoichiometric silicon oxide are detected. Recorded with a pass energy of 20 eV.

peak at 533.3 eV has reduced in intensity compared to the AP-XPS in the previous figure. If this were SiO₂ as in previous figures, the ratio would not decrease when taken back to UHV. Thus, for this sample, it is assigned to hydroxyls on the surface of the sample. It is not clear whether or not these hydroxyls can be assigned to either the TiO₂ or sub-stoichiometric oxide components of the fit, in a similar manner to what was attempted in figure 6.17b for the powder sample, but it does not seem as though another peak would particularly improve the fit. Given the high pass energy of the spectrum, there is likely not the resolution to resolve hydroxyls bound to individual sites of the sample.

6.3.6 Solar Water Splitting with TiSi₂

The biggest takeaway from the water AP-XPS of minimally oxidised TiSi₂ is that the growth of SiO₂ is either minimal, or entirely absent. When comparing figures 6.1 and 6.4 for powdered TiSi₂ before and after AP-XPS with water and oxygen, the feature assigned to SiO₂ does appear to have grown in the Si 2*p*. The same can not be said for the Si 2*p* for thin film sample discussed here, which has been oxidised by water alone. This is important, as the increase can not be attributed to overlapping hydroxyl peaks remaining at UHV pressures in the Si 2*p* spectrum. The work describing TiSi₂'s ability to split water in reference [173] was linked to a number of conditions; namely, illumination in initial stages of the reaction and the water not being completely degassed. From the work herein, the cause of these stringent initial conditions could be related to avoiding the growth of SiO₂ domains on the sample, an insulating material, which appears to be caused by the reaction of TiSi₂ with oxygen. However, the authors claim some residual oxygen is necessary for catalytic activity [173], which may be important

for the growth of the sub-stoichiometric feature seen in both the AP-XPS of the powder and thin film TiSi_2 . Further study is needed to confirm the exact nature of this feature, however if it is indeed a sub-stoichiometric oxide of TiSi_2 , it may possess a high concentration of defects. Defects have been suggested to be important in solar water splitting, as they facilitate the absorption of water molecules [64]. Consequently, solar water splitting with TiSi_2 may not be a question of how a novel phase grows that is unique to TiSi_2 , but rather how naturally occurring passivation and favourable defect chemistry synergise. However, it is worth repeating that further experiments are vital to confirm this, likely involving a selection of characterisation techniques.

6.4 Conclusion

In this chapter, the ability of AP-XPS to provide insight into the reaction chemistry at a catalyst's surface has been demonstrated. In the system studied here, the oxidation of TiSi_2 by oxygen and water has been studied. For the powder samples, the inability to remove the oxide layer meant that the most interesting chemistry had likely already occurred. Combined with issues around charging, these samples were deemed ineffective to understand the origin of TiSi_2 's activity for solar water splitting. With this being said, some useful information was extracted; namely, the existence of a phase at the surface attributed to a sub-stoichiometric oxide of Si.

To improve conductivity and allow the oxide to be removed, thin film samples were grown on MgO by magnetron sputtering. Initially, keeping the samples from being oxidised by air was difficult, where depth profiling by sputtering showed significant oxygen content throughout the TiSi_2 layer.

AP-XPS on one such air-oxidised sample showed no further oxidation. Thus, titanium and gold passivating overlayers were employed to protect the sample. Gold was determined to work best, as once the overlayer was removed, minimally oxidised TiSi_2 was revealed. Subsequent AP-XPS on this sample allowed the oxidation of the surface to be monitored, where growth of TiO_2 and sub-stoichiometric Si oxide phases was observed. However, major growth of SiO_2 seemed absent compared to the powder, which underwent both oxygen and water AP-XPS. The intensity in this region was instead attributed to surface hydroxyls. Taken together, these results imply that the catalytic activity of TiSi_2 may be related to the growth of the sub-stoichiometric oxide without full oxidation to SiO_2 .

Chapter 7

Conclusions

The aim of this thesis was to use core-level spectroscopies to gain a deeper understanding of the charge transfer dynamics in dye-sensitised solar cells and how the surface of a solar water splitting catalyst can change under reaction conditions. The work on dyes began with the study of a relatively simple dye, C343, which demonstrated how these spectroscopies can provide both chemical and electronic information. In doing so, two conclusions were drawn. Firstly, it was suggested that the energetics for charge transfer for C343 on SrTiO₃ were less favourable compared to TiO₂. Secondly, the XAS may show some evidence for an alternative bonding mode of the dye involving its nitrogen atom. Both findings will require further investigation; the core-hole clock implementation of either RPES or RAES of C343 on both substrates would quantify the effect of the perceived favourable alignment of the TiO₂ sample. Repeat measurements of XAS at the N 1s edge could confirm the presence of the unknown peak, possibly on C343 deposited in-situ. This combined with scanning tunneling microscopy would help identify any unexpected bonding geometries.

Next, the same techniques, in combination with RAES, were used to in-

investigate the charge transfer dynamics of N3 on TiO₂. This dye is more complicated than C343, however has been investigated extensively previously at the N 1s edge. However, in order to study if charge transfer from thiocyanate is possible, and to improve the precision of the core-hole clock implementation of RPES and RAES, measurements were taken at the S 1s and Ru 2p_{3/2} edges. In doing so, how long the excited electron takes to relax, and inject, was quantified. The relative similarity in these values was suggested to reflect that injection from N3 proceeds from both its singlet and triplet states, and that the thiocyanate ligand must be involved in the former. The results presented in this chapter would benefit from DFT calculations, which would solidify the picture of charge injection presented from the RAES data.

RAES was again utilised for two more ruthenium complex dyes, in conjunction with RPES and XPS. Here, similar to N3, the goal was to determine the charge injection and relaxation times of RuP and RuC. The former binds to TiO₂ using PO(OH)₂ and the latter through the familiar COOH moiety. This was achieved at the Ru 2p_{3/2} edge, where it was found that relaxation in RuP was much slower compared to RuC. Only an upper bound could be calculated for both dyes due to noise, but injection was shown to occur on the attosecond timescale. As a result, it was stated that the injection times themselves are not reliable indicators of which anchoring group facilitates injection more effectively. Instead, injection was compared to relaxation, which in the case of RuP was taken to favour injection from the singlet state of RuP. The converse was interpreted for RuC; relaxation competes with direct injection thus likely originates from a triplet state. As a result, PO(OH)₂ was taken to be superior to COOH. Given the particularly rapid transfer times calculated in this chapter, it would be prudent for them to be confirmed by further measurements. This would provide an opportunity

to reduce the noise on the RPES, particularly in the case of RuC, and also to check the calibration of the photon energy.

Aside from dye-sensitised solar cells, the solar water splitting catalyst TiSi_2 was investigated using AP-XPS. Powder samples were studied first, however the results were affected by charging and exposure to air had already heavily oxidised the material. As a result, thin film TiSi_2 samples were produced in order to improve the conductivity and allow the oxide layer to be removed by sputtering. Unfortunately, this was only partially successful as sputtering was unable to fully eliminate the oxygen signal from the sample. Gold was subsequently used to passivate the surface against oxidation, which was then able to be removed from the TiSi_2 . This allowed AP-XPS of minimally oxidised TiSi_2 to be conducted, and it was suggested that its catalytic activity may be related to a sub-stoichiometric silicon oxide phase combined with the minimisation of SiO_2 . Further work is needed to confirm this, including additional AP-XPS, however. Exposing thin film TiSi_2 to oxygen would show if SiO_2 is grown at the surface, allowing a direct comparison to the results presented here with water. Similarly, minimally oxidised TiSi_2 could be oxidised in the presence of light to highlight any differences. Such experiments would likely benefit from being conducted at a synchrotron, where higher pressures and resolution is possible.

For the dyes investigated, new chemical information is proposed, and competition between relaxation and direct injection discussed. For TiSi_2 , an origin of its solar water splitting activity was proposed. The work presented on both systems demonstrates the ability of core-level spectroscopies to provide insight into the chemical and electronic processes that occur in solar energy materials.

Bibliography

- [1] IEA, “Renewables 2021,” tech. rep., IEA, 2021.
- [2] IEA, “Solar PV 2021,” tech. rep., IEA, Sept 2021.
- [3] W. Cole, B. Frew, P. Gagnon, A. Reimers, J. Zuboy, and R. Margolis, “Envisioning a low-cost solar future: Exploring the potential impact of achieving the sunshot 2030 targets for photovoltaics,” *Energy*, vol. 155, pp. 690–704, 2018.
- [4] C. A. Hill, M. C. Such, D. Chen, J. Gonzalez, and W. M. Grady, “Battery energy storage for enabling integration of distributed solar power generation,” *IEEE Transactions on smart grid*, vol. 3, no. 2, pp. 850–857, 2012.
- [5] T. L. LeValley, A. R. Richard, and M. Fan, “The progress in water gas shift and steam reforming hydrogen production technologies—a review,” *International Journal of Hydrogen Energy*, vol. 39, no. 30, pp. 16983–17000, 2014.
- [6] N. Vlachopoulos, A. Hagfeldt, I. Benesperi, M. Freitag, G. Hashmi, G. Jia, R. A. Wahyuono, J. Plentz, and B. Dietzek, “New approaches in component design for dye-sensitized solar cells,” *Sustainable Energy & Fuels*, vol. 5, no. 2, pp. 367–383, 2021.

- [7] M. R. N. Thomas, V. J. K. Lourdusamy, A. A. Dhandayuthapani, and V. Jayakumar, “Non-metallic organic dyes as photosensitizers for dye-sensitized solar cells: a review,” *Environmental Science and Pollution Research*, pp. 1–15, 2021.
- [8] K. Sharma, V. Sharma, and S. Sharma, “Dye-sensitized solar cells: fundamentals and current status,” *Nanoscale research letters*, vol. 13, no. 1, pp. 1–46, 2018.
- [9] M. Freitag, J. Teuscher, Y. Saygili, X. Zhang, F. Giordano, P. Liska, J. Hua, S. M. Zakeeruddin, J.-E. Moser, M. Grätzel, *et al.*, “Dye-sensitized solar cells for efficient power generation under ambient lighting,” *Nature Photonics*, vol. 11, no. 6, pp. 372–378, 2017.
- [10] M. Kokkonen, P. Talebi, J. Zhou, S. Asgari, S. A. Soomro, F. Elsehrawy, J. Halme, S. Ahmad, A. Hagfeldt, and S. G. Hashmi, “Advanced research trends in dye-sensitized solar cells,” *Journal of Materials Chemistry A*, vol. 9, no. 17, pp. 10511–11082, 2021.
- [11] C. Wu, B. Chen, X. Zheng, and S. Priya, “Scaling of the flexible dye sensitized solar cell module,” *Solar Energy Materials and Solar Cells*, vol. 157, pp. 438–446, 2016.
- [12] Y. Ren, D. Sun, Y. Cao, H. N. Tsao, Y. Yuan, S. M. Zakeeruddin, P. Wang, and M. Grätzel, “A stable blue photosensitizer for color palette of dye-sensitized solar cells reaching 12.6% efficiency,” *Journal of the American Chemical Society*, vol. 140, no. 7, pp. 2405–2408, 2018.
- [13] H. J. Snaith, “Estimating the maximum attainable efficiency in dye-sensitized solar cells,” *Advanced Functional Materials*, vol. 20, no. 1, pp. 13–19, 2010.

- [14] S. Mathew, A. Yella, P. Gao, R. Humphry-Baker, B. F. Curchod, N. Ashari-Astani, I. Tavernelli, U. Rothlisberger, M. K. Nazeeruddin, and M. Grätzel, “Dye-sensitized solar cells with 13% efficiency achieved through the molecular engineering of porphyrin sensitizers,” *Nature chemistry*, vol. 6, no. 3, pp. 242–247, 2014.
- [15] K. Kakiage, Y. Aoyama, T. Yano, K. Oya, J.-i. Fujisawa, and M. Hanaya, “Highly-efficient dye-sensitized solar cells with collaborative sensitization by silyl-anchor and carboxy-anchor dyes,” *Chemical communications*, vol. 51, no. 88, pp. 15894–15897, 2015.
- [16] M. Green, E. Dunlop, J. Hohl-Ebinger, M. Yoshita, N. Kopidakis, and X. Hao, “Solar cell efficiency tables (version 57),” *Progress in photovoltaics: research and applications*, vol. 29, no. 1, pp. 3–15, 2021.
- [17] C.-C. Chiang, C.-Y. Hung, S.-W. Chou, J.-J. Shyue, K.-Y. Cheng, P.-J. Chang, Y.-Y. Yang, C.-Y. Lin, T.-K. Chang, Y. Chi, *et al.*, “PtCoFe nanowire cathodes boost short-circuit currents of Ru (II)-based dye-sensitized solar cells to a power conversion efficiency of 12.29%,” *Advanced Functional Materials*, vol. 28, no. 3, p. 1703282, 2018.
- [18] D. Chalkias, D. Loizos, and G. Papanicolaou, “Evaluation and prediction of dye-sensitized solar cells stability under different accelerated ageing conditions,” *Solar Energy*, vol. 207, pp. 841–850, 2020.
- [19] F. De Rossi, G. Mincuzzi, F. Di Giacomo, J. Fahlteich, S. Amberg-Schwab, K. Noller, and T. M. Brown, “A systematic investigation of permeation barriers for flexible dye-sensitized solar cells,” *Energy Technology*, vol. 4, no. 11, pp. 1455–1462, 2016.

- [20] H. S. Jung and J.-K. Lee, "Dye sensitized solar cells for economically viable photovoltaic systems," *The journal of physical chemistry letters*, vol. 4, no. 10, pp. 1682–1693, 2013.
- [21] B. O'regan and M. Grätzel, "A low-cost, high-efficiency solar cell based on dye-sensitized colloidal TiO₂ films," *nature*, vol. 353, no. 6346, pp. 737–740, 1991.
- [22] M. K. Nazeeruddin, E. Baranoff, and M. Grätzel, "Dye-sensitized solar cells: A brief overview," *Solar energy*, vol. 85, no. 6, pp. 1172–1178, 2011.
- [23] G. Boschloo, "Improving the performance of dye-sensitized solar cells," *Frontiers in chemistry*, vol. 7, p. 77, 2019.
- [24] M. Grätzel, "Dye-sensitized solar cells," *Journal of photochemistry and photobiology C: Photochemistry Reviews*, vol. 4, no. 2, pp. 145–153, 2003.
- [25] G. Boschloo and A. Hagfeldt, "Characteristics of the iodide/triiodide redox mediator in dye-sensitized solar cells," *Accounts of chemical research*, vol. 42, no. 11, pp. 1819–1826, 2009.
- [26] S. A. Haque, Y. Tachibana, R. L. Willis, J. E. Moser, M. Grätzel, D. R. Klug, and J. R. Durrant, "Parameters influencing charge recombination kinetics in dye-sensitized nanocrystalline titanium dioxide films," *The Journal of Physical Chemistry B*, vol. 104, no. 3, pp. 538–547, 2000.
- [27] S. A. Haque, E. Palomares, B. M. Cho, A. N. Green, N. Hirata, D. R. Klug, and J. R. Durrant, "Charge separation versus recombination in dye-sensitized nanocrystalline solar cells: the minimization of kinetic

- redundancy,” *Journal of the American Chemical Society*, vol. 127, no. 10, pp. 3456–3462, 2005.
- [28] P. Wang, S. M. Zakeeruddin, J. E. Moser, M. K. Nazeeruddin, T. Sekiguchi, and M. Grätzel, “A stable quasi-solid-state dye-sensitized solar cell with an amphiphilic ruthenium sensitizer and polymer gel electrolyte,” *Nature materials*, vol. 2, no. 6, pp. 402–407, 2003.
- [29] D.-W. Kim, Y.-B. Jeong, S.-H. Kim, D.-Y. Lee, and J.-S. Song, “Photovoltaic performance of dye-sensitized solar cell assembled with gel polymer electrolyte,” *Journal of Power Sources*, vol. 149, pp. 112–116, 2005.
- [30] M. I. Asghar, K. Miettunen, J. Halme, P. Vahermaa, M. Toivola, K. Aitola, and P. Lund, “Review of stability for advanced dye solar cells,” *Energy & Environmental Science*, vol. 3, no. 4, pp. 418–426, 2010.
- [31] M. K. Nazeeruddin, P. Liska, J. Moser, N. Vlachopoulos, and M. Grätzel, “Conversion of light into electricity with trinuclear ruthenium complexes adsorbed on textured TiO₂ films,” *Helvetica Chimica Acta*, vol. 73, no. 6, pp. 1788–1803, 1990.
- [32] M. K. Nazeeruddin, A. Kay, I. Rodicio, R. Humphry-Baker, E. Müller, P. Liska, N. Vlachopoulos, and M. Grätzel, “Conversion of light to electricity by cis-X₂bis (2, 2'-bipyridyl-4, 4'-dicarboxylate) ruthenium (II) charge-transfer sensitizers (x= Cl⁻, Br⁻, I⁻, CN⁻, and SCN⁻) on nanocrystalline titanium dioxide electrodes,” *Journal of the American Chemical Society*, vol. 115, no. 14, pp. 6382–6390, 1993.
- [33] M. K. Nazeeruddin, F. De Angelis, S. Fantacci, A. Selloni, G. Viscardi, P. Liska, S. Ito, B. Takeru, and M. Grätzel, “Combined experi-

- mental and DFT-TDDFT computational study of photoelectrochemical cell ruthenium sensitizers,” *Journal of the American Chemical Society*, vol. 127, no. 48, pp. 16835–16847, 2005.
- [34] L. Mauri, A. Colombo, C. Dragonetti, D. Roberto, and F. Fagnani, “Recent investigations on thiocyanate-free ruthenium (II) 2, 2'-bipyridyl complexes for dye-sensitized solar cells,” *Molecules*, vol. 26, no. 24, p. 7638, 2021.
- [35] C.-H. Siu, C.-L. Ho, J. He, T. Chen, P. Majumda, J. Zhao, H. Li, and W.-Y. Wong, “Optimizing the photovoltaic performance of thiocyanate-free ruthenium photosensitizers by structural modification of C^N cyclometalating ligand in dye-sensitized solar cells,” *Polyhedron*, vol. 82, pp. 71–79, 2014.
- [36] M. R. Elmorsy, R. Su, A. A. Fadda, H. Etman, E. H. Tawfik, and A. El-Shafei, “Effect of terthiophene spacer position in Ru (II) bipyridyl complexes on the photocurrent and photovoltage for high efficiency dye-sensitized solar cells,” *Dyes and Pigments*, vol. 156, pp. 348–356, 2018.
- [37] C.-P. Lee, C.-T. Li, and K.-C. Ho, “Use of organic materials in dye-sensitized solar cells,” *Materials today*, vol. 20, no. 5, pp. 267–283, 2017.
- [38] S. M. Feldt, G. Wang, G. Boschloo, and A. Hagfeldt, “Effects of driving forces for recombination and regeneration on the photovoltaic performance of dye-sensitized solar cells using cobalt polypyridine redox couples,” *The Journal of Physical Chemistry C*, vol. 115, no. 43, pp. 21500–21507, 2011.
- [39] M. Younas and K. Harrabi, “Performance enhancement of dye-sensitized solar cells via co-sensitization of ruthenium (II) based N749

- dye and organic sensitizer RK1,” *Solar Energy*, vol. 203, pp. 260–266, 2020.
- [40] S. Mozaffari, M. R. Nateghi, and M. B. Zarandi, “An overview of the challenges in the commercialization of dye sensitized solar cells,” *Renewable and Sustainable Energy Reviews*, vol. 71, pp. 675–686, 2017.
- [41] J. Jia, L. C. Seitz, J. D. Benck, Y. Huo, Y. Chen, J. W. D. Ng, T. Bilir, J. S. Harris, and T. F. Jaramillo, “Solar water splitting by photovoltaic-electrolysis with a solar-to-hydrogen efficiency over 30%,” *Nature communications*, vol. 7, no. 1, pp. 1–6, 2016.
- [42] B. A. Pinaud, J. D. Benck, L. C. Seitz, A. J. Forman, Z. Chen, T. G. Deutsch, B. D. James, K. N. Baum, G. N. Baum, S. Ardo, *et al.*, “Technical and economic feasibility of centralized facilities for solar hydrogen production via photocatalysis and photoelectrochemistry,” *Energy & Environmental Science*, vol. 6, no. 7, pp. 1983–2002, 2013.
- [43] R. Van de Krol and M. Grätzel, *Photoelectrochemical hydrogen production*, vol. 90, ch. 1, p. 9. Springer, 2012.
- [44] A. Fujishima and K. Honda, “Electrochemical photolysis of water at a semiconductor electrode,” *nature*, vol. 238, no. 5358, pp. 37–38, 1972.
- [45] B. H. Julian Keable, *Photoelectrochemical hydrogen production*, vol. 90, ch. 8, p. 283. Springer, 2012.
- [46] C. Jiang, S. J. Moniz, A. Wang, T. Zhang, and J. Tang, “Photoelectrochemical devices for solar water splitting—materials and challenges,” *Chemical Society Reviews*, vol. 46, no. 15, pp. 4645–4660, 2017.

- [47] M. F. Weber and M. J. Dignam, “Efficiency of splitting water with semiconducting photoelectrodes,” *Journal of The Electrochemical Society*, vol. 131, no. 6, p. 1258, 1984.
- [48] A. Murphy, P. Barnes, L. Randeniya, I. Plumb, I. Grey, M. Horne, and J. Glasscock, “Efficiency of solar water splitting using semiconductor electrodes,” *International journal of hydrogen energy*, vol. 31, no. 14, pp. 1999–2017, 2006.
- [49] N. M. Gupta, “Factors affecting the efficiency of a water splitting photocatalyst: a perspective,” *Renewable and Sustainable Energy Reviews*, vol. 71, pp. 585–601, 2017.
- [50] K. Afroz, M. Moniruddin, N. Bakranov, S. Kudaibergenov, and N. Nuraje, “A heterojunction strategy to improve the visible light sensitive water splitting performance of photocatalytic materials,” *Journal of Materials Chemistry A*, vol. 6, no. 44, pp. 21696–21718, 2018.
- [51] O. Khaselev and J. A. Turner, “A monolithic photovoltaic-photoelectrochemical device for hydrogen production via water splitting,” *Science*, vol. 280, no. 5362, pp. 425–427, 1998.
- [52] D. Sabba, M. H. Kumar, L. H. Wong, J. Barber, M. Grätzel, and N. Mathews, “Perovskite–hematite tandem cells for efficient overall solar driven water splitting,” *Nano letters*, vol. 15, no. 6, pp. 3833–3839, 2015.
- [53] L. Pan, J. H. Kim, M. T. Mayer, M.-K. Son, A. Ummadisingu, J. S. Lee, A. Hagfeldt, J. Luo, and M. Grätzel, “Boosting the performance of Cu_2O photocathodes for unassisted solar water splitting devices,” *Nature Catalysis*, vol. 1, no. 6, pp. 412–420, 2018.

- [54] Z. Tian, P. Zhang, P. Qin, D. Sun, S. Zhang, X. Guo, W. Zhao, D. Zhao, and F. Huang, “Novel black $\text{BiVO}_4/\text{TiO}_{2-x}$ photoanode with enhanced photon absorption and charge separation for efficient and stable solar water splitting,” *Advanced Energy Materials*, vol. 9, no. 27, p. 1901287, 2019.
- [55] J. Qiu, G. Zeng, P. Pavaskar, Z. Li, and S. B. Cronin, “Plasmon-enhanced water splitting on TiO_2 -passivated GaP photocatalysts,” *Physical Chemistry Chemical Physics*, vol. 16, no. 7, pp. 3115–3121, 2014.
- [56] M. M. Momeni and Y. Ghayeb, “Fabrication, characterization and photoelectrochemical behavior of Fe– TiO_2 nanotubes composite photoanodes for solar water splitting,” *Journal of Electroanalytical Chemistry*, vol. 751, pp. 43–48, 2015.
- [57] Y. Lin, Z. Jiang, C. Zhu, R. Zhang, X. Hu, X. Zhang, H. Zhu, and S. H. Lin, “The electronic structure, optical absorption and photocatalytic water splitting of (Fe + Ni)-codoped TiO_2 : A DFT + U study,” *International Journal of Hydrogen Energy*, vol. 42, no. 8, pp. 4966–4976, 2017.
- [58] D. Hu, P. Diao, D. Xu, and Q. Wu, “Gold/ WO_3 nanocomposite photoanodes for plasmonic solar water splitting,” *Nano Research*, vol. 9, no. 6, pp. 1735–1751, 2016.
- [59] F. E. Osterloh, “Inorganic nanostructures for photoelectrochemical and photocatalytic water splitting,” *Chemical Society Reviews*, vol. 42, no. 6, pp. 2294–2320, 2013.
- [60] C. Dette, M. A. Pérez-Osorio, C. S. Kley, P. Punke, C. E. Patrick, P. Jacobson, F. Giustino, S. J. Jung, and K. Kern, “ TiO_2 anatase

- with a bandgap in the visible region,” *Nano letters*, vol. 14, no. 11, pp. 6533–6538, 2014.
- [61] J. H. Park, S. Kim, and A. J. Bard, “Novel carbon-doped TiO₂ nanotube arrays with high aspect ratios for efficient solar water splitting,” *Nano letters*, vol. 6, no. 1, pp. 24–28, 2006.
- [62] D. E. Starr, M. Favaro, F. F. Abdi, H. Bluhm, E. J. Crumlin, and R. van de Krol, “Combined soft and hard X-ray ambient pressure photoelectron spectroscopy studies of semiconductor/electrolyte interfaces,” *Journal of Electron Spectroscopy and Related Phenomena*, vol. 221, pp. 106–115, 2017.
- [63] G. Ketteler, S. Yamamoto, H. Bluhm, K. Andersson, D. E. Starr, D. F. Ogletree, H. Ogasawara, A. Nilsson, and M. Salmeron, “The nature of water nucleation sites on TiO₂(110) surfaces revealed by ambient pressure X-ray photoelectron spectroscopy,” *The Journal of Physical Chemistry C*, vol. 111, no. 23, pp. 8278–8282, 2007.
- [64] M. J. Jackman, A. G. Thomas, and C. Muryn, “Photoelectron spectroscopy study of stoichiometric and reduced anatase TiO₂(101) surfaces: the effect of subsurface defects on water adsorption at near-ambient pressures,” *The Journal of Physical Chemistry C*, vol. 119, no. 24, pp. 13682–13690, 2015.
- [65] M. H. M. Ahmed, R. H. Temperton, and J. N. O’Shea, “An in situ exploration of subsurface defect migration to a liquid water-exposed rutile TiO₂(110) surface by XPS,” *Surface and Interface Analysis*, vol. 53, no. 11, pp. 1013–1019, 2021.
- [66] R. Berera, R. van Grondelle, and J. Kennis, “Ultrafast transient absorption spectroscopy: principles and application to photosynthetic systems,” *Photosynthesis research*, vol. 101, no. 2, pp. 105–118, 2009.

- [67] B. Pashaei and H. Shahroosvand, "Molecularly engineered ruthenium polypyridyl complexes for using in dye-sensitized solar cell," *Inorganic Chemistry Communications*, vol. 112, p. 107737, 2020.
- [68] M. Planells, L. Pelleja, J. N. Clifford, M. Pastore, F. De Angelis, N. López, S. R. Marder, and E. Palomares, "Energy levels, charge injection, charge recombination and dye regeneration dynamics for donor-acceptor π -conjugated organic dyes in mesoscopic TiO₂ sensitized solar cells," *Energy & Environmental Science*, vol. 4, no. 5, pp. 1820–1829, 2011.
- [69] G. Benkő, J. Kallioinen, J. E. Korppi-Tommola, A. P. Yartsev, and V. Sundström, "Photoinduced ultrafast dye-to-semiconductor electron injection from nonthermalized and thermalized donor states," *Journal of the American Chemical Society*, vol. 124, no. 3, pp. 489–493, 2002.
- [70] W. Wurth and D. Menzel, "Ultrafast electron dynamics at surfaces probed by resonant auger spectroscopy," *Chemical Physics*, vol. 251, no. 1-3, pp. 141–149, 2000.
- [71] L. C. Mayor, J. Ben Taylor, G. Magnano, A. Rienzo, C. J. Satterley, J. N. O'Shea, and J. Schnadt, "Photoemission, resonant photoemission, and X-ray absorption of a Ru (II) complex adsorbed on rutile TiO₂(110) prepared by in situ electrospray deposition," *The Journal of chemical physics*, vol. 129, no. 11, p. 114701, 2008.
- [72] A. J. Gibson, R. H. Temperton, K. Handrup, M. Weston, L. C. Mayor, and J. N. O'Shea, "Charge transfer from an adsorbed ruthenium-based photosensitizer through an ultra-thin aluminium oxide layer and into a metallic substrate," *The Journal of chemical physics*, vol. 140, no. 23, p. 234708, 2014.

- [73] M. Weston, K. Handrup, T. J. Reade, N. R. Champness, and J. N. O'Shea, "Experimental observation of sub-femtosecond charge transfer in a model water splitting dye-sensitized solar cell," *The Journal of chemical physics*, vol. 137, no. 22, p. 224706, 2012.
- [74] M. Hahlin, M. Odelius, M. Magnuson, E. M. Johansson, S. Plogmaker, D. P. Hagberg, L. Sun, H. Siegbahn, and H. Rensmo, "Mapping the frontier electronic structures of triphenylamine based organic dyes at TiO₂ interfaces," *Physical Chemistry Chemical Physics*, vol. 13, no. 8, pp. 3534–3546, 2011.
- [75] J. W. John F. Watts, *An Introduction to Surface Analysis by XPS and AES*, ch. 2, pp. 41–47. Wiley, 2019.
- [76] M. Repoux, "Comparison of background removal methods for XPS," *Surface and interface analysis*, vol. 18, no. 7, pp. 567–570, 1992.
- [77] S. Tougaard, W. Braun, E. Holub-Krappe, and H. Saalfeld, "Test of algorithm for background correction in XPS under variation of XPS peak energy," *Surface and interface analysis*, vol. 13, no. 4, pp. 225–227, 1988.
- [78] S. Tougaard, "Practical guide to the use of backgrounds in quantitative XPS," *Journal of Vacuum Science & Technology A: Vacuum, Surfaces, and Films*, vol. 39, no. 1, p. 011201, 2021.
- [79] A. Herrera-Gomez, M. Bravo-Sanchez, F. Aguirre-Tostado, and M. Vazquez-Lepe, "The slope-background for the near-peak regimen of photoemission spectra," *Journal of Electron Spectroscopy and Related Phenomena*, vol. 189, pp. 76–80, 2013.
- [80] G. H. Major, N. Fairley, P. M. Sherwood, M. R. Linford, J. Terry, V. Fernandez, and K. Artyushkova, "Practical guide for curve fitting

- in X-ray photoelectron spectroscopy,” *Journal of Vacuum Science & Technology A: Vacuum, Surfaces, and Films*, vol. 38, no. 6, p. 061203, 2020.
- [81] J. M. Kahk, I. J. Villar-Garcia, L. Grechy, P. J. Bruce, P. E. Vincent, S. K. Eriksson, H. Rensmo, M. Hahlin, J. Åhlund, M. O. Edwards, *et al.*, “A study of the pressure profiles near the first pumping aperture in a high pressure photoelectron spectrometer,” *Journal of Electron Spectroscopy and Related Phenomena*, vol. 205, pp. 57–65, 2015.
- [82] K. A. Stoerzinger, W. T. Hong, E. J. Crumlin, H. Bluhm, and Y. Shao-Horn, “Insights into electrochemical reactions from ambient pressure photoelectron spectroscopy,” *Accounts of Chemical Research*, vol. 48, no. 11, pp. 2976–2983, 2015.
- [83] J. Schnadt, J. O’Shea, L. Patthey, J. Krempaský, N. Mårtensson, and P. Brühwiler, “Alignment of valence photoemission, X-ray absorption, and substrate density of states for an adsorbate on a semiconductor surface,” *Physical Review B*, vol. 67, no. 23, p. 235420, 2003.
- [84] G. S. Brown, M. H. Chen, B. Crasemann, and G. E. Ice, “Observation of the auger resonant raman effect,” *Physical Review Letters*, vol. 45, no. 24, p. 1937, 1980.
- [85] E. Kukk, S. Aksela, and H. Aksela, “Features of the auger resonant raman effect in experimental spectra,” *Physical Review A*, vol. 53, no. 5, p. 3271, 1996.
- [86] F. Gel’mukhanov and H. Ågren, “Resonant X-ray raman scattering,” *Physics Reports*, vol. 312, no. 3-6, pp. 87–330, 1999.

- [87] M. Piancastelli, “Auger resonant raman studies of atoms and molecules,” *Journal of Electron Spectroscopy and Related Phenomena*, vol. 107, no. 1, pp. 1–26, 2000.
- [88] P. Brühwiler, O. Karis, and N. Mårtensson, “Charge-transfer dynamics studied using resonant core spectroscopies,” *Reviews of Modern Physics*, vol. 74, no. 3, p. 703, 2002.
- [89] K. Wille, “Synchrotron radiation sources,” *Reports on Progress in Physics*, vol. 54, no. 8, p. 1005, 1991.
- [90] H. A. Padmore, “Optimization of soft X-ray monochromators,” *Review of Scientific Instruments*, vol. 60, no. 7, pp. 1608–1615, 1989.
- [91] K. Burke and L. O. Wagner, “DFT in a nutshell,” *International Journal of Quantum Chemistry*, vol. 113, no. 2, pp. 96–101, 2013.
- [92] K. Hara, T. Sato, R. Katoh, A. Furube, Y. Ohga, A. Shinpo, S. Suga, K. Sayama, H. Sugihara, and H. Arakawa, “Molecular design of coumarin dyes for efficient dye-sensitized solar cells,” *The Journal of Physical Chemistry B*, vol. 107, no. 2, pp. 597–606, 2003.
- [93] K. Hara, K. Sayama, Y. Ohga, A. Shinpo, S. Suga, and H. Arakawa, “A coumarin-derivative dye sensitized nanocrystalline TiO₂ solar cell having a high solar-energy conversion efficiency up to 5.6%,” *Chemical Communications*, no. 6, pp. 569–570, 2001.
- [94] Z.-S. Wang, Y. Cui, Y. Dan-oh, C. Kasada, A. Shinpo, and K. Hara, “Thiophene-functionalized coumarin dye for efficient dye-sensitized solar cells: electron lifetime improved by coadsorption of deoxycholic acid,” *The Journal of Physical Chemistry C*, vol. 111, no. 19, pp. 7224–7230, 2007.

- [95] H. N. Ghosh, J. B. Asbury, and T. Lian, "Direct observation of ultrafast electron injection from coumarin 343 to TiO₂ nanoparticles by femtosecond infrared spectroscopy," *The Journal of Physical Chemistry B*, vol. 102, no. 34, pp. 6482–6486, 1998.
- [96] J. M. Rehm, G. L. McLendon, Y. Nagasawa, K. Yoshihara, J. Moser, and M. Grätzel, "Femtosecond electron-transfer dynamics at a sensitizing dye-semiconductor (TiO₂) interface," *The Journal of Physical Chemistry*, vol. 100, no. 23, pp. 9577–9578, 1996.
- [97] J. Schnadt, P. A. Brühwiler, L. Patthey, J. N. O'shea, S. Södergren, M. Odellius, R. Ahuja, O. Karis, M. Bäessler, P. Persson, *et al.*, "Experimental evidence for sub-3-fs charge transfer from an aromatic adsorbate to a semiconductor," *Nature*, vol. 418, no. 6898, pp. 620–623, 2002.
- [98] J. Schnadt, J. O'shea, L. Patthey, L. Kjeldgaard, J. Åhlund, K. Nilsson, J. Schiessling, J. Krempaský, M. Shi, O. Karis, *et al.*, "Excited-state charge transfer dynamics in systems of aromatic adsorbates on TiO₂ studied with resonant core techniques," *The Journal of chemical physics*, vol. 119, no. 23, pp. 12462–12472, 2003.
- [99] M. Weston, A. J. Britton, and J. N. O'Shea, "Charge transfer dynamics of model charge transfer centers of a multicolor water splitting dye complex on rutile TiO₂(110)," *The Journal of chemical physics*, vol. 134, no. 5, p. 054705, 2011.
- [100] L. Cao, Y.-Z. Wang, T.-X. Chen, W.-H. Zhang, X.-J. Yu, K. Ibrahim, J.-O. Wang, H.-J. Qian, F.-Q. Xu, D.-C. Qi, *et al.*, "Charge transfer dynamics of 3,4,9,10-perylene-tetracarboxylic-dianhydride molecules on Au (111) probed by resonant photoemission spectroscopy," *The Journal of chemical physics*, vol. 135, no. 17, p. 174701, 2011.

- [101] L. Cao, Y.-Z. Wang, J.-Q. Zhong, Y.-Y. Han, W.-H. Zhang, X.-J. Yu, F.-Q. Xu, D.-C. Qi, and A. T. Wee, “Molecular orientation and site dependent charge transfer dynamics at PTCDA/TiO₂(110) interface revealed by resonant photoemission spectroscopy,” *The Journal of Physical Chemistry C*, vol. 118, no. 8, pp. 4160–4166, 2014.
- [102] M. Hahlin, E. M. Johansson, S. Plogmaker, M. Odellius, D. P. Hagberg, L. Sun, H. Siegbahn, and H. Rensmo, “Electronic and molecular structures of organic dye/TiO₂ interfaces for solar cell applications: a core level photoelectron spectroscopy study,” *Physical Chemistry Chemical Physics*, vol. 12, no. 7, pp. 1507–1517, 2010.
- [103] R. H. Temperton, J. Hart, N. Verykokkos, E. Gibson, and J. N. O’Shea, “A soft X-ray probe of a titania photoelectrode sensitized with a triphenylamine dye,” *The Journal of Chemical Physics*, vol. 154, no. 23, p. 234707, 2021.
- [104] C. Castellarin-Cudia, T. Caruso, E. Maccallini, A. Li Bassi, P. Carozzo, O. De Luca, A. Goldoni, V. Lyamayev, K. C. Prince, F. Bondino, *et al.*, “Chemical bonds and charge-transfer dynamics of a dye–hierarchical-TiO₂ hybrid interface,” *The Journal of Physical Chemistry C*, vol. 119, no. 16, pp. 8671–8680, 2015.
- [105] C. Nicolas and C. Miron, “Lifetime broadening of core-excited and-ionized states,” *Journal of Electron Spectroscopy and Related Phenomena*, vol. 185, no. 8-9, pp. 267–272, 2012.
- [106] J. Schnadt, J. O’Shea, L. Patthey, J. Schiessling, y. J. Krempaský, M. Shi, N. Mårtensson, and P. Brühwiler, “Structural study of adsorption of isonicotinic acid and related molecules on rutile TiO₂(110) ii: Xps,” *Surface science*, vol. 544, no. 1, pp. 74–86, 2003.

- [107] N. Domingo, E. Pach, K. Cordero-Edwards, V. Pérez-Dieste, C. Escudero, and A. Verdaguer, “Water adsorption, dissociation and oxidation on SrTiO₃ and ferroelectric surfaces revealed by ambient pressure X-ray photoelectron spectroscopy,” *Physical Chemistry Chemical Physics*, vol. 21, no. 9, pp. 4920–4930, 2019.
- [108] J. N. O’Shea, J. B. Taylor, and E. F. Smith, “X-ray photoelectron spectroscopy of fluorescein adsorbed on model solar-cell surfaces,” *Surface science*, vol. 548, no. 1-3, pp. 317–323, 2004.
- [109] M. Weston, T. J. Reade, A. J. Britton, K. Handrup, N. R. Champness, and J. N. O’Shea, “A single centre water splitting dye complex adsorbed on rutile TiO₂(110): Photoemission, X-ray absorption, and optical spectroscopy,” *The Journal of chemical physics*, vol. 135, no. 11, p. 114703, 2011.
- [110] A. Rienzo, L. C. Mayor, G. Magnano, C. J. Satterley, E. Ataman, J. Schnadt, K. Schulte, and J. N. O’Shea, “X-ray absorption and photoemission spectroscopy of zinc protoporphyrin adsorbed on rutile TiO₂(110) prepared by in situ electrospray deposition,” *The Journal of chemical physics*, vol. 132, no. 8, p. 084703, 2010.
- [111] R. H. Temperton, A. Gibson, and J. N. O’Shea, “In situ XPS analysis of the atomic layer deposition of aluminium oxide on titanium dioxide,” *Physical Chemistry Chemical Physics*, vol. 21, no. 3, pp. 1393–1398, 2019.
- [112] Y. Shao, Z. Gan, E. Epifanovsky, A. T. Gilbert, M. Wormit, J. Kussmann, A. W. Lange, A. Behn, J. Deng, X. Feng, D. Ghosh, M. Goldey, P. R. Horn, L. D. Jacobson, I. Kaliman, R. Z. Khaliullin, T. Kuš, A. Landau, J. Liu, E. I. Proynov, Y. M. Rhee, R. M. Richard, M. A.

Rohrdanz, R. P. Steele, E. J. Sundstrom, H. L. W. III, P. M. Zimmerman, D. Zuev, B. Albrecht, E. Alguire, B. Austin, G. J. O. Beran, Y. A. Bernard, E. Berquist, K. Brandhorst, K. B. Bravaya, S. T. Brown, D. Casanova, C.-M. Chang, Y. Chen, S. H. Chien, K. D. Closser, D. L. Crittenden, M. Diedenhofen, R. A. D. Jr., H. Do, A. D. Dutoi, R. G. Edgar, S. Fatehi, L. Fusti-Molnar, A. Ghysels, A. Golubeva-Zadorozhnaya, J. Gomes, M. W. Hanson-Heine, P. H. Harbach, A. W. Hauser, E. G. Hohenstein, Z. C. Holden, T.-C. Jagau, H. Ji, B. Kaduk, K. Khistyayev, J. Kim, J. Kim, R. A. King, P. Klunzinger, D. Kosenkov, T. Kowalczyk, C. M. Krauter, K. U. Lao, A. D. Laurent, K. V. Lawler, S. V. Levchenko, C. Y. Lin, F. Liu, E. Livshits, R. C. Lochan, A. Luenser, P. Manohar, S. F. Manzer, S.-P. Mao, N. Mardirossian, A. V. Marenich, S. A. Maurer, N. J. Mayhall, E. Neuscamman, C. M. Oana, R. Olivares-Amaya, D. P. O'Neill, J. A. Parkhill, T. M. Perrine, R. Peverati, A. Prociuk, D. R. Rehn, E. Rosta, N. J. Russ, S. M. Sharada, S. Sharma, D. W. Small, A. Sodt, T. Stein, D. Stück, Y.-C. Su, A. J. Thom, T. Tsuchimochi, V. Vanovschi, L. Vogt, O. Vydrov, T. Wang, M. A. Watson, J. Wenzel, A. White, C. F. Williams, J. Yang, S. Yeganeh, S. R. Yost, Z.-Q. You, I. Y. Zhang, X. Zhang, Y. Zhao, B. R. Brooks, G. K. Chan, D. M. Chipman, C. J. Cramer, W. A. G. III, M. S. Gordon, W. J. Hehre, A. Klamt, H. F. S. III, M. W. Schmidt, C. D. Sherill, D. G. Truhlar, A. Warshel, X. Xu, A. Aspuru-Guzik, R. Baer, A. T. Bell, N. A. Besley, J.-D. Chai, A. Dreuw, B. D. Dunietz, T. R. Furlani, S. R. Gwaltney, C.-P. Hsu, Y. Jung, J. Kong, D. S. Lambrecht, W. Liang, C. Ochsenfeld, V. A. Rassolov, L. V. Slipchenko, J. E. Subotnik, T. V. Voorhis, J. M. Herbert, A. I. Krylov, P. M. Gill, and M. Head-Gordon, "Advances in molecular quantum chemistry contained in the q-chem 4 program package," *Molecular Physics*,

vol. 113, no. 2, pp. 184–215, 2015.

- [113] P. J. Stephens, F. J. Devlin, C. F. Chabalowski, and M. J. Frisch, “Ab initio calculation of vibrational absorption and circular dichroism spectra using density functional force fields,” *The Journal of physical chemistry*, vol. 98, no. 45, pp. 11623–11627, 1994.
- [114] R. Krishnan, J. S. Binkley, R. Seeger, and J. A. Pople, “Self-consistent molecular orbital methods. XX. a basis set for correlated wave functions,” *J. Chem. Phys.*, vol. 72, pp. 650–654, 1980.
- [115] B. P. Pritchard, D. Altarawy, B. Didier, T. D. Gibson, and T. L. Windus, “New basis set exchange: An open, up-to-date resource for the molecular sciences community,” *Journal of chemical information and modeling*, vol. 59, no. 11, pp. 4814–4820, 2019.
- [116] IQmol. Available at: <http://iqmol.org>.
- [117] N. A. Besley, M. J. Peach, and D. J. Tozer, “Time-dependent density functional theory calculations of near-edge X-ray absorption fine structure with short-range corrected functionals,” *Physical Chemistry Chemical Physics*, vol. 11, no. 44, pp. 10350–10358, 2009.
- [118] E. M. Johansson, M. Hedlund, H. Siegbahn, and H. Rensmo, “Electronic and molecular surface structure of Ru(tcterpy)(NCS)₃ and Ru(dcbpy)₂(NCS)₂ adsorbed from solution onto nanostructured TiO₂: a photoelectron spectroscopy study,” *The Journal of Physical Chemistry B*, vol. 109, no. 47, pp. 22256–22263, 2005.
- [119] M. Kudo, T. Hikita, T. Hanada, R. Sekine, and M. Kawai, “Surface reactions at the controlled structure of SrTiO₃(001),” *Surface and interface analysis*, vol. 22, no. 1-12, pp. 412–416, 1994.

- [120] H. Shin, T.-H. Byun, S. Lee, S.-T. Bae, and H. S. Jung, “Surface hydroxylation of TiO₂ yields notable visible-light photocatalytic activity to decompose rhodamine B in aqueous solution,” *Journal of Physics and Chemistry of Solids*, vol. 74, no. 8, pp. 1136–1142, 2013.
- [121] A. Subramanian and H.-W. Wang, “Effect of hydroxyl group attachment on TiO₂ films for dye-sensitized solar cells,” *Applied surface science*, vol. 258, no. 20, pp. 7833–7838, 2012.
- [122] K. E. Lee, M. A. Gomez, C. Charbonneau, and G. P. Demopoulos, “Enhanced surface hydroxylation of nanocrystalline anatase films improves photocurrent output and electron lifetime in dye sensitized solar cell photoanodes,” *Electrochimica acta*, vol. 67, pp. 208–215, 2012.
- [123] R. Sánchez-de Armas, M. Á. San Miguel, J. Oviedo, and J. F. Sanz, “Coumarin derivatives for dye sensitized solar cells: a TD-DFT study,” *Physical Chemistry Chemical Physics*, vol. 14, no. 1, pp. 225–233, 2012.
- [124] Z.-S. Wang, K. Hara, Y. Dan-oh, C. Kasada, A. Shinpo, S. Suga, H. Arakawa, and H. Sugihara, “Photophysical and (photo) electrochemical properties of a coumarin dye,” *The Journal of Physical Chemistry B*, vol. 109, no. 9, pp. 3907–3914, 2005.
- [125] A. Fattori, L. M. Peter, S. R. Belding, R. G. Compton, and F. Marken, “Cis-bis(isothiocyanato)-bis(2, 2'-bipyridyl-4, 4'dicarboxylato)-Ru(II)(N719) dark-reactivity when bound to fluorine-doped tin oxide (FTO) or titanium dioxide (TiO₂) surfaces,” *Journal of Electroanalytical Chemistry*, vol. 640, no. 1-2, pp. 61–67, 2010.

- [126] A. Schöll, Y. Zou, M. Jung, T. Schmidt, R. Fink, and E. Umbach, “Line shapes and satellites in high-resolution X-ray photoelectron spectra of large π -conjugated organic molecules,” *The Journal of chemical physics*, vol. 121, no. 20, pp. 10260–10267, 2004.
- [127] R. R. Frontiera, J. Dasgupta, and R. A. Mathies, “Probing interfacial electron transfer in coumarin 343 sensitized TiO₂ nanoparticles with femtosecond stimulated Raman,” *Journal of the American Chemical Society*, vol. 131, no. 43, pp. 15630–15632, 2009.
- [128] T. Alammar, V. Smetana, H. Pei, I. Hamm, M. Wark, and A.-V. Mudring, “The power of ionic liquids: Crystal facet engineering of SrTiO₃ nanoparticles for tailored photocatalytic applications,” *Advanced Sustainable Systems*, vol. 5, no. 2, p. 2000180, 2021.
- [129] S. Burnside, J.-E. Moser, K. Brooks, M. Grätzel, and D. Cahen, “Nanocrystalline mesoporous strontium titanate as photoelectrode material for photosensitized solar devices: increasing photovoltage through flatband potential engineering,” *The Journal of Physical Chemistry B*, vol. 103, no. 43, pp. 9328–9332, 1999.
- [130] E. Farfan-Arribas and R. J. Madix, “Characterization of the acid-base properties of the TiO₂(110) surface by adsorption of amines,” *The Journal of Physical Chemistry B*, vol. 107, no. 14, pp. 3225–3233, 2003.
- [131] M. U. Munshi, G. Berden, J. Martens, and J. Oomens, “Gas-phase vibrational spectroscopy of triphenylamine: the effect of charge on structure and spectra,” *Physical Chemistry Chemical Physics*, vol. 19, no. 30, pp. 19881–19889, 2017.
- [132] S. A. Chambers, T. Droubay, T. C. Kaspar, M. Gutowski, and M. Van Schilfgaarde, “Accurate valence band maximum determina-

- tion for SrTiO₃(001),” *Surface science*, vol. 554, no. 2-3, pp. 81–89, 2004.
- [133] K. Van Benthem, C. Elsässer, and R. French, “Bulk electronic structure of SrTiO₃: Experiment and theory,” *Journal of applied physics*, vol. 90, no. 12, pp. 6156–6164, 2001.
- [134] O. Diwald, T. L. Thompson, T. Zubkov, E. G. Goralski, S. D. Walck, and J. T. Yates, “Photochemical activity of nitrogen-doped rutile TiO₂(110) in visible light,” *The journal of physical chemistry B*, vol. 108, no. 19, pp. 6004–6008, 2004.
- [135] A. Listorti, B. O’regan, and J. R. Durrant, “Electron transfer dynamics in dye-sensitized solar cells,” *Chemistry of Materials*, vol. 23, no. 15, pp. 3381–3399, 2011.
- [136] P. Kao, S. Neppl, P. Feulner, D. L. Allara, and M. Zharnikov, “Charge transfer time in alkanethiolate self-assembled monolayers via resonant auger electron spectroscopy,” *The Journal of Physical Chemistry C*, vol. 114, no. 32, pp. 13766–13773, 2010.
- [137] F. Johansson, M. Ivanovic, S. Svanström, U. B. Cappel, H. Peisert, T. Chassé, and A. Lindblad, “Femtosecond and attosecond electron-transfer dynamics in PCPDTBT:PCBM bulk heterojunctions,” *The Journal of Physical Chemistry C*, vol. 122, no. 24, pp. 12605–12614, 2018.
- [138] M. Schmid, H.-P. Steinrück, and J. M. Gottfried, “A new asymmetric pseudo-voigt function for more efficient fitting of XPS lines,” *Surface and Interface Analysis*, vol. 46, no. 8, pp. 505–511, 2014.
- [139] J. Campbell and T. Papp, “Widths of the atomic K–N7 levels,” *Atomic Data and Nuclear Data Tables*, vol. 77, no. 1, pp. 1–56, 2001.

- [140] D. S. Jensen, S. S. Kanyal, N. Madaan, M. A. Vail, A. E. Dadson, M. H. Engelhard, and M. R. Linford, “Silicon (100)/SiO₂ by XPS,” *Surface Science Spectra*, vol. 20, no. 1, pp. 36–42, 2013.
- [141] L. Patthey, H. Rensmo, P. Persson, K. Westermark, L. Vayssieres, A. Stashans, Å. Petersson, P. Brühwiler, H. Siegbahn, S. Lunell, *et al.*, “Adsorption of bi-isonicotinic acid on rutile TiO₂(110),” *The Journal of chemical physics*, vol. 110, no. 12, pp. 5913–5918, 1999.
- [142] S. Chaveanghong, T. Nakamura, Y. Takagi, B. Cagnon, T. Uruga, M. Tada, Y. Iwasawa, and T. Yokoyama, “Sulfur poisoning of Pt and PtCo anode and cathode catalysts in polymer electrolyte fuel cells studied by operando near ambient pressure hard X-ray photoelectron spectroscopy,” *Physical Chemistry Chemical Physics*, vol. 23, no. 6, pp. 3866–3873, 2021.
- [143] D. J. Morgan, “Resolving ruthenium: XPS studies of common ruthenium materials,” *Surface and Interface Analysis*, vol. 47, no. 11, pp. 1072–1079, 2015.
- [144] A. A. Shamsaldeen, L. Kloo, Y. Yin, C. Gibson, S. G. Adhikari, and G. G. Andersson, “Influence of TiO₂ surface defects on the adsorption of N719 dye molecules,” *Physical Chemistry Chemical Physics*, vol. 23, no. 38, pp. 22160–22173, 2021.
- [145] E. M. Johansson, T. Edvinsson, M. Odelius, D. P. Hagberg, L. Sun, A. Hagfeldt, H. Siegbahn, and H. Rensmo, “Electronic and molecular surface structure of a polyene-diphenylaniline dye adsorbed from solution onto nanoporous TiO₂,” *The Journal of Physical Chemistry C*, vol. 111, no. 24, pp. 8580–8586, 2007.
- [146] J. B. Martins, C. E. de Moura, G. Goldsztejn, O. Travnikova, R. Guillemin, I. Ismail, L. Journal, D. Kouliantianos, M. Barbatti,

- A. F. Lago, *et al.*, “Electron delocalisation in conjugated sulfur heterocycles probed by resonant auger spectroscopy,” *Physical Chemistry Chemical Physics*, vol. 24, no. 14, pp. 8477–8487, 2022.
- [147] R. Guillemin, S. Sheinerman, R. Püttner, T. Marchenko, G. Goldsztejn, L. Journel, R. Kushawaha, D. Céolin, M. N. Piancastelli, and M. Simon, “Postcollision interaction effects in KLL auger spectra following argon 1s photoionization,” *Physical Review A*, vol. 92, no. 1, p. 012503, 2015.
- [148] F. Gel’mukhanov and H. Ågren, “Stokes doubling in auger spectra,” *Physics Letters A*, vol. 193, no. 4, pp. 375–379, 1994.
- [149] R. Feifel, A. Baev, F. Gel’mukhanov, H. Ågren, M. Andersson, G. Öhrwall, M.-N. Piancastelli, C. Miron, S. Sorensen, A. N. de Brito, *et al.*, “Role of stray light in the formation of high-resolution resonant photoelectron spectra: an experimental and theoretical study of N₂,” *Journal of electron spectroscopy and related phenomena*, vol. 134, no. 1, pp. 49–65, 2004.
- [150] J. E. Monat, J. H. Rodriguez, and J. K. McCusker, “Ground-and excited-state electronic structures of the solar cell sensitizer bis (4, 4’-dicarboxylato-2, 2’-bipyridine) bis (isothiocyanato) ruthenium (II),” *The Journal of Physical Chemistry A*, vol. 106, no. 32, pp. 7399–7406, 2002.
- [151] J. Yang, P. Ganesan, J. Teuscher, T. Moehl, Y. J. Kim, C. Yi, P. Comte, K. Pei, T. W. Holcombe, M. K. Nazeeruddin, *et al.*, “Influence of the donor size in D- π -A organic dyes for dye-sensitized solar cells,” *Journal of the American Chemical Society*, vol. 136, no. 15, pp. 5722–5730, 2014.

- [152] K. Hanson, M. K. Brennaman, H. Luo, C. R. Glasson, J. J. Concepcion, W. Song, and T. J. Meyer, “Photostability of phosphonate-derivatized, Ru^{II} polypyridyl complexes on metal oxide surfaces,” *ACS applied materials & interfaces*, vol. 4, no. 3, pp. 1462–1469, 2012.
- [153] F. Ambrosio, N. Martsinovich, and A. Troisi, “What is the best anchoring group for a dye in a dye-sensitized solar cell?,” *The journal of physical chemistry letters*, vol. 3, no. 11, pp. 1531–1535, 2012.
- [154] F. Ambrosio, N. Martsinovich, and A. Troisi, “Effect of the anchoring group on electron injection: theoretical study of phosphonated dyes for dye-sensitized solar cells,” *The Journal of Physical Chemistry C*, vol. 116, no. 3, pp. 2622–2629, 2012.
- [155] R. Ernstorfer, L. Gundlach, S. Felber, W. Storck, R. Eichberger, and F. Willig, “Role of molecular anchor groups in molecule-to-semiconductor electron transfer,” *The Journal of Physical Chemistry B*, vol. 110, no. 50, pp. 25383–25391, 2006.
- [156] C. F. Negre, R. L. Milot, L. A. Martini, W. Ding, R. H. Crabtree, C. A. Schmuttenmaer, and V. S. Batista, “Efficiency of interfacial electron transfer from Zn-porphyrin dyes into TiO₂ correlated to the linker single molecule conductance,” *The Journal of Physical Chemistry C*, vol. 117, no. 46, pp. 24462–24470, 2013.
- [157] H. Park, E. Bae, J.-J. Lee, J. Park, and W. Choi, “Effect of the anchoring group in Ru-bipyridyl sensitizers on the photoelectrochemical behavior of dye-sensitized TiO₂ electrodes: carboxylate versus phosphonate linkages,” *The Journal of Physical Chemistry B*, vol. 110, no. 17, pp. 8740–8749, 2006.

- [158] I. Grządka, M. Gierszewski, J. Karolczak, and M. Ziólek, “Comparison of charge transfer dynamics in polypyridyl ruthenium sensitizers for solar cells and water splitting systems,” *Physical Chemistry Chemical Physics*, vol. 20, no. 11, pp. 7710–7720, 2018.
- [159] J.-P. Rueff, J. Ablett, D. Céolin, D. Prieur, T. Moreno, V. Balédent, B. Lassalle-Kaiser, J. Rault, M. Simon, and A. Shukla, “The GALAXIES beamline at the SOLEIL synchrotron: inelastic X-ray scattering and photoelectron spectroscopy in the hard X-ray range,” *Journal of Synchrotron Radiation*, vol. 22, no. 1, pp. 175–179, 2015.
- [160] G. Guerrero, J. G. Alauzun, M. Granier, D. Laurencin, and P. H. Mutin, “Phosphonate coupling molecules for the control of surface/interface properties and the synthesis of nanomaterials,” *Dalton Transactions*, vol. 42, no. 35, pp. 12569–12585, 2013.
- [161] F. Brodard-Severac, G. Guerrero, J. Maquet, P. Florian, C. Gervais, and P. H. Mutin, “High-field ^{17}O MAS NMR investigation of phosphonic acid monolayers on titania,” *Chemistry of Materials*, vol. 20, no. 16, pp. 5191–5196, 2008.
- [162] P. Persson, S. Lunell, P. A. Brühwiler, J. Schnadt, S. Södergren, J. N. O’Shea, O. Karis, H. Siegbahn, N. Mårtensson, M. Bässler, *et al.*, “N 1s X-ray absorption study of the bonding interaction of bi-isonicotinic acid adsorbed on rutile $\text{TiO}_2(110)$,” *The Journal of Chemical Physics*, vol. 112, no. 9, pp. 3945–3948, 2000.
- [163] C. I. Oprea, B. Frecuș, B. F. Minaev, and M. A. Gîrțu, “DFT study of electronic structure and optical properties of some Ru- and Rh-based complexes for dye-sensitized solar cells,” *Molecular Physics*, vol. 109, no. 21, pp. 2511–2523, 2011.

- [164] B. C. O'Regan and J. R. Durrant, "Kinetic and energetic paradigms for dye-sensitized solar cells: moving from the ideal to the real," *Accounts of chemical research*, vol. 42, no. 11, pp. 1799–1808, 2009.
- [165] J. R. Durrant, S. A. Haque, and E. Palomares, "Towards optimisation of electron transfer processes in dye sensitised solar cells," *Coordination Chemistry Reviews*, vol. 248, no. 13-14, pp. 1247–1257, 2004.
- [166] S. E. Koops, B. C. O'Regan, P. R. Barnes, and J. R. Durrant, "Parameters influencing the efficiency of electron injection in dye-sensitized solar cells," *Journal of the American Chemical Society*, vol. 131, no. 13, pp. 4808–4818, 2009.
- [167] S. Yu, S. Ahmadi, M. Zuleta, H. Tian, K. Schulte, A. Pietzsch, F. Hennies, J. Weissenrieder, X. Yang, and M. Göthelid, "Adsorption geometry, molecular interaction, and charge transfer of triphenylamine-based dye on rutile TiO₂(110)," *The Journal of chemical physics*, vol. 133, no. 22, p. 224704, 2010.
- [168] K. Westermark, H. Rensmo, J. Schnadt, P. Persson, S. Södergren, P. Brühwiler, S. Lunell, and H. Siegbahn, "Electron dynamics within Ru-2, 2'-bipyridine complexes—an N1s core level excitation study," *Chemical physics*, vol. 285, no. 1, pp. 167–176, 2002.
- [169] B. P. Rimgard, J. Föhlinger, J. Petersson, M. Lundberg, B. Zietz, A. M. Woys, S. A. Miller, M. R. Wasielewski, and L. Hammarström, "Ultrafast interligand electron transfer in cis-[Ru(4,4'-dicarboxylate-2,2'-bipyridine)₂(NCS)₂]⁴⁻ and implications for electron injection limitations in dye sensitized solar cells," *Chemical science*, vol. 9, no. 41, pp. 7958–7967, 2018.
- [170] A. Kafizas, L. Francas, C. Sotelo-Vazquez, M. Ling, Y. Li, E. Glover, L. McCafferty, C. Blackman, J. Darr, and I. Parkin, "Optimizing the

- activity of nanoneedle structured WO_3 photoanodes for solar water splitting: direct synthesis via chemical vapor deposition,” *The Journal of Physical Chemistry C*, vol. 121, no. 11, pp. 5983–5993, 2017.
- [171] M. Ekman and V. Ozoliņš, “Electronic structure and bonding properties of titanium silicides,” *Physical Review B*, vol. 57, no. 8, p. 4419, 1998.
- [172] P. Weijs, M. Czyżyk, J. Fuggle, W. Speier, D. Sarma, and K. Buschow, “Electronic structure and bonding properties in TiSi_2 ,” *Zeitschrift für Physik B Condensed Matter*, vol. 78, no. 3, pp. 423–430, 1990.
- [173] P. Ritterskamp, A. Kuklya, M.-A. Wüstkamp, K. Kerpen, C. Weidenthaler, and M. Demuth, “A titanium disilicide derived semiconducting catalyst for water splitting under solar radiation—reversible storage of oxygen and hydrogen,” *Angewandte Chemie International Edition*, vol. 46, no. 41, pp. 7770–7774, 2007.
- [174] M. Hannula, H. Ali-Löytty, K. Lahtonen, J. Saari, A. Tukiainen, and M. Valden, “Highly efficient charge separation in model Z-scheme $\text{TiO}_2/\text{TiSi}_2/\text{Si}$ photoanode by micropatterned titanium silicide interlayer,” *Acta Materialia*, vol. 174, pp. 237–245, 2019.
- [175] Y. Lin, S. Zhou, X. Liu, S. Sheehan, and D. Wang, “ $\text{TiO}_2/\text{TiSi}_2$ heterostructures for high-efficiency photoelectrochemical H_2O splitting,” *Journal of the American Chemical Society*, vol. 131, no. 8, pp. 2772–2773, 2009.
- [176] Y. Lin, S. Zhou, S. W. Sheehan, and D. Wang, “Nanonet-based hematite heteronanostructures for efficient solar water splitting,” *Journal of the American Chemical Society*, vol. 133, no. 8, pp. 2398–2401, 2011.

- [177] W. Y. Yang, H. Iwakuro, H. Yagi, T. Kuroda, and S. Nakamura, “Study of oxidation of TiSi_2 thin film by XPS,” *Japanese journal of applied physics*, vol. 23, no. 12R, p. 1560, 1984.
- [178] P. Ravindran, L. Fast, P. A. Korzhavyi, B. Johansson, J. Wills, and O. Eriksson, “Density functional theory for calculation of elastic properties of orthorhombic crystals: Application to TiSi_2 ,” *Journal of Applied Physics*, vol. 84, no. 9, pp. 4891–4904, 1998.
- [179] H. Sezen and S. Suzer, “Dynamical XPS measurements for probing photoinduced voltage changes,” *Surface science*, vol. 604, no. 21-22, pp. L59–L62, 2010.

Appendices

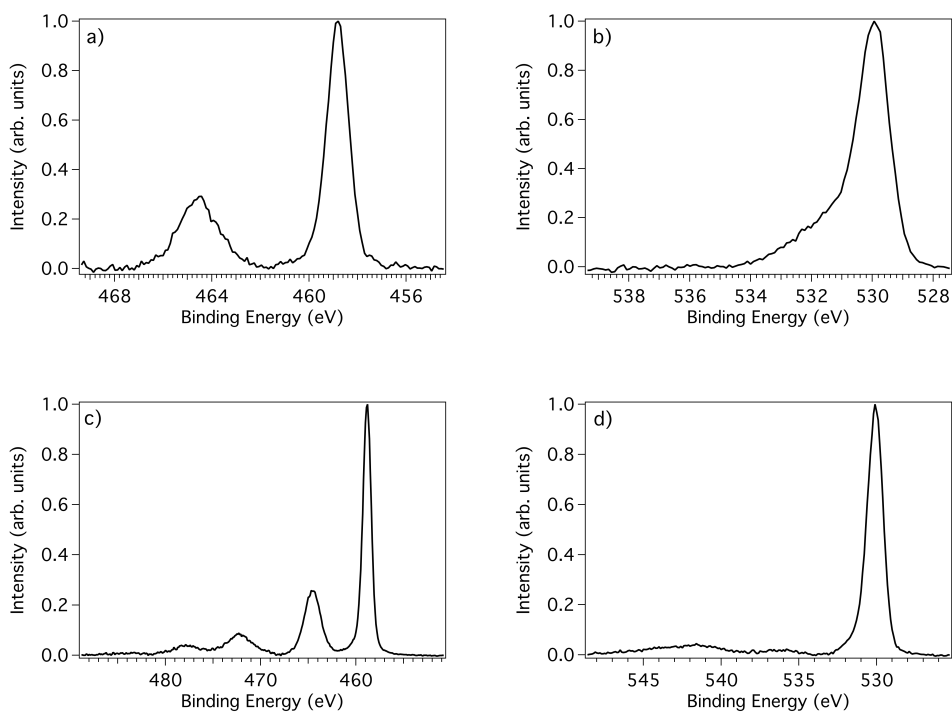


Figure A1: XPS of unsensitised, mesoporous, SrTiO₃ (a, b) and TiO₂ (c, d). The left spectra show the Ti 2*p*, and the right the O 1*s*. As for the spectra presented in the main text, the binding energy scale has been calibrated to the Ti 2*p*_{3/2} at 458.8 eV. The spectra were recorded using 1486.6 eV X-rays on a laboratory-based XPS. High binding energy shoulders are observed in both (b) and (d), which are attributed to hydroxyl contamination from the atmosphere, and in the case of SrTiO₃, potentially defects.

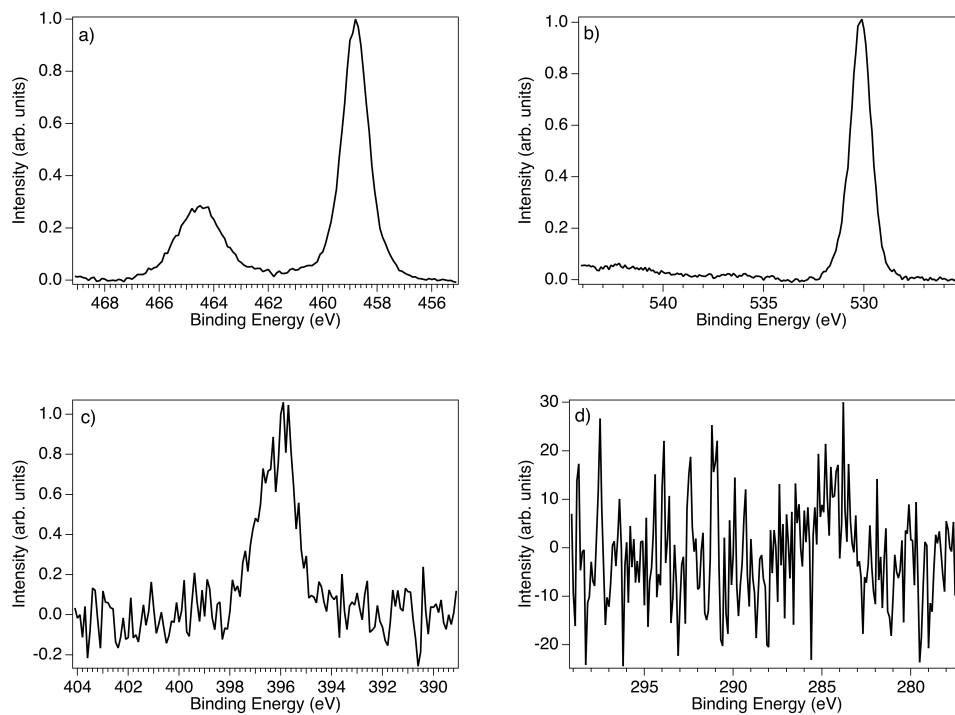


Figure A2: XPS of clean, unsensitised, $\text{TiO}_2(110)$: Ti $2p$ (a), O $1s$ (b), N $1s$ (c), and C $1s$ (d). Each spectrum is again calibrated to 458.8 eV and recorded using laboratory XPS with 1486.6 eV X-rays. The substrate shows a nitrogen peak unrelated to C343.

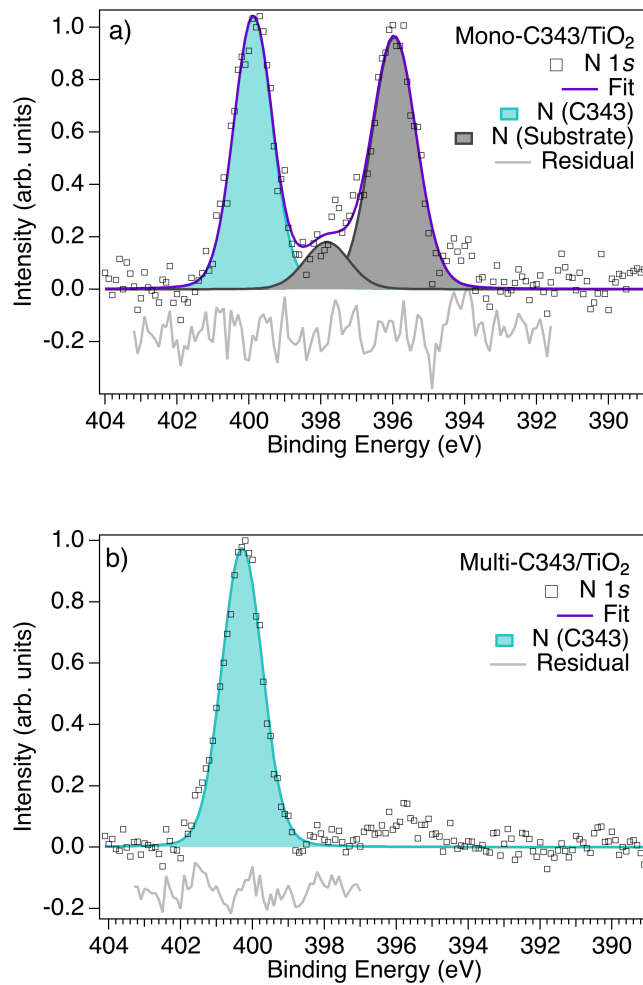


Figure A3: N 1s XPS of monolayer (a) and multilayer (b) C343 evaporated onto TiO₂(110). The spectra were calibrated to 458.8 eV, have had Shirley backgrounds subtracted, and were recorded using laboratory XPS with 1486.6 eV X-rays. Only one peak corresponding to C343 is observed.

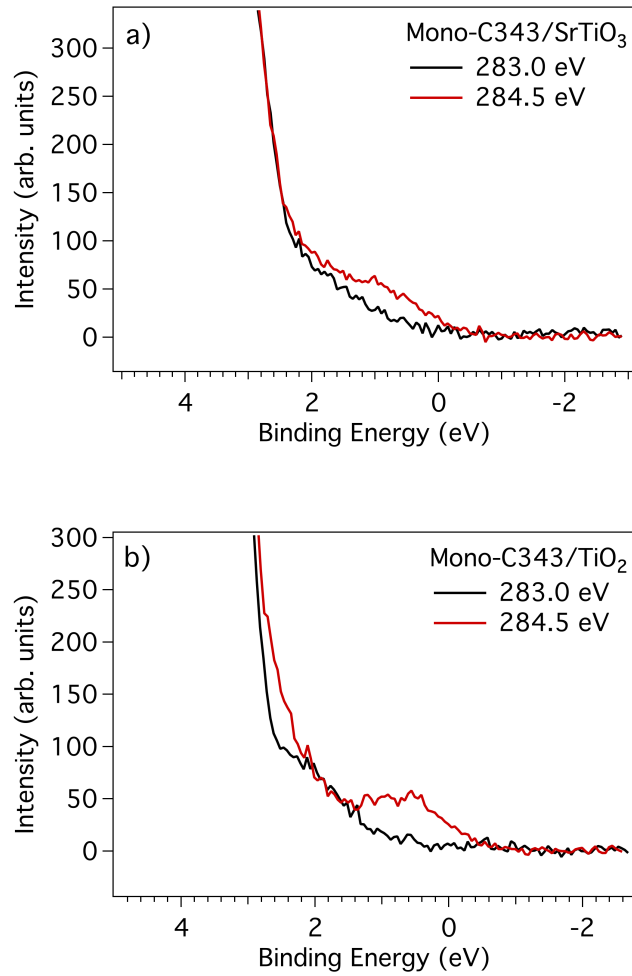


Figure A4: Zoomed-in view of the C K-edge RPES of C343 on SrTiO₃ (a) and TiO₂ (b). In both plots, the off-resonant scan (283.0 eV) is compared to an on-resonant scan (284.5 eV), illustrating that the feature caused by C 1s photoemission from second order light overlaps with the expected position of the HOMO.

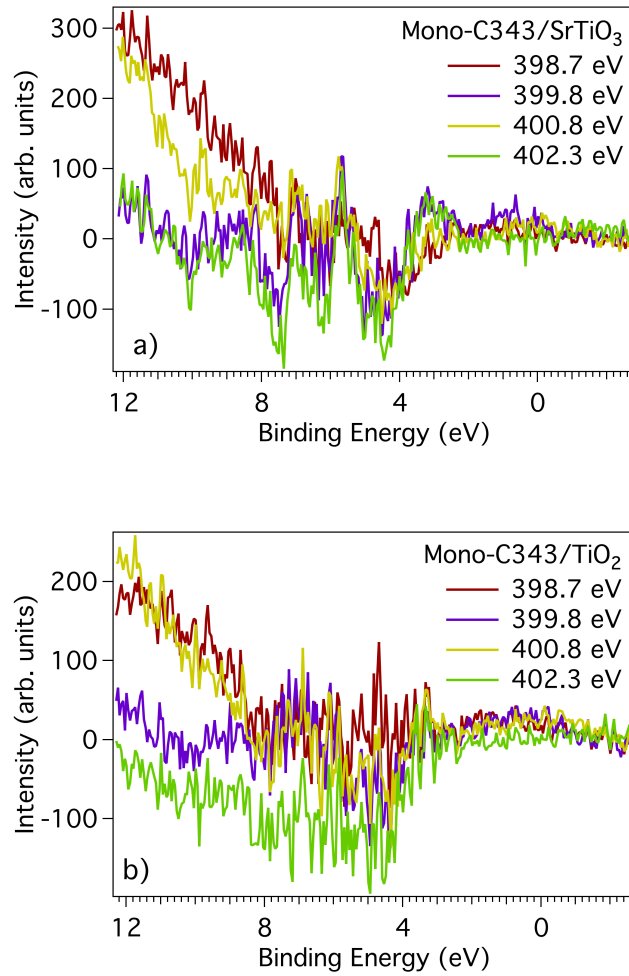


Figure A5: Difference spectra of the N K-edge RPES of C343 on SrTiO₃ (a) and TiO₂ (b) measured over the N K-edge. An off-resonant scan recorded at 397.0 eV has been subtracted from each subsequent scan to generate the difference spectra.

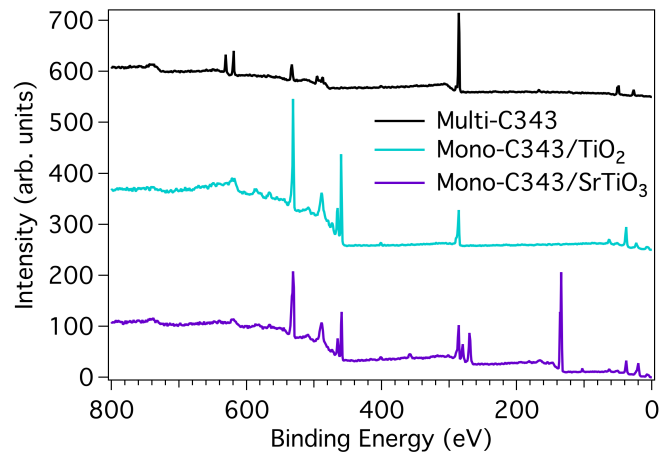


Figure A6: Wide XPS of each ex-situ C343 sensitised sample recorded using 1000 eV photons and a pass energy of 200 eV. The difference in thickness of the dye layer is illustrated by the C 1s signal, which is far more intense than other regions attributed to the molecule, such as the N 1s.

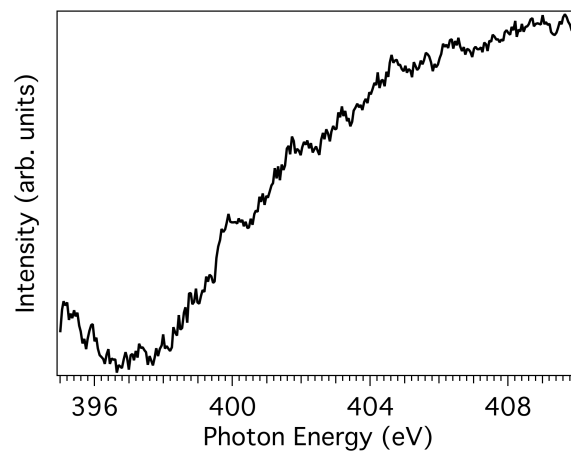


Figure A7: N K-edge NEXAFS of a mesoporous TiO_2 electrode soaked in acetonitrile for 30 minutes. No strong structure is observed, ruling out acetonitrile as the cause of the unknown peaks in the C343 XAS.

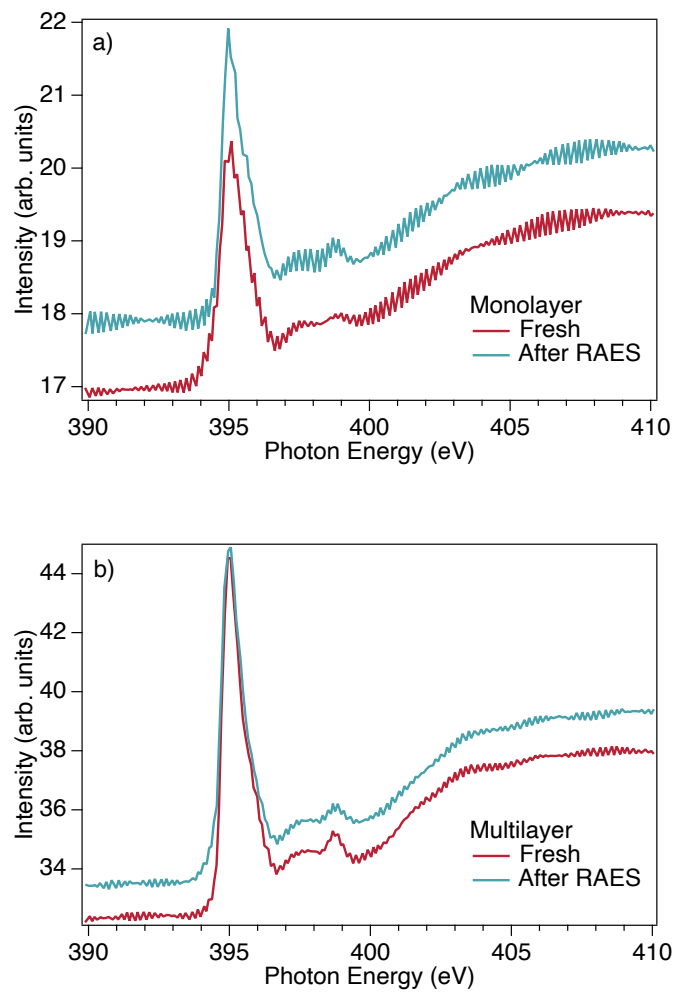


Figure A8: N 1s XAS of monolayer (a) and multilayer (b) N3 dye. No significant change is observed between before and after a RAES map was recorded, showing beam damage to be minor on the whole. The source of the oscillations in the signal is unknown.

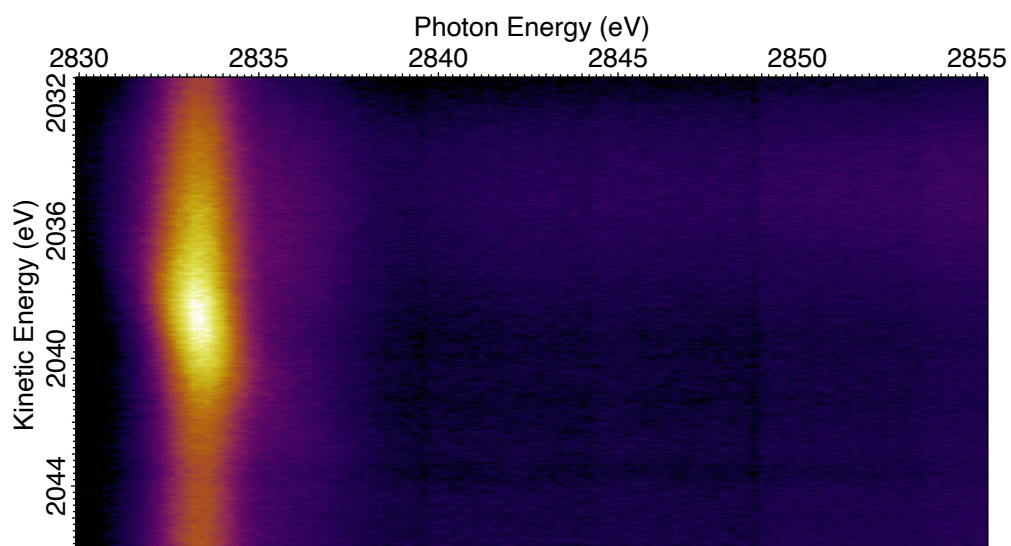


Figure A9: Ru LMM RAES recorded at the Ru $2p_{3/2}$ on multilayer N3. No behaviour indicative of any PCI is seen.

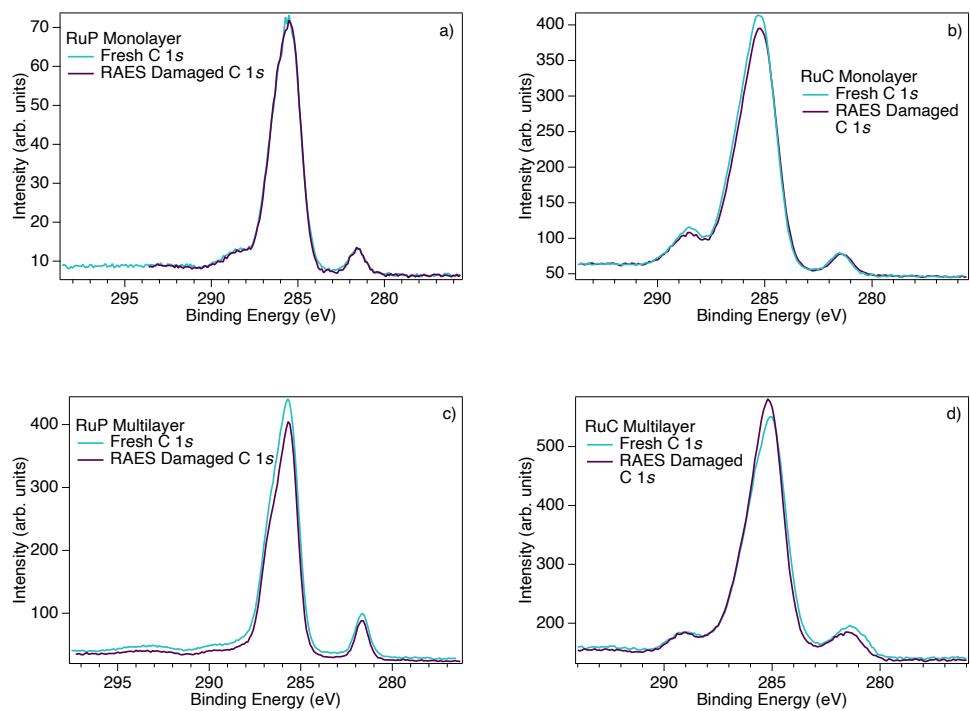


Figure A10: C 1s XPS of RuP (a, c) and RuC (b, d) monolayers and multilayers, before and after a RAES map was recorded. There is little sign that major beam damage has occurred.

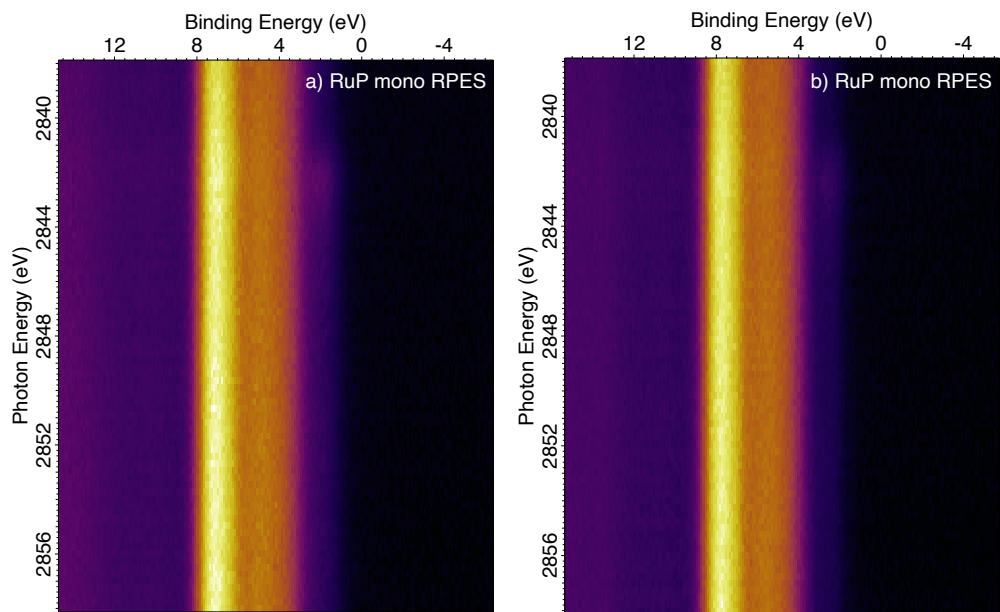


Figure A11: Ru $2p_{3/2}$ RPES maps for monolayer RuP (a) and RuC (b). The enhancement is weak when viewed in the map itself.

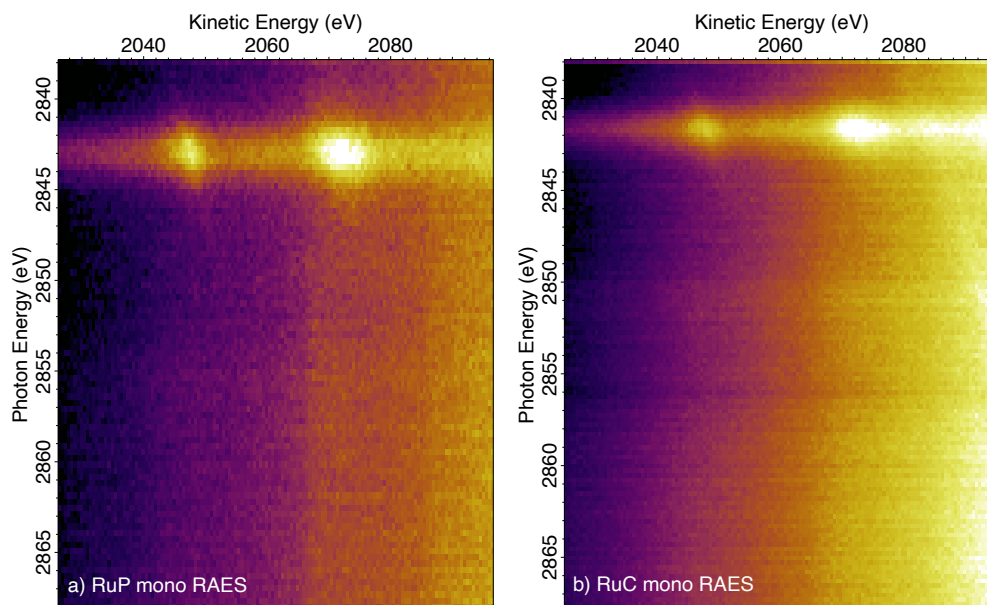


Figure A12: Ru $2p_{3/2}$ RAES maps for monolayer RuP (a) and RuC (b). These maps were integrated to obtain the auger yield XAS used in the core-hole clock implementation of RPES. No second resonance is seen in the map.